FERMILAB-THESIS-2021-53

Deep Inelastic Lepton-Nucleus Scattering

THESIS

submitted for the award of

Doctor of Philosophy

in

PHYSICS

by

FAIZA AKBAR

Supervisor
Prof. Mohammad Sajjad Athar
Department of Physics
Aligarh Muslim University, Aligarh

2020

Contents

Acknowledgments

All praises to the Almighty Allah for the blessings and patience to overcome obstacles in my life.

The work in this manuscript will be published with only my name printed on the cover page but there are lots of people who helped me to accomplish this huge task. First of all, I would like to express my sincere gratitude to my supervisor Prof. Mohammad Sajjad Athar at the Aligarh Muslim University and my co-supervisor Prof. Deborah Harris at the Fermilab for their guidance, motivation and immense support throughout my PhD work. I could not have imagined having better supervisors for my PhD course. Their kindness and consistent help with sympathetic attitude always helped to remain on track and not get diverged because of the complicacy of the subject. I would like to extend my gratitude to Prof. S. K. Singh for being a remarkable mentor and sharing his immense knowledge with me. I also want to thank Ms. Fouzia Ahmed for always being a caring and supportive person in my life.

My sincere thanks to the Chairman, Department of Physics, Prof. B. P. Singh for providing me all the required facilities for the completion of my research work.

I also want to thank the non teaching staff of my department, especially Mr. Naseem Ahmad Khan, Mr. Ashish Jacob, Mr. Musharraf Ali and Mr. Zeeshan Fazal, who relentlessly have been supportive, kind and always attentive to any kind of help I asked for. Thanks are due to seminar staff of the department, specially to Mr. Shakeel Kirmani for his support.

I must extend special thanks to Dr. Huma Haider for being an amazing adviser, senior and friend for all these years. You have always helped me irrespective of my problems and kept me sane.

I wholeheartedly thank my lab-mates, Dr. Shikha Chauhan, Dr. Farhana Zaidi, Dr. Atika Fatima, Mr. Zubair Ahmad Dar for helping me and providing a healthy working environment. I also thank Dr. Rafi Alam, for helping and encouraging me to learn new research tools and ideas.

I am thankful to every member of the MINERvA collaboration especially, Prof. Laura Fields, Prof. Kevin McFarland, Prof. Jorge Morfin, Prof. Gabe Perdue, Dr. Minerba Betancourt and Dr. Dan Ruterbories for sharing their advice and wisdom. I would also like to thank conveners of the inclusive working group, Prof. Jeff Nelson and Prof. Heather Ray, and inclusive group members: Anne, Maya, Dipak, Amy, Jennica, Gian, Adrian, Christian, Oscar for helping me in my analysis work. I also want to thank all the members of the LAIF group for the discussions and operation group especially, Howard Budd, Steve Hahn and Nuruzzaman.

Sincere thanks to my friends at home institution: Anisa Khatoon, Omveer Singh, Meeran Zuberi, Shaista Khan, Mariyah Siddique, Tabassum Naaz and at Fermilab: Anushree Ghosh, Maya Wospakrik, Mehreen Sultana, Jose Sepulveda, Deepika Jena, Barbara Yaeggy, Marvin Ascencio, Amit Bashyal, Andrew Oliver for helping and sorting out problems.

Last but not least, I want to express my extreme gratitude to the two pillars of my life, my parents(Ms Zakia Sultana and Mr. Akbar Husain) and my brother Mr. Mahmood Akbar for giving me their unwavering and unconditional love at all times and being supportive of all of my decisions. I love you.

Faiza Akbar

List of Publications

International

↬ Theoretical

1. **F. Akbar**, M. Sajjad Athar and S. K. Singh, "*Neutrino-nucleus cross sections in* ^{12}C *and* ^{40}Ar *with KDAR neutrinos*," J. Phys. G **44**, 125108 (2017).
2. **F. Akbar**, M. Sajjad Athar, A. Fatima and S. K. Singh, "*Weak quasielastic electroproduction of hyperons with polarization observables*," Eur. Phys. J. A **53**, 154 (2017).
3. **F. Akbar**, M. Rafi Alam, M. Sajjad Athar and S. K. Singh, "*Quasielastic production of polarized hyperons in antineutrino–nucleon reactions*," Phys. Rev. D **94**, 114031 (2016).
4. **F. Akbar**, M. R. Alam, M. S. Athar, S. Chauhan, S. K. Singh and F. Zaidi, "*Electron and Muon production cross sections in quasielastic* $\nu(\bar{\nu})$*-Nucleus scattering for* $E_\nu < 1$ *GeV*," Int. J. Mod. Phys. E **24**, 1550079 (2015).
5. **F. Akbar**, M. R. Alam, M. S. Athar, S. Chauhan and S. K. Singh, "*Study of Hyperon Polarization at T2K, MicroBooNE and MINER*ν*A*," Springer Proc. Phys. **203**, 475 (2018).

6. **F. Akbar**, M. R. Alam, M. S. Athar, S. Chauhan, S. K. Singh and F. Zaidi, "*Revisiting $\nu_\mu(\bar{\nu}_\mu)$ and $\nu_e(\bar{\nu}_e)$ Induced Quasielastic Scattering from Nuclei in Sub-GeV Energy Region*," JPS Conf. Proc. **12**, 010053 (2016).

↬ Experimental

1. A. Filkins *et al.* [**MINERvA Collaboration**], "*Double differential inclusive charged current ν_μ cross sections on hydrocarbon in MINERvA at $< E_\nu > \sim$ 3.5 GeV*" Phys. Rev. D **101**, 112007 (2020).
2. D. Coplowe *et al.* [**MINERvA Collaboration**], "*Probing Nuclear Effects with Neutrino-induced Charged-Current Neutral Pion Production*," Phys. Rev. D **102**, 072007 (2020).
3. M. F. Carneiro *et al.* [**MINERvA Collaboration**], "*High-statistics measurement of neutrino quasielastic-like scattering at $< E_\nu > \simeq 6$ GeV on a hydrocarbon target*," Phys. Rev. Lett. **124**, 121801 (2020).
4. T. Cai *et al.* [**MINERvA Collaboration**], "*Nuclear Binding Energy and Transverse Momentum Imbalance in Neutrino-Nucleus Reaction*," Phys. Rev. D **101**, 092001 (2020).
5. T. Le *et al.* [**MINERvA Collaboration**], "*Measurement of $\bar{\nu}_\mu$ Charged-Current Single π^- Production on Hydrocarbon in the Few-GeV Region using MINERvA*," Phys. Rev. D **100**, 052008 (2019).
6. E. Valencia *et al.* [**MINERvA Collaboration**], "*Constraint of the MINERνA medium energy neutrino flux using neutrino-electron elastic scattering*," Phys. Rev. D **100**, 092001 (2019).
7. P. Stowell *et al.* [**MINERvA Collaboration**], "*Tuning the GENIE Pion Production Model with MINERνA Data*," Phys. Rev. D **100**, 072005 (2019).
8. M. Elkins *et al.* [**MINERvA Collaboration**], "*Neutron measurements from antineutrino hydrocarbon reactions*," Phys. Rev. D **100**, 052002 (2019).

9. D. Ruterbories *et al.* [**MINERvA Collaboration**], "*Measurement of Quasielastic-Like Neutrino Scattering at* $\langle E_\nu \rangle \sim 3.5$ *GeV on a Hydrocarbon Target*," Phys. Rev. D **99**, 012004 (2019).
10. G. N. Perdue *et al.* [**MINERvA Collaboration**], "*Reducing model bias in a deep learning classifier using domain adversarial neural networks in the MINERvA experiment*," JINST **13**, P11020 (2018).
11. X. G. Lu *et al.* [**MINERvA Collaboration**], "*Measurement of final-state correlations in neutrino muon-proton meson less production on hydrocarbon at* $\langle E_\nu \rangle = 3$ *GeV*," Phys. Rev. Lett. **121**, 022504 (2018).
12. R. Gran *et al.* [**MINERvA Collaboration**], "*Antineutrino Charged-Current Reactions on Hydrocarbon with Low Momentum Transfer*," Phys. Rev. Lett. **120**, 221805 (2018).

National

↬ **F. Akbar**, F. Zaidi, S. Chauhan, M. R. Alam, M. S. Athar and S. K. Singh, "*Effect of second class currents in the few GeV energy region*," **DAE Symp. Nucl. Phys. 60**, 684 (2015).

↬ **F. Akbar**, F. Zaidi, S. Chauhan, and M. R. Alam "*Effect of lepton mass in neutrino induced quasielastic scattering*," **DAE Symp. Nucl. Phys. 59**, 660 (2014).

Chapter 1

Introduction

The quest of mankind is to search for the basic building blocks of matter. The knowledge which we have gathered till now tells us that the visible universe is made up of molecules, which in turn are made up of atoms. These atoms have structure and are made up of subatomic particles. The subatomic particles can be composite particles such as the neutron and proton, which themselves are made up of quarks (which are the elementary ones) or the elementary particles, like the electrons which are structureless. The first elementary particle in physics was born in 1897, when Thomson discovered the electron. Later in order to explain the structure of atom he thought that the electrons were suspended in a heavy, positively charged paste, like the plums in a pudding. However, very soon it was realized that Thomson's model was not correct and Rutherford decisively repudiated Thomson's hypothesis in alpha particle scattering experiment on gold foil, which showed that the positive charge, and most of the mass, was concentrated in a tiny core called the nucleus, at the center of the atom. Later Rutherford's model which had problem in explaining the stability of atom was better explained by Bohr in 1914 when he proposed a model for hydrogen atom as an object where a single electron orbits the proton and the orbit is quantized. A few years prior to that photon was another particle that had been added to the growing catalogue of elementary particles in physics when Einstein explained photoelectric effect con-

sidering photon as bundle of energy. The protons were discovered in 1917 and till the beginning of 1930s only the electron, proton and photon were the experimentally observed particles. In 1932, Anderson discovered positron, the antiparticle of the electron predicted by the Dirac's quantum field theory. After the positron's discovery almost a year later neutrons were discovered by Chadwick. In 1937, Anderson and Niedermeyer discovered a new particle which was initially called as meson but later this particle was identified as the heavy electron contemporarily known as "muon" and not the meson which were proposed by Yukawa in 1935 to be the carrier of the strong nuclear force. In 1947, the charged pions (the mesons predicted by Yukawa) were discovered in the photographic emulsion experiments. Many new particles (both mesons and baryons) were observed in the emulsion, bubble chamber and accelerator experiments during 1940s and 50s which led to the development of the quark model by Gell-Mann [1] and Zweig [2] independently in 1964. The quark model is used to classify all the mesons and baryons discovered at that time as well as the ones that had been observed later in terms of the different combinations of three quarks in the case of baryons and a quark-antiquark pair in the case of mesons. Since then particle physics has travelled a long way and now we know that the basic building blocks of matter are:

- the quarks, which exists in six flavors *viz.* up, down, strange, charm, top and bottom, and each flavor comes in three colors viz. red, blue and green,
- the leptons *viz.* electron, muon and tauon as well as their corresponding neutrinos,
- the mediating quanta *viz.* the photon (the quanta of electromagnetic interactions), gluons (the quanta of strong interactions) and $W^{\pm}$, Z^0 bosons (the quanta of weak interactions), and
- the Higgs boson.

The quarks and leptons are all spin $\frac{1}{2}$ particles and are called as fermions while the mediating quanta for the strong, electromagnetic and weak interactions, are

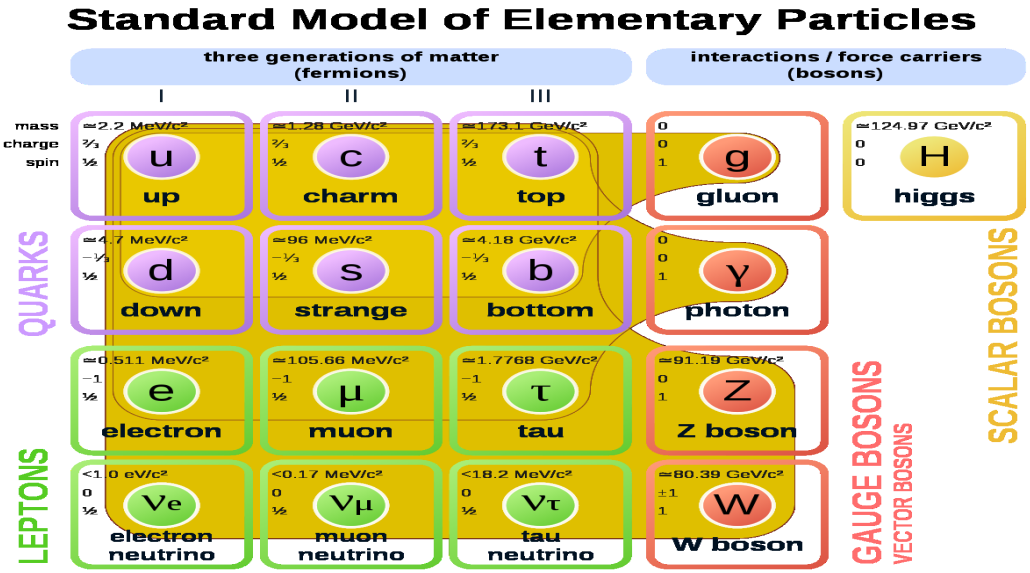

Figure 1.1: Building blocks of the Standard Model of particle physics.

spin 1 particles and belongs to the category of vector bosons. The Higgs is a scalar boson with spin 0 and is responsible for giving the masses to the particles through spontaneous symmetry breaking in the Standard Model. Corresponding to each quark and lepton, there is an associated antiquark and an antilepton, for example for up quark, an antiup, for an electron, the antiparticle is positron, etc.

Presently the best theory that describes the most basic building blocks of the matter is the Standard Model, which is a quantum field theory. It explains how particles called quarks and leptons make up all known matter and describes the fundamental particles and fields, along with their dynamics. In the Standard Model, there are presently 61 particles (Fig. 1.1), among which there are neutral leptons which are almost massless and interact only via the weak interaction with matter. These neutral leptons are called as neutrinos, which come in three flavors viz. ν_e, ν_μ and ν_τ as well as their antiparticles. Since these neutrinos are weakly interacting, therefore, they are very difficult to detect (mean free path of neutrinos in water is $\approx 10^{17}$m, and even in a highly dense matter like lead it is $\approx 10^{16}$m). In fact, they have never been directly observed although they are the second most abundant particles after the photons in the Universe. Now we shall present in

brief, why the neutrinos were required, if they have not been directly observed till date. The neutrinos have played a significant role since the beginning of the Universe. Without neutrinos, no element heavier than helium would have ever been synthesized. That means without the neutrinos there could not be carbon in our cell, nitrogen in our DNA, oxygen in air, and for that matter no water, and hence no life. Moreover, the neutrinos are responsible for the nuclear fusion processes that are taking place in the core of the Sun and all the stars in the Universe.

The journey of neutrino is quite interesting one which all started with the hypothesis by Pauli, in 1930, in order to explain the continuous nature of beta spectrum as well as to resolve the anomalies in spin-statistics. In a beta decay, a parent nucleus X is transformed into a slightly lighter nucleus Y, with the emission of an electron(or a positron):

$$X \longrightarrow Y + e^{-}(e^{+}). \tag{1.1}$$

Conservation of charge requires that Y carry one more(less) unit of positive charge than X, and the energy of the outgoing electron(positron) for a nucleus that decays at rest must be given by

$$E_e = \frac{M_X^2 - M_Y^2 + m_e^2}{2M_X}, \tag{1.2}$$

implying that E_e is fixed once the three masses are known and that is to say all the emitted electrons should have unique energy which corresponds to a discrete spectrum, while the experimentally observed spectrum was contrary to this expectation. For the first time, in 1911, multiple lines on a diffuse background of the kinetic energy distribution of beta particles was observed by Meitner and Hahn, however, the results were inconclusive about the continuous nature of the beta spectrum. A few years later, in 1914, Chadwick made more accurate measurements and concluded that the spectrum was continuous. During 1920-27, Ellis, Chadwick and others further confirmed the continuous nature of the beta spectrum.

The other problem was associated with angular momentum conservation law. It was observed that in beta decay like for the process

$$^{14}C(J=0) \rightarrow ^{14} N(J=1) + e^{-}(J=\frac{1}{2}), \tag{1.3}$$

the change of nuclear spin must be an integer in order to conserve angular momentum, whereas the presence of electron only was implying that angular momentum would not be conserved if beta decays were simply electron emission.

To overcome the problems associated with energy and angular momentum conservations, Pauli [3] proposed the existence of a new neutral weakly interacting particle of spin $\frac{1}{2}$ as the constituent of nuclei and called it as a "neutron" with the properties that the neutrons do not travel with the speed of light, have non-zero mass but less than 0.01 times the proton mass and have a magnetic moment of the order of $e \times 10^{-13}$ cm. For a more pedagogical development of the theory of neutrinos, one may look at Ref.[4].

In 1933, Fermi re-christened Pauli's "neutron" to contemporary "neutrino" and build the first theory of the β-decay. Fermi considered a beta decay to be a process of a quantum transition of a neutron into a proton with the creation of an electron-neutrino pair, in analogy with Quantum Electrodynamics, which is the theory of interaction of photons with matter. Fermi considered the Hamiltonian of the decay $n \rightarrow p + e^{-} + \bar{\nu}_e$ to be the interaction of four fermion fields and is the scalar product of the two vector interactions viz. $\bar{\psi}_p(x)\gamma^{\mu}\psi_n(x)$ involving hadrons, and $\bar{\psi}_{\nu_e}(x)\gamma_{\mu}\psi_e(x)$ involving leptons, which could be written as:

$$H^{\beta}(x) = G\bar{\psi}_p(x)\gamma^{\mu}\psi_n(x)\ \bar{\psi}_{\nu_e}(x)\gamma_{\mu}\psi_e(x) + Hermitian\ conjugate(h.c.), \tag{1.4}$$

where G is known as the weak coupling constant. Using the above Hamiltonian, he obtained the spectrum of electrons emitted in the β-decay and also suggested that using this method the mass of neutrino can be measured.

Later it was realized that there are beta decay processes which not only occur through Fermi transition ($\Delta J = J_f - J_i = 0$ with $0 \rightarrow 0$ transition) and no change in parity, but also take place via Gamow-Teller transition ($\Delta J = J_f - J_i = 0$

or ± 1 with $0 \rightarrow 0$ transition and change in parity being not allowed). Now the Hamiltonian given in Eq.1.4 had to be extended to include such transitions. To include both the Fermi as well as Gamow-Teller transitions, the Hamiltonian could be obtained using all the five bilinear covariants viz. 1(scalar (S)), γ_μ(vector (V)), $\gamma_\mu\gamma_5$(axial vector (A)), γ_5(pseudoscalar (P)),$\sigma_{\mu\nu}$ (tensor (T)) and can be written as:

$$H_i^\beta(x) = \sum_{i=S,V,A,P,T} G\bar{\psi}_p(x)O^i\psi_n(x)\ \bar{\psi}_{\nu_e}(x)O_i\psi_e(x) + h.c. \tag{1.5}$$

These beta decays involve very low energies, and in the non-relativistic limit, pseudoscalar term vanishes and the scalar and vector terms reduce to the Fermi interaction, while tensor and axial vector terms reduce to the Gamow-Teller interaction. Initially, many experimental results were supporting weak interaction Hamiltonian to contain scalar and tensor terms while only a few were favoring vector and axial vector combination. Sudarshan and Marshak [5] were of the view that it should be of V-A type, idea of which was also supported by Feynman and Gell Mann [6] and Sakurai [7]. With the discovery of parity violation in beta decay by Wu et al. [8] in 1956, the development of two-component theory of massless neutrino by Salam [9], Landau [10], Lee and Yang [11], almost about the same time, and immediate confirmation of the two-component neutrino theory in the experiment on the measurement of the neutrino helicity by Goldhaber et al. [12] in 1958, finally resulted to conclude that the weak interaction vertex should be of V-A nature. Later it was observed that the phenomenological $V-A$ theory of weak interactions explains all the weak interaction processes in the low energy region. However, when the theory was applied to higher energies, the cross section was observed to diverge with the increase in energy. This problem is generally called as the divergence in the theory of weak interactions and is resolved by taking instead of Fermi four point weak interaction to the weak interactions mediated by intermediate vector bosons. All the fermions, i.e. leptons and baryons participate in the weak interaction through their left handed component i.e. $\psi_L = (1-\gamma_5)\psi$, instead of ψ so that the interacting currents for the leptonic (l^μ) and the hadronic (J^μ) currents can be written as:

$$l^\mu \ = \ \bar{\psi}_e\gamma^\mu(1-\gamma_5)\psi_\nu \tag{1.6}$$

$$J^{\mu} = \bar{\psi}_p \gamma^{\mu}(1 - \lambda\gamma_5)\psi_n, \tag{1.7}$$

where λ is the relative strength of the axial current coupling compared to the vector current in hadronic sector.

A very important property associated with the neutrinos is that they oscillate, which was first theoretically proposed by Pontecorvo [13] in 1957-58. He suggested that if neutrino has nonzero mass then a neutrino may oscillate into an antineutrino $\nu_e \rightleftarrows \bar{\nu}_e$ in analogy with the $K^0 - \bar{K}^0$ oscillation [14]. It was suggested by Maki et al. [15] that if $\nu_e \neq \nu_\mu$; then ν_e could oscillate into ν_μ and vice versa. This possibility called the flavour oscillation was later formulated by Gribov and Pontecorvo [16] and Bahcall [17]. For oscillation to happen neutrino's mass should be nonzero. Interest in the neutrino oscillation physics started to grow after the early results of the solar neutrino experiments reported by Davis and his collaborators from the Homestake mines lab in USA [18, 19, 20], who observed ν_e flux from the sun which was smaller than the flux predicted by the contemporary solar models [21]. Later the deep underground detectors at Kamiokande [22, 23] in Japan and IMB collaboration [24] in USA, succeeded in detecting a depletion in the ν_μ flux relative to ν_e flux in the atmospheric neutrinos as compared to the theoretical calculations. The conclusion drawn from the observation of solar neutrinos by the SNO collaboration [25, 26] in Canada and atmospheric neutrinos by Super-Kamiokande collaboration [27, 28], Japan confirmed that neutrinos do oscillate.

The neutrino flavor states are different from the neutrino mass eigenstates and the flavor and mass eigenstates are related by the Pontecorvo-Maki-Nagakava-Sakata (PMNS) matrix. The main aim of the present day neutrino oscillation experiments is to measure precisely the different components of the PMNS matrix. The components of the PMNS matrix are expressed in terms of the three mixing angles θ_{12}, θ_{23} and θ_{13} and a CP violating phase δ_{CP}. Using the PMNS matrix, the transition probability for a neutrino of flavor α transforming into the flavor β is calculated in terms of the mixing angles as well as in terms of the neutrino mass squared differences Δm^2_{12}, Δm^2_{23} and Δm^2_{13}, where $\Delta m^2_{ij} = m^2_i - m^2_j;\ i, j = 1, 2, 3$

and $m_{1,2,3}$ corresponds to the mass of the neutrino mass eigenstates. The mass of ν_e, ν_μ and ν_τ are expressed in terms of the different combinations of m_1, m_2 and m_3.

These oscillation studies have been performed using solar, reactor, atmospheric and accelerator neutrino sources. Using accelerators, several experiments have been performed with a reasonably high statistics like K2K, LSND, CNGS, MiniBooNE, MicroBooNE, MINOS, MINOS+, etc. and many are going on like T2K and NOvA or planned with like DUNE and T2HyperK. For a general review of these experiments one may look at [29]. These experiments are working in the appearance and/or the disappearance modes which require a near as well as a far detector. In the disappearance experiments, the near as well as the far detector observe the same flavor of neutrinos as produced at the source and the difference in the number of neutrinos tells us how many neutrinos have disappeared i.e. oscillated into different flavors while traversing the distance between the near and far detectors. On the other hand, in the appearance experiments, the near detector detects the same flavor of neutrinos as produced by the source while the far detector is sensitive to the different flavor of neutrino, for example in a pure ν_μ beam at the production site, the flux of which is determined using a near detector, and the neutrinos that would be detected at the far detector may be a ν_e or ν_τ depending upon the detector sensitivity. Some of the oscillation experiments were the short baseline(SBL) experiments like LSND, MiniBooNE, MicroBooNE, etc., while some are the long baseline(LBL) experiments like K2K, CNGS, T2K, MINOS, NOvA, etc. or the proposed experiments like DUNE and T2HyperK. Some of the recent experiments are using neutrinos in the few GeV energy region, for example K2K had an average energy 1.3GeV, NOvA off axis has average neutrino energy about 2GeV or the proposed DUNE experiment is expected to have flux averaged neutrino energy of about 4GeV while the beam energy is expected to peak around 2.5GeV. Since the neutrino interactions are very weak, therefore, in order to observe a significant number of events, the detectors are using moderate to heavy nuclear targets like ^{12}C, ^{16}O, ^{40}Ar, ^{56}Fe, ^{208}Pb, etc., where the scattering

of neutrino/antineutrino takes place with a nucleon bound inside a nuclear target. Neutrino-nucleon and neutrino-nucleus reactions have played an important role in determining the various properties of the neutrino and the nucleon. Both the neutral current and the charged current interaction are being used to extract information on the neutrino properties, their interaction with matter and various parameters describing the weak interaction physics.

In the energy region of a few GeV the contribution to the cross section comes from all the possible channels viz. quasielastic(QE) scattering, inelastic(IE) scattering and the deep inelastic scattering(DIS) processes. The basic reactions for neutrino/antineutrino scattering from the nucleon target are

$$\begin{aligned}
\nu_l(k)/\bar{\nu}_l(k) + N(p) &\rightarrow l^-(k')/l^+(k') + N'(p') \\
\nu_l(k)/\bar{\nu}_l(k) + N(p) &\rightarrow l^-(k')/l^+(k') + N(p') + n\pi(p_\pi) \;\; ; \;\; n = 1, 2, 3, ... \\
\bar{\nu}_l(k) + N(p) &\rightarrow l^+(k') + Y(p') \\
\nu_l(k)/\bar{\nu}_l(k) + N(p) &\rightarrow l^-(k')/l^+(k') + \eta(p_\eta) + N'(p') \\
\nu_l(k)/\bar{\nu}_l(k) + N(p) &\rightarrow l^-(k')/l^+(k') + X(p'),
\end{aligned}$$

where N, N' stands for a nucleon(neutron or proton), Y is a hyperon and the quantities in the parenthesis represent the four momenta of the particles. The Feynman diagram for the above processes are shown in Fig. 1.2 for the weak interaction induced charged current processes.

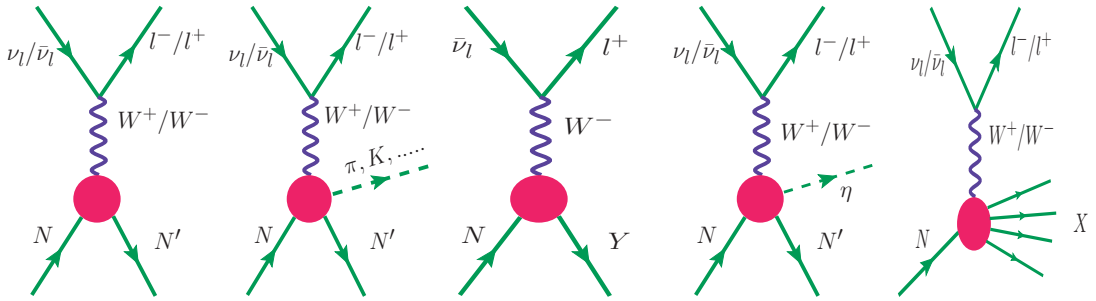

Figure 1.2: Feynman diagram representing(Left to Right) quasielastic scattering process, one pion production, one kaon production, single hyperon production, eta production, and the deep inelastic scattering process.

In Fig. 1.3, the total scattering cross sections for the neutrino and antineutrino induced processes are shown against the energy of the projectile beam and are compared with the results of earlier experiments. From the figure, it may be seen that QE process gives dominant contribution to the scattering cross section in the energy region of less than 1 GeV, however, in the region of 1 GeV $< E <$ 2 GeV resonance processes (mainly dominated by 1π production in the Δ resonance region) make significant contribution and beyond $E >$ 3 GeV DIS dominates. Furthermore, it is important to emphasize that in the intermediate energy region(1 GeV $< E_\nu <$ 3 GeV), $\nu_l/\bar{\nu}_l$ scattering processes lie mainly between the inelastic production of resonance excitation and the onset of DIS process.

In the case of QE and IE processes, the hadronic current consists of the hadronic form factors which gives information about the internal structure of the hadron. For the hadronic form factors, there is not very precise information even for a quasielastic scattering process as recently a wide range of axial dipole mass M_A(this will be discussed later in my thesis) has been discussed in literature. This becomes more true in the intermediate energy region(1 – 3GeV), where many resonances(R) contribute, and nucleon to resonance transition form factors are not very well understood. In the case of nuclear targets the things become more complicated as the nuclear medium effects come into play, which contribute significantly to the systematic uncertainties arising in these experiments. Moreover, it must be pointed out the nuclear medium effects(NME) arising in CCQE, IE and DIS processes are different from one another. For example, in the case of quasielastic scattering there is effect of Fermi motion, Pauli blocking, multinucleon correlation effects, etc, while in one pion production, there are additional effects that arises due to the modification of the Δ properties like mass and width in the nuclear medium and the final state interaction of pions with the residual nucleus. Thus, in order to determine precisely the neutrino oscillation parameters, or to understand CP violation in the leptonic sector, we have to first understand both theoretically as well as experimentally NMEs arising in the different neutrino energy regions. In recent past theorists as well as experimenters have started

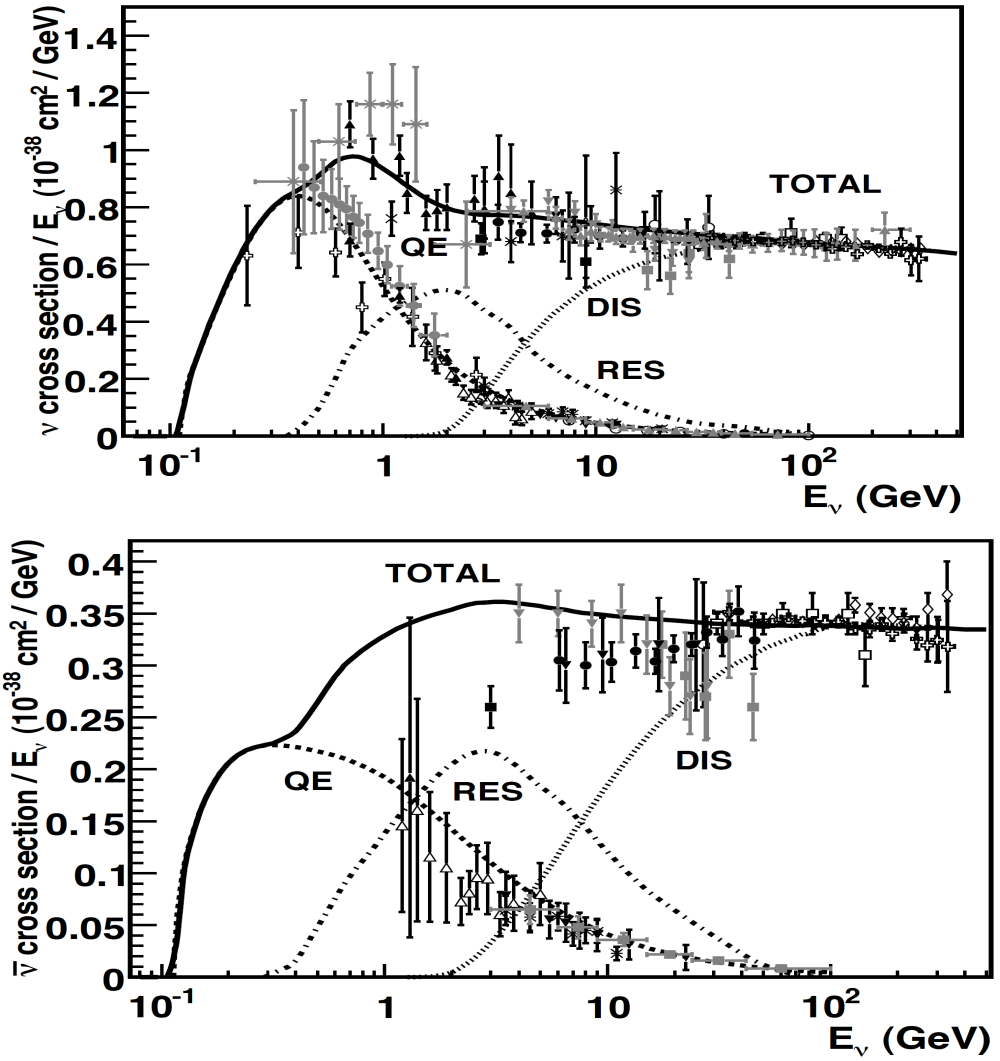

Figure 1.3: Different contributions to the neutrino cross section. The figure has been taken from Ref. [30].

making joint efforts to understand NME in the neutrino and antineutrino-nucleus scattering cross section. For more discussion please see [31]. At smaller scale ArgoNeuT [32, 33] and MicroBooNE [34] experiments have tried to undertstand neutrino interaction physics and more recently cross section measurements have also been performed in the T2K [35] and NOvA [36] experiments.

The most promising and dedicated neutrino interaction experiment using several nuclear targets like ^{4}He, ^{12}C, ^{16}O, ^{56}Fe and ^{208}Pb was planned at the Fermilab, acronymed MINERvA "Main Injector Experiment for ν(Neutrino)-A(Nucleus)" which has used neutrinos as well as antineutrinos obtained from the NuMI(Neutrinos

at the Main Injector) beamline and experiments were performed using $\nu/\bar{\nu}$ in the average energy range of 3GeV and 6GeV. The aim was to perform EMC (European Muon Collaboration experiment using charged lepton beam on several nuclear targets) kind of measurements to understand NME in both the neutrino as well as antineutrino modes in the wide region of x (Bjorken scaling variable) and Q^2(four momentum transfer square), covering the quasielastic, inelastic and the deep inelastic scattering regions [37, 38, 39]. This is expected to help a lot in understanding NME in the analysis of various neutrino/antineutrino oscillation experiments which are using some of these nuclear targets.

I have worked at MINERvA for almost four years and I am involved in the analysis of antineutrino interactions with the nuclear targets in the DIS region. I am one of the first Ph.D. students to use higher statistics antineutrino data obtained by the MINERvA detector. Before joining MINERvA, I have also worked at my home institution(Aligarh Muslim University, India) for almost three years on the theoretical understanding of neutrino-nucleon and neutrino-nucleus scattering cross sections. These studies were more confined to quasielastic scattering processes. Therefore, my work is divided into two parts. First I will introduce the work which I am performing during my stay at the Fermilab and will be discussed in Chapters 2 – 6 and then I will introduce the theoretical work, which will be discussed in Chapters 7 – 10. Finally I will conclude my findings in Chapter -11.

1.1 Experimental Work at the Fermilab

The NuMI beam facility [40], providing neutrinos in the energy range 1 – 10GeV, is a very high intensity beam facility developed almost two decades ago at the Fermi National Accelerator Laboratory, USA. Initially the aim was to provide neutrinos for the Main Injector Neutrino Oscillation Experiment(MINOS) and an another experiment(COSMOS) the plan for which was later abandoned. Later this facility was used to perform experiments like ArgoNeuT which was a Mini

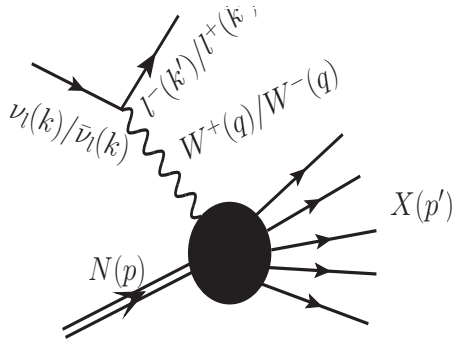

Figure 1.4: Feynman representation for the $\nu_l/\bar{\nu}_l$ induced DIS process off free nucleon target.

LArTPC(Liquid Argon Time Projection Chamber) detector and the experiments were performed in 2010, the MINOS+ experiment NOvA(NuMI Off-axis ν_e Appearance) experiment which is going on, and the MINERvA experiment, which has recently completed data taking initially in the neutrino mode and then in the antineutrino mode. Among these ArgoNeuT, MINOS and MINERvA were the cross section measuring experiments. MINERvA used neutrino/antineutrino beams in the two energy modes viz. Low Energy(LE) beam(peak energy $\sim$ 3GeV) and Medium Energy(ME) beam(peak energy $\sim$ 6 GeV) and experiments have been performed using several nuclear targets. In the medium energy region it is expected that more than 30% of the events would arise due to DIS processes. Before we present analysis for the DIS measurements at MINERvA, I am presenting in brief the expression for neutrino/antineutrino induced DIS cross section on a free nucleon target.

The basic reaction for the (anti)neutrino induced charged current deep inelastic scattering process on a free nucleon target is given by

$$\nu_l(k)/\bar{\nu}_l(k) + N(p) \rightarrow l^-(k')/l^+(k') + X(p') \quad l = e, \mu \tag{1.8}$$

where k and k' are the four momenta of incoming and outgoing lepton, p and p' are the four momenta of the target nucleon and the jet of hadrons produced in the final state, respectively. This process is mediated by the W-boson ($W^{\pm}$) and the invariant matrix element corresponding to the reaction given in Eq.1.8 is written

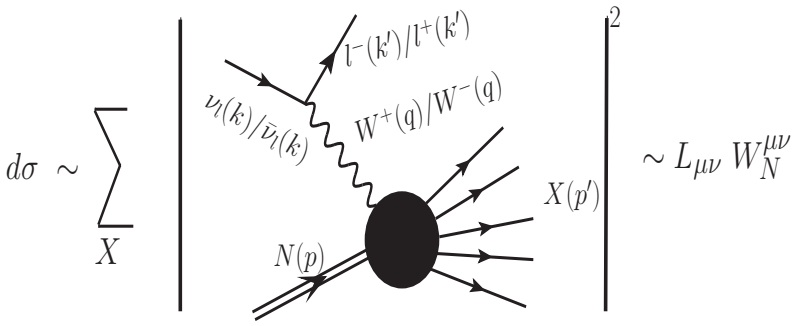

Figure 1.5: $\nu_\mu(\bar{\nu}_\mu) - N$ inclusive scattering where the summation sign represents the sum over all the hadronic states such that the cross section($d\sigma$) for the deep inelastic scattering $\propto L_{\mu\nu}W_N^{\mu\nu}$.

as

$$-i\mathcal{M} = \frac{iG_F}{\sqrt{2}}\, l_\mu \left(\frac{M_W^2}{q^2 - M_W^2}\right) \langle X|J^\mu|N\rangle \,, \tag{1.9}$$

where G_F is the Fermi coupling constant, M_W is the mass of W boson, and $q^2 = (k - k')^2$ is the four momentum transfer square. l_μ is the leptonic current and $\langle X|J^\mu|N\rangle$ is the hadronic current for the neutrino induced reaction (shown in Fig. 1.4).

The general expression of the double differential scattering cross section (DCX) corresponding to the reaction given in Eq. 1.8 (depicted in Fig. 1.5) in the laboratory frame is expressed as:

$$\frac{d^2\sigma}{dxdy} = \frac{yM_N}{\pi}\, \frac{E}{E'}\, \frac{|\mathbf{k}'|}{|\mathbf{k}|} \bar{\sum}\sum |\mathcal{M}|^2 \,, \tag{1.10}$$

where x and y are the scaling variables which lie in the ranges 0 to 1 in the limit $m_e, m_\mu \to 0$ and $\bar{\sum}\sum|\mathcal{M}|^2$ is the invariant matrix element square which is given in terms of the leptonic ($L_{\mu\nu}$) and hadronic ($W_N^{\mu\nu}$) tensors as

$$\bar{\sum}\sum |\mathcal{M}|^2 = \frac{G_F^2}{2} \left(\frac{M_W^2}{Q^2 + M_W^2}\right)^2 L_{\mu\nu}\, W_N^{\mu\nu}, \tag{1.11}$$

with $Q^2 = -q^2 \geq 0$. $L_{\mu\nu}$ is given by

$$L_{\mu\nu} \;=\; 8(k_\mu k'_\nu + k_\nu k'_\mu - k.k' g_{\mu\nu} \pm i\epsilon_{\mu\nu\rho\sigma}k^\rho k'^\sigma) \,. \tag{1.12}$$

Here the antisymmetric term arises due to the contribution from the axial-vector components with +ve sign for antineutrino and -ve sign for neutrino. The hadronic tensor $W_N^{\mu\nu}$ is written in terms of the weak nucleon structure functions $W_{iN}(\nu, Q^2)$ $(i = 1-6)$ as

$$\begin{aligned} W_N^{\mu\nu} &= \left(\frac{q^\mu q^\nu}{q^2} - g^{\mu\nu}\right) W_{1N}(\nu, Q^2) + \frac{W_{2N}(\nu, Q^2)}{M_N^2}\left(p^\mu - \frac{p.q}{q^2}\, q^\mu\right) \\ &\times \left(p^\nu - \frac{p.q}{q^2}\, q^\nu\right) - \frac{i}{2M_N^2}\epsilon^{\mu\nu\rho\sigma} p_\rho q_\sigma W_{3N}(\nu, Q^2) + \frac{W_{4N}(\nu, Q^2)}{M_N^2} q^\mu q^\nu \\ &+ \frac{W_{5N}(\nu, Q^2)}{M_N^2}(p^\mu q^\nu + q^\mu p^\nu) + \frac{i}{M_N^2}(p^\mu q^\nu - q^\mu p^\nu) W_{6N}(\nu, Q^2)\,. \quad (1.13) \end{aligned}$$

The contribution of the term with $W_{6N}(\nu, Q^2)$ vanishes when contracted with the leptonic tensor and the contributions of the terms with $W_{4N}(\nu, Q^2)$ and $W_{5N}(\nu, Q^2)$ are proportional to charged lepton mass, therefore, it vanishes in the case of ν_e and ν_μ induced DIS process as $m_l \to 0$. When Q^2 and ν become large the structure functions $W_{iN}(\nu, Q^2)$; $(i = 1-3)$ are generally expressed in terms of the dimensionless nucleon structure functions $F_{iN}(x)$, $i = 1-3$ as:

$$\begin{aligned} F_{1N}(x) &= W_{1N}(\nu, Q^2), \qquad F_{2N}(x) = \frac{Q^2}{2xM_N^2} W_{2N}(\nu, Q^2) \\ F_{3N}(x) &= \frac{Q^2}{xM_N^2} W_{3N}(\nu, Q^2). \end{aligned}$$

Now the hadronic tensor may be written in terms of dimensionless nucleon structure functions $F_{iN}(x, Q^2)$ $(i = 1-3)$ as:

$$W_N^{\mu\nu} = -g_{\mu\nu} F_{1N}(x, Q^2) + \frac{p_\mu p_\nu}{p.q} F_{2N}(x, Q^2) - i\epsilon_{\mu\nu\rho\sigma}\frac{p^\rho q^\sigma}{2p_1 \cdot q} F_{3N}(x, Q^2). \quad (1.14)$$

The expression for the differential scattering cross section given in Eq. 1.10 is written by using Eqs. 1.12 and 1.14 as:

$$\begin{aligned} \frac{d^2\sigma}{dxdy} &= \frac{G_F^2 M_N E_\nu}{\pi(1 + \frac{Q^2}{M_W^2})^2}\Big\{\Big[y^2 x + \frac{m_l^2 y}{2E_\nu M_N}\Big] F_{1N}(x, Q^2) + \Big[\Big(1 - \frac{m_l^2}{4E_\nu^2}\Big) - \Big(1 + \frac{M_N x}{2E_\nu}\Big) y\Big] F_{2N}(x, Q^2) \\ &\pm \Big[xy\Big(1 - \frac{y}{2}\Big) - \frac{m_l^2 y}{4E_\nu M_N}\Big] F_{3N}(x, Q^2)\Big\}. \quad (1.15) \end{aligned}$$

In general, the dimensionless nucleon structure functions are derived in the quark-parton model assuming Bjorken scaling in which they are written in terms of the parton distribution functions $q_i(x)$ and $\bar{q}_i(x)$ at the leading order as

$$F_2(x) = \sum_i x[q_i(x) + \bar{q}_i(x)]\ ;\ xF_3(x) = \sum_i x[q_i(x) - \bar{q}_i(x)] \quad (1.16)$$

In the case of $\nu(\bar{\nu})$-proton scattering above the charm production threshold, $F_{2,3}(x)$ are given by:

$$\begin{aligned} F_{2p}^{\nu}(x) &= 2x[d(x)+s(x)+\bar{u}(x)+\bar{c}(x)] \quad F_{2p}^{\bar{\nu}}(x) = 2x[u(x)+c(x)+\bar{d}(x)+\bar{s}(x)] \\ xF_{3p}^{\nu}(x) &= 2x[d(x)+s(x)-\bar{u}(x)-\bar{c}(x)] \quad xF_{3p}^{\bar{\nu}}(x) = 2x[u(x)+c(x)-\bar{d}(x)-\bar{s}(x)] \end{aligned} \tag{1.17}$$

and for the $\nu(\bar{\nu})$-neutron scattering $F_{2,3}(x)$ are given by

$$\begin{aligned} F_{2n}^{\nu}(x) &= 2x[u(x)+s(x)+\bar{d}(x)+\bar{c}(x)]\,; \quad F_{2n}^{\bar{\nu}}(x) = 2x[d(x)+c(x)+\bar{u}(x)+\bar{s}(x)] \\ xF_{3n}^{\nu}(x) &= 2x[u(x)+s(x)-\bar{d}(x)-\bar{c}(x)] \quad xF_{3n}^{\bar{\nu}}(x) = 2x[d(x)+c(x)-\bar{u}(x)-\bar{s}(x)]. \end{aligned} \tag{1.18}$$

For an isoscalar nucleon target, we use

$$F_{iN} = \frac{F_{ip}+F_{in}}{2}, \quad i = 1-3 \tag{1.19}$$

The structure functions $F_{1N}(x)$ at the leading order are written using Callan-Gross [41] relation as:

$$F_1(x) = \frac{F_2(x)}{2x}$$

The parton distribution functions (defined in Eqs.1.16, 1.17 and 1.18) for the nucleon have been determined by various groups and they are known in the literature by the acronyms MRST [42], GRV [43], GJR [44], MSTW [45], ABMP [46], ZEUS [47], HERAPDF [48], NNPDF [49], CTEQ [50], CTEQ-Jefferson Lab (CJ) [51], MMHT [52], etc.

The main focus of the experimental part of my thesis, is the understanding of the antineutrino induced charged current (CC) interactions with different nuclear targets(Carbon, Iron, Lead, Oxygen in water) in the DIS region using higher statistics. For the data set used in analysis, the peak energy of the antineutrino beam is ~ 6 GeV. The goal is to obtain the differential scattering cross sections with respect to different kinematical variables(x, y, Q^2, etc.) for all the nuclear targets used in the MINERvA detector and to take ratio of the cross sections with scintillator(CH) as the reference material. As MINERvA detector provides an opportunity to study the interactions of antineutrinos with different nuclear targets exposed to the same beam, this provides a good opportunity to understand the nuclear medium effects in the DIS processes.

After joining the collaboration, I got an opportunity to learn how to operate and debug different particle detectors during my training as the detector expert for MINERvA and MINOS-near detectors. While working on the detector, I tested photomultiplier tubes so that any leakage if identified could be repaired. Before starting our analysis, I have been involved in many groundwork studies like the data quality checks, removing bugs, etc. The bugs are then fixed on run by run basis and the data is made available for the analyzers.

The process of obtaining (anti)neutrino beam from NuMI facility at the Fermilab used in this analysis is explained in Chapter-2. NuMI beam travels to the MINERvA detector which is situated 330 feet below the ground in a cavern. In Chapter-3, different components and features of the MINERvA detector are described briefly. (Anti)Neutrino interactions in the detector are measured indirectly by measuring the scintillation light created by the charged particles. Finally, we have reconstructed these events so that it could be used for the physics information and this procedure has been explained in Chapter-4.

Depending on the experience, human mind can tackle a task with ease, more the experience better execution of the task at hand. This is also applicable to computers more precisely to artificial intelligence (AI). An application of AI that uses computer science along with statistics and enable computers to learn and improve without being explicitly programmed is known as Machine learning (ML). In ML, data is provided to the AI without prior programming, AI learns from statistical patterns of this data and performs the task. The most important advantage of machine learning is that it reduces the amount of hand-tuning done by the programmer. Instead, it utilizes the computer to extract the crucial features from the data and establishes the algorithms by which future data will be sorted. In the case of medium energy beam, (anti)neutrino reactions with nuclear targets give rise to lots of interactions and the analysis of these interactions become difficult as the interactions deposit a lot more energy in several parts of the detector, which makes the reconstruction more difficult than in the LE beam. For a nuclear target analysis, knowing the exact location of the interaction vertex is of utmost

importance. This problem is solved after employing ML approach for interaction vertex finding. In MINERvA detector, vertex finding problem is treated as image classification using Deep learning Neural Network (DNN) which is explain further in Chapter-5.

Chapter-6 includes the results obtained from the different analysis steps (event selection, efficiency calculation, background subtraction, unfolding) that lead to the extraction of the DIS cross section for different nuclear targets.

1.2 Theoretical Work at AMU

Precise calculations for quasielastic reactions in nuclei induced by $\nu_\mu(\bar{\nu}_\mu)$ and $\nu_e(\bar{\nu}_e)$ are required to study the CP violation and mass hierarchy in present experiments done in the sub-GeV energy region. Therefore, in this energy region, it is important to understand the differences that may arise in the electron vs muon production cross sections for neutrino/antineutrino scattering off free nucleon target as well as when the scattering takes place with a nuclear target, due to the lepton mass, the axial dipole mass M_A, pseudoscalar form factor and the inclusion of second class currents. Recently, Day and McFarland [53] studied the effect of lepton mass, radiative corrections and uncertainties in the nucleon electroweak form factors including the second class currents(SCC) on the (anti)neutrino CCQE scattering cross sections from the free nucleon targets. In their work, it has been shown that the radiative corrections at the tree level CCQE process may lead to important difference between electron and muon production cross sections [53], as it is proportional to $\log(\frac{E_l^*}{m_l})$, where E_l^* is the outgoing lepton energy in the center of mass frame and m_l is the mass of the charged lepton. Furthermore, the variation in the axial dipole mass M_A which has been recently discussed in the literature will also lead to difference in electron and muon cross sections. In literature, there exists different parameterizations of the pseudoscalar form factor based on the partially conserved axial vector current(PCAC) and Goldberger-Treiman (GT) relation,

Chiral Perturbation Theory and Lattice calculations, etc., which have been used to study the effect of pseudoscalar form factor [54, 55, 56, 57, 58]. Moreover, if one considers the presence of the second class currents, then there would be additional contribution to the (anti)neutrino nucleon cross sections due to the form factors in the vector and axial vector sector associated with them. The inclusion or non-inclusion of these contributions may translate into the systematic uncertainties in the determination of event rates. Some of these effects have not been taken into account in the (anti)neutrino Monte Carlo generators like GENIE [59], NEUT [60], NUANCE [61], NuWro [62], GiBUU [63], etc. In Chapter-7, we have studied the CCQE scattering cross sections from free as well as bound nucleons like in ^{12}C, ^{16}O, ^{40}Ar and ^{208}Pb nuclear targets in $E_{\nu(\bar{\nu})} \leq 1$ GeV energy region. The theoretical results are obtained using local Fermi gas model with and without random phase approximation(RPA) effects as well as these results have been compared with the other variants of the Fermi gas model available in the literature like that of Smith and Moniz [64], Llewellyn Smith [65] and Gaisser and O'Connell [66]. The dependence of M_A, vector, axial vector and pseudoscalar form factors and the effect of second class current on $\nu_e(\bar{\nu}_e)$ vs $\nu_\mu(\bar{\nu}_\mu)$ induced reactions on the nucleon as well as nuclear targets have been studied [67].

In Chapter-8, we have studied CCQE induced reaction for the high intensity monoenergetic muon neutrinos of energy 236 MeV obtained from kaon decay at rest (KDAR). KDAR experiment has been recently performed by MiniBooNE collaboration [68]. We have studied neutrino-nucleus cross sections in ^{12}C and ^{40}Ar and studied the theoretical uncertainties arising due to the nuclear medium effects in the neutrino-nucleus cross sections as well as in the angular and energy distributions of the charged leptons produced in the charged current induced reactions by ν_μ and ν_e in the energy region of $E_{\nu_e(\nu_\mu)} < 300$ MeV. The calculations have been done using the local density approximation which takes into account the nuclear effects due to the Fermi motion, binding energy and long range correlations. The results are also compared with the other calculations available in the literature [69].

For quasielastic(QE) process induced by antineutrinos, there is an additional channel where an antilepton is produced from nucleon target through the reaction $\bar{\nu}_l + N \rightarrow l^+ + Y(Y = \Lambda,\ \Sigma)$ i.e. a hyperon is produced in the final state. This channel is not allowed in the neutrino sector due to $\Delta S = \Delta Q$ selection rule. This process although Cabibbo suppressed has lower energy threshold (0.19 GeV for $\bar{\nu}_e p \rightarrow e^+\Lambda$ and 0.32 GeV for $\bar{\nu}_\mu p \rightarrow \mu^+\Lambda$), in comparison to strangeness conserving associated particle production process (0.9 GeV for $\bar{\nu}_e p \rightarrow e^+ Y K$ and 1.1 GeV for $\bar{\nu}_\mu p \rightarrow \mu^+ Y K$).

The knowledge of the transition form factors in the antineutrino induced quasielastic process of hyperon production is far from satisfactory. Recently, with the development of high intensity (anti)neutrino beams in the few GeV region, considerable interest has developed in understanding these weak transition form factors specially in the axial vector sector. These form factors have been determined experimentally and theoretically using Cabibbo theory assuming SU(3) symmetry and other symmetries of weak hadronic currents in the Standard Model. Most of these form factors are determined from the analysis of semileptonic decay of hyperons and neutron which are limited to very low momentum transfer. These form factors are found to be consistent with SU(3) symmetry which relates them to the form factors in $\Delta S = 0$ sector of (anti)neutrino–nucleon scattering and to the various couplings in semileptonic hyperon decays. However, the status of G–invariance, conservation of vector current(CVC), PCAC, etc. which seem to work quite well in the nucleon sector are not well understood when extended to octet of baryons using SU(3) symmetry which is known to be an approximate symmetry. Even though, the vast amount of data available on semileptonic decay of hyperons is consistent with the assumption of SU(3) symmetry, the violation of G–invariance and SU(3) symmetry is not ruled out [70]. There is no unambiguous way to implement SU(3) symmetry as far as CVC and PCAC are concerned but the prescriptions which have been used in literature to implement the symmetry, seem to work well [70, 71, 72]. The charged current quasielastic production of hyperons by antineutrinos is the most appropriate place to study

the nucleon-hyperon transition form factors which enables us to extend the study of form factors to higher Q^2 beyond the Q^2 values accessible in semileptonic hyperon decays. There are some experimental studies performed to determine these form factors from the cross section measurements done for these processes at CERN [73, 74, 75], BNL [76], FNAL [77, 78] and Serpukhov [79] which are limited by low statistics. Theoretically, these reactions have been studied for more than 50 years [80, 81, 82, 83, 84, 85, 86, 87, 88, 89, 90] but recently there has been renewed interest in studying these reactions [91, 92, 93, 94, 95, 96] due to the feasibility of doing experiments with the availability of high intensity antineutrino beams [97, 98, 99, 100, 101, 102].

Therefore, now there is possibility of studying the production cross section of hyperons and other strange particles as well as polarization of hyperons at present facilities at the Fermilab [97] and J-PARC [98] where high intensity beams of (anti)neutrino are available. The experiments planned with LArTPC detectors at MicroBooNE [99], and ArgoNeuT [100], and the proposed DUNE [101] and LAr1-ND, ICARUS-T600 [103] experiments at the Fermilab will be able to see charged hadrons in coincidence, thus making it possible to measure polarization in addition to the cross section measurements being done at MINERνA [102].

Keeping the above considerations in mind, in Chapter-9, we present the results for antineutrino induced quasielastic hyperon production from nucleon and nuclear targets. The inputs are the nucleon-hyperon(N–Y) transition form factors determined from the analysis of neutrino-nucleon scattering and semileptonic decays of neutron and hyperons using SU(3) symmetry. The calculations for the nuclear targets are done in local density approximation. The NME like Fermi motion, Pauli blocking and FSI effects due to hyperon-nucleon scattering have been taken into account. We have also studied the polarization components of the final hyperon produced in these reaction for free nucleons as well as for the heavy nuclear targets [104].

In Chapter-10, we have studied the weak quasielastic hyperon production off

the free proton target induced by electrons, *i.e.*, $e^- p \to \nu_e Y; Y = \Lambda, \Sigma^0$. The numerical results for the total cross section, differential cross section as well as the longitudinal and perpendicular components of polarization of the final hyperons (Λ and Σ^0 produced in these reactions) are presented and the sensitivity of these observables on the different vector and axial vector form factors has been compared. In this chapter, we have also compared the results of the total cross section for Λ, Σ^0 and Δ^0 productions and have shown that in the threshold region ($E_e < 0.4$GeV), the Λ production dominates the Δ production cross section [105].

Finally, in Chapter-11, we summarize the present work and conclude our findings.

Chapter 2

NuMI Beam

2.1 Introduction

NuMI is the acronym for "Neutrinos at the Main Injector". This is an accelerator source from which neutrino/antineutrino beams at the Fermi National Accelerator Laboratory(Fermilab) are finally obtained. Using NuMI beam many neutrino/antineutrino oscillation experiments like MINOS(Main Injector Neutrino Oscillation Search), MINOS+(Extended MINOS run using two detectors), NOvA(NuMI off axis ν_e Appearance), etc. and cross section experiments like ArgoNEUT(Mini LArTPC Exposure to NuMI beam), MINERvA (Main INjector Experiment:ν-A) have been performed. NuMI produces most intense neutrino/antineutrino beam in the world. It provides broad spectrum beam in different energy settings mainly classified as the Low Energy beam(peak energy $\sim$ 3GeV) and Medium Energy(ME) beam(peak energy $\sim$ 6 GeV) for both neutrinos as well as antineutrinos. The work described in this thesis has used MINERvA detectors. The goal of the MINERvA experiment was to perform a high statistics neutrino-nucleus scattering experiments. It was the first (anti)neutrino experiment in the world which has different nuclear targets viz. Helium, Carbon, Oxygen in water, Iron and Lead in the extreme range of mass number(A = 4 in Helium vs 208 in Lead) and the aim

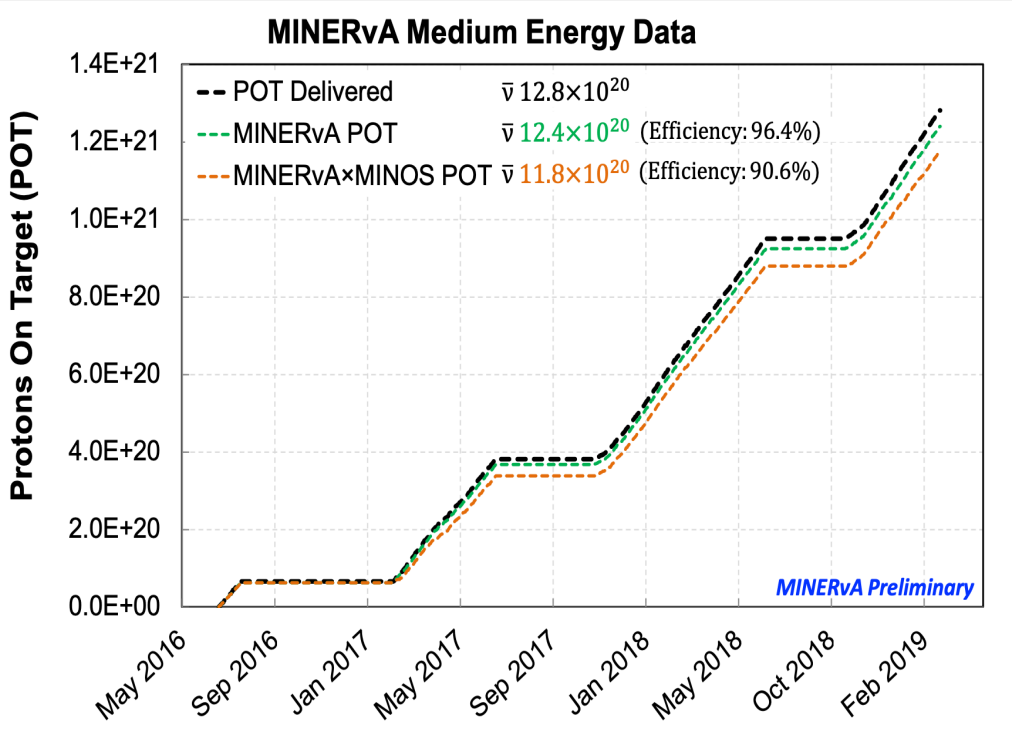

Figure 2.1: Protons on target (POT) received in antineutrino mode by MINERvA detector in ME configuration with respect to the time in months[106].

was to perform EMC (European Muon Collaboration experiment using charged lepton beam on several nuclear targets) kind of measurements to understand nuclear medium effects(NME) in both the neutrino as well as antineutrino modes in the wide region of x (Bjorken scaling variable) and Q^2(four momentum transfer square), covering the quasielastic, inelastic and the deep inelastic scattering regions. This was aimed to better understand NME in the analysis of various neutrino/antineutrino oscillation experiments which are using some of these nuclear targets as almost 25-30% uncertainty in the systematics arises due to the lack in the knowledge of NME. My work is mainly focussed on the interactions of antineutrinos on these nuclear targets. The complete duration of data taking in antineutrino mode for entire ME exposure of the MINERvA detector is shown in Fig. 2.1. The total number of protons on target (POT) received in antineutrino mode is 12.4×10^{20} [106]. In the next sections, we are going to describe in brief about the main features of NuMI beam and how neutrinos/antineutrinos are obtained.

Particle	Decay mode	Branching ratio(%)	Particle	Decay mode	Branching ratio(%)
π^+	$\mu^+\nu_\mu$	99.98770± 0.00004	K_s	$\pi^0\pi^0$	30.69± 0.05
	$\mu^+\nu_\mu\gamma$	$\sim 10^{-4}$		$\pi^+\pi^-$	69.20± 0.05
	$e^+\nu_e$	$\sim 10^{-4}$		$\pi^\pm e^\mp\bar{\nu}_e(\nu_e)$	$\sim 10^{-4}$
				$\pi^\pm\mu^\mp\bar{\nu}_\mu(\nu_\mu)$	$\sim 10^{-4}$
π^0	2γ	98.823 ±0.034			
	$e^+e^-\gamma$	1.174 ± 0.035			
$K^\pm$	$\mu^+\nu_\mu(\mu^-\bar{\nu}_\mu)$	63.56±0.11	K_l	$\pi^\pm e^\mp\bar{\nu}_e(\nu_e)$	40.55± 0.11
	$e^+\nu_e(e^-\bar{\nu}_e)$	$\sim 10^{-5}$		$\pi^\pm\mu^\mp\bar{\nu}_\mu(\nu_\mu)$	27.04± 0.07
	$\pi^0\ e^+\ \nu_e$	5.07± 0.04		$\pi^0\pi^0\pi^0$	19.52± 0.12
	$\pi^0\mu^+\nu_\mu$	3.352± 0.033		$\pi^+\pi^-\pi^0$	12.54±0.05
	$\pi^+\pi^0$	20.67± 0.08		$\pi^+\pi^-$	$\sim 10^{-3}$
	$\pi^0\pi^+\pi^0$	1.760± 0.023		$\pi^0\pi^0$	$\sim 10^{-4}$
	$\pi^+\pi^+\pi^-$	5.583± 0.024			

Table 2.1: Decay modes with the corresponding branching ratios of charged as well as neutral pions and kaons.

2.2 Neutrinos at NuMI beam

The neutrino beam at the NuMI facility is generated by bombarding protons of momentum 120 GeV/c on a meter long narrow graphite target (mainly proton-carbon collision). The collision produces mesons, mainly pions ($\geq$ 96 %) and kaons. The charged mesons are focused in a relatively narrow beam using a pair of pulsed magnetic horns to focus π^+ or π^- beam which decay (Table-2.1) in a pipe which is 2m wide, 675m long, and held at a vacuum of $\sim$ 1 atm, to give rise to ν_μ or $\bar{\nu}_\mu$, respectively. To achieve pure neutrino beam, secondary hadrons and the non-interacting protons are flushed out from the beam at the end of the decay pipe with the help of a hadron absorber consisting of aluminum, steel and concrete structure just downstream of the decay pipe. The beam passes through 240m of dolomite to filter out muons in the beam. The NuMI beam monitoring system has arrays of four helium gas ionization chambers. The first array is to monitor the hadrons and it measures the spatial distribution of the protons as well as hadrons

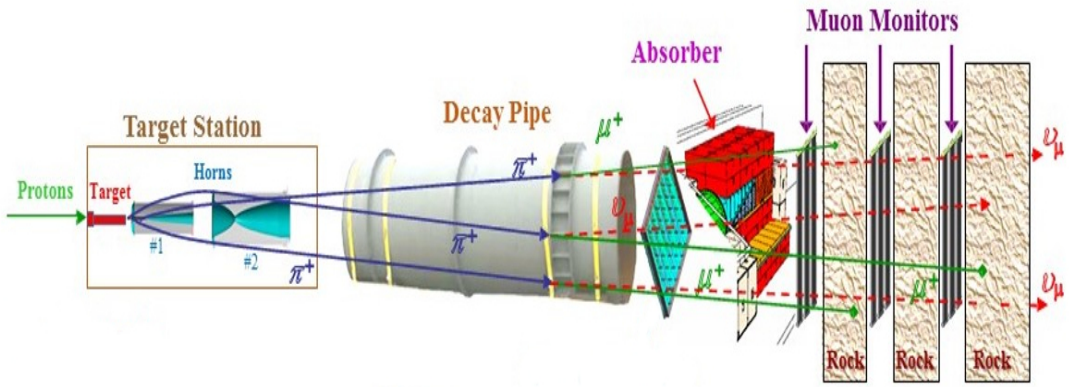

Figure 2.2: NuMI beam line[108].

those were produced due to proton interactions. Then the other three arrays are the muon monitors to measure the spatial distribution of the muon beams. Neutrino/Antineutrino beam traverse 240m of earth crust to reach MINERvA detector. The schematic diagram of NuMI beam line is shown in Fig. 2.2 [107].

2.3 The Proton beam and slip stacking

The proton beam at the Fermilab originates as hydrogen ions which are accelerated to 400 MeV using roughly 500-foot long, 40 years old Linear Accelerator at the Fermilab Accelerator Complex(Fig. 2.3). The hydrogen atoms are converted to positively charged protons as they enter to the rapid-cycling-synchrotron (RCS) Booster by passing through a carbon foil. It further accelerate the protons to 8 GeV [109, 110]. From there, protons move to the Recycler ring, which is seven times bigger than the Booster ring in circumference. This enables the Recycler ring to host seven batches simultaneously, only six batches are used and one slot is reserved to enable the extraction kicker to ramp up. In total, six batches are delivered in the duration of 10 μs. Each batch is 1525 ns long and 92 ns apart from each other. The Main Injector(MI) ring is right underneath the Recycler ring. MI captures the proton batches from Recycler ring, accelerates them to 120 GeV and every 1.3s sends the beam to the NuMI target.

MI sends six batches of protons to the NuMI target however, to increase the intensity of the beam, the Fermilab Accelerator Division can inject six more batches in the MI ring in addition to six original batches, making the total of 12 batches. This is called *slip-stacking* technique. Using this technique, the intensity of the beam is increased incrementally for the neutrino mode. In the antineutrino mode, all the data collected have 6+6 batch sizes. For the 6+6 configuration, the batches have the same timing structure as the no slip-stacking batches but they have much higher intensity.

2.4 NuMI target

NuMI target hall is an underground cavern that accommodates all the major beam components like NuMI target, focusing horns etc. The NuMI target is a rectangular graphite rod made of 48 segments as show in Fig. 2.4. Length of each fin is 24 mm along the beam direction, 63 $\times$ 7.4 mm^2 in cross sectional view. The NuMI target is surrounded by two stainless steel pipes acting as coolant and enclosed in an aluminum alloy container filled with gaseous helium. The total length of the target is 2.5 nuclear interaction lengths[107, 111]. When a collimated proton beam accelerated to 120 GeV strikes on the target, many hadrons are produced. The gap between the fins prevent the interactions of the secondary mesons with the target. In the final calculation of the cross section, these *tertiary interactions* causes systematic uncertainty as they affect how well we know our final antineutrino flux [112, 113].

2.5 Focusing horns

Mesons created by the interaction of the proton beam with the NuMI target are focused in a particular direction using two magnetic horns. The length of each horn is between 3.4 and 3.6m and they are made up of aluminum, shown in Fig. 2.5.

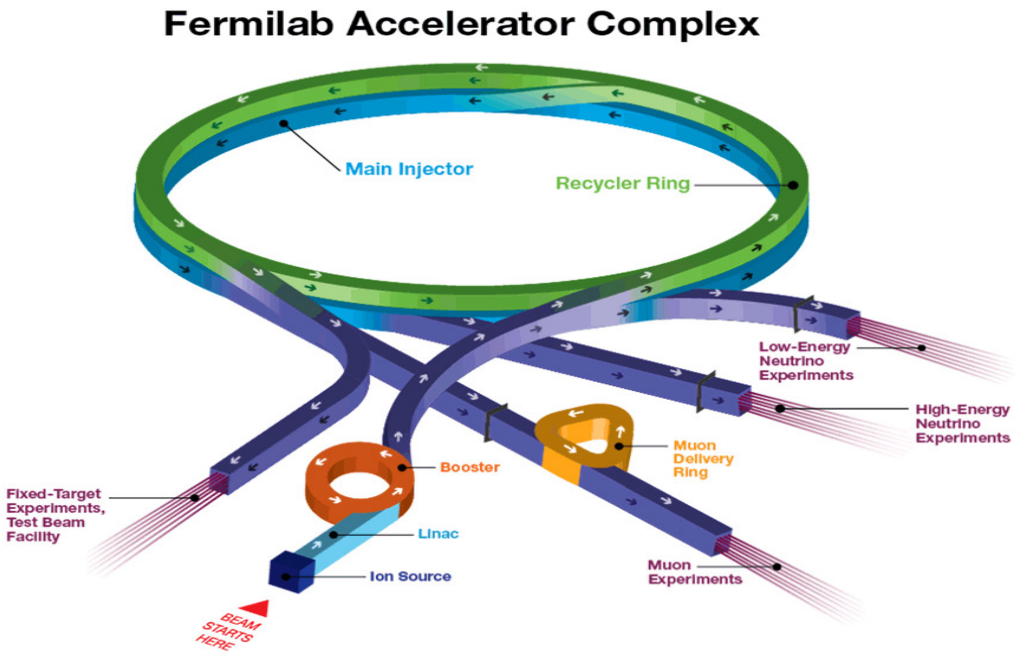

Figure 2.3: The Fermilab Accelerator Complex[114].

The horns are pulsed with 200kA current in a loop from the outer conductor to the inner conductor, this generates a toroidal magnetic field in the volume between the conductors. The direction of the current determines the polarity of the mesons focused by the horns. If horns have -200kA current (Forward Horn Current mode) applied then positively charged mesons are focused, leading to a neutrino dominant beam. Similarly, if +200kA current (Reverse Horn Current mode) is applied to the horns then negatively charged mesons are focused, leading to an antineutrino dominant beam. The data used in this analysis are collected in the Reverse Horn Current mode(RHC).

When the NuMI target is not very close to the first horn, in the thin lens approximation, the horns act as lenses to the incoming mesons. By Ampere's law

$$B = \frac{\mu_0 I}{2\pi R},$$

when constant current(I = 200kA) is applied along the inner conductor, then

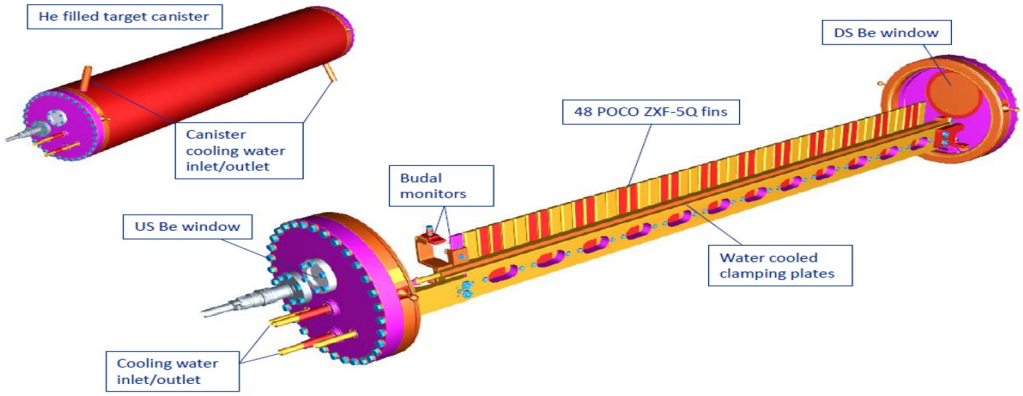

Figure 2.4: NuMI medium energy-era target[115].

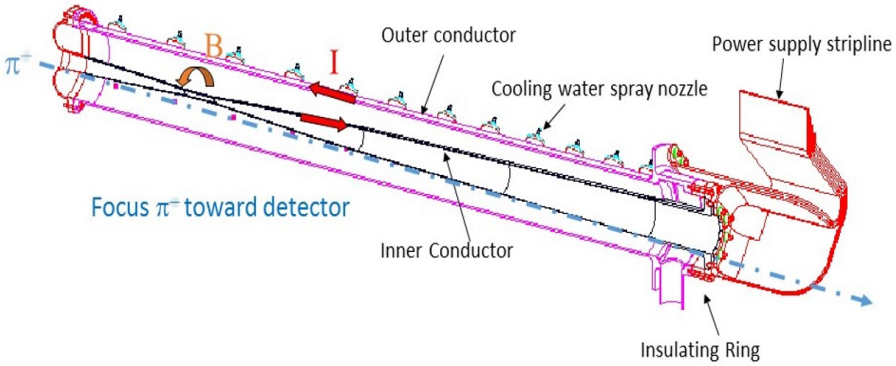

Figure 2.5: Magnetic horns[116].

the generated magnetic field (B) drops to zero at radii(R) smaller than the inner conductor. For radii greater than the inner conductor, between the inner and outer conductors B is inversely proportional to the R. Mesons produced with very high longitudinal momentum passes through the horns unaffected. Mesons having desired charge for neutrino or antineutrino beam which are over or under focused by the first horn, may get aptly focused by the second horn (shown in Fig. 2.6). Wrong sign mesons are de-focused by the horns. Wrong sign charged meson with very high longitudinal momentum ends up contaminating the beam. As the interaction of the protons with the target results in the production of more positively charged mesons then negatively charged, this leads to significant wrong sign contamination in the antineutrino beam at high energies. The energy range of the secondary mesons focused by the horns depends on the position of the NuMI target with respect to the first horn. The distance between the target and the first

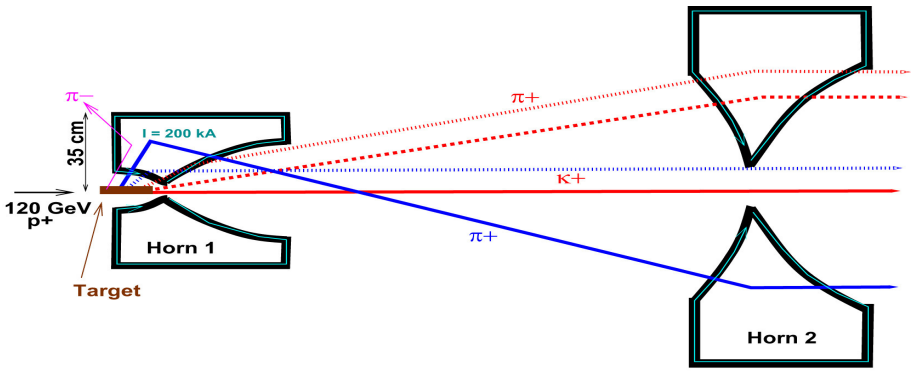

Figure 2.6: View of horns along the beam direction operating in FHC mode[118].

horn can be changed and the separation between two horns is also adjustable. The setup of the target and the two horns corresponds to three different energy settings for the beam. From the upstream end of the first horn, second horn can be moved to 10 m, 23 m, and 37 m apart downstream corresponding to low, medium and high energy respectively, combined with appropriate target movement upstream [107]. In the NuMI beam configuration, this is the last place where the beam can be actively controlled.

The distribution of correct and wrong sign neutrinos for RHC is shown in Fig. 2.7.

2.6 Decay volume

The next piece in the NuMI beam ensemble is Decay pipe. Secondary charged mesons created by the interactions of primary proton beam with the NuMI target, focused by the two magnetic horns enters in a 675m long and 2 m wide decay pipe filled with 1 atm of helium. The length of the decay pipe is chosen 675 m as it is approximately the length required for the decay of a 10 GeV pion[119]. The opening angle of the low energy mesons is greater than that of high energy mesons, and thus a wider radius for the decay pipe would accommodate more meson trajectories and produce more neutrinos. The decay pipe starts 46 m downstream

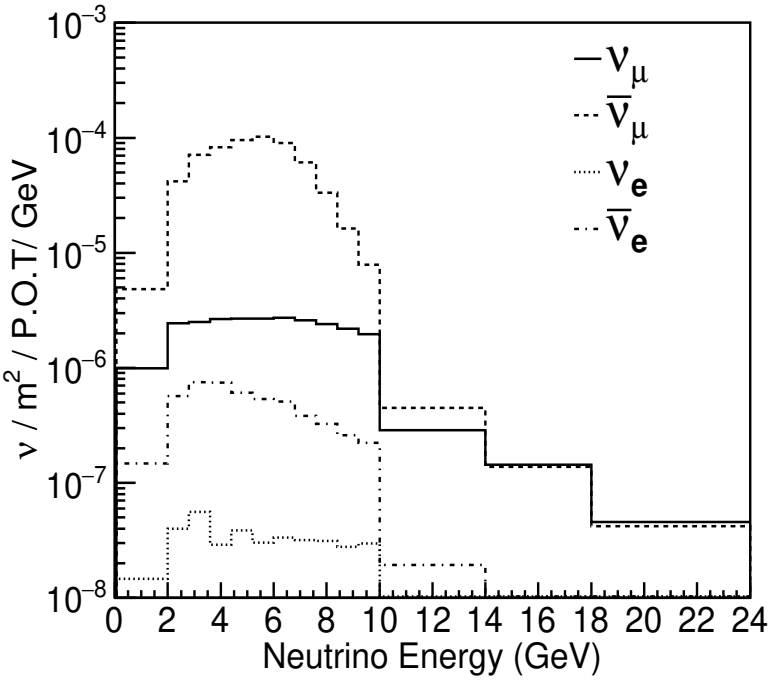

Figure 2.7: Medium energy flux in Reverse Horn Current mode[117].

of the NuMI target. In the decay pipe, secondary mesons(mainly pions, kaons) decay into tertiary neutrinos. Charged kaons have several significant decay modes that produce neutrinos. They do not just decay in muons and neutrinos but also decay in electrons creating a small fraction of electrons neutrinos (Table-2.1) in NuMI beam.

2.7 Absorber and Muon Shield

The beam exiting decay pipe is comprised of primary protons that did not interact with NuMI target, secondary mesons that have not yet decayed and tertiary neutrinos. To get a pure beam of tertiary neutrinos, massive aluminum, steel and concrete structure are assembled just downstream of the decay pipe known as absorber. It is essentially a box approximately 5.5 m wide, 5.6 m tall and 8.5 m long. The absorber is multi-functional:

- most of the protons still remaining in the beam are stopped in the absorber as beam passes; neutrinos and muons pass through it virtually unaffected.
- it serves to protect ground-water from irradiation.
- it limits the levels of radiation in the areas accessed by personnel in both beam-on and beam-off conditions.

Downstream of absorber and upstream of MINOS-ND hall, there is 240 m long solid dolomite rock which acts as muon shield leaving only neutrinos in NuMI beam. In the dolomite rock, three muon monitors are installed at the distances where 4, 10, and 20 GeV muons would range out to monitor the shape of the muon beam, which is expected to approximately mimic the shape of the neutrino beam.

In the next chapter, we are going to briefly discuss the main features of the MINERvA detector.

Chapter 3

MINERvA Detector

3.1 Introduction

MINERvA is a multi layered detector, placed about a kilometer away from the NuMI target and 330 feet below the ground in a cavern originally used for housing MINOS near detector. The core of the detector is hexagonal in shape and is approximately 5m long and has inner and outer regions. Further, the inner detector, consists of four sub-detectors arranged longitudinally. These four sub-detectors are (i) the nuclear target region, (ii) the fully active tracking region, (iii) downstream electromagnetic calorimeters, and (iv) downstream hadronic calorimeters. While the outer detector is a shell of hadronic calorimeters that surround the inner detector and also to physically support the inner detectors. Fortunately, MINERvA has the advantage of MINOS near detector which sits downstream and serves as a toroidal muon spectrometer.

The high intensity neutrino/antineutrino beam generated at NuMI reaches the MINERvA detector after passing through 240m of dolomite rock. Neutrinos can interact with the rock resulting in the production of muon, known as *rock muon* in the MINERvA experiment. Most upstream component of the MINERvA detector is *veto wall*, used to monitor the rock muons entering the detector, followed

by a 250 kg liquid helium target. 120 hexagonal *modules* are stacked together along the beam axis to form the 5m long body of the detector. Each of these modules are comprised of inner detector(ID) and outer detector(OD). ID consists of passive nuclear targets(iron, lead, carbon and water) and active scintillator planes. Downstream of the detector has electromagnetic calorimeter(ECAL) and hadronic calorimeter(HCAL). MINOS near detector is situated 2 m downstream from the end point of MINERvA detector, used as toroidal muon spectrometer. The schematic of the MINERvA detector along the beamline axis is shown in Fig. 3.1. The components of MINERvA detector and the calibration process are summarized below, and explained in detail in [120].

The passive targets are numbered upstream to downstream 1–5. The targets are built out of transverse segments of carbon, iron, and lead. The material of each target is spread around the detector in both the longitudinal and transverse direction to reduce systematic errors.

3.1.1 MINERvA Coordinate System

A right-handed Cartesian coordinate system is used in MINERvA experiment. In this co-ordinate system, the origin is located at the center of inner detector. Z-axis is defined along the beam line parallel to the surface of the earth. X-Y plane being orthogonal to the beam line with Y-axis pointing vertically upwards and X-axis, perpendicular to both of the other axes, horizontal pointing to beam left. In this system the beam central axis is in the Y-Z plane and points slightly downward at 3.34°.

3.2 Tracking Modules

The major portion of the ID is assembled using hexagonal planes. These planes are stacked together along the beam line to make the body of the detector. Each

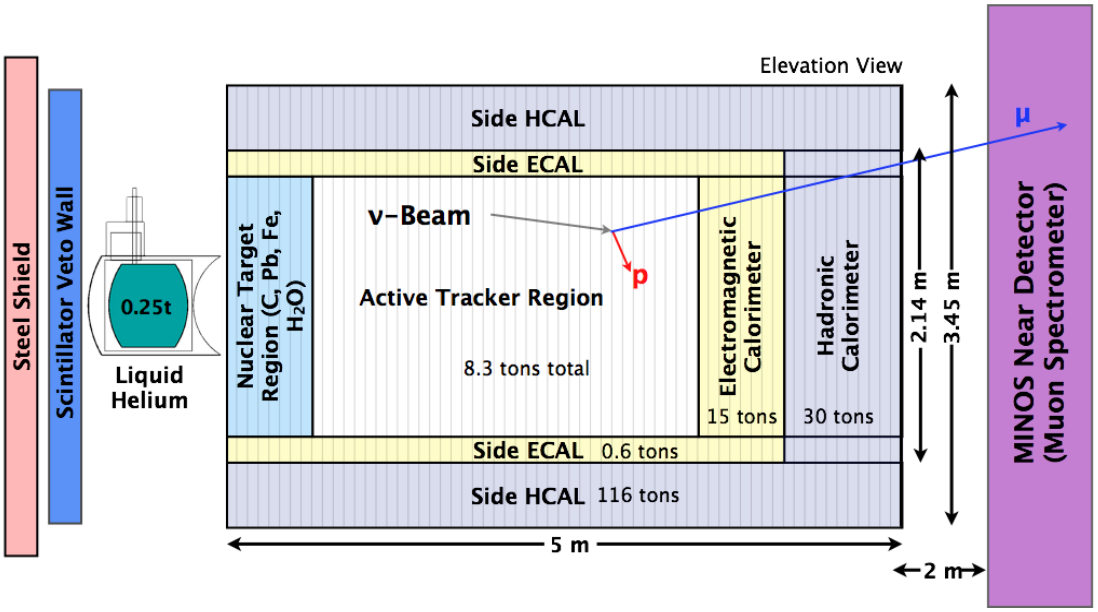

Figure 3.1: Side(along the beam axis) view of the MINERvA detector[121].

plane is assembled using 127 triangular shaped plastic scintillator(CH) "strips" glued together with 3M-DP190 translucent epoxy. The planes are made light tight and sturdy by covering them with Lexan sheets and attached with 3M-DP190 gray epoxy. The dimensions of these triangular strips(Fig. 3.2): 33 ± 0.5 mm base and 17 ± 0.5 mm height, length depends on which position they are in the plane. Each ID strip has a 2.6± 0.2 mm diameter cavity centered at 8.5 ± 0.25 mm above the widest part of the triangular strip. These cavities contain "wavelength shifting(WLS)" fibers, used in the light collection system. The extruded scintillator strips are made from polystyrene pellets (Dow Styron 663 W) doped with 1% (by weight) 2,5-diphenyloxazole (PPO) and 0.03% (by weight) 1,4-bis(5-phenyloxazol-2-yl) benzene (POPOP). PPO and POPOP are used for their spectroscopic properties[120]. The plastic scintillator strips are put together in alternating orientation to form a plane, this placement ensures that scintillation will be produced in at least two strips by any charged particle passing through the plane. Two planes are stacked to make a module used for tracking charged particles as shown in Fig. 3.3. To outline three dimensional reconstruction of the track made by a charged particle in the detector, these planes are arranged in three different orientations(called "views") in X-Y plane of MINERvA co-ordinate

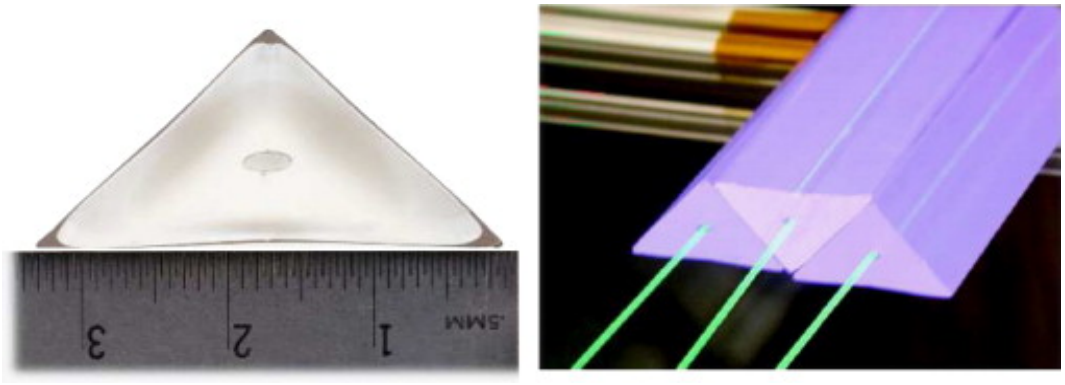

Figure 3.2: Triangular plastic scintillator strips used in making tracking modules[120].

system. These orientations(Fig. 3.4):

- ↬ X-view – all scintillator strips in an X plane are parallel to the Y axis.
- ↬ U-view – all scintillator strips in U view are rotated +60 degrees relative to the X-view.
- ↬ V-view – all scintillator strips in U view are rotated −60 degrees relative to the X-view.

In a module, either U or V orientation is followed by X, along the Z-axis, the planes are stacked in UXVXUX progression. In this work, total of 84 modules have been used to study antineutrino interactions.

3.3 Outer Detector

Each hexagonal plane in MINERvA detector is composed of ID and OD components. OD includes the steel structure that surround all six sides of each plane. This framework serves as both a hadronic calorimeter and a supporting mold for the detector modules. Alternating sets of steel and scintillator bars in the OD

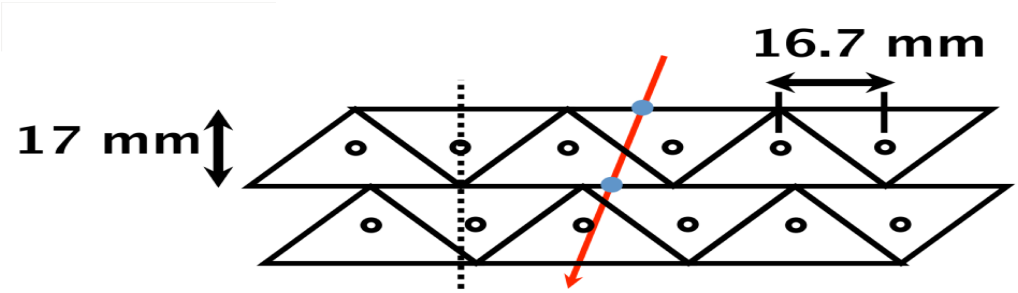

Figure 3.3: Tracking modules[120]

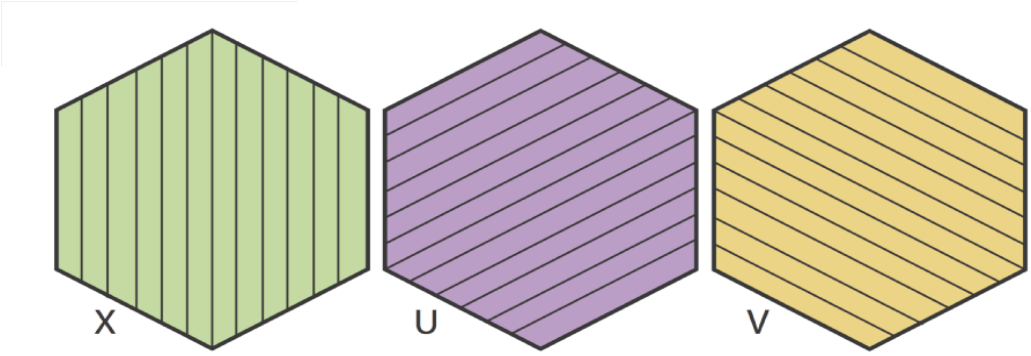

Figure 3.4: different orientations of scintillator planes[113].

makes it possible to contain the hadronic showers generated in the ID and measure the energy of the sideways going particles.

3.4 Veto Wall

The most upstream component of the MINERvA detector is "Veto Wall". It constitutes of vertically arranged alternating layers of passive steel plates and scintillator planes in the order: a steel plate 5 cm thick, a 1.9 cm thick plane of scintillator, a 2.5 cm thick steel plate, and a second scintillator plane of 1.9 cm thickness. The main objective of the veto wall is to tag muons(called "rock muons") produced in the neutrino interactions with the dolomite rock upstream of the MINERvA detector, so, they can not be confused with the muons produced in the neutrino interactions in the initial planes of the detector. The passive helium target is

placed in between veto wall and the MINERvA detector. Tagging of the rock muons is most important for helium analysis. Veto wall also absorbs any hadrons remaining in the beam. The veto wall is not used for this analysis.

3.5 Nuclear Targets

The MINERvA detector hosts five different nuclear targets materials viz. helium, iron, lead, carbon and water other than plastic scintillator(CH). Passive nuclear target planes are interspersed with active tracking modules. Nuclear target region has 22 modules in total, each of the passive nuclear target has four or two tracking planes in between. Other than a cubic meter cryogenic vessel as helium target upstream of the main body of the MINERvA detector, there are five passive nuclear targets (excluding water target) using some combination of the three target materials(iron, lead, carbon). The position of the passive nuclear targets in the MINERvA detector and the orientations of the nuclear materials planes along the axis of the beamline is shown in the Fig. 3.5.

- Target 1, 2 and 5 have mixed iron and lead. In the hexagonal plane, iron(steel) covers more area than lead, with the dividing line 20.5 cm from the plane center. They have different orientations in the X-Y plane for iron and lead areas. This gives an opportunity to minimize the effect of acceptance differences for different regions of the detector.

- Target 3 has carbon(graphite) in addition to iron and lead. Carbon covers maximum of the hexagonal plane area(50%), the iron covers 33.33%, and the lead covers 16.67%.

- Target 4 is pure lead. It is the thinnest of all targets.

- The water target is placed between target 3 and 4. The diameter of the steel frame that holds water is slightly larger than the size of ID in MINERvA.

3.6 Tracker region

Downstream of the nuclear target region, 54 scintillator modules constitute the completely active region of the inner detector called as tracker region. Charged particles produced in the neutrino interactions with the nuclear targets can be easily tracked in this region and it also acts as a hydrocarbon target. It weighs around 8.3 tons.

3.7 Electromagnetic Calorimeter

The electromagnetic calorimeter(ECAL) region in the MINERvA detector is 10 modules downstream of the tracker region. The scintillator planes in ECAL are similar to the planes in the tracking region, except that the 2 mm thick lead border in the ID is replaced by a 2 mm thick sheet of lead that covers whole area in X-Y plane. In ECAL, a lead absorber is placed directly upstream of each module. This is ensured by putting a 2 mm thick lead sheet as the transition module between the downstream part of the tracker region and the ECAL. The lead in the ECAL is used to stimulate electromagnetic showers which helps in containing energies from the photons, electrons and pions.

3.8 Hadronic Calorimeter

The most downstream part of the MINERvA detector is hadronic calorimeter(HCAL). It includes last 20 modules of the detector. Each module of the HCAL in ID contains a scintillator plane with a 2.54 cm thick steel plate. The planes in HCAL are placed in UXVX progression same as in the tracking region. The purpose of HCAL is to contain hadronic particles produced by the neutrino interactions in the tracker region of the detector.

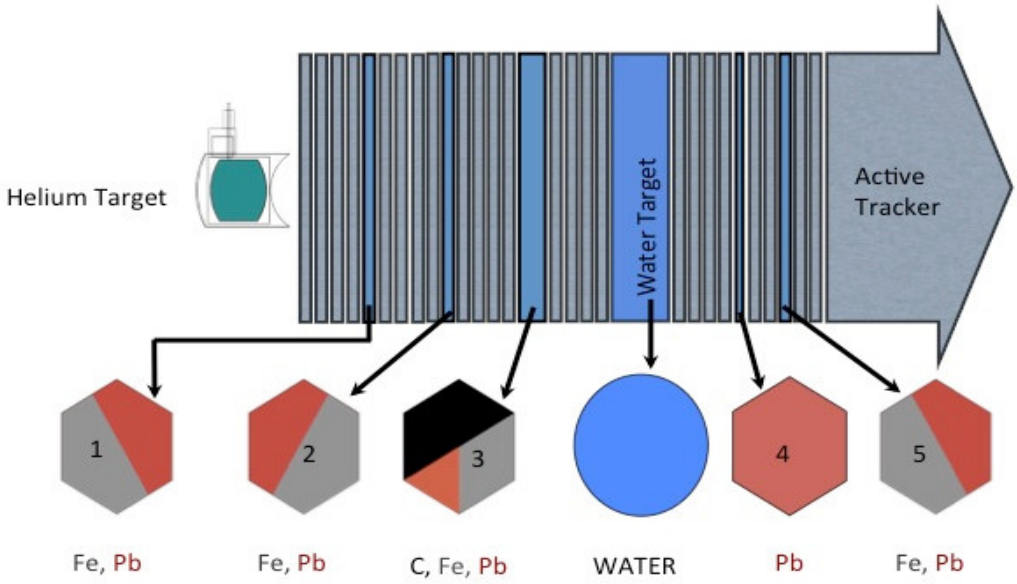

Figure 3.5: The position of the passive nuclear targets in the MINERvA detector and the orientations of the nuclear materials planes along the axis of the beamline[122].

3.9 MINOS Near Detector

The Main Injector Neutrino Oscillation Search (MINOS), was the original user of the neutrino beam produced at NuMI beamline and first detector assembled in the underground "MINOS hall" cavern. It was active during 2005-2016. The main objective of MINOS was to perform measurements of the neutrino oscillation parameters precisely in the atmospheric neutrino sector associated with muon neutrino disappearance[123]. It was a long base-line experiment with near detector hosted at the Fermilab, Illinois and far detector 735 km downstream in the Soudan Underground Laboratory in northern Minnesota. In this thesis, data sets are obtained by using MINOS near detector as spectrometer only. Fig. 3.6 shows upstream transverse view of the MINOS near detector[124]. Detailed description of the MINOS detector technology and readout are given in Ref.[123].

The MINOS near detector is located approximately 2 m downstream from the end of the MINERvA. For a neutrino interaction to be reconstructed as a muon

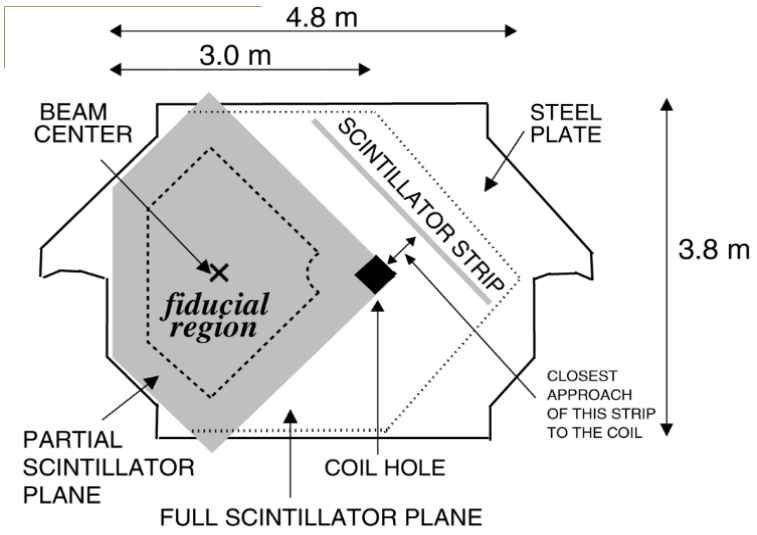

Figure 3.6: Upstream transverse view of the MINOS near detector[120].

neutrino charged current event in MINERvA, muon track must travel from the point of interaction in MINERvA to MINOS planes. The magnetized MINOS spectrometer is used to analyze the momentum of the muons exiting MINERvA detector volume in the forward direction. It weighs 1 kTon, designed with the magnetized steel plates of 2.54 cm thickness interspersed with 1 cm thick layers of plastic scintillator in between. The steel plates are arranged alternating in two different orientations, $\pm$ 45 degrees w.r.t. the vertical axis(Y-axis in MINERvA coordinate system) creating two *views* for the MINOS near detector. In total, MINOS near detector has 282 steel plates(Fig. 3.7). The first 120 planes are fully instrumented this region acts as the calorimeter section. For the downstream 162 planes, only every fifth plane is fully instrumented and the other 4 out of 5 planes are not instrumented. This region is used as the spectrometer section to measure the momenta of energetic muons. MINOS near detector has current-carrying coil passing through the entire length of the detector which generates a toroidal magnetic field of average strength of 1.3 T. Depending on the charge and momentum of the incoming muon, magnetic field curves the path of the charged muon towards or away from the coil. The momentum of a muon is determined, either if it completely stops in the detector(*range*) or curves before it exits (*curvature*). Better resolution for muon momentum is achieved by measurements based on range. In

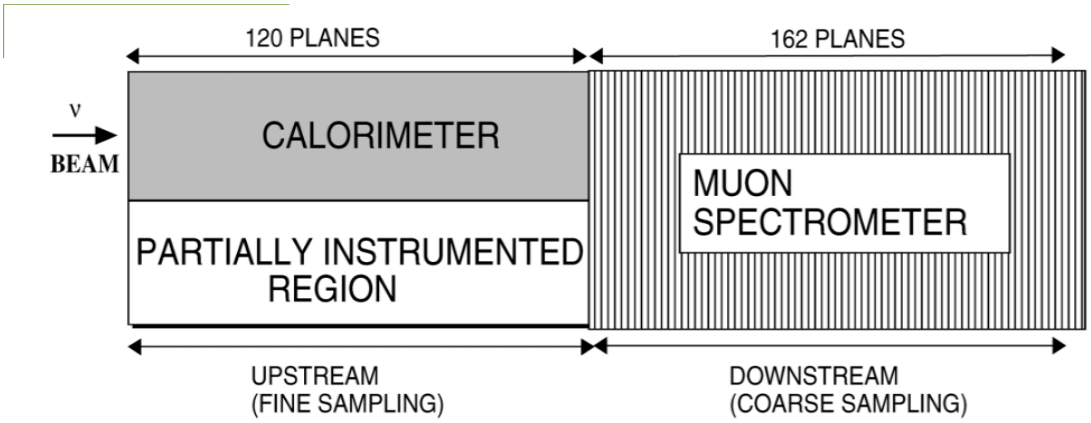

Figure 3.7: Side view along the beamline of the MINOS near detector[120].

this analysis both methods (range and curvature) are used.

3.10 MINERvA detector readout electronics

This section describes how the energy produced by a charged particle is measured in the MINERvA detector. Fig. 3.8 represents a schematic diagram of a single optical readout channel in the MINERvA[120].

3.10.1 Wavelength Shifting (WLS) fibers

When a charged particle passes through the scintillation material in the MINERvA detector, it generates light. This light is absorbed and re-emitted by the extruded plastic scintillator strips. Re-emitted light is collected by WLS fibers at the center of each strip and transmitted to 64-anode photo-multiplier tubes (PMTs) mounted above the detector through clear optical cables. Light collection is maximized by mirroring the unread end of each fiber as MINERvA detector reads out only one end of the WLS fibers. The MINERvA detector employes over 32 thousand scintillator strips, light signals from these strips must be converted to electrical pulses. The amplitudes of these pulses are proportional to the energies deposited and also carry accurate timing information[120].

3.10.2 Photo multiplier tubes (PMT)

For the photosensor chosen to serve as the experiment's signal readout system, it is important to:

- ↬ distinguish between overlapping events within a single spill of the NuMI beamline,
- ↬ measuring decay times of charged mesons created in neutrino interactions,
- ↬ measuring time-of-flight of charged mesons.

For all that, the multi-anode photomultiplier tube (PMT) model number H8804MOD-2 manufactured by Hamamatsu Photonics was used. Collectively, 507 PMTs are used in the fully instrumented detector. Each PMT is enclosed within a cylindrical, light tight case made of 2.36 mm thick steel. Scintillation light reaches to PMTs via clear optical cables. A single PMT is connected to eight fiber connector, which in turn have eight clear optical cables connected to them. This makes a PMT to have an 8×8 array of pixels arranged on a 2 cm $\times$ 2 cm grid, i.e. 64 pixels per PMT with each pixel having an effective size of 2×2 mm^2. The fibers from the end plate of each case to the front face of the PMT are arranged in a checker-board style *weave* pattern on the 8×8 *cookie* to ensure that the signal from one pixel does not induces current in the adjacent pixel. This reduces the cross talk in PMTs[120].

3.10.3 Data Acquisition

The signal for neutrino interactions in the MINERvA detector passes from PMTs to custom built front-end boards (FEB) attached to the opposite end of each PMT. FEBs digitizes and amplifies the analog signal received from PMTs. Each FEB has 6 Application-Specific Integrated Circut (ASIC) chips called *TriP-t* chips

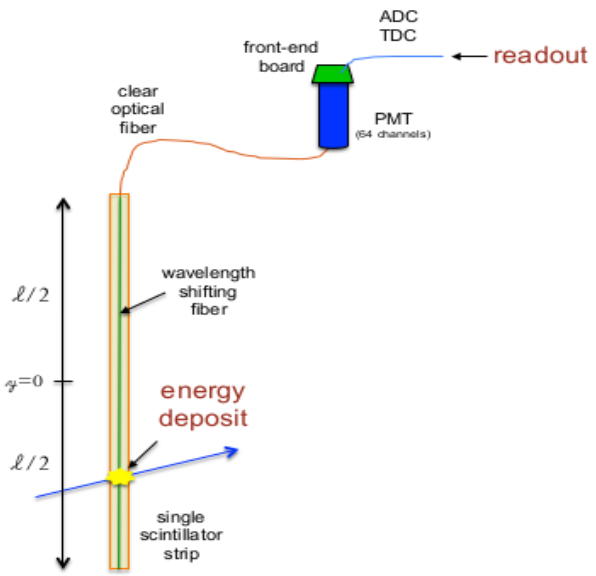

Figure 3.8: Schematic diagram of a single optical readout channel in MINERvA[120].

which have a programmable threshold voltage. TriP-t starts integrating charge in a 16 μs window(10 μs NuMI beam spill + additional 6 μs to record delayed detector activity, this duration is called a "gate") when a signal above discriminator threshold is detected. Subsequently, the entire pulse height and timing information is "sent" to the on-board memory of the FEB from pairs of TriP-ts. After each cycle, the TriP-t pair requires to reset this takes 20 clock ticks, during which the pixels are effectively *dead* to incoming signal.

The FEBs are connected in *daisy chains* on the detector, with the longest chain having around ten FEBs. These chains are given as input to a custom VME(virtual machine environment) module called Chain Readout Controller-Ethernet (CROC-E) board, each CROC-E can support four chains. The CROCs in turn receive timing and trigger commands from another custom VME module, the CROC Interface Module(CRIM), which services up to four CROC-Es. At the end of each spill, the readout system collects at the data and writes it to a binary file on disk.

Chapter 4

Reconstruction and Simulation

In the MINERvA detector, neutrino interaction is measured indirectly by measuring the scintillation light created when charged particles passes through the detector, and collecting this with the electronics. From the readout units, we receive information about different quantities like, hit energy, hit location, and hit timing. Reconstruction is the process to convert this information in the physics information which we can actually use for the analysis. This is done by running reconstruction algorithms on collected data. These algorithms separate individual event interactions from the larger readout window and groups them in time slices, identify energy formed into distinct clusters, muon tracks, matching these tracks in MINOS, and counting the dispersed energy in the detector. These steps are briefly explained below; more detailed description can be found in Ref.[120]. Following are the quantities we get after reconstruction process is done:

- Energy of the outgoing muon, E_{μ}
- Energy of the hadrons in the final state of the interaction, also called recoil energy, E_{had}
- Angle between the incoming neutrino and outgoing muon, θ_{μ}

In the DIS analysis, we use these three quantities and derive the other physics variable required to characterize the kinematics of the DIS event.

- Neutrino energy: $E_\nu = E_\mu + E_{had}$.
- The square of the four momentum transfer: $Q^2 = 4E_\nu E_\mu sin^2(\frac{\theta_\mu}{2})$.
- Invariant Mass of the hadronic system: $W = \sqrt{M_N^2 - 2M_N E_{had} + Q^2}$
- The fraction of the momentum carried by the struck quark: Bjorken-x $x_{Bj} = \frac{Q^2}{2M_N E_{had}}$
- Inelasticity, $y = \frac{E_{had}}{E_\nu}$

4.1 Time slicing

The width of a *gate* in MINERvA detector is 16 μs. First step of reconstruction is separate multiple events in a gate and to combine all the *hits* that are coming from a single neutrino interaction. This is done by dividing the *gate* in small time slots of 80 ns called "time slices" and collect the hits that have the discriminator exceed a total charge threshold of 10 photoelectrons. The window then slides forward until the threshold is no longer met. Activity from a single neutrino interaction is accommodated in a single time slice, except for electrons coming from the decay of stopped muons. In Fig. 4.1, colored peaks show the sets of hits in one readout gate.

4.2 Cluster formation

Time slicing is done completely on the basis of time, no spatial information is used. After time slicing, next step in the reconstruction is "cluster formation". It is done by combining the hits together that are adjacent in space. Charged

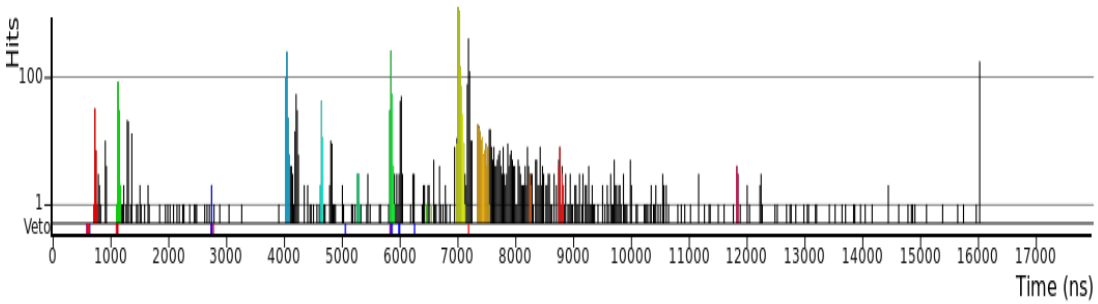

Figure 4.1: This is a plot of the arrival times of scintillation light during the 16 microsecond gate, where the first 10 microseconds had beam passing through in the MINERvA experiment. Different colored peaks represent different time slices within the same gate. Black lines represent the hits below discriminator level. This display is taken from run 18692, subrun 38 and gate 571.

particles deposit energy in a minimum of two strips when they transverse through the detector plane, combining and forming a group of neighboring hits within the same time slice called as a cluster. Even if only one hit in an isolated strip is registered, it is also labeled as a cluster. The time of the hit with the maximum energy in the cluster determines the time for the cluster, also the energy deposition in the strips determines its position which is the energy-weighted sum of all the positions of the different hits in the cluster. There are different categories of cluster on the basis of the hit energy sum and the size and distribution of the hits shown in Fig. 4.2, viz.:

- *Trackable clusters:* total cluster energy lies between 1 – 12 MeV. The cluster is not wide, must have four or fewer hits with at least one hit having energy more than 0.5 MeV. If two or more hits have energy deposited greater than 0.5 MeV, they must be adjacent to each other. These are clusters that look like they could be part of a muon track.

- *Cross-talk:* Do not arise from a neutrino interaction. Cross talk within the PMT pixels results in the clusters with extremely low total photoelectrons in a single strip, whose pixel is located next to a pixel from a different cluster with a large energy deposition (section-3.10.2). These clusters are

not included in later event reconstruction.

↬ *Low activity:* total energy deposit must be less than 1 MeV but they are not classified as cross talk.

↬ *Heavily ionizing:* same criteria as trackable clusters: total cluster energy lies between 1 – 12 MeV. These clusters are small in space but they have large amount of energy deposited. These clusters must have 1 – 3 hits having energy more than 0.5 MeV and they must be adjacent to each other. Heavily ionizing clusters are important in forming high angle tracks. Generally, these clusters are formed by the heavy ionization, low velocity particle like a proton.

↬ *Superclusters:* They do not meet the criteria for either trackable or heavily ionizing clusters. They are wide and have five or more hits. Overlapping particles in electromagnetic or hadronic showers produce Superclusters.

4.3 Track Reconstruction in the MINERvA detector

Clusters are grouped together to form tracks of the charged particles in the detector. Origin and direction of a charged particle can be determined by a reconstructed track. Track reconstruction is done in two steps. First, identify the longest track in the neutrino event, usually the muon track, called as "anchor track". Then trace it back to find the vertex of the interaction and build other tracks in the same time slice. To form the tracks, three clusters in same view(X or U or V) are grouped in to a *track seed*. These clusters must be in the consecutive planes of the detector. The track seeds are combined together to form "tracks candidates", if track seeds contain common clusters and fit to a straight line between the three seeds (Fig. 4.3). The track candidates may contain gaps in between as there is no limitation that track candidates must share clusters. This

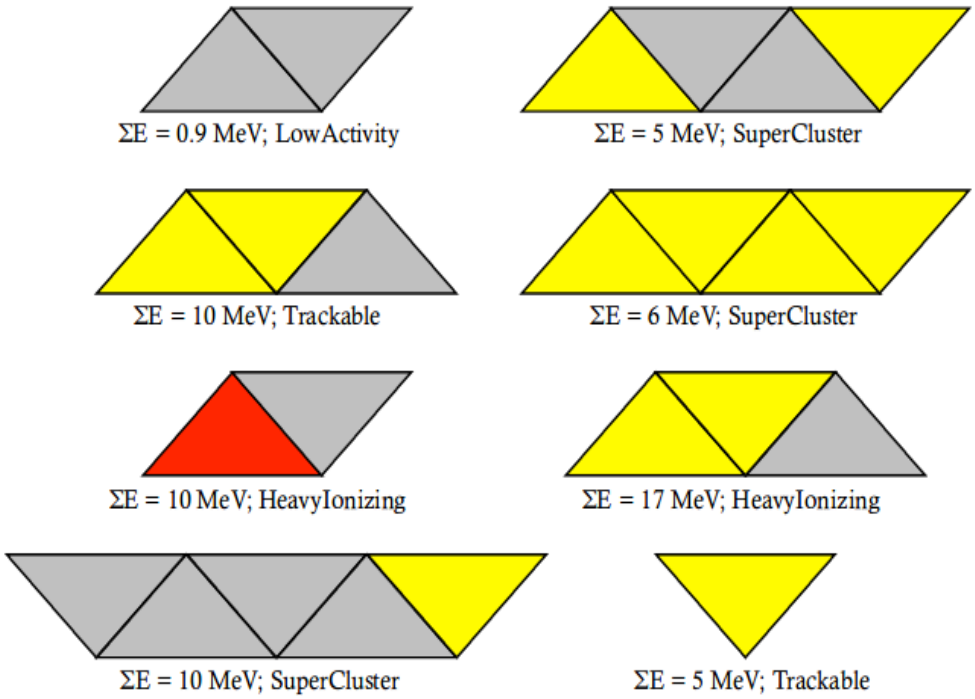

Figure 4.2: Different categories of cluster on the basis of the hit energy sum and the size and distribution of the hits[125]. Grey color is for low energy(E $<$ 1 MeV), yellow color is for medium energy(1 MeV $<$ E $<$ 8 MeV) and red color is for high energy (E $>$ 8 MeV).

allows a track candidate to accurately follow particle trajectories that intersect dead regions in the detector. These 2D track candidates from different views are merged in to three dimensional objects by overlapping the three different 2D candidates and checking the trajectory consistency with the track seeds. The merging process of the candidates in to a track starts at the downstream end of the detector and works its way to upstream end, this makes possible to avoid high amounts of activity near the vertex of the interaction. As the track propagates through the detector, a custom Kalman fitter implementation is used to fit the track which takes multiple scattering into account[126, 127]. An example of a antineutrino interaction with tracks in MINERvA detector display is shown in Fig. 4.4.

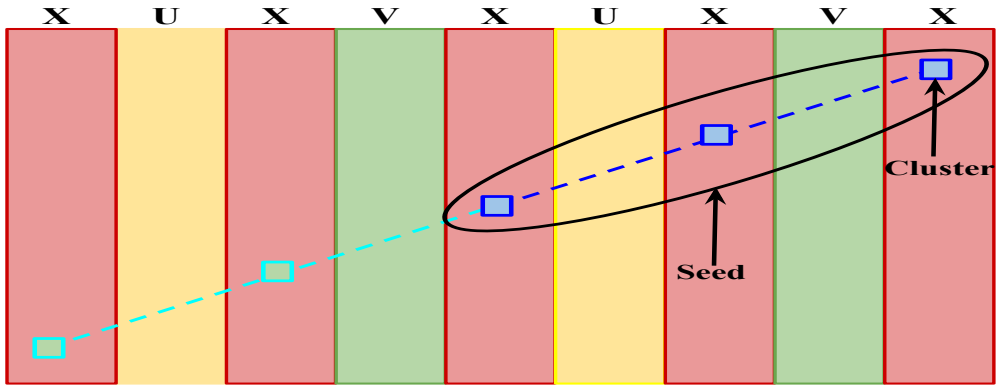

Figure 4.3: Schematic diagram for an example of track candidate using two seeds. Each small box in X view represent a cluster and three clusters form a seed[113].

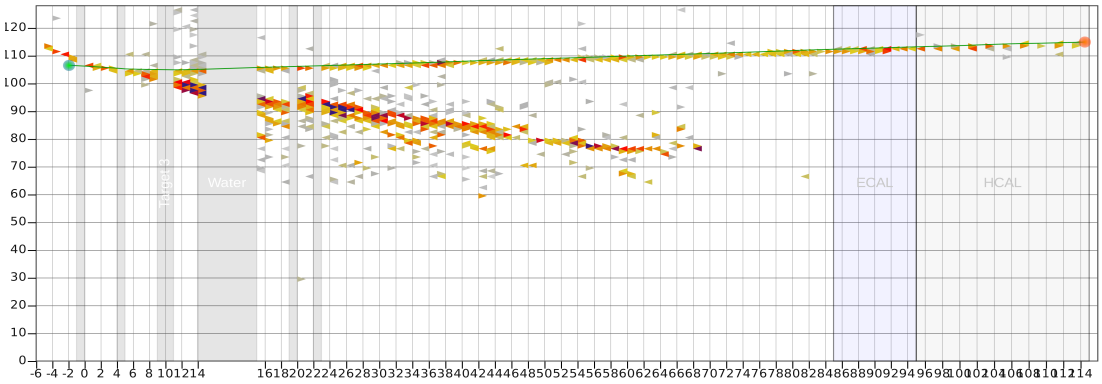

Figure 4.4: Example of a DIS event in MINERvA detector. Colored triangle represents the intensity of the hit in the strip. Number of modules is on x-axis and number of strips on y-axis.

4.4 Track Matching with the MINOS Near Detector

In this analysis, (anti)neutrino interaction event is described having a long muon track that exits the back of MINERvA detector and matches in MINOS near detector(ND), and hadronic activity near the vertex of the interaction. The muon tracks are reconstructed in both MINERvA and MINOS ND(it is 2 m downstream of MINERvA detector) to measure the charge and energy of muons. For a track to be MINOS matched at reconstruction level must be within 200 ns in time in both detectors, there should be activity in last five planes of MINERvA and first four planes of MINOS ND.

There are two different methods for track matching: a closest approach method and a track projection method. In track projection method, the vertex of the track in MINOS ND is extrapolated backwards to the plane where the track stops in MINERvA and the track is also extrapolated from the end point in MINERvA to the plane where it starts in MINOS ND. The track is considered to be MINOS matched if the interception points are within 40 cm of each other. The track with the smallest difference in the points of interception is assigned as the MINOS-matched track in the case of more than one possible match. When the points of interception are not within 40 cm of each other then the closest approach method is used for matching tracks between MINERvA and MINOS detectors. It is done in a similar way as the track projection method, track is extrapolated from MINERvA to MINOS and in the same fashion from MINOS to MINERvA. Euclidean distance minimization formula is employed to find the point of closest approach of the two extrapolated tracks. For the track to be MINOS matched in closest approach method, the minimization must converge within 1000 steps otherwise the track is declared unmatched. This method can be useful if the muon undergoes a hard scatter in any of the passive material between the two detectors.

4.5 Charge Determination and Energy Reconstruction

The MINOS ND is magnetized and also used to measure and reconstruct the charges and momenta of muons leaving from the downstream end of the MINERvA detector. Generally, in the MINERvA detector, muons created with the momenta lying between 0.5 and 6 GeV and get matched to MINOS ND are contained in the calorimeter region of MINOS ND. Muons with the higher momenta stop in the MINOS ND downstream spectrometer region or completely exits MINOS ND. Due to the geometry and position of MINERvA and MINOS ND detectors relative to each other, only the muons created in MINERvA with angle 20 degrees or less with respect to the Z-axis(beam axis) are matched to MINOS properly. Magnetic field of the MINOS coil deflect charged muons passing through the detector. Information about the charge and momentum of the muon is extracted on the basis of deflection. The magnetic coil's polarity is normally set in way which will ensure that the dominant charged muon is focused by the spectrometer. The reverse horn current mode produces antineutrino enhanced beam, which is used in this analysis. In this mode, positively charged muons are focused by the magnetic field towards the coil and negatively charged muons produced by the presence of neutrino background in the beam are deflected away from the coil.

Momentum of muons($\mu^{\pm}$) entering the MINOS ND is determined by two different methods: curvature and range. If a muon, completely contained inside the calorimeter region, deposits all of its energy in the MINOS ND through interactions then its momentum is determined by the range method. Curvature method is used for the muons exiting out of the MINOS after depositing some of their energy. A track fitting algorithm developed by the MINOS collaboration[128] is used for the reconstruction of the muon momentum in case of the curvature method. The curvature of the track (K) is the inverse of its radius (R in cm) and is related to the momentum component perpendicular to the field (P in MeV) and magnetic

field (B in kilogauss) by the following equation:

$$K = \frac{1}{R} = \frac{0.3\ B}{P}.$$

In MINOS ND, the muon momentum resolution is 5%(10%) for momentum measured be range(curvature)[129]. The range method for the determination of the muon momentum is more precise as compared to the curvature method.

4.6 Recoil Energy Reconstruction

A DIS signal in MINERvA is described as having one long track(muon) matched to MINOS ND and rest of the activity in the detector is taken as recoil or hadronic energy. For kinematic reconstruction, the hadronic system of the interaction is extremely important. In the MINERvA detector, hadronic energy can be lost due to passive targets, neutral particles in the final state along with energy leakage out of the side of the detector. Energy deposited in the detector by charged particles(excluding primary lepton) within a -25 to 35 ns window around the interaction vertex in the event time defined by the muon is summed after being calorimetrically corrected. In this sum, energy deposition by cross-talk or low activity is not included to prevent incorporation of the energy from muon track.

In the MINERvA detector, true recoil energy is defined as the difference of neutrino energy(E_ν) and outgoing lepton energy(E_l),

$$\text{true } \mathrm{E_{recoil}} = \mathrm{E}_\nu - \mathrm{E}_l.$$

and calorimetrically reconstructed recoil energy is calculated by aggregating energy deposits in the sub-detectors(tracker, ECAL, HCAL, SideECAL, OD) after being weighted to account for the additional passive absorber and is given as:

$$\text{calorimetric } \mathrm{E_{recoil}} = \alpha \times \sum_{\mathrm{i}} \mathrm{c_i E_i},$$

where

- $\alpha \rightarrow$ overall scale factor, calculated to compensate the loss of visible energy due to neutral particles, energy leakage from the side of the detector, binding energy of the struck nucleon within the nucleus by fitting calorimetric-corrected reconstructed recoil energy to true recoil energy.

- $c_i \rightarrow$ the calorimetric constant or weight for sub-detector i, determined by the dE/dx of a minimum ionizing particle at normal incidence in an idealized detector.

- $E_i \rightarrow$ total energy in sub-detector i.

α is calculated by minimizing error:

$$\text{error} = \sum \frac{(\arctan(\text{calorimetric/true}) - \frac{\pi}{4})^2}{\text{N}}$$

using, N as the total number of true events in the energy range of 1 GeV to 10 GeV.

Fractional energy resolution of the calorimetric energy is used for per-bin energy correction after fitting α in bins of true recoil energy in the simulation,

$$\frac{\Delta E}{E_{recoil}} = \frac{(E_{calorimetric} - E_{true})}{E_{true}}$$

Spline is calculated using average true recoil energy of each bin as y point. After fitting the fractional recoil energy distribution to a Gaussian distribution, mean(η) is extracted. The x and y point of a spline are defined as follows:

$$\begin{aligned} x(E_{recoil}) &= <E>(1+\eta) \\ y(E'_{recoil}) &= <E> \end{aligned}$$

For the calculation of splines, two points at (0,0) and (50,50) are fixed and then by a linear interpolation of points which are above 300 MeV a spline is created[130, 131]. Splines are used to reconstruct the specific samples for which they are calculated.

For the tracker region(consisted of plastic scintillator), a single passive material correction per sub-detector is applied but same is not true for the nuclear target region. As the particles created in the neutrino interaction taking place in the most upstream passive target (target 1) will travel through the material of other passive targets before reaching the tracker as compared event taking place in most downstream passive target(target 5) . For the nuclear target region, correction is applied on the hit-by-hit basis. As it is not clear if the hit is coming from backward or forward going particle, a passive-material correction is applied on either side of a passive target based on half the width of the passive target.

Chapter 5

Machine learning in MINERvA

In the MINERvA experiment, there are different nuclear targets exposed to the same antineutrino flux at the same time, this provides an opportunity to study the nuclear medium effects in the antineutrino-nucleus interactions. Therefore, for the analysis that depends on different nuclear targets, its important to exactly locate the vertex of the interaction in the detector. Traditional way of track reconstruction in the MINERvA detector is explained in the previous chapter. DIS events in the MINERvA detector are characterized by having a long muon track and hadronic energy deposited around vertex of the interaction. Track reconstruction done in traditional manner fails to locate exact interaction vertex when it is obscured by large amount of hadronic energy resulting from a shower activity or tracks created by secondary interactions or decays. Example of the failure of traditional reconstruction for a DIS event is shown in Fig. 5.1. In the example it is clearly depicted that due to the large concentration of the hadronic energy around the interaction vertex, traditional way of track reconstruction provides different vertex of interaction than the true vertex of interaction. This leads to mis-identification of the nuclear target from which the event is originating. The analyses which are not sensitive to the origin of the event, like the analyses in the plastic scintillator part(called as tracker) of the MINERvA detector, misreconstruction of the interaction vertex by a few centimeters does not affect the cross-

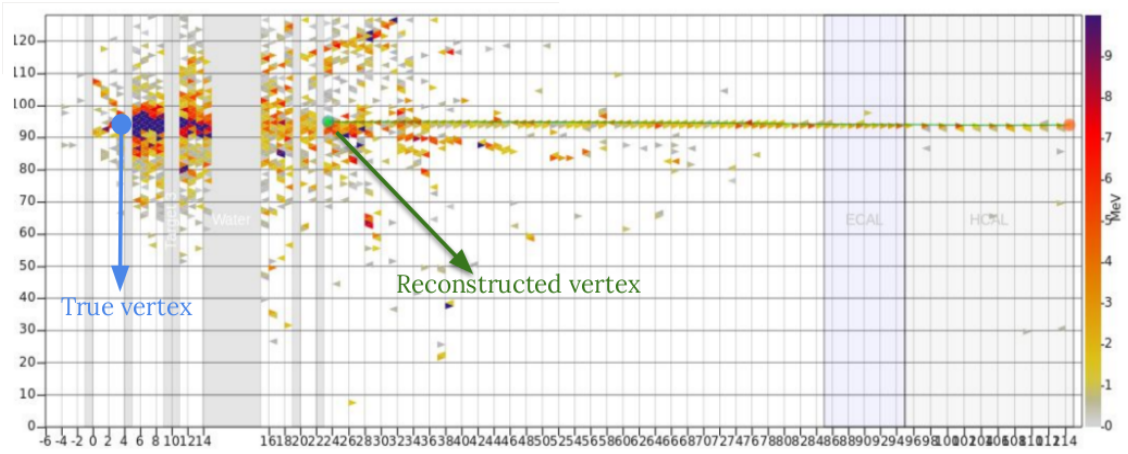

Figure 5.1: Example of the failure of traditional reconstruction for a DIS event.

section calculations. Unlike the tracker analyses, misreconstruction of the vertex by few centimeters in nuclear target analyses will cause the mis-identification the material from where the antineutrino interaction took place. This can lead to a dramatic impact on the purity and efficiency of the event sample, resulting in the biasing of the measured cross section [132, 131]. To get the DIS sample for analysis, events with interaction vertex misreconstruction are rejected by applying a set of event selection criteria, or cuts. Data used in this analysis is collected in medium energy(ME) era (peak $E_\nu \sim 6$ GeV), resulting in higher statistics then low energy(LE) era (peak $E_\nu \sim 3$ GeV). In the ME configuration antineutrino flux is higher and the antineutrino events are also more energetic than LE configuration, this gives rise to more events with larger hadronic energy deposition near interaction vertex. This may lead to more events being rejected from the selection sample, resulting in lower efficiencies across all passive nuclear targets. It is not feasible to dismiss all of the events having vertex misreconstruction. To solve this problem, another approach for the track reconstruction is employed which is known as *Machine learning*.

To find the precise location of the interaction vertex, events in the MINERvA can be depicted as images, and vertex finding can be regarded as image categorizing problem which is well suited for a machine learning application. As the images of the DIS interactions have large amount of energy deposited around the

interaction vertex, regression techniques can not be applied for the classification. Deep convolutional neural networks (DCNN) are used to identify antineutrino interaction vertices in the nuclear target region.

In this chapter, machine learning techniques utilized are described briefly but they are well beyond the scope of this thesis. More information about machine learning algorithms and applications, and language used to discuss them can be found here [133, 134, 135, 136].

5.1 Machine learning and Deep Neural networks (DNN)

Depending on the experience, human mind can tackle a task with ease, more the experience better execution of the task at hand. This is also applicable to computers more precisely to artificial intelligence (AI). An application of AI that uses computer science along with statistics and enable computers to learn and improve without being explicitly programmed is known as Machine learning (ML). In ML, data is provided to the AI without prior programming, AI learns from statistical patterns of this data and performs the task. The most important advantage of machine learning is that it reduces the amount of hand-tuning done by the programmer. Instead, it utilizes the computer to extract the crucial features from the data and establishes the algorithms by which future data will be sorted. In MINERvA, interaction vertex finding is treated as image classification problem. For classification, supervised ML approach is used. In this case, computer is fed some data as examples related to the problem and from these examples model learns about the features related to the task at hand, this is called *feature extraction* method. After learning about the necessary variables needed to describe the data set, ML model uses that information to classify unseen data set.

Model learns from the given examples, this process is known as *training* of the

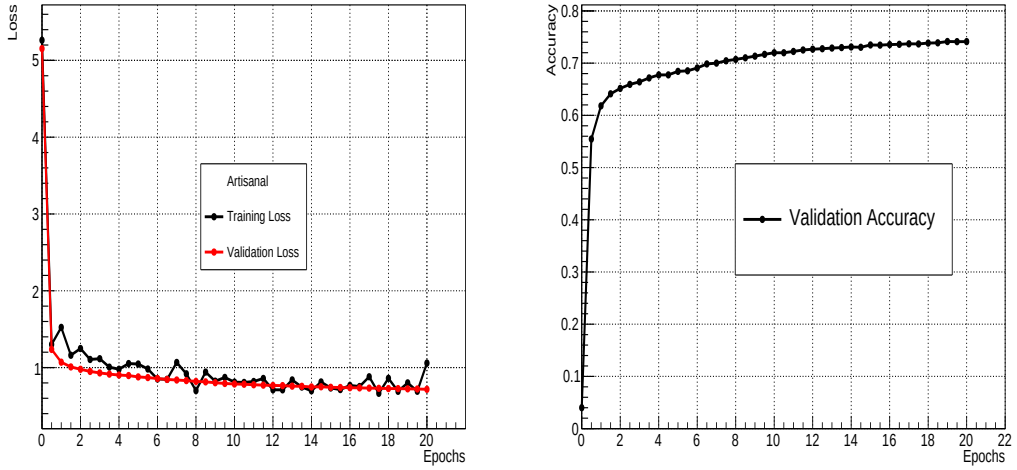

Figure 5.2: Loss(left) and accuracy(right) plots with respect to number of the epochs for an artisanal model[138].

model. To deal with all of the unseen data, ML algorithms must be extensive enough. If the model is too intricate, this may lead to the overfitting of the model resulting in inclusion of the irrelevant information in the ML model, vice-versa, if the model is too straight-forward, then it skips over important information while training. An overfitted model gives impeccable results for the known data while training but fails at predicting when the unknown data set is fed to the model. Progress of the model during training and validation stages can be evaluated by a summation of errors. This can be done by assigning the penalty to the errors using the mean square errors or softmax function[137] by plotting a loss function. The objective of the training process is to acquire the best parameter values of the model by minimizing this loss. The accuracy of the model is calculated after the optimization of the ML model parameters. Exemplary plots for the loss function and the accuracy of a ML model are shown in Fig. 5.2 versus number of epochs. Epoch is running whole input set once for training. To make the model learn well, the input data set is ran more than once.

In human brain, all the information is processed by the neurons. Each neuron is connected to multiple other neurons in a complicated network. In AI, analogous to the human neural network, a set of algorithms is used to process all the infor-

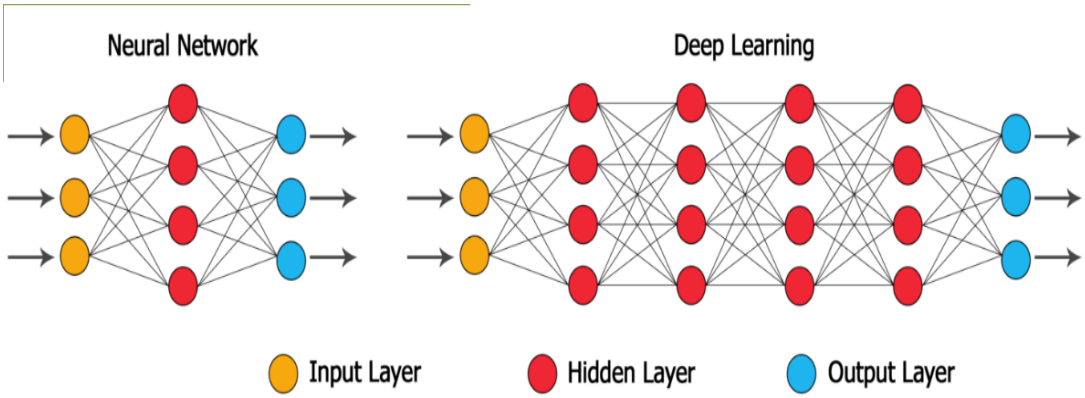

Figure 5.3: An example of Deep convolutional neural networks (DCNN). This figure is reprinted from Ref. [140]

mation provided through input examples. Fig. 5.3 depicts a schematic diagram of neural network and deep learning. There are three important layers in a neural network[139]:

- Input layer: passes data set to the ML model for training without modifying it.
- Hidden layer: most of the computation happens in the hidden layer
- Output layer: passes the output of the hidden layer after training.

There are multiple nodes in a layer and similar to the neurons in a brain, all the nodes are connected to other multiple nodes which receives input and computes its own interest score of a function (concept), or activation value. In Fig. 5.3, a circle represents a node in a layer and different color circles represent multiple nodes in a single layer which are connected to nodes of the preceding and succeeding layers.

Each node in a layer receives information from the nodes of the previous layer and to learn from the information, nodes integrate a set of weights and bais. This helps in assigning a significance to information of the task which the algorithm is trying to learn. The weighted information is summed in the end and passed through an activation function that determines the outcome of the classification.

Deep convoluted neural network has many hidden layers for the learning as compared to neural network, it helps DCNN to learn more deeply about all the significant features of the input information and train the model with much less hand-tuning. In DCNN, output of one hidden layer becomes the input of the succeeding hidden layer.

5.2 Methodology

To use ML approach for interaction vertex identification in MINERvA, the whole detector is classified in 174 segments. Nuclear passive targets and plastic scintillator planes are assigned numbers starting from 1 to 174. Segment 0 includes all the region upstream of the detector and rest 174 segments are assigned to the inner detector and the downstream calorimeter region. Schematic diagram of the detector assigned with the segment numbers is shown in Fig. 5.4 and explained in detail in [132]. These segment numbers related to the physical planes of the MINERvA detector are used as the input given to neural network. Each (anti)neutrino interaction is taken as an image which contains all the information about the energy and the time when that energy is deposited in the detector, similar to a grid of numbers that represent the darkness of each pixel in an image. The information of the energy and the time of hit is stored in a lattice. The muon vertex time is used as the reference time and to teach the network that the time associated with the track that is matched to MINOS detector is special.

The information of the inner detector and downstream calorimeter region is stored in the lattice is used as the input given to ML models for training. In MINERvA we have used TensorFlow package as ML software. It is an open source machine learning platform developed by Google[141]. A subset of the simulated data in the ME configuration is used for the training, validation, and testing of the ML model. Once the training and testing of the model is done, it is used to make predictions on the rest of the unseen data sets in MINERvA(both simulated

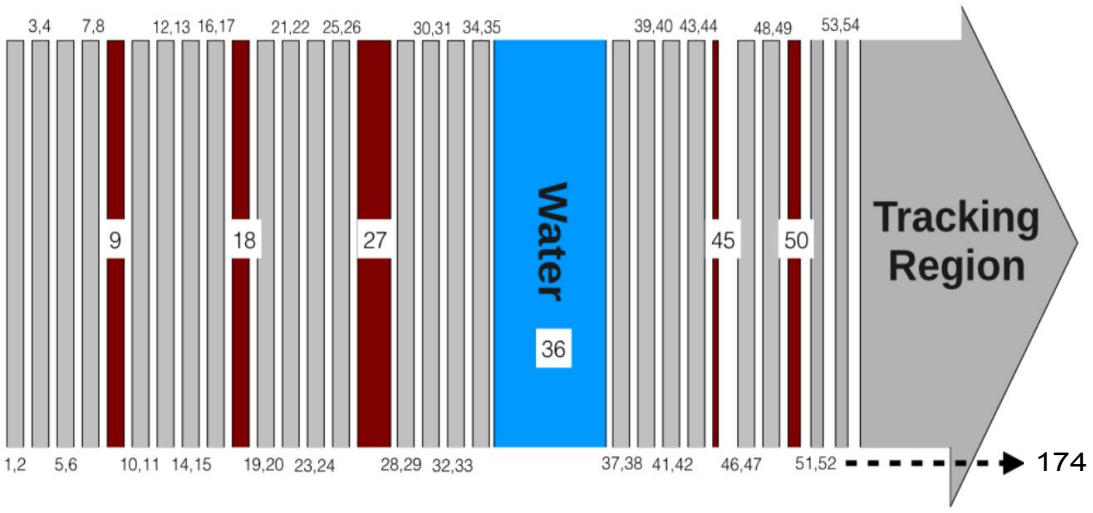

Figure 5.4: An example of Deep convolutional neural networks (DCNN). This figure is reprinted from Ref. [140]

and reconstructed). Before starting with the analysis, the information about the interaction vertex of the (anti)neutrino events from the ML predictions is included in the data sets[132].

5.3 Comparison between ML and track based vertex finding approach

Next step is to investigate the outcome from the DCNN ML approach and compare physics results with the track based vertex finding approach. For comparison, the plots are made with respect to a variable *Vertex Z* which is closely related to the actual position of the nuclear targets and scintillator planes in the MINERvA detector.

In track based approach, all the events coming from one plane upstream and two plane downstream of the nuclear target are considered as the event coming from the passive nuclear targets, where as in DCNN approach a (anit)neutrino interaction is taken as an event if it is originating from the same target location

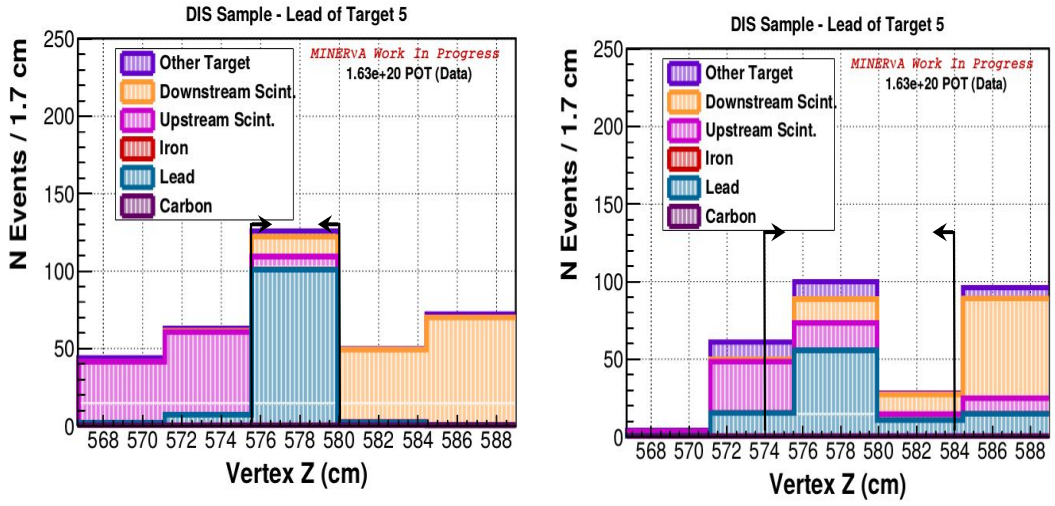

Figure 5.5: Event distribution for lead in target 5 using ML (left) and traditional (right) approaches. Black arrows in both plots represent the planes from which the number of events are considered to be coming from the target.

as predicted by the ML model.

In Fig. 5.5, results for event distribution for lead nuclear material in target 5 are shown with respect to *Vertex Z* using antineutrino simulated data set in DIS region. In the plots, other than the event distributions coming from the nuclear target(lead), number of events coming from the plastic scintillator upstream and downstream of the nuclear targets are also presented. Target 5 is composed of iron and lead, so when the event distribution for iron is taken, then lead is shown as other target in the plots. From the Fig. 5.5, an improvement in event selection after implementing ML approach is visible. There is less signal leakage from the passive target region to the surrounding scintillator tracker and less contamination coming from the scintillator tracker around the passive target.

Chapter 6

The Cross Section Extraction Procedure

The goal of this dissertation is to measure muon-antineutrino deep inelastic scattering (DIS) cross section ratios of the passive nuclear targets (^{12}C, ^{56}Fe, ^{208}Pb) with the plastic scintillator using antineutrinos from a beam with peak energy of 6 GeV. The signature of DIS event is that it has a charged lepton(muon in this case) and a large hadronic energy deposition in addition to the muon in the final state. The interaction equation is:

$$\bar{\nu}_\mu + N \rightarrow \mu^+ + X,$$

where N is a nucleon bound inside a nucleus of one of the nuclear target in MINERvA detector(carbon, iron, or lead) and X is represents hadrons in the final state of the DIS interaction.

6.1 Cross section formula

Experimental expression of total cross section as a function of neutrino energy is given as follows:

$$\sigma_i = \frac{U_{ij}(N_j - b_j)}{\Delta_i \ \epsilon_i \ \Phi_i \ N}, \tag{6.1}$$

where:

- $N_j \rightarrow$ total number of selected events in data in j^{th} reconstructed energy bin,
- $b_j \rightarrow$ number of background events in j^{th} reconstructed energy bin,
- $U_{ij} \rightarrow$ an unfolding matrix used to map events reconstructed in the j^{th} bin to their true i^{th} bin,
- $\Delta_i \rightarrow$ width of i^{th} bin,
- $\epsilon_i \rightarrow$ total event selection efficiency,
- $\Phi_i \rightarrow$ neutrino flux integrated over i^{th} energy bin.
- $N \rightarrow$ number of scattering centers (nucleons) in a particular target, C, CH, Fe or Pb.

In this chapter, signal definition and event selection for this analysis with the studies of background classifications are presented.

6.2 Event selection and signal definition

Knowing exactly the number of events(both real and simulated) passing a set of signal selection cuts is an important and first step in the process of measuring cross section. MINERvA detector record events for broad range of kinematical variables Q^2(four momentum transfer) and W(invariant mass of hadronic system). DIS events from all the events recorded are isolated after passing them from a set of selection cuts, then on the basis of reconstruction, selected events are distributed in the bins of E_ν(neutrino energy) and x_{bj}(Bjorken variable).

6.2.1 Event Selection Cuts

Following are the cuts used to select the data sets for the analysis:

- Only events having MINOS-matched muon tracks are reconstructed and analyzed as MINOS is used to measure and reconstruct charge and momentum of the muons and it is difficult to differentiate muons that stop in MINERvA from pions.

- The MINOS-matched muons must have positive curvature in the MINOS magnet field to ensure that the muon is positively charge and thus a $\bar{\nu}_\mu$ event.

- Curvature significance of 5σ or more are included in the analysis for the muon tracks reconstructed by curvature in the MINOS magnetic field.

- The endpoints of muon tracks must lie within the range of 210 mm to 2500 mm in the MINOS magnetic coil($210 < \mathrm{R} < 2500$ mm).

- The interaction vertex must fall inside an 850 mm apothem hexagonal fiducial area in x-y plane, to restrict the fiducial area to a region where the acceptance into MINOS changes less rapidly than at the outer edges of the detector.

- For the events occurring in targets 1, 2, 3 or 5, the interaction vertex must be 25 mm away from the barrier of materials in the targets. This cut helps in identifying the nucleus within the target with which the interaction occurred. Target 4 is just lead so no cut is required.

- The z position of the (anti)neutrino interaction vertex must be located within 1 plane upstream and 1 planes downstream of the passive nuclear targets.

- Events having average energy between 1.5 MeV and 6.5 MeV in 7 or more planes upstream of the interaction vertex are rejected. This selection cut removes events in the target coming from backward track from a target upstream.

- Due to the MINOS detector acceptance, angle of muon track w.r.t the (anti)neutrino beam must be less than 17 degrees($\theta_\mu \leq 17^o$) and neutrino energy must lie within 5 GeV $\leq E_\nu <$ 50 GeV.

	Upstream	Downstream
Iron	1.05 ± 0.01	1.05 ± 0.01
Lead	1.07 ± 0.01	1.04 ± 0.01
Carbon	1.02 ± 0.01	1.02 ± 0.01

Table 6.1: Plastic background scale factors for Inclusive sample.

Events passing all the above cuts are called *Inclusive events*. To separate DIS events from these inclusive events, cuts are employed on the variables Q^2 and W. For the events to be safely in the DIS region, an event is selected to have reconstructed $Q^2 \geq 1$ GeV^2 and $W \geq 2$ GeV and Monte Carlo (MC) event must have true generated $Q^2 \geq 1$ GeV^2 and true generated $W \geq 2$ GeV along with GENIE channel = 3 (i.e. DIS). GENIE channel = 3 cut ensures the elimination of the CCQE events producing charm quarks that can potentially pass the DIS Q^2 and W cuts. The events passing DIS cut on the basis of reconstructed(true) Q^2 and W are called *reconstructed(true) events*, events passing both reconstructed and true cuts are called *true reconstructed events*. MC events may have all three categories but for data events may only be reconstructed events or not reconstructed events.

6.3 Background studies

For the accurate measurement of DIS cross section in the nuclear targets, separating signal and background events is of utmost importance. In this analysis, events passing DIS definition($Q^2 \geq 1$ GeV^2 and $W \geq 2$ GeV) are taken as signal and rest as background. Depending on the position of the interaction vertex in the detector and events passing the cuts of kinematical variables, there are two types of background.

↬ Wrong target background

↬ Non-DIS background

After estimating the amount of background using MC sample, it is subtracted from the data.

6.3.1 Wrong target background

The wrong target background, as the name suggest, arise from the misreconstruction of the event in the passive nuclear target but its true interaction material is plastic scintillator that is next to the nuclear targets. This background is also called *plastic background*. To calculate plastic background, *inclusive* sample is used instead of DIS sample. Used sample includes both true DIS and non-DIS events, and for the calculation of signal events, wrong target background is subtracted first. In this analysis, interaction vertex reconstruction is done using machine learning approach, which considerably reduces this background as the misreconstruction of the events on the basis of the vertex position is minimized. Plastic background subtraction is performed after calculating the level of background by using simulation data constrained to the real data. For higher statistics, materials in the targets are combined and a scale factor for each material is obtained. The strategy adopted is given as:

- For a specific nuclear target material, events are looped over all targets.

- Leaving one plane in the upstream as well as in the downstream next to the nuclear targets, number of MC events coming from the plastic scintillator in 6 planes up and downstream are constrained to the reconstructed data as a function of variable called *planeDNN* which is directly related to the physical position of the planes in the detector.

- Using χ^2 minimization, a scale factor for upstream and downstream of each material is obtained and applied to the reconstructed events in the passive target.

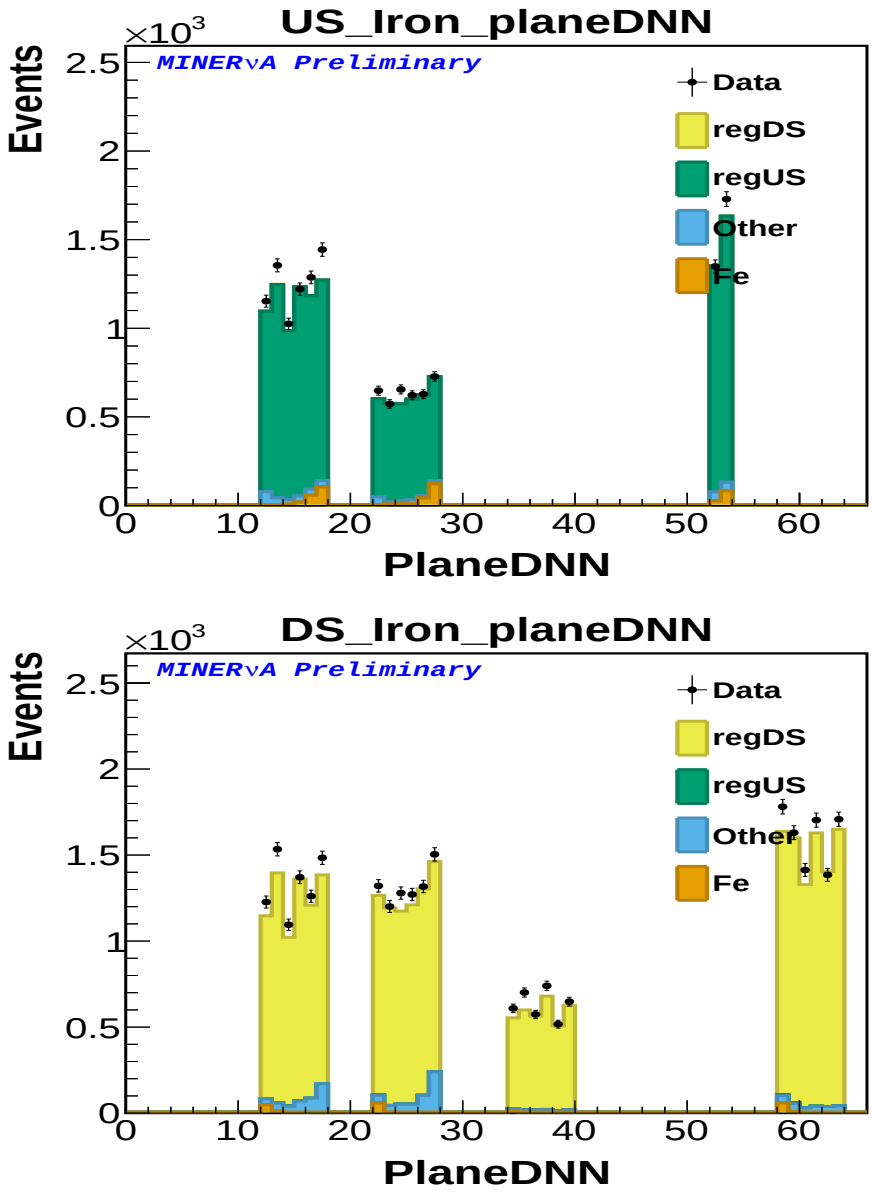

Figure 6.1: Wrong target background: Upstream (top), Downstream (bottom) using variable planeDNN. Stacked plots include events coming from upstream (regUS), downstream (regDS) regions, nuclear material(^{56}Fe) and *Other* represents the number of events coming from the other material in each target other than Iron. Black dots are for reconstructed data with statistical errors only.

Table-6.1 presents scale factor calculated for each material using Inclusive sample. Figs. 6.1, 6.2 and 6.3 show plots for MC and reconstructed data in the plastic scintillator upstream and downstream of all targets in the detector before applying fit for iron, lead and carbon, respectively and Figs. 6.4, 6.5 and 6.6 after applying

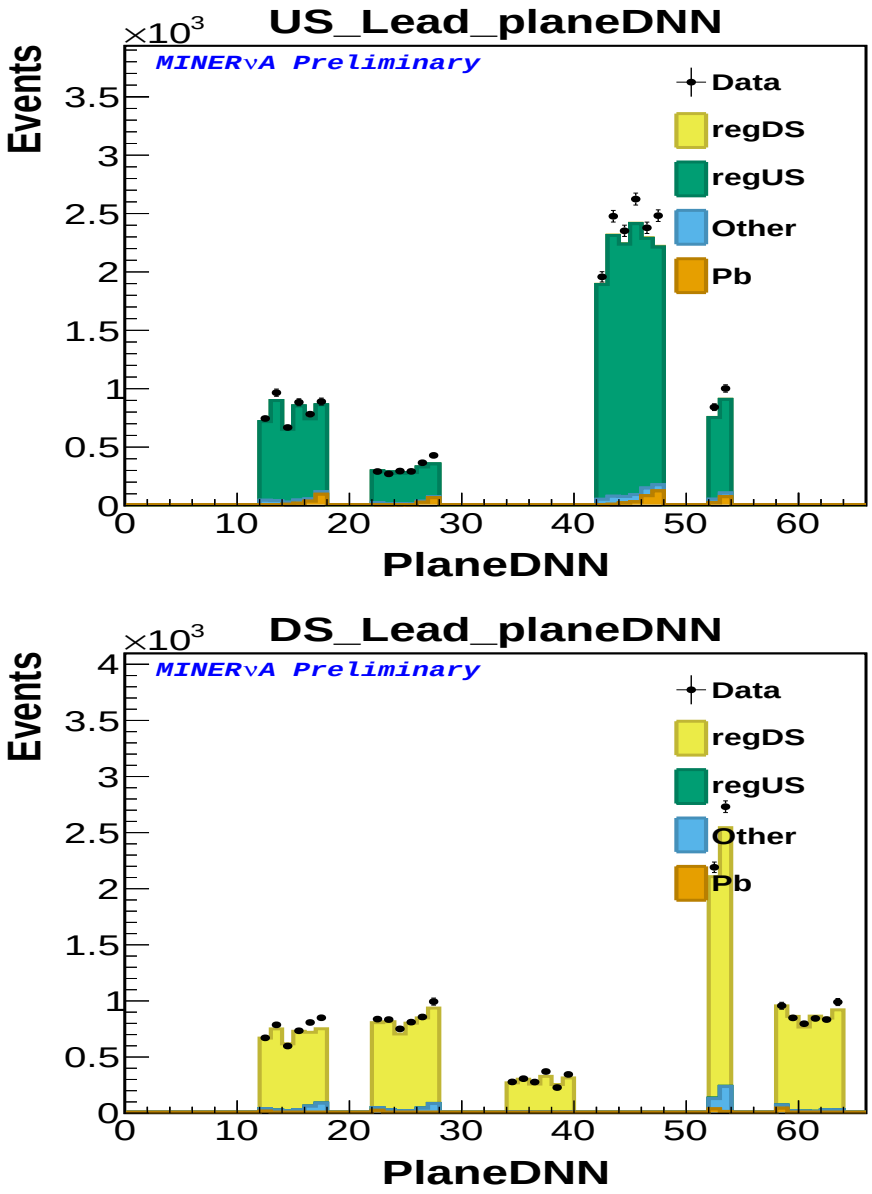

Figure 6.2: Wrong target background: Upstream (top), Downstream (bottom) using variable planeDNN. Stacked plots include events coming from upstream (regUS), downstream (regDS) regions, nuclear material(^{208}Pb) and *Other* represents the number of events coming from the other material in each target other than lead. Black dots are for reconstructed data with statistical errors only.

fit for iron and lead, respectively.

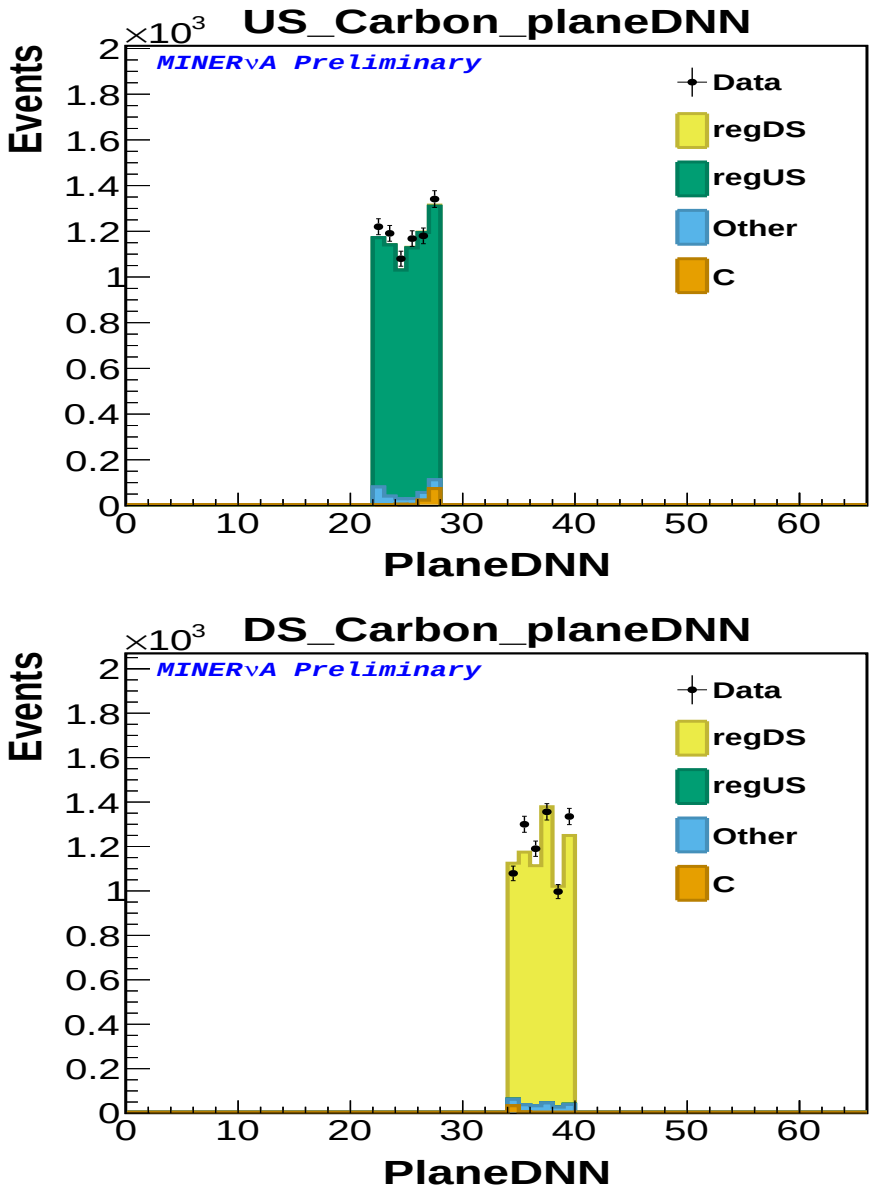

Figure 6.3: Wrong target background: Upstream (top), Downstream (bottom) using variable planeDNN. Stacked plots include events coming from upstream (regUS), downstream (regDS) regions, nuclear material(^{12}C) and *Other* represents the number of events coming from the other material in each target other than lead. Black dots are for reconstructed data with statistical errors only.

6.3.2 Non-DIS Background

After subtracting the plastic background, available data sample is only left with a mixture of true DIS and non-DIS events. So, next step is to remove non-DIS

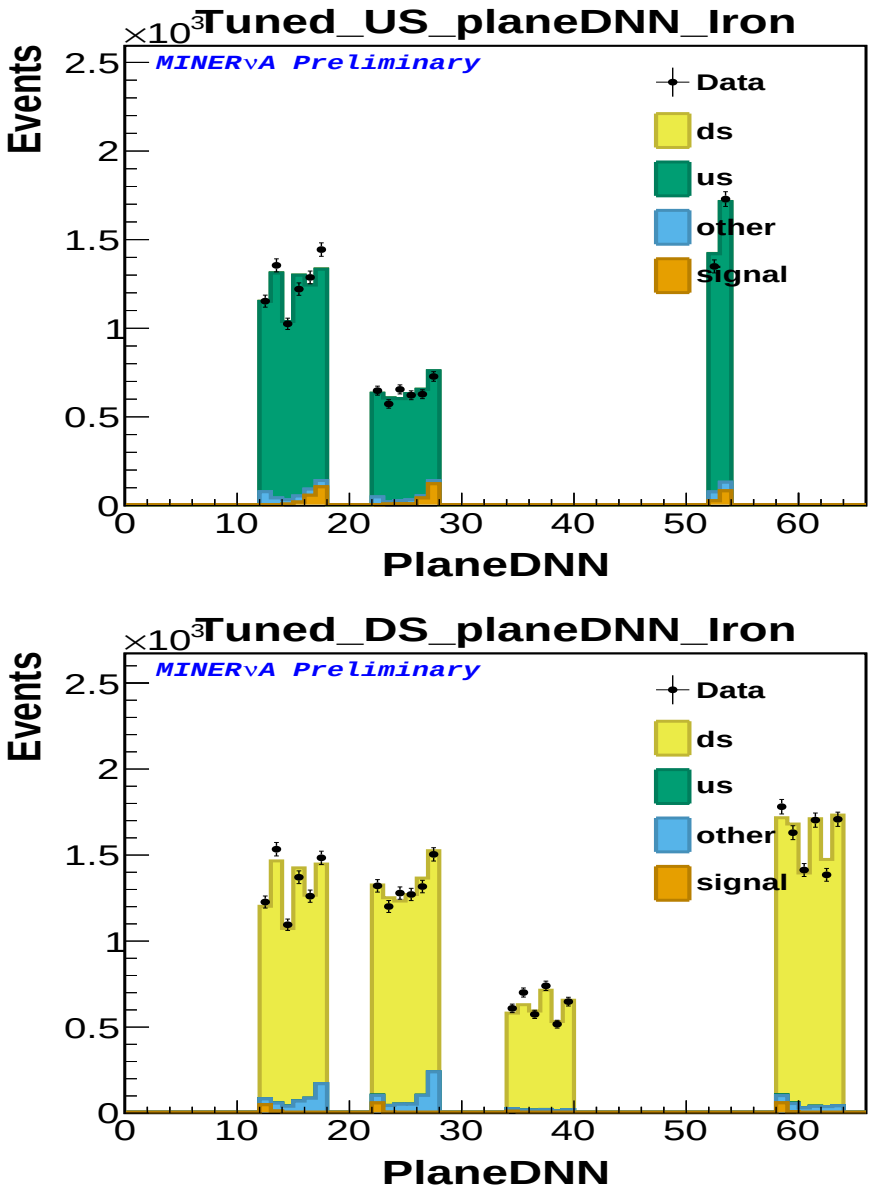

Figure 6.4: Wrong target background: Upstream (top), Downstream (bottom) using variable planeDNN. Stacked plots include events coming from upstream (regUS), downstream (regDS) regions, nuclear material(^{56}Fe) and *Other* represents the number of events coming from the other material in each target other than Iron. Black dots are for reconstructed data with statistical errors only.

background and obtain pure DIS events for the further steps in analysis. DIS sample has events passing boundaries set using kinematic variables $Q^2(\geq 1$ GeV$^2)$ and $W(\geq)$ 2 GeV but there are some events that passes the kinematic selection cuts by error but they are not truly DIS events. Depending on the basis of the

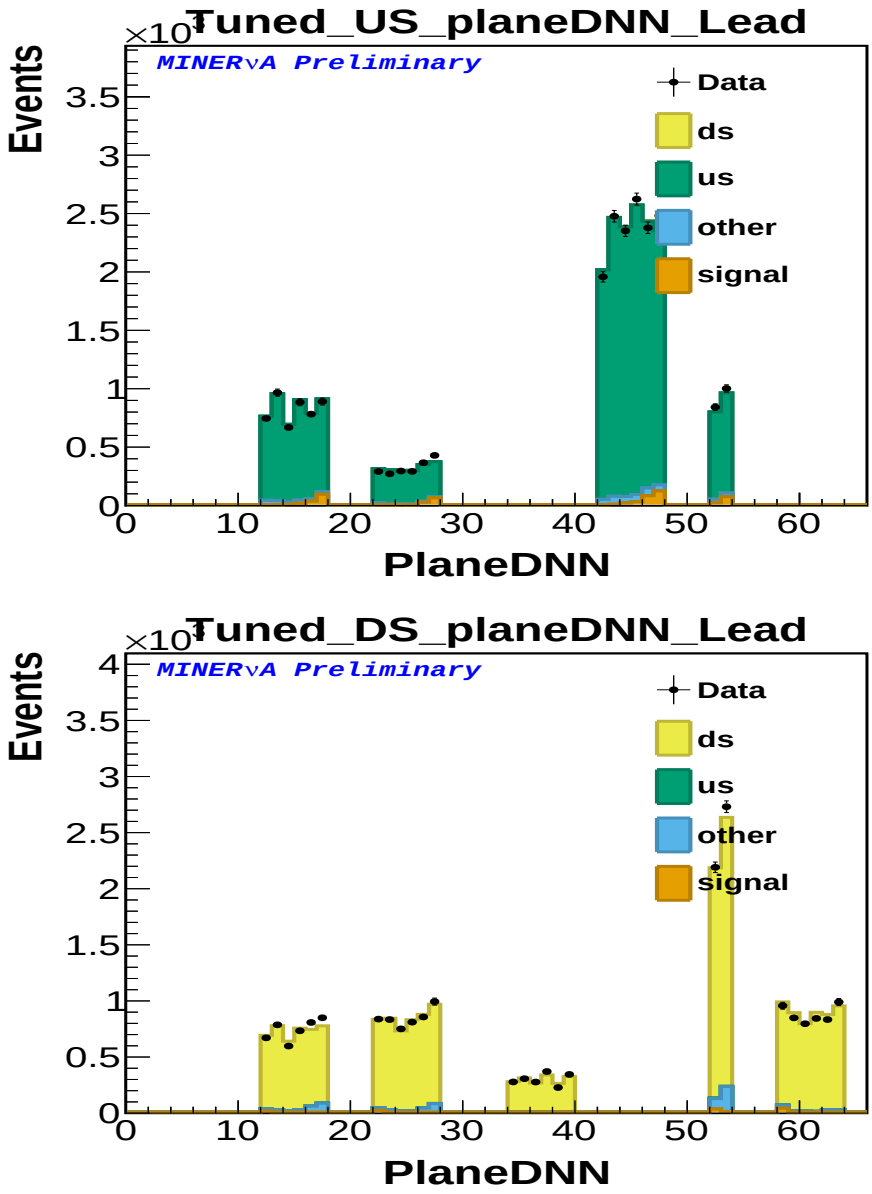

Figure 6.5: Wrong target background: Upstream (top), Downstream (bottom) using variable planeDNN. Stacked plots include events coming from upstream (regUS), downstream (regDS) regions, nuclear material(^{208}Pb) and *Other* represents the number of events coming from the other material in each target other than lead. Black dots are for reconstructed data with statistical errors only.

two kinematic variables, non-DIS background is also divided into two categories:

↬ *Low* Q^2 sideband called as *Continuum* sideband.

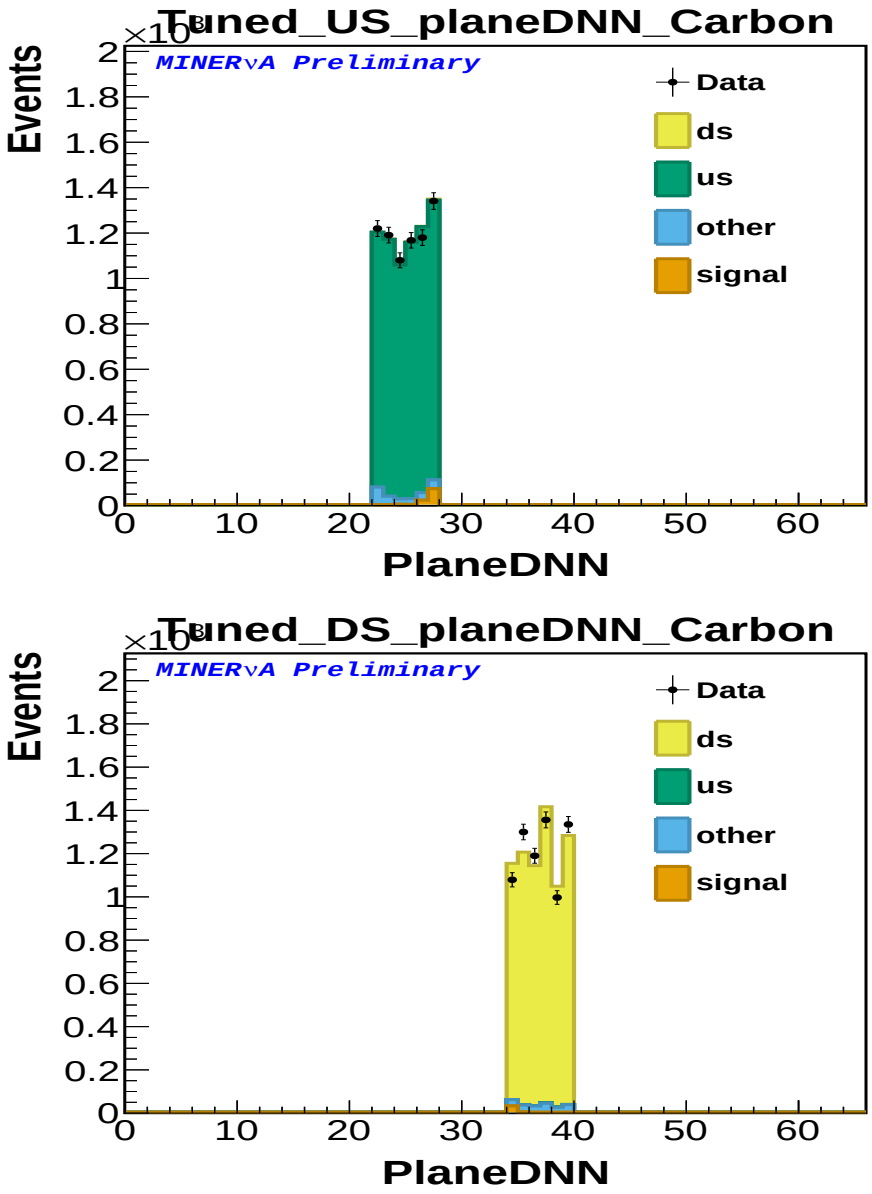

Figure 6.6: Wrong target background: Upstream (top), Downstream (bottom) using variable planeDNN. Stacked plots include events coming from upstream (regUS), downstream (regDS) regions, nuclear material(^{12}C) and *Other* represents the number of events coming from the other material in each target other than lead. Black dots are for reconstructed data with statistical errors only.

↪ kinematic region used: $Q^2 < 1$ GeV^2 and $W \geq 2$ GeV

↬ *Low W* sideband called as *Transition* sideband.

↪ kinematic region used: $Q^2 \geq 1$ GeV^2 and $W < 2$ GeV

	Upstream	Downstream
Iron	1.19 ± 0.04	0.91 ± 0.03
Lead	1.20 ± 0.04	0.90 ± 0.03
Carbon	1.23 ± 0.10	0.89 ± 0.06

Table 6.2: Physics background scale factors for each material and their statistical error.

The two sidebands with reconstructed 0.3 GeV^2 $< Q^2 <$ 0.9 GeV^2, W $\geq$ 2.0 GeV (low Q^2 sideband) and 1.5 GeV $\leq$ W $<$ 1.9 GeV, $Q^2 \geq$ 1.0 GeV^2 (low W sideband) are selected to estimate the background present in the DIS signal region. Fig. 6.7 represents these two backgrounds and DIS sample in the $Q^2 - W$ space.

Analysis in ME inherits the framework with many updates for the procedure used for the construction of DIS sideband in LE. Similar to the plastic background, a χ^2 minimization between the reconstructed data and the MC is performed the muon energy distribution and a scale factors are extracted for each nuclear material(^{12}C, ^{56}Fe and ^{208}Pb) in the detector and given in the table 6.2. Figs. 6.8 and 6.9 present the before and after fit distribution of the two non-DIS backgrounds for iron and Figs. 6.10 and 6.11 for lead.

6.4 Unfolding

To calculate numerator of the cross section formula(Eq. 6.2), we need signal sample which has background events subtracted and unfolding matrix(U_{ij}). When an event is measured in the detector, its reconstructed value differ from the true value because measuring introduce some deviations or smearing in the measurement. Some possible reasons for the smearing may be the finite resolution of the detector, energy losses due to the efficiency of the detector(known as acceptance of the detector). Before proceeding further to the calculation of the cross section, it is important to remove the detector effects from the measurement of the variables.

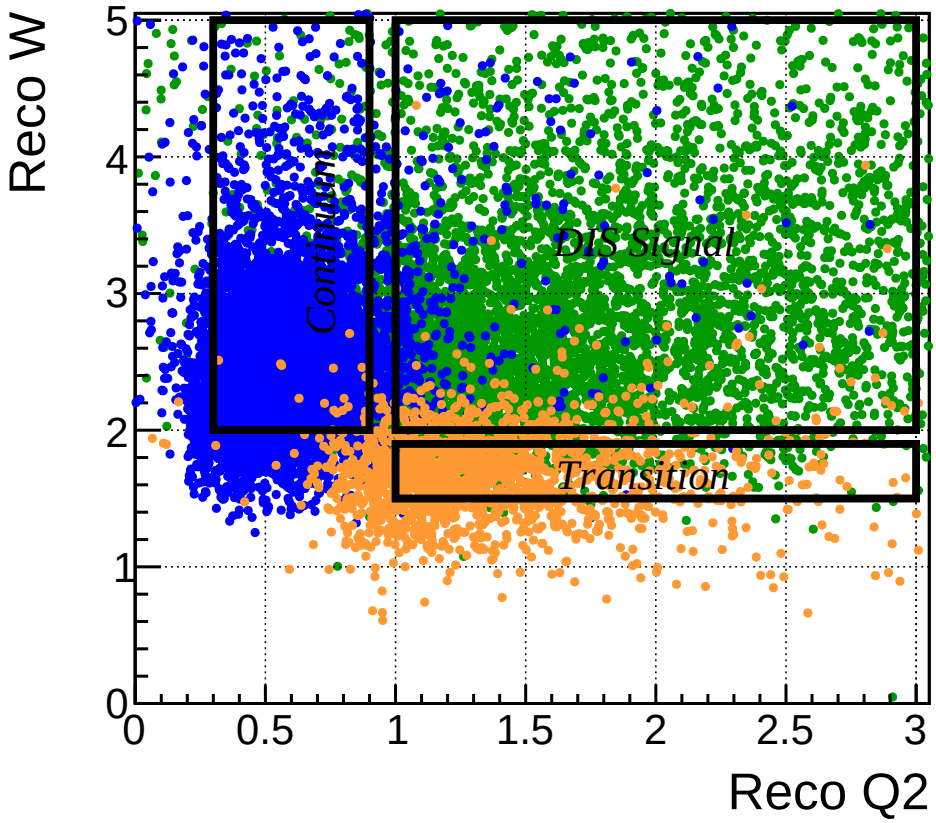

Figure 6.7: Reconstructed W vs. reconstructed Q^2 , with the two sidebands labeled. The green dots are true DIS events with the boundaries of the box to be $Q^2 \geq 1$ GeV^2 and $W \geq 2$ GeV. The blue and orange dots in two boxes are from non-DIS backgrounds. Boundaries for blue dots(continuum sideband) box are 0.3 GeV^2 $< Q^2 <$ 0.9 GeV^2, W $\geq$ 2.0 GeV and for orange dots(transition sideband) box, 1.5 GeV $\leq$ W $<$ 1.9 GeV, $Q^2 \geq$ 1.0 GeV^2.

This is done by the unfolding matrix. U_{ij} is used for mapping a reconstructed variable from the j bin to true variable in the i bin. Relation between the true & reconstructed value of the variable and migration matrix is given as:

$$a_i = M_{ij} a_j,$$

where M_{ij} is computed separately from the MC for each target. Unfolding(unsmearing) matrix(U_{ij}) is the inverse of the migration(smearing) matrix(M_{ij}):

$$a_j = M_{ij}^{-1} a_i$$

A migration matrix is often not directly invertible. Inverting the migration matrix might results in the inflation of the the statistical uncertainty in bins of the reconstructed variable and may lead to large fluctuations in the data. To regularize

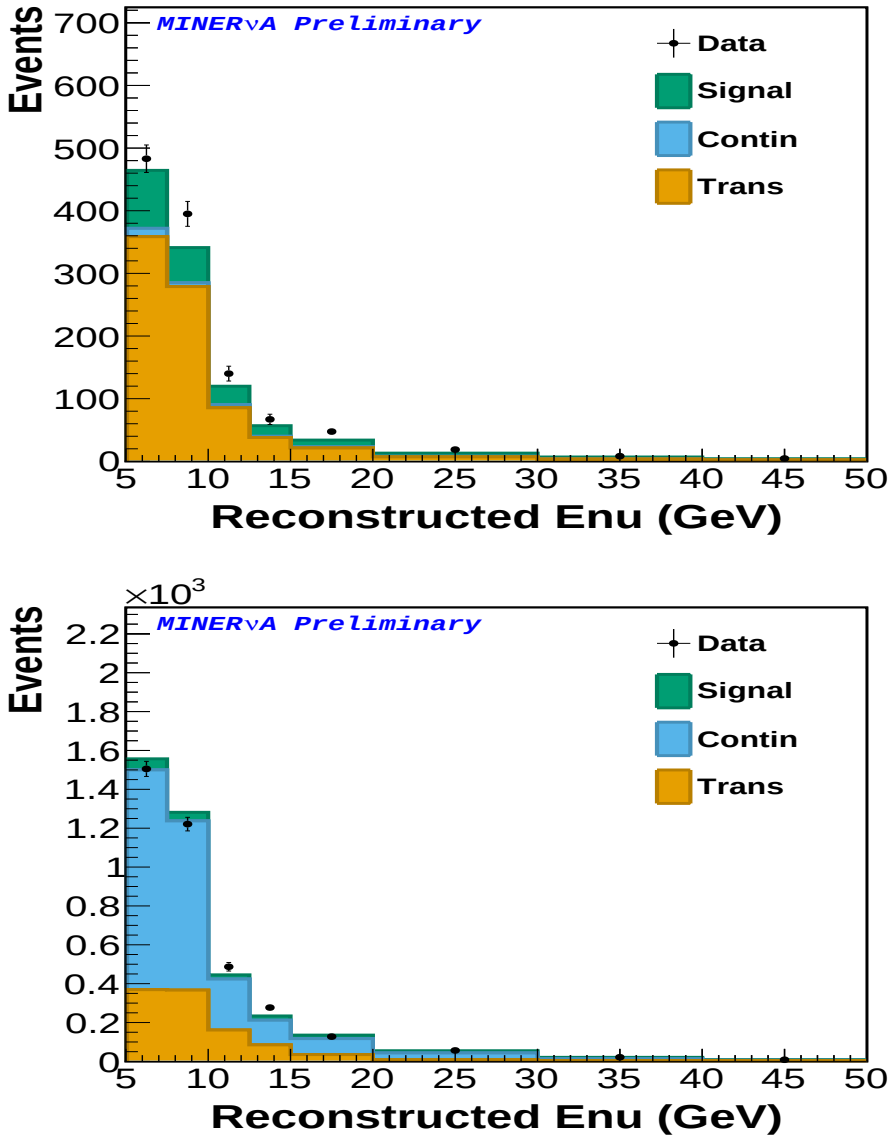

Figure 6.8: Non-DIS backgrounds: transition (top) and continuum (bottom) before fitting for iron. Black dots are for reconstructed data with statistical errors only. Fraction of events coming from signal in the background region are represented by green color. Orange and blue colors represent fraction of events coming from transition and continuum parts of the background region, respectively.

unfolding results, the Bayesian unfolding method is used. This unfolding method

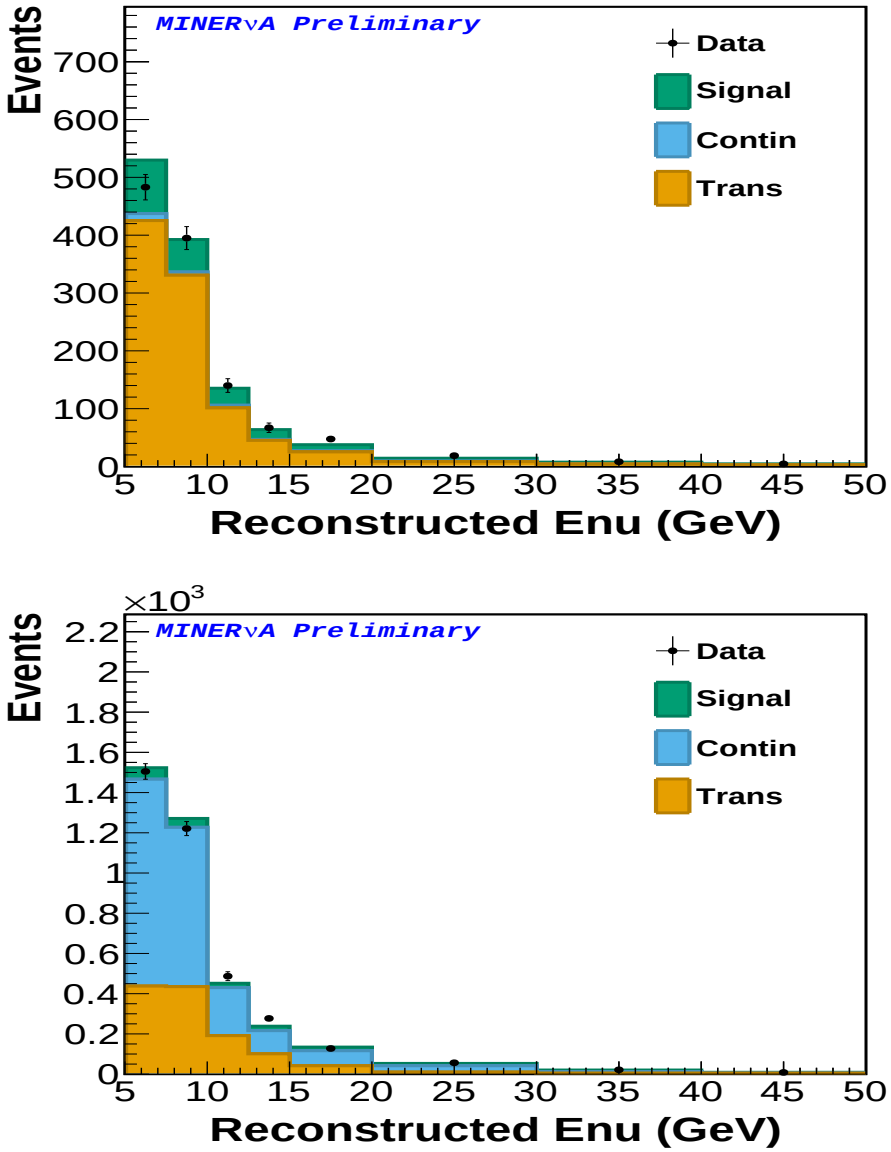

Figure 6.9: Non-DIS backgrounds: transition (top) and continuum (bottom) after fitting for iron. Black dots are for reconstructed data with statistical errors only. Fraction of events coming from signal in the background region are represented by green color. Orange and blue colors represent fraction of events coming from transition and continuum parts of the background region, respectively.

is fully described in [142]. Neutrino energy(E_ν) and Bjorken variable(x_j) are two variables selected for unfolding in this analysis.

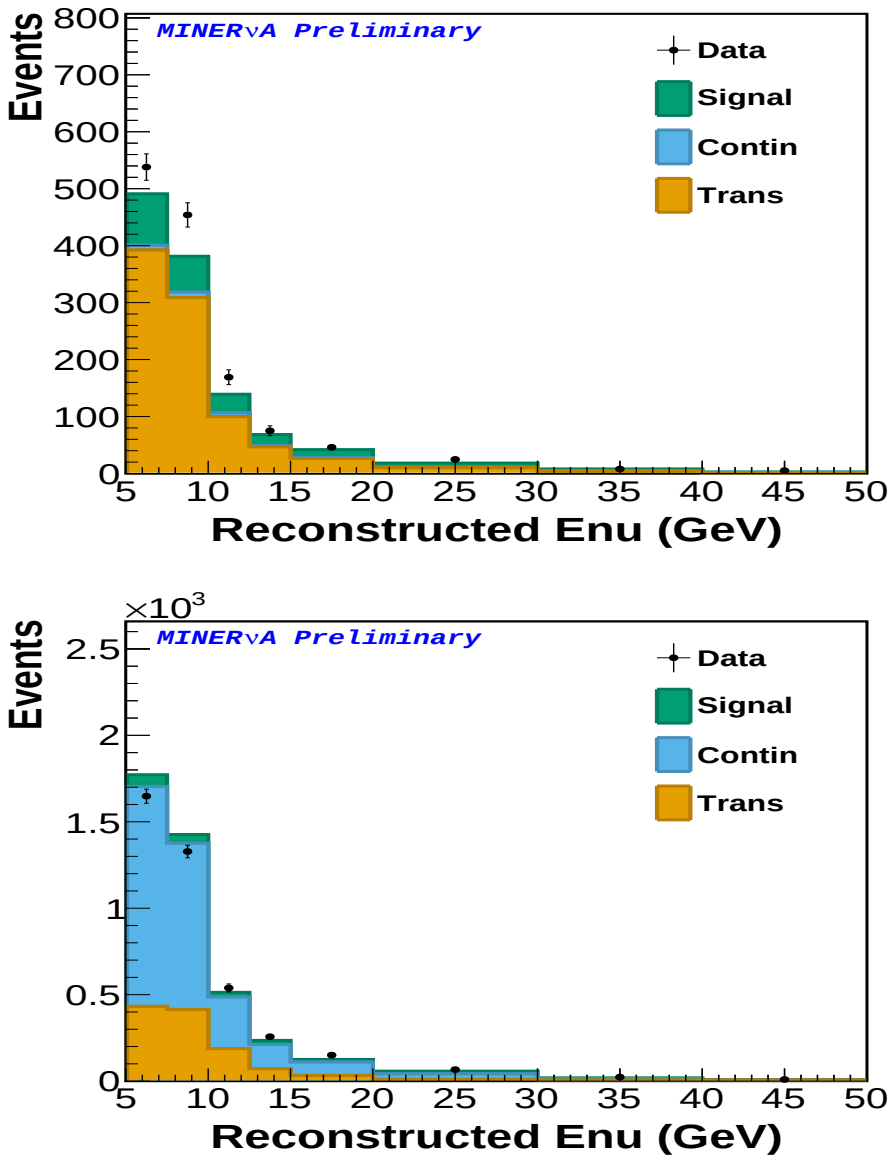

Figure 6.10: Non-DIS backgrounds: transition (top) and continuum (bottom) before fitting for lead. Black dots are for reconstructed data with statistical errors only. Fraction of events coming from signal in the background region are represented by green color. Orange and blue colors represent fraction of events coming from transition and continuum parts of the background region, respectively.

6.5 Efficiency correction and Flux division

In Eq. 6.2, next step for the calculation of the cross section is to obtain the denominator, which includes:

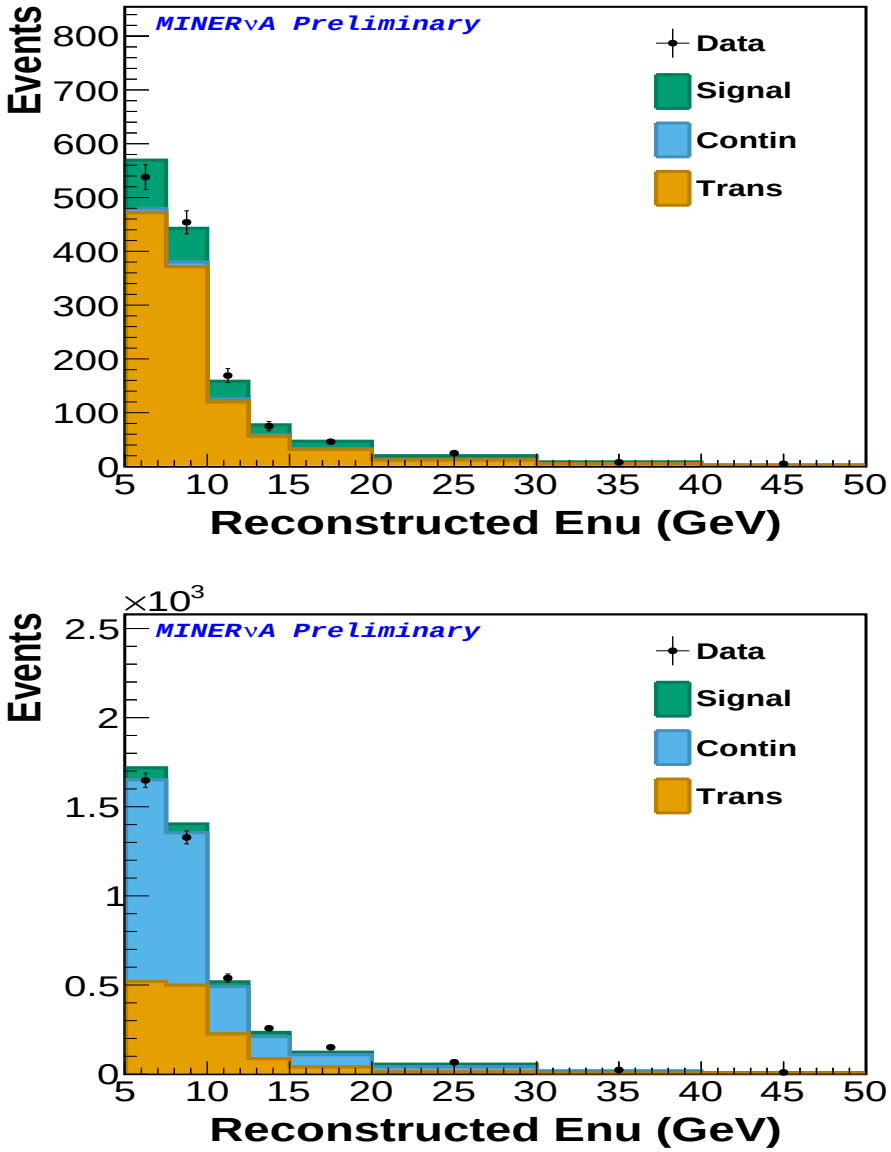

Figure 6.11: Non-DIS backgrounds: transition (top) and continuum (bottom) after fitting for lead. Black dots are for reconstructed data with statistical errors only. Fraction of events coming from signal in the background region are represented by green color. Orange and blue colors represent fraction of events coming from transition and continuum parts of the background region, respectively.

↬ Efficiency correction

↬ Flux

↬ Number of targets

6.5.1 Efficiency correction

Prior to dividing by the flux for the measurement of the total cross section, it is important to account for the inefficiency of the detector and analysis. For this reason, a efficiency correction is calculated and applied to the cross-section calculation. Only the simulated sample(MC events) is used for the calculation of the efficiency correction and the expression used is given below:

↬ Numerator of the efficiency correction: *Reconstructed DIS events passing the true DIS cuts, truly in a nuclear target A.*

↬ Denominator of the efficiency correction: *The total number of DIS events generated by the MC in nuclear target A.*

The efficiency correction for each material in each target is calculated individually as acceptance of the muon in the MINOS is different for each target.

6.5.2 Flux division, Number of scattering centers

The flux is computed from the simulated sample(MC). Regardless of event type, total number of the CC events of the simulated sample are measured with no cuts applied. The only requirement is that primary antineutrino must be a $\bar{\nu}_\mu$. For the calculation of the total cross section, the flux is averaged over each neutrino energy bin i (Eq. 6.2), and for differential cross section ($\frac{d\sigma}{dx}$) with respect to Bjorken variable(x), it is integrated over 2GeV $\geq E_\nu \geq$ 120GeV and $\frac{d\sigma}{dx}$ is divided by the width of the bin(Δ_i). The expression of the differential cross section is given as:

$$\frac{d\sigma_i}{dx} = \frac{U_{ij}(N_j - b_j)}{\Delta_i \ \epsilon_i \ \Phi \ N}. \tag{6.2}$$

The cross section is calculated per nucleon, for that σ is divided by the number of nucleons inside the fiducial volume. Using the measured density of the materials in the targets, the number of nucleons(N) are computed.

6.6 Cross section

All the components explained briefly in earlier sections are combined together to calculate the absolute cross section per nucleon. Work is in progress to measure the components and the absolute cross section per nucleon and the results will be communicated elsewhere.

Chapter 7

Electron and Muon production cross sections in quasielastic $\nu(\bar{\nu})$-Nucleus scattering for $E_\nu < 1\ GeV$

7.1 Introduction

In this chapter, we have studied ν_l, $\bar{\nu}_l$; $(l = e,\ \mu)$ induced CCQE scattering from some nuclear targets like ^{12}C, ^{40}Ar, ^{56}Fe and ^{208}Pb in the energy region of $E_\nu < 1\ GeV$ including the effect due to lepton mass and its kinematic implications, radiative corrections, form factors, second class currents, etc. We have performed the calculations using Local Fermi Gas Model(LFG) [143, 144, 145, 146] and also compared the numerical results with the different Fermi gas models of Smith and Moniz [64], Llewellyn Smith [65], Gaisser and O'Connell [66]. Using the different nuclear models we have studied the difference in the lepton(electron vs muon) cross sections due to the axial dipole mass, pseudoscalar form factor, radiative corrections and effect of the second class currents. Furthermore, in the Local Fermi Gas Model [143, 144, 145, 146] we have also included the nucleon-nucleon interactions due to which response of electroweak transition strength is

modified. These modifications are calculated by incorporating the interactions of particle-hole(1p-1h) excitation in the nuclear medium in a random phase approximation(RPA) [147, 148]. Our aim of this work is to study the role of dominant nuclear medium effects like Fermi motion, binding energy and nucleon correlations on the various physics inputs which lead to difference in electron and muon scattering cross sections in the case of per nucleon target. In section-7.2, we present the formalism in brief, in section-7.3, results and discussions are presented.

7.2 Formalism

7.2.1 Neutrino/Antineutrino scattering off a Nucleon target

The basic reaction for the quasielastic process is a neutrino/antineutrino interacting with a neutron(proton) target given by

$$\left.\begin{array}{rcl} \nu_l(k) + n(p) & \rightarrow & l^-(k') + p(p') \\ \bar{\nu}_l(k) + p(p) & \rightarrow & l^+(k') + n(p') \end{array}\right\} \quad l = e, \mu \tag{7.1}$$

where $k,\ k'$ are the four momenta of incoming and outgoing lepton and $p,\ p'$ are the four momenta of initial and final nucleon, respectively.

The invariant matrix element for the charged current reaction of (anti)neutrino, given by Eq. 7.1 is written as

$$\mathcal{M} = \frac{G_F}{\sqrt{2}} \cos\theta_c\ l_\mu\ J^\mu \tag{7.2}$$

where G_F is the Fermi coupling constant (=1.16639$\times 10^{-5}\ GeV^{-2}$), $\theta_c (= 13.1^0)$ is the Cabibbo angle. The leptonic weak current is given by

$$l_\mu \ = \ \bar{u}(k')\gamma_\mu(1 \pm \gamma_5)u(k), \tag{7.3}$$

where (+ve)$-$ve sign is for (antineutrino)neutrino.

J^μ is the hadronic current given by

$$J^\mu = \bar{u}(p')\Gamma^\mu u(p), \tag{7.4}$$

with

$$\begin{aligned}\Gamma^\mu &= F_1^V(Q^2)\gamma^\mu + F_2^V(Q^2)i\sigma^{\mu\nu}\frac{q_\nu}{M_p+M_n} + F_3^V(Q^2)\frac{2q^\mu}{M_p+M_n} \\ &+ F_A(Q^2)\gamma^\mu\gamma^5 + F_P(Q^2)\frac{2q^\mu}{M_p+M_n}\gamma^5 + F_3^A(Q^2)\frac{2(p+p')^\mu}{M_p+M_n}\gamma^5,\end{aligned} \tag{7.5}$$

where $q = k-k' = p'-p$ is the four momentum transfer, $Q^2(=-q^2) \geq 0$ is the four momentum transfer square, M_p=0.93827GeV is the proton mass, M_n=0.93956GeV is the neutron mass. We have taken $M_p \sim M_n = M$, where $M = \frac{M_p+M_n}{2}$ is the nucleon mass. $F_1^V(Q^2)$, $F_2^V(Q^2)$ and $F_3^V(Q^2)$ are the isovector vector, weak magnetic and induced scalar form factors and $F_A(Q^2)$, $F_3(Q^2)$ and $F_P(Q^2)$ are the axial vector, induced tensor (or weak electric) and induced pseudoscalar form factors, respectively. According to the classification of G-invariance introduced by Weinberg [149], the hadronic current J^μ in the matrix element(Eq.7.2) containing the form factors $F_{1,2}^V(Q^2)$, $F_{A,P}(Q^2)$ is known as the first class currents, while the hadronic current containing the form factors $F_3^V(Q^2)$ and $F_3^A(Q^2)$ correspond to the second class currents(SCC).

Using the leptonic and hadronic currents given in Eq.7.3 and Eq.7.4, the matrix element square is obtained by using Eq.7.2 as

$$|\mathcal{M}|^2 = \frac{G_F^2}{2}\cos^2\theta_c\ L_{\mu\nu}J^{\mu\nu} \tag{7.6}$$

$L_{\mu\nu}$ is the leptonic tensor calculated to be

$$L_{\mu\nu} = \bar{\Sigma}\Sigma {l_\mu}^\dagger l_\nu = L^S_{\mu\nu} \pm iL^A_{\mu\nu}, \quad \text{where} \tag{7.7}$$

$$L^S_{\mu\nu} = 8\ \left[k_\mu k'_\nu + k'_\mu k_\nu - g_{\mu\nu}\ k\cdot k'\right] \quad \text{and}$$

$$L^A_{\mu\nu} = 8\ \epsilon_{\mu\nu\alpha\beta}\ k'^\alpha k^\beta, \tag{7.8}$$

where the + sign(− sign) is for neutrino(antineutrino).

The hadronic tensor $J^{\mu\nu}$ is given by:

$$J^{\mu\nu} = \bar{\Sigma}\Sigma J^{\mu\dagger}J^\nu = \frac{1}{2}\mathrm{Tr}\left[(\not{p}'+M)\Gamma^\mu(\not{p}+M)\tilde{\Gamma}^\nu\right] \tag{7.9}$$

where $\tilde{\Gamma}^\nu = \gamma^0\ \Gamma^{\nu\dagger}\ \gamma^0$ and a factor of $\frac{1}{2}$ in $J^{\mu\nu}$ arises due to averaging over the spin of the nucleon in the initial state.

The hadronic current contains isovector vector form factors $F^V_{1,2}(Q^2)$ of the nucleons, which are given as

$$F^V_{1,2}(Q^2) = F^p_{1,2}(Q^2) - F^n_{1,2}(Q^2) \tag{7.10}$$

where $F_1^{p(n)}(Q^2)$ and $F_2^{p(n)}(Q^2)$ are the Dirac and Pauli form factors of proton(neutron) which in turn are expressed in terms of the experimentally determined Sach's electric $G_E^{p,n}(Q^2)$ and magnetic $G_M^{p,n}(Q^2)$ form factors as

$$F_1^{p,n}(Q^2) = \left(1+\frac{Q^2}{4M^2}\right)^{-1}\ \left[G_E^{p,n}(Q^2) + \frac{Q^2}{4M^2}\ G_M^{p,n}(Q^2)\right] \tag{7.11}$$

$$F_2^{p,n}(Q^2) = \left(1+\frac{Q^2}{4M^2}\right)^{-1}\ \left[G_M^{p,n}(Q^2) - G_E^{p,n}(Q^2)\right] \tag{7.12}$$

$G_E^{p,n}(Q^2)$ and $G_M^{p,n}(Q^2)$ are taken from different parameterizations [150, 151, 152, 153, 154] and the expressions of which is given in Appendix-A.1.

The isovector axial form factor is obtained from the quasielastic neutrino and antineutrino scattering as well as from pion electroproduction data and is parameterized as

$$F_A(Q^2) = F_A(0)\ \left[1+\frac{Q^2}{M_A^2}\right]^{-2};\quad F_A(0) = -1.267. \tag{7.13}$$

The pseudoscalar form factor is determined by using PCAC which gives a relation between $F_P(Q^2)$ and pion-nucleon form factor $g_{\pi NN}(Q^2)$ and is given by [65]:

$$F_P(Q^2) = \frac{2M^2F_A(0)}{Q^2}\left(\frac{F_A(Q^2)}{F_A(0)} - \frac{m_\pi^2}{(m_\pi^2+Q^2)}\frac{g_{\pi NN}(Q^2)}{g_{\pi NN}(0)}\right), \tag{7.14}$$

where m_π is the pion mass and $g_{\pi NN}(0)$ is the pion-nucleon coupling constant.

$F_P(Q^2)$ is dominated by the pion pole and is given in terms of axial vector form factor $F_A(Q^2)$ using the Goldberger-Treiman(GT) relation [65]

$$F_P(Q^2) = \frac{2M^2F_A(Q^2)}{m_\pi^2+Q^2}. \tag{7.15}$$

The form of pseudoscalar form factor $F_P(Q^2)$ using PCAC may also be written as [57]

$$F_p(Q^2) = \frac{M}{Q^2}\left[\left(\frac{2m_\pi^2F_\pi}{m_\pi^2+Q^2}\right)\ \left(\frac{MF_A(0)}{F_\pi} + \frac{g_{\pi NN}(0)\Delta Q^2}{m_\pi^2}\right) + 2MF_A(Q^2)\right], \tag{7.16}$$

where $g_{\pi NN}(0) = 13.21$, $F_\pi = 92.42\ MeV$ and $\Delta = 1 + \frac{MF_A(0)}{F_\pi g_{\pi NN}(0)}$.

Pseudoscalar form factor using Chiral Perturbation Theory(ChPT) is given by [54, 155, 57, 58]

$$F_P(Q^2) = \frac{2Mg_{\pi NN}(0)F_\pi}{m_\pi^2 + Q^2} + \frac{F_A(0)M^2 r_A^2}{3} \tag{7.17}$$

where axial radius $r_A = \frac{2\sqrt{3}}{M_A}$.

The form factors $F_3^V(Q^2)$ and $F_3^A(Q^2)$ are associated with the second class current(SCC). There are no compelling reasons for their existence as they violate charge or time symmetry and in the case of $F_3^V(Q^2)$ also the conserved vector current hypothesis. Almost all the current calculations of neutrino reactions assume SCC to be zero. However, there are some experimental analyses of semileptonic weak interactions like beta decays, muon capture and neutrino scattering in the $|\Delta S| = 0$ sector which give upper limits on these form factors which are consistent with the constraints of the present data on these processes [53, 156, 157, 158]. In Ref.[156] an upper limit (1.9) for the second class vector current obtained from neutrino experiments is given.

We have used the following expressions for $F_3^V(Q^2)$ as given in Ref. [156]

$$F_3^V(Q^2) = \frac{F_3^V(0)}{\left(1 + \frac{Q^2}{M_3^{V2}}\right)^2}. \tag{7.18}$$

To observe the maximum effect of the second class vector current we have taken $F_3^V(0) = 1.6$ on the upper side of the limit with $M_3^V = 1\ GeV$ [156] for our numerical calculations. Another expression for $F_3^V(Q^2)$ as given in Ref.[53] is

$$F_3^V(Q^2) = 4.4\ F_1^V(Q^2). \tag{7.19}$$

The axial form factor associated with the second class current $F_3^A(Q^2)$ is taken as [53, 156]

$$F_3^A(Q^2) = 0.15\ F_A(Q^2). \tag{7.20}$$

The parameterization of form factors discussed above will be used in the evaluation of the CCQE cross section. The differential scattering cross section for reaction

given in Eq.(7.1) in the laboratory frame is in general written as,

$$d\sigma = \frac{(2\pi)^4\delta^4(k+p-p'-k')}{4(k\cdot p)}\frac{d^3\mathbf{k}'}{(2\pi)^3 2E_l}\frac{d^3\mathbf{p}'}{(2\pi)^3 2E_p}\bar{\Sigma}\Sigma|\mathcal{M}|^2. \tag{7.21}$$

The double differential cross section $\sigma_{free}(E_l, \Omega_l)$ on free nucleon is then obtained as

$$\sigma_{free}(E_l,\Omega_l) \equiv \frac{d^2\sigma}{dE_l\, d\Omega_l} = \frac{|\mathbf{k}'|}{64\pi^2 E_\nu E_n E_p}\bar{\Sigma}\Sigma|\mathcal{M}|^2\delta[q_0 + E_n - E_p], \tag{7.22}$$

where $q_0(= E_\nu - E_l)$ is the energy transferred to the nucleon target. When the integration over lepton energy and angular variables are done one gets the total cross section for a free nucleon target.

7.2.2 Neutrino/Antineutrino scattering off a Nuclear target

When the processes given by Eq.7.1 take place in a nucleus, various nuclear medium effects like Pauli blocking, Fermi motion, binding energy corrections and multi nucleon correlations, etc. come into play. Moreover, the charged lepton produced in the final state moves in the Coulomb field of the residual nucleus and which affects its energy and momenta. We have taken into account these effects which are briefly discussed below:

1. In the Fermi gas model, it is assured that the nucleons in a nucleus (or nuclear matter) occupy one nucleon per unit cell in phase space so that the total number of nucleons N is given by($\hbar = c = 1$):

   $$N = 2V\int_0^{p_F}\frac{d\mathbf{p}}{(2\pi)^3},$$

   where a factor of two to account spin degree of freedom. All states upto a maximum momentum p_F ($p < p_F$) are filled. The momentum states higher than $\mathbf{p} > \mathbf{p_F}$ are unoccupied.

   The occupation number $n(\mathbf{p})$ is defined as:

   $$\begin{aligned} n(\mathbf{p}) &= 1, \mathbf{p} < \mathbf{p_F} \\ &= 0, \mathbf{p} > \mathbf{p_F} \end{aligned} \tag{7.23}$$

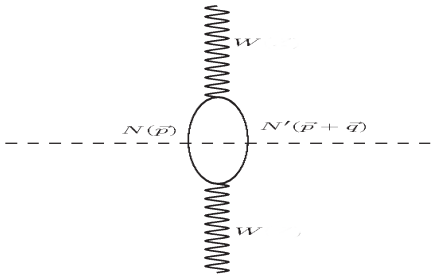

Figure 7.1: Diagrammatic representation of the particle - hole(p-h) excitation induced by W boson in the large mass limit of intermediate vector boson($M_W \to \infty$).

$$\begin{aligned} \Rightarrow \rho &= \frac{N}{V} = \frac{p_F^3}{3\pi^2} \\ \text{therefore,} \quad p_F &= (3\pi^2\rho)^{\frac{1}{3}}, \end{aligned} \tag{7.24}$$

where ρ is the average density of the nucleon in the nucleus.

Since the protons and neutrons are supposed to have different Fermi sphere, therefore,

$$p_{F_p} = \left(3\pi^2\rho_p\right)^{\frac{1}{3}} \qquad \text{and} \qquad p_{F_n} = \left(3\pi^2\rho_n\right)^{\frac{1}{3}}, \tag{7.25}$$

The representative values of the Fermi momentum are $p_F = 221\ MeV$ for carbon, $p_F = 251\ MeV$ for iron, etc.

2. Under a weak interaction induced by (anti)neutrino a nucleon is excited from an occupied state to an unoccupied state i.e. creating a hole in the Fermi sea and a particle above the sea. This is known as 1p-1h excitation (Fig.7.1), with the condition that the initial momentum: $\mathbf{p} < \mathbf{p_F^i}$ and the final momentum: $|\mathbf{p}+\mathbf{q}| > \mathbf{p_F^f}$.

   This condition is incorporated in the expression for the free nucleon cross section for the scattering of(anti)neutrino from the free nucleon at rest, i.e.

$$\begin{aligned} \frac{d^2\sigma_{\nu l}}{d\Omega(\hat{k'})dE_l'} &= \frac{M^2}{E_n E_p}\frac{|\mathbf{k}'|}{|\mathbf{k}\ |}\frac{G^2}{4\pi^2}L_{\mu\nu}J^{\mu\nu}\delta(q_0 + E_n - E_p), \\ \text{where} \quad J^{\mu\nu} &= \frac{1}{2}\mathrm{Tr}\left[(\not{p}' + M)\Gamma^\mu(\not{p} + M)\tilde{\Gamma}^\nu\right] \end{aligned} \tag{7.26}$$

and $G = G_F cos\theta_c$.

Nucleus	Binding Energy (MeV)	Q-Value(ν) (MeV)	Q-Value($\bar{\nu}$) (MeV)	R_p (fm)[148]	R_n (fm)[148]	a $(fm)^*$[148]
^{12}C	25	17.84	13.90	1.69	1.692	1.082(MHO)
^{16}O	27	19.70	14.30	1.83	1.833	1.544(MHO)
^{40}Ar	30	3.64	8.05	3.47	3.64	0.569(2pF)
^{56}Fe	36	6.52	4.35	3.97	4.05	0.593(2pF)
^{208}Pb	44	5.20	5.54	6.62	6.89	0.549(2pF)

Table 7.1: Binding energy and Q-value of the reaction for various nuclei. Last three columns are the parameters for modified harmonic oscillator(MHO) and 2 parameter Fermi(2pF) densities. * is dimensionless for the MHO density.

Inside the nucleus

$$\left.\frac{d^2\sigma_{\nu l}}{d\Omega(\hat{k'})dE'_l}\right|_{Nucleus} = \frac{G^2}{4\pi^2}\int \frac{M^2}{E_nE_p}2d\mathbf{p}\frac{1}{(2\pi)^3}n_n(\mathbf{p})(1-n(\mid \mathbf{p}+\mathbf{q}\mid))\frac{|\mathbf{k'}|}{|\mathbf{k}\mid} \times \delta(q_0+E_n-E_p)L_{\mu\nu}J^{\mu\nu}. \quad (7.27)$$

3. In the local Fermi gas (LFG) model, the Fermi momenta of the initial and final nucleons are not constant, but depend upon the interaction point **r** and are bounded by their respective Fermi momentum at r i.e. $p_{F_n}(r)$ and $p_{F_p}(r)$ for neutron and proton, respectively, where $p_{F_n}(r) = [3\pi^2\rho_n(r)]^{\frac{1}{3}}$ and $p_{F_p}(r) = [3\pi^2\rho_p(r)]^{\frac{1}{3}}$, $\rho_n(r)$ and $\rho_p(r)$ being the neutron and proton nuclear densities, respectively. The proton density is expressed in terms of the nuclear charge density $\rho(r)$ as $\rho_p(r) = \frac{Z}{A}\rho(r)$ and neutron density given by $\rho_n(r) = \frac{A-Z}{A}\rho(r)$, where $\rho(r)$ is the nuclear density determined experimentally by the electron-nucleus scattering experiments [159, 160] for the proton and using neutron matter density obtained using Hartree-Fock calculation for the neutron [160]. Some of the density parameters for different nuclei used in the present calculation are tabulated in Table 7.1.

4. Thus in the local density approximation the total scattering cross section(σ) for the ν_l scattering from a nucleon moving in the nucleus with a momentum **p** is given by [161]:

$$\sigma(q^2,k') = \int 2d\mathbf{r}d\mathbf{p}\frac{1}{(2\pi)^3}n_n(\mathbf{p}(\mathbf{r}))[1-n_p(\mathbf{p}(\mathbf{r})+\mathbf{q}(\mathbf{r}))]\sigma_{\text{free}}(\mathbf{q^2},\mathbf{k'},\mathbf{p}), \quad (7.28)$$

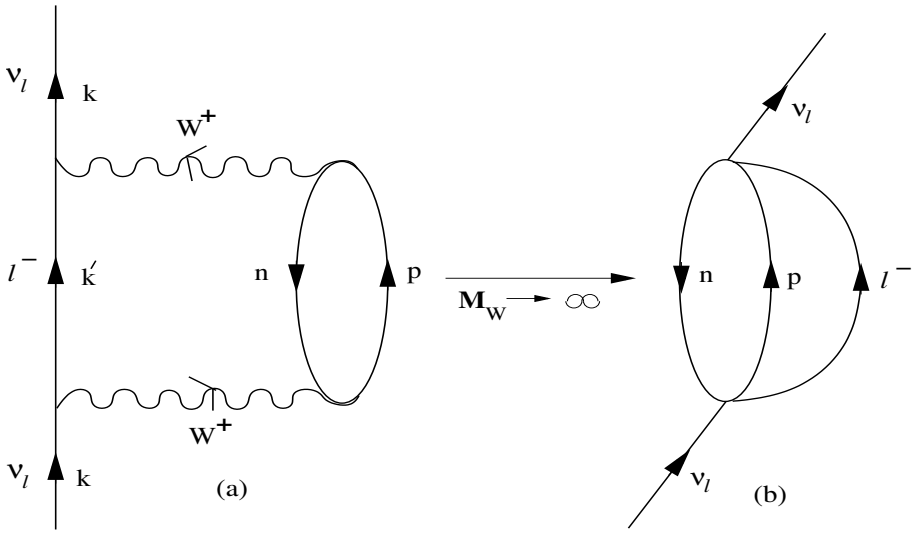

Figure 7.2: Diagrammatic representation of the neutrino self-energy corresponding to the ph-excitation leading to $\nu_l + n \to l^- + p$ in nuclei. In the large mass limit of the intermediate vector boson(i.e. $M_W \to \infty$) the diagram (a) is reduced to (b) which is used to calculate $|\mathcal{M}|^2$ in Eq.(7.6).

where σ_{free} is given by Eq.7.22. In the above expression, $n_n(\mathbf{p}(\mathbf{r}))$ and $n_p(\mathbf{p}(\mathbf{r}) + \mathbf{q}(\mathbf{r}))$ represent the occupation numbers for the neutron and proton respectively i.e. at a given position $\mathbf{r}$, $n_n(\mathbf{p}(\mathbf{r}))$=1 for $p \leq p_{F_n}(r)$, and 0 otherwise, and $n_p(\mathbf{p}(\mathbf{r})+\mathbf{q}(\mathbf{r}))$=1 for $|\mathbf{p}(\mathbf{r})+\mathbf{q}(\mathbf{r})| \geq p_{F_p}(r)$, and 0 otherwise.

5. Instead of using Eqs. 7.22 and 7.28, we use the methods of many body field theory [162], where the reaction cross section for the process $\nu_l + n \to l^- + p$ in a nuclear medium is given in terms of the imaginary part of the Lindhard function $U_N(q_0, \mathbf{q})$ corresponding to the p-h excitation diagram shown in Fig.7.2 [161].

   This imaginary part $U_N(q_0, \mathbf{q})$ is obtained by cutting the W self energy diagram along the horizontal line (Fig.7.2) and applying the Cutkowsky rules [163]. This is equivalent to replacing the expression

$$\int \frac{d\mathbf{p}}{(2\pi)^3} n_n(\mathbf{p})[1 - n_p(\mathbf{p}+\mathbf{q})] \frac{M_n M_p}{E_n(\mathbf{p}) E_p(\mathbf{p}+\mathbf{q})} \delta[q_0 + E_n - E_p] \qquad (7.29)$$

   occurring in Eq.(7.28) by $-(1/\pi)\text{Im}U_N(q_0, \mathbf{q})$. The imaginary part of the Lindhard function is calculated in Appendix-A.3 following Ref. [161].

6. When the reaction $\nu_l + n \rightarrow l^- + p$ takes place in the nucleus, the first consideration is the Q value which inhibits the reaction in the nucleus. The experimental Q values corresponding to the ground state(g.s.) $\rightarrow$ ground state(g.s.) transition are given in Table-7.1 for the different nuclei considered in this work. We also introduce $Q_F(r) = E_{F_2}(r) - E_{F_1}(r)$ to take into account the difference in the Fermi levels of the initial and final nuclei, which results in an effective value of $Q = Q - Q_F(r)$ to be used in the local Fermi Gas model. These considerations imply that q_0 should be modified to $q_0^{eff}(r) = q_0 - (Q - Q_F(r))$ in the calculation of the Lindhard function.

7. In the charged current reaction, the energy and momentum of the outgoing charged lepton are modified due to the Coulomb interaction with the final nucleus. The Coulomb distortion effect on the outgoing lepton has been taken into account in an effective momentum approximation(EMA) [164, 165, 166, 167] in which the lepton momentum and energy are modified by replacing E_l by $E_l + V_c(r)$. The form of the Coulomb potential $V_c(r)$ considered here is:

$$V_c(r) = -\alpha\ 4\pi \left(\frac{1}{r} \int_0^r \frac{\rho_p(r')}{Z} r'^2 dr' + \int_r^\infty \frac{\rho_p(r')}{Z} r' dr' \right), \tag{7.30}$$

where α is fine structure constant and $\rho_p(r)$ is the proton density of the final nucleus.

Incorporation of these considerations results in the modification of the argument of the Lindhard function, i.e.

$$ImU_N(q_0, \mathbf{q}) \longrightarrow ImU_N(q_0^{eff}(r) - V_c(r), \mathbf{q}). \tag{7.31}$$

With the inclusion of these nuclear effects, the cross section $\sigma(E_\nu)$ is written as

$$\begin{aligned} \sigma(E_\nu) &= -2{G_F}^2 \cos^2\theta_c \int_{r_{min}}^{r_{max}} r^2 dr \int_{{k'}_{min}}^{{k'}_{max}} k' dk' \int_{Q^2_{min}}^{Q^2_{max}} dQ^2 \frac{1}{E_{\nu_l}^2 E_l} \\ &\times L_{\mu\nu} J^{\mu\nu} ImU_N(q_0^{eff}(r) - V_c(r), \mathbf{q}). \end{aligned} \tag{7.32}$$

We must point out that in the above expression the outgoing lepton momentum and energy are r-dependent i.e. $k' = k'(r)$ and $E_l = E_l(r)$, and only in the asymptotic limit ($r \rightarrow \infty$) they become independent of r. With

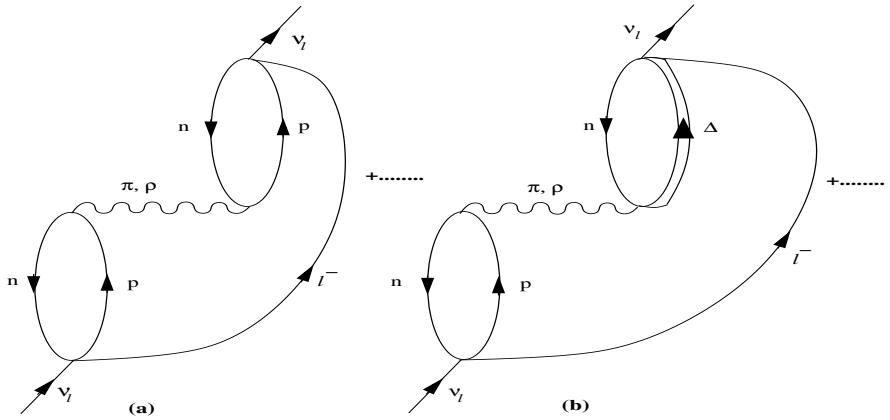

Figure 7.3: Many body Feynman diagrams (drawn in the limit $M_W \to \infty$) accounting for the medium polarization effects contributing to the process $\nu_l + n \to l^- + p$.

the incorporation of the Coulomb effect, $E_l(r)$ is modified to $E_l(r) + V_c(r)$, and $|\mathbf{k}'(\mathbf{r})| = \sqrt{(\mathbf{E_l(r)} + \mathbf{V_c(r)})^2 - \mathbf{m_l^2}}$. Accordingly the energy transfer q_0 modifies to $q_0^{eff}(r) = q_0^{eff}(r) - V_c(r)$, and the three momentum transfer $\mathbf{q}$ modifies to $\mathbf{q}(\mathbf{r}) = \mathbf{k} - \mathbf{k}'(\mathbf{r})$.

8. In a nucleus there are many nucleons, which are strongly interacting particles. These nucleons interact through π, ρ, etc. exchange of mesons(Fig.7.3). Therefore, in the nucleus the strength of the electroweak couplings may change from their free nucleon values due to the presence of strongly interacting nucleons. CVC forbids any change in the charge coupling while the magnetic and the axial vector couplings are likely to change from their free nucleon values. There exists considerable work in understanding the quenching of magnetic moment and axial charge in nuclei due to nucleon-nucleon correlations. In our approach these are reflected in the modification of nuclear response in longitudinal and transverse channels leading to some reduction which has been illustrated in brief in Appendix-A.4 We calculate this reduction in the vector-axial(VA) and axial-axial(AA) response functions due to the long range nucleon-nucleon correlations treated in the random phase approximation(RPA), which has been diagrammatically shown in Fig.7.3.

The weak nucleon current described by Eq.7.4 gives in the non-relativistic limit, terms like $F_A\sigma\tau_+$ and $iF_2^V\frac{\sigma\times\mathbf{q}}{2M}\tau_+$ which generate spin-isospin transitions in nuclei. While the term $iF_2^V\frac{\sigma\times\mathbf{q}}{2M}\tau_+$ couples with the transverse excitations, the term $F_A\sigma\tau_+$ couples with the transverse as well as longitudinal channels. These channels produce different RPA responses in the longitudinal and transverse channels due to the different NN potential in these channels when the diagrams of Fig.7.4 are summed up.

The effect of the Δ degrees of freedom in the nuclear medium is included in the calculation of the RPA response by considering the effect of ph-Δh and Δh-Δh excitations. This is done by replacing $U_N \rightarrow U'_N = U_N + U_\Delta$, where U_Δ is the Lindhard function for the Δh excitation in the nuclear medium. The expressions for U_N and U_Δ are taken from Ref.[168]. The different couplings of N and Δ are incorporated in U_N and U_Δ and then the same interaction strengths (V_l and V_t) are used to calculate the RPA response.

With the incorporation of these nuclear medium effects the expression for the total scattering cross section $\sigma(E_\nu)$ is given by Eq.(7.32) with $J^{\mu\nu}$ replaced by $J^{\mu\nu}_{RPA}$ i.e.

$$\begin{aligned}\sigma(E_\nu) &= -2{G_F}^2 cos^2\theta_c \int_{r_{min}}^{r_{max}} r^2 dr \int_{{k'}_{min}}^{{k'}_{max}} k' dk' \int_{Q^2_{min}}^{Q^2_{max}} dQ^2 \frac{1}{E^2_{\nu_l} E_l} \\ &\times L_{\mu\nu} J^{\mu\nu}_{RPA} Im U_N(q_0^{eff}(r) - V_c(r)), \end{aligned} \tag{7.33}$$

where $J^{\mu\nu}_{RPA}$ is the hadronic tensor with its various components modified due to long range correlation effects treated in RPA for the leading term proportional to F_A^2. The explicit expressions for $J^{\mu\nu}_{RPA}$ is given in the Appendix-A.5

7.2.3 Other versions of the Fermi gas model

Now we present in brief the form of the various other Fermi gas model used in the literature [65, 66]. In the Llewellyn Smith Fermi gas model [65], the cross section per nucleon in a nucleus is equal to the cross section for a free nucleon i.e. σ_{free}

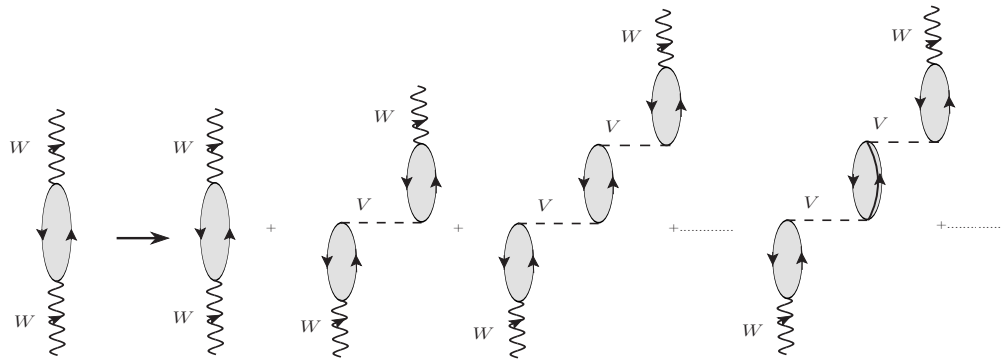

Figure 7.4: RPA effects in the 1p1h contribution to the W self energy, where particle-hole, Δ-hole, Δ-Δ, etc. excitations contribute.

defined in Eq.7.22, multiplied by $\left[1-\frac{D}{N}\right]$, where

$$\begin{aligned} D &= Z \quad for \quad 2x < u - v \\ &= \frac{1}{2}A\left\{1 - \frac{3x}{4}(u^2+v^2) + \frac{x^3}{2} - \frac{3}{32x}(u^2-v^2)^2\right\} \qquad for \quad u-v < x < u+v \\ &= 0 \quad for \quad x > u+v \end{aligned} \tag{7.34}$$

with $x = \frac{|\mathbf{q}|}{2p_F}$, $u = (\frac{2N}{A})^{1/3}$, $v = (\frac{2Z}{A})^{1/3}$ and $N(=A-Z),\ Z,\ A$ are neutron, proton and mass numbers of the initial nucleus, respectively. p_F is the Fermi momentum and the three momentum transfer $|\mathbf{q}| = \sqrt{\mathbf{q_0^2} + \mathbf{Q^2}}$.

Smith and Moniz [64] used the following expression for the double differential cross section in the Fermi gas model:

$$\begin{aligned} \frac{d^2\sigma}{dk' d\Omega_l} &= \frac{G_F^2 k'^2 \cos^2(\frac{1}{2}\chi)}{2\pi^2 M}\left\{W_2 + [2W_1 + \frac{m_l^2}{M^2}W_\alpha]\tan^2(\frac{1}{2}\chi)\right. \\ &+ (W_\beta + W_8)m_l^2/(ME_l\ \cos^2(\frac{1}{2}\chi)) - 2W_8/M\ \tan(\frac{1}{2}\chi) \\ &\times \left.\sec(\frac{1}{2}\chi)[-Q^2\ \cos^2(\frac{1}{2}\chi) + |\mathbf{q}|^2\ \sin^2(\frac{1}{2}\chi) + m_l^2]^{\frac{1}{2}}\right\}, \end{aligned} \tag{7.35}$$

where $\cos\chi = \frac{k'}{E_l}\cos\theta$. The form of W_i's and other details are given in Ref. [64].

Gaisser and O'Connell [66] have used relativistic response function $R(q, q_0)$, in a Fermi gas model to take into account nuclear medium effects, the expression for

the double differential scattering cross section is given by

$$\begin{aligned}
\frac{d^2\sigma}{d\Omega_l dE_l} &= C\ \frac{d\sigma_{free}}{d\Omega_l}\ R(q,q_0), \\
R(q,q_0) &= \frac{1}{\frac{4}{3}\pi p_{F_N}^3}\int \frac{d^3p_N\ M^2}{E_N E_{N'}}\delta(E_N+q_0-E_B-E_{N'})\theta(p_{F_N}-|\mathbf{p_N}|) \\
&\times\ \theta(|\mathbf{p_N}+\mathbf{q}|-p_{F_{N'}}),
\end{aligned} \tag{7.36}$$

where p_{F_N} is the Fermi momentum for the initial nucleon, N, N'=n or p and $C = A - Z$ for neutrino induced process and $C = Z$ for the antineutrino induced process. $\frac{d\sigma_{free}}{d\Omega_l}$ is the differential scattering cross section for the (anti)neutrino reaction on free (proton)neutron target and we have used the same expression for the form factors as used in the LFG for the numerical calculations. Different parameters associated with nuclear densities, $Q-$value of the reaction, binding energy and Fermi momentum used in the numerical calculations are summarized in Table-7.1.

7.3 Results and Discussion

In this section, we have presented the results for the total scattering cross section using the expression given in Eq. 7.32 (without RPA effects) and Eq. 7.33(with RPA effects) and discussed the findings.

7.3.1 Nuclear model dependence

In Fig. 7.5, the results are presented for the ratio of scattering cross section per interacting nucleon to the scattering cross section on free nucleon target for (anti)neutrino induced processes in ^{12}C, ^{40}Ar, ^{56}Fe and ^{208}Pb in the energy region from threshold to 0.8 GeV. The results are obtained using Local Fermi Gas Model(LFG) i.e. the expression given in Eq.7.32 and the Local Fermi Gas Model with RPA effect(LFG+RPA) i.e. using Eq.7.33 to the cross section obtained for the free nucleon case using Eq.7.21 on neutron(proton) target induced by neu-

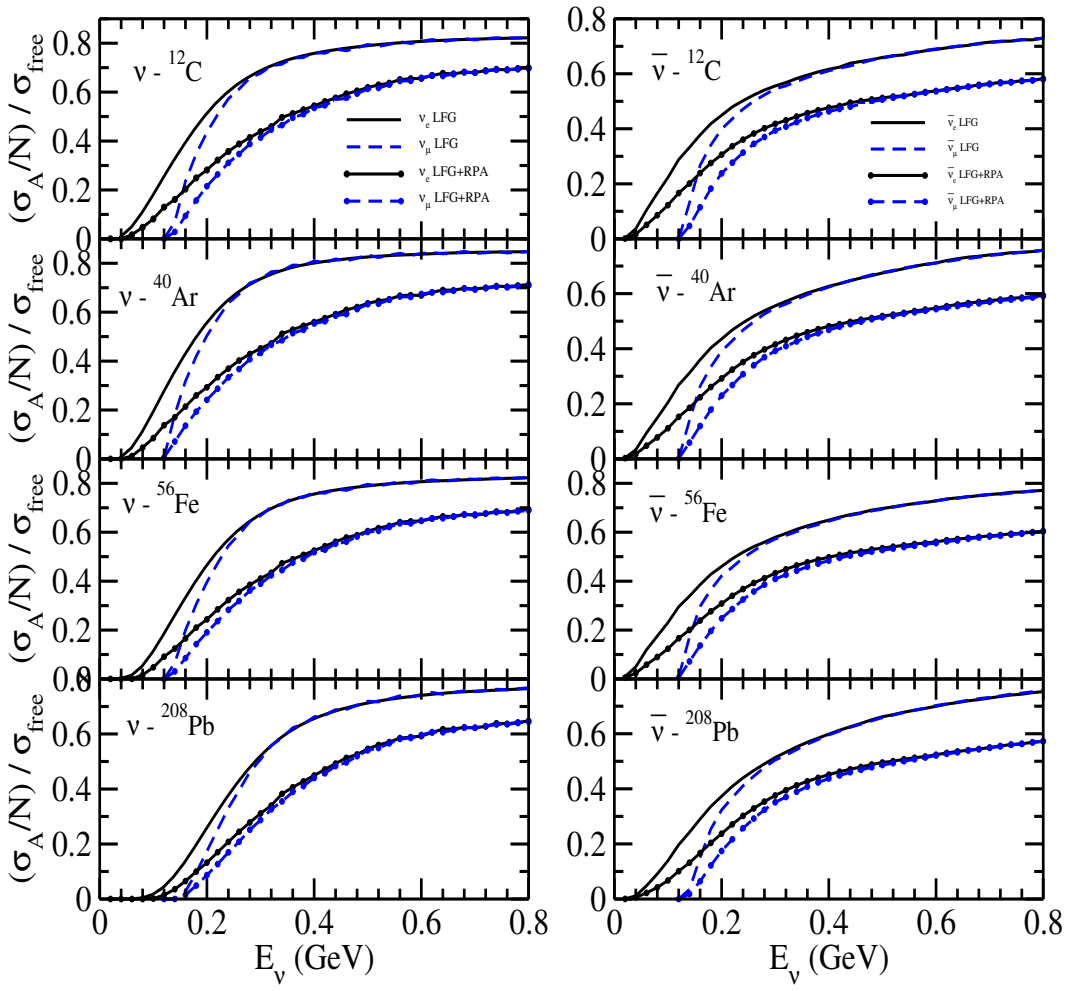

Figure 7.5: Ratio $\frac{\sigma_{A/N}}{\sigma_{free}}$ vs E_ν, for neutrino(Left panel) and antineutrino(Right panel) induced processes in ^{12}C, ^{40}Ar, ^{56}Fe and ^{208}Pb. The solid(dashed) line represent cross section obtained from electron(muon) type neutrino and antineutrino beams. For neutrino induced process $N = A - Z$, is neutron number and for antineutrino induced process $N = Z$, is proton number. σ_A is cross section in nuclear target and has been evaluated using Local Fermi Gas Model(LFG) and LFG with RPA effect(LFG+RPA) and σ_{free} is the cross section for the free nucleon case.

trino(antineutrino). Performing calculations using LFG, we find that in ^{12}C the nuclear medium effects like Fermi motion, Pauli blocking, binding energy, result in the reduction of cross section by $\sim$ 30(42)% at $E_\nu = 0.3\ GeV$ and around 20(30)% at $E_\nu = 0.6\ GeV$ from the free nucleon case for $\nu_e(\bar{\nu}_e)$ induced processes. Inclusion of RPA correlation in LFG, reduces the cross section for $\nu_e(\bar{\nu}_e)$ scat-

tering from the free nucleon by $\sim$ 55(56)% at $E_\nu = 0.3\ GeV$ and 35(45)% at $E_\nu = 0.6\ GeV$. Similar results may be observed for ^{40}Ar, ^{56}Fe and ^{208}Pb nuclear targets. In general, the reduction in the cross section increases with the increase in mass number. For ν_μ and $\bar{\nu}_\mu$ induced processes at lower energies the reduction is larger and for $E_\nu > 0.4\ GeV$, the reduction in $\nu_e(\bar{\nu}_e)$ and $\nu_\mu(\bar{\nu}_\mu)$ cross sections is almost the same. This will be discussed separately in the next section when we compare electron and muon scattering cross sections.

To compare our results with other variants of Fermi gas model, we have obtained total scattering cross section in ^{40}Ar using the Fermi gas model of Smith and Moniz (Eq.7.34), Llewellyn Smith (Eq.7.35) and Gaisser and O'Connell (Eq.7.36) and calculated fractional difference $\delta\sigma_{Model}(= \frac{\sigma_{free}-\sigma_{Model}}{\sigma_{free}})$, the results for which are shown in Fig.7.6. Here σ_{free} stands for the (anti)neutrino induced interaction cross section on free nucleon target and σ_{Model} stands for the (anti)neutrino induced interaction cross section for the nucleons bound inside the nucleus. The results for neutrino is different from antineutrino and is mainly due to the interference terms with F_A which come with an opposite sign. In the case of LFG with RPA effects, the effect of renormalization is large and this suppresses the terms with F_2 and F_A which results in a large change in neutrino vs antineutrino results. We find appreciable difference in the results when various nuclear models are used. For example, when the calculations are performed by using the Fermi gas model of Llewellyn Smith [65], the cross sections get reduced from the free nucleon case by $\sim$ 16(45)% at $E_\nu = 0.3\ GeV$ and around 8(30)% at $E_\nu = 0.6\ GeV$ for $\nu_e(\bar{\nu}_e)$ induced scattering processes. While when one uses Fermi gas model of Smith and Moniz [64] this reduction in the cross section from the free nucleon case is $\sim$ 42(45)% at $E_\nu = 0.3\ GeV$ and $\sim$ 24(22)% at $E_\nu = 0.6\ GeV$. When the calculations are performed using the Fermi gas model of Gaisser and O' Connell [66] the reduction from the free nucleon case is $\sim$ 38(52)% at $E_\nu = 0.3\ GeV$ which becomes 20(35)% at $E_\nu = 0.6\ GeV$ for $\nu_e(\bar{\nu}_e)$ induced processes. Performing calculations in the LFG, reduces the cross sections by $\sim$ 25(44)% at $E_\nu = 0.3\ GeV$ and around 15(30)% at $E_\nu = 0.6\ GeV$ for $\nu_e(\bar{\nu}_e)$ induced processes. Including RPA correlation

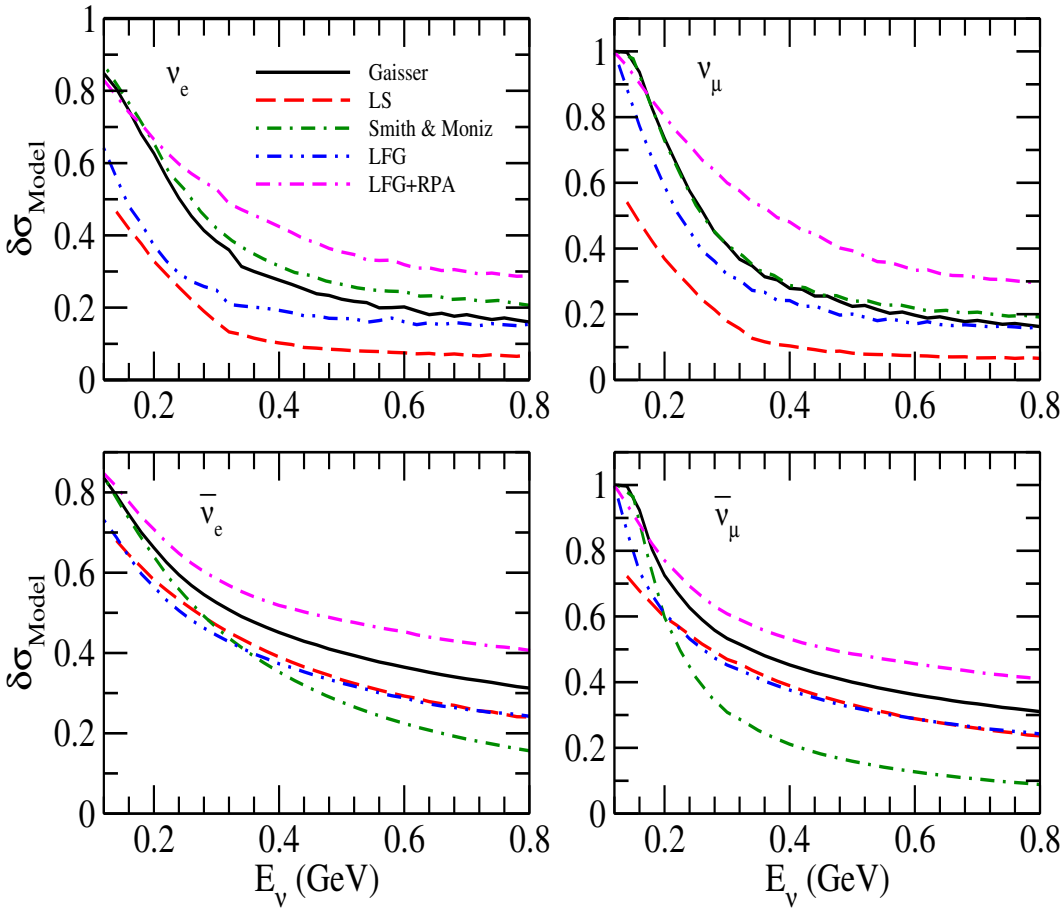

Figure 7.6: The fractional suppression in cross section $\delta\sigma_{\rm Model}(= \frac{\sigma_{free} - \sigma_{Model}}{\sigma_{free}})$ vs E_ν, where σ_{free} is the cross section obtained for free nucleon and σ_{Model} is per interacting nucleon cross section in ^{40}Ar obtained by using different nuclear models. The results are presented for the cross sections obtained from different models of Fermi gas(σ_{Model}) viz. Smith and Moniz [64](dashed dotted line), Llewellyn Smith [65](dashed line), Gaisser O' Connell [66](solid line), and with(double dashed dotted line) & without RPA(dashed double dotted line) effect using Local Fermi Gas Model. The top panel is for neutrino and bottom panel is for antineutrino induced processes.

with LFG, reduces the cross section by $\sim 54(58)\%$ at $E_\nu = 0.3\ GeV$ and $32(45)\%$ at $E_\nu = 0.6\ GeV$. The nuclear model dependence is found to be larger in the case of $\nu_\mu(\bar{\nu}_\mu)$ scattering than in the case of $\nu_e(\bar{\nu}_e)$ scattering in the energy region of $E_\nu < 0.8\ GeV$.

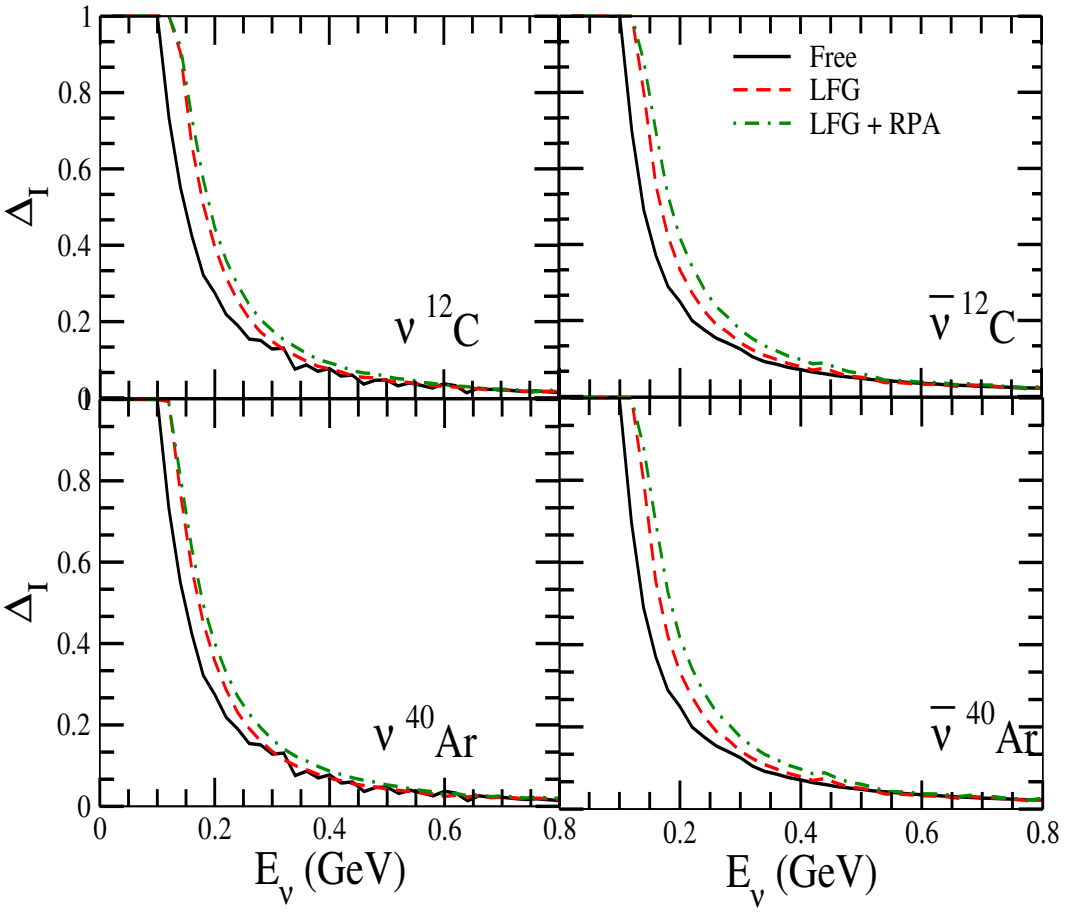

Figure 7.7: $\Delta_I = \frac{\sigma_{\nu_e(\bar{\nu}_e)} - \sigma_{\nu_\mu(\bar{\nu}_\mu)}}{\sigma_{\nu_e(\bar{\nu}_e)}}$ for neutrino(left panel) and antineutrino(right panel) induced processes in ^{12}C and ^{40}Ar targets. Here I stands for the results of the cross sections obtained (i) for the free nucleon case(solid line) (ii) in the Local Fermi Gas Model(dashed line) and (iii) for LFG with RPA effect(dashed dotted line).

For $\nu_\mu(\bar{\nu}_\mu)$ induced scattering processes, reduction in the cross section from the free nucleon case is $\sim$ 18(47)% at $E_\nu = 0.3\ GeV$ and $\sim$ 7(30)% at $E_\nu = 0.6\ GeV$, when cross sections are obtained using the Fermi gas model of Llewellyn Smith [65]. Fermi gas model of Smith and Moniz [64] reduces the cross section from the free nucleon case by $\sim$ 40(30)% at $E_\nu = 0.3\ GeV$ and around 22(12)% at $E_\nu = 0.6\ GeV$. When the calculations are performed by using the Fermi gas model of Gaisser and O' Connell [66] the reduction from the free nucleon case is $\sim$ 40(52)% at $E_\nu = 0.3\ GeV$ which becomes 20(35)% at $E_\nu = 0.6\ GeV$. The calculations are also performed in the LFG and we find that the cross sections get

reduced by $\sim 26(45)\%$ at $E_\nu = 0.3\ GeV$ and around $15(30)\%$ at $E_\nu = 0.6\ GeV$ for $\nu_\mu(\bar{\nu}_\mu)$ induced processes. Inclusion of RPA correlation with LFG, reduces the cross section for ν_μ scattering from the free nucleon value by $\sim 58\%$ at $E_\nu = 0.3\ GeV$ and 32% at $E_\nu = 0.6\ GeV$, which for $\bar{\nu}_\mu$ induced scattering is $\sim 60\%$ at $E_\nu = 0.3\ GeV$ and $\sim 45\%$ at $E_\nu = 0.6\ GeV$.

7.3.2 Effect of lepton mass and its kinematic implications

There are two types of corrections which appear when lepton mass $m_l(l = e, \mu)$ is taken into account in the cross section calculations for the reaction $\nu_l(\bar{\nu}_l) + N \rightarrow l^-(l^+) + N'$, $(N, N' = n, p)$ which can be classified as kinematical and dynamical in origin. The kinematical effects arise due to $E_l \neq |\mathbf{k}'|$ in the presence of m_l and the minimum and maximum values of four momentum transfer square ($Q^2 = -q^2 \geq 0$) i.e. Q^2_{min} and Q^2_{max} gets modified, affecting the calculations of the total cross sections. These effects are negligible for highly relativistic leptons but could become important at low energies near threshold specially for muons. On the other hand, the dynamical corrections arise as additional terms proportional to $\frac{m_l^2}{M^2}$ in the existing contribution of vector and axial vector form factors as well as new contributions due to induced pseudoscalar and other form factors associated with the second class currents. In fact all the contributions from the pseudoscalar form factor $F_P(Q^2)$ and the second class vector form factor $F_3^V(Q^2)$ are proportional to $\frac{m_l^2}{M^2}$ while the contribution from the second class axial vector form factor $F_3^A(Q^2)$ is proportional either to $\frac{m_l^2}{M^2}$ or $\frac{Q^2}{M^2}$ or both.

To study the lepton mass dependence on $\nu_e(\bar{\nu}_e)$ and $\nu_\mu(\bar{\nu}_\mu)$ induced scattering cross sections in free nucleon as well as in nuclear targets, we define $\Delta_I = \frac{\sigma_{\nu_e(\bar{\nu}_e)} - \sigma_{\nu_\mu(\bar{\nu}_\mu)}}{\sigma_{\nu_e(\bar{\nu}_e)}}$ for neutrino/antineutrino induced reaction in ^{12}C and ^{40}Ar nuclear targets, where $I = i,\ ii,\ iii$, which respectively stands for the cross sections obtained in (i) free neutrino/antineutrino-nucleon case, (ii) the Local Fermi Gas Model(LFG) and (iii) the Local Fermi Gas Model with RPA effect(LFG+RPA). The results are presented in Fig.7.7, which show that the differences in the electron

and muon production cross sections for $\nu_l(\bar{\nu}_l)$ induced reactions on ^{12}C target are appreciable at low energies $E_\nu < 0.4\ GeV$. For example, this fractional change is about 27(25)% at $E_\nu = 0.2\ GeV$ and reduces to $\sim 8(7)\%$ at $E_\nu = 0.4\ GeV$ in the case of free nucleon. While in ^{12}C, using LFG it is approximately 40(33)% at $E_\nu = 0.2\ GeV$ and $\sim 8\%$ for both neutrino and antineutrino at $0.4\ GeV$, respectively. However, using RPA effect with LFG, the difference is around 44(42)% and $\sim 9(10)\%$ at $E_\nu = 0.2\ GeV$ and $0.4\ GeV$, respectively. While for the case of neutrino(antineutrino) induced process on ^{40}Ar target using LFG, this fractional change is approximately 35(33)% and $\sim 7(8)\%$ at $E_\nu = 0.2\ GeV$ and $0.4\ GeV$, respectively. However, using RPA effect with LFG, the difference is around 40(42)% and $\sim 9(10)\%$ at $E_\nu = 0.2\ GeV$ and $0.4\ GeV$, respectively.

7.3.3 Form factor dependence

The hadronic current defined in Eq.7.5 consists of six form factors; three isovector $(F_i^V(Q^2), i = 1,3)$ and three axial vector$(F_i^A(Q^2), i = 1,3)$ form factors. Among them, $F_i^V(Q^2), i = 1,2$, are parameterized in terms of Sach's form factors $G_E^{p,n}(Q^2)$ and $G_M^{p,n}(Q^2)$, for which various parameterizations are available in the literature [150, 151, 152, 153, 154]. $F_3^V(Q^2)$, which arises due to the second class current is generally ignored in calculations. Similarly, the axial current consists of three form factors viz. $F_1^A(Q^2) = F_A(Q^2)$, $F_2^A(Q^2) = F_P(Q^2)$ and $F_3^A(Q^2)$, among them $F_A(Q^2)$ is dominant and is parameterized in a dipole form with axial dipole mass(M_A). The pseudoscalar form factor $F_P(Q^2)$ is given in terms of $F_A(Q^2)$ and $F_3^A(Q^2)$ arises due to second class currents and is generally ignored. In a standard calculation of (anti)neutrino nucleon scattering cross sections, form factors associated with the first class current are $F_1^V(Q^2)$, $F_2^V(Q^2)$, $F_A(Q^2)$ and $F_P(Q^2)$ and we have used these form factors to calculate cross sections and presented the results in section 7.3.1 and 7.3.2. However there are alternate parameterizations of the vector form factors [150, 151, 152, 153, 154] and pseudoscalar form factor and a range of parameter values for the axial dipole mass M_A which have also been used

in the literature to evaluate these cross sections. In the following subsection, we give an estimate of the uncertainty in the cross sections associated with the use of alternate parameterizations and/or parameter values of these form factors.

Vector form factors

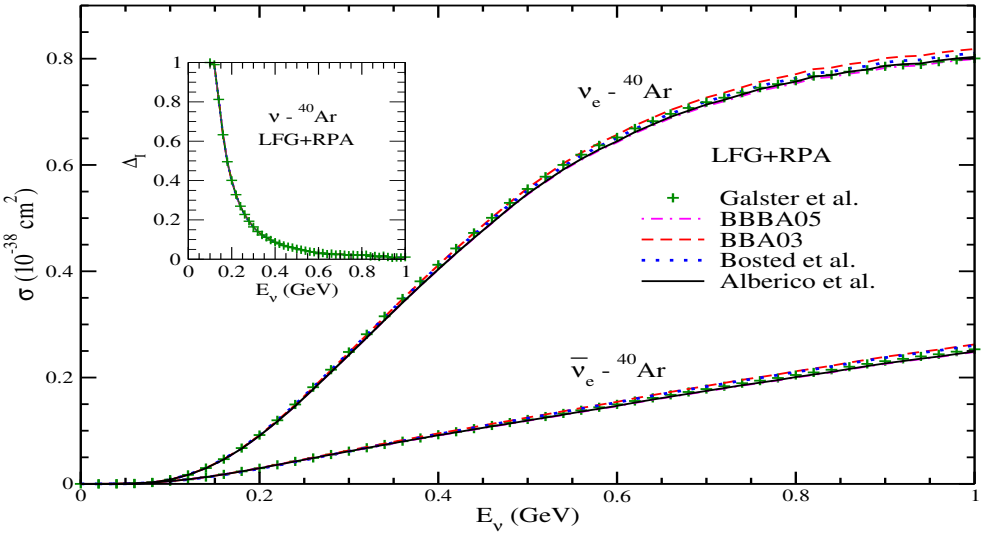

Figure 7.8: Results of total scattering cross section for $\nu_e(\bar{\nu}_e)$ induced processes on ^{40}Ar are shown using different parameterization of the vector form factors [154, 152, 151, 153, 150]. Symbol + (Galster et al.[150]), dashed dotted line(Bradford et al. [151]), dashed line(Budd et al. [152]), dotted line(Bosted et al.[153]) and solid line(Alberico et al. [154]) are the results obtained using various parameterizations for total scattering cross section. Inside the inset $\Delta_I = \frac{\sigma_{\nu_e} - \sigma_{\nu_\mu}}{\sigma_{\nu_e}}$ for neutrino induced process using these form factors have also been shown.

We have studied the different parameterizations of Sachs electric and magnetic form factors to observe their effect on scattering cross sections for (anti)neutrino induced CCQE processes on nuclear target like ^{40}Ar in local density approximation with RPA effect, i.e. LFG+RPA and the results are shown in Fig.7.8. From the figure it may be observed that the cross sections obtained using parameterizations of Galster et al. [150], Budd et al. [152], Bosted et al. [153] and Alberico et al. [154] are in agreement with each other within 1% which also agrees with the recent parameterization discussed by Bradford et al. [151] in the energy region of $0.4\ GeV - 0.8\ GeV$. We have also shown the fractional change $\Delta_I = \frac{\sigma_{\nu_e} - \sigma_{\nu_\mu}}{\sigma_{\nu_e}}$ (in

Experiment	M_A (GeV)	Experiment	M_A (GeV)
MINERνA [102, 169]	0.99	SciBooNE [170]	1.21±0.22
NOMAD [171]	1.05±0.02±0.06	K2K-SciBar [172]	1.144±0.077
MiniBooNE [173, 174, 175]	1.23±0.20	K2K-SciFi [172]	1.20±0.12
MINOS [176]	$1.19(Q^2 > 0)$ $1.26(Q^2 > 0.3GeV^2)$	World Average	1.026± 0.021 [155] 1.014±0.014 [177]

Table 7.2: Recent measurements of the axial dipole mass(M_A).

the inset of Fig.7.8) for ν_l induced CCQE process using different parameterizations and found that the dependence on the choice of parameterizations for $F_1^V(Q^2)$ and $F_2^V(Q^2)$ is almost negligible.

Axial vector form factor

The value of axial dipole mass M_A used in Eq. 7.13 has come recently in debate due to large deviations found in the experiments like MiniBooNE [173, 174, 175], SciBooNE [170], K2K [172], etc. from the world average value [155, 177]. Earlier measurements for M_A were obtained using ν_l and $\bar{\nu}_l$ induced processes on deuterium targets where the nuclear effects are expected to play negligible role and the average value is quoted as $M_A = 1.026 \pm 0.021\ GeV$ while a combined analysis performed by Bodek et al. [177] using $\nu_\mu d$, $\overline{\nu}_\mu$H and $\pi^\pm$ electroproduction data have found $M_A = 1.014 \pm 0.014$ GeV. Recent measurements at NOMAD [171] and MINERνA [169] are close to the world average value. On the other hand, the experiments like MiniBooNE [173, 174, 175], SciBooNE [170], K2K [172], etc. report a higher value of M_A. These experiments were performed with different nuclear targets like ^{12}C, ^{16}O, ^{56}Fe as well as some of them have used the same nuclear target, for example, NOMAD [171], MiniBooNE [173, 174, 175] K2K [172], MINERνA [169] have used carbon as nuclear target. In Table-7.2, we tabulate the values of axial dipole mass obtained from analyses of some recent cross section measurements [102, 169, 170, 171, 172, 173, 174, 175, 155, 176] in the neutrino experiments in the few GeV energy range. It is believed that if the quasielastic like events which arise due to 2p-2h excitations, meson exchange currents and multinucleon correlations are taken into account then the recent ex-

perimental results can also be considered to be consistent with a smaller value of M_A [178, 179, 180, 181, 182]. However, it may be observed from Table-7.2 that even with the same nuclear target different values of M_A have been obtained.

To study the explicit dependence of cross sections on the axial dipole mass for neutrino/antineutrino scattering processes, we have changed M_A from the base value (taken as the world average value) and obtained the results for δ_{M_A} defined below in Eq. 7.37 and Δ_{M_A} defined in Eq. 7.38 by taking the two different values of M_A as 0.9 GeV and 1.2 GeV. These results are obtained for the (anti)neutrino induced processes on free nucleon as well as in the LFG with and without RPA effect for ^{40}Ar nuclear target.

The dependence on axial dipole mass is shown in Fig.7.9, by defining δ_{M_A} as

$$\delta_{M_A} = \frac{\sigma_{\nu_l}(M_A^{modified}) - \sigma_{\nu_l}(M_A = WA)}{\sigma_{\nu_l}(M_A = WA)}, \qquad WA = 1.026\ GeV \tag{7.37}$$

where $l = e$ or $l = \mu$. We observe from Fig.7.9 that for free nucleon when a modified value of M_A i.e. $M_A^{modified} = 0.9(1.2)\ GeV$ is used instead of world average value of 1.026 GeV then a decrease(increase) of $5 - 15\%$ is obtained for ν_e/ν_μ reactions in the energy range of 0.2 GeV to 0.8 GeV. In the case of $\bar{\nu}_e/\bar{\nu}_\mu$-nucleon reactions this decrease(increase) is about $5 - 10\%$ in the same energy range. When nuclear medium effects are taken into account, for example, in the case of ^{40}Ar nucleus this decrease(increase) remains almost same. Therefore, the uncertainty in the (anti)neutrino-nucleus cross sections is the same as in the case of free (anti)neutrino-nucleon scattering processes.

We have also studied the sensitivity of the difference in electron and muon production cross sections due to the uncertainty in the choice of M_A. For this we define

$$\begin{aligned}
\Delta_1(E_\nu) &= \frac{\sigma_{\nu_\mu}(M_A^{modified}) - \sigma_{\nu_e}(M_A^{modified})}{\sigma_{\nu_e}(M_A^{modified})}, \\
\Delta_2(E_\nu) &= \frac{\sigma_{\nu_\mu}(M_A = WA) - \sigma_{\nu_e}(M_A = WA)}{\sigma_{\nu_e}(M_A = WA)}, \\
\Delta_{M_A} &= \Delta_1(E_\nu) - \Delta_2(E_\nu).
\end{aligned} \tag{7.38}$$

and show the numerical values for Δ_{M_A} for free nucleon and nuclei in Fig. 7.10. We observe that for free nucleon some sensitivity to the difference in the electron and muon production cross sections exists at low energies $E_\nu < 0.4\ GeV$ which does not exceed 1%. In a nuclear target, when nuclear medium effects are taken into account this sensitivity remains almost the same as in the case of free neutrino-nucleon scattering processes. Similar effects are found for the case of antineutrino induced reactions.

From Figs. 7.9 and 7.10, it may be observed that the cross section is very sensitive to the choice of axial dipole mass M_A. Therefore, while calculating the charged lepton production cross sections, the value of M_A should be carefully taken.

Pseudoscalar form factor

To study the effect of pseudoscalar form factor $F_P(Q^2)$ on muon production cross sections, we define

$$\delta_{F_P}(E_\nu) = \frac{\sigma_{\nu_\mu}(F_P \neq 0) - \sigma_{\nu_\mu}(F_P = 0)}{\sigma_{\nu_\mu}(F_P = 0)}, \tag{7.39}$$

and similar expression for the antineutrino induced process is used. For the numerical calculations, the expression for $F_P(Q^2)$ given in Eq. 7.15 has been used. The results are presented in Fig.7.11. We find that δ_{F_P} is more sensitive in the case of $\bar{\nu}_\mu$ induced CCQE process than ν_μ induced process for the free nucleon case as well as for ^{40}Ar nuclear target. This sensitivity decreases with the increase in $\nu_\mu/\bar{\nu}_\mu$ energy and almost vanishes beyond 0.6 GeV.

We have also studied the sensitivity of pseudoscalar form factor $F_P(Q^2)$ to find out the difference in the electron vs muon production cross sections that are obtained using Eq.7.15. For this purpose we define

$$\Delta_1(E_\nu) = \frac{\sigma_{\nu_\mu}(F_P \neq 0) - \sigma_{\nu_e}(F_P \neq 0)}{\sigma_{\nu_e}(F_P \neq 0)}, \tag{7.40}$$

$$\Delta_2(E_\nu) = \frac{\sigma_{\nu_\mu}(F_P = 0) - \sigma_{\nu_e}(F_P = 0)}{\sigma_{\nu_e}(F_P = 0)}, \tag{7.41}$$

$$\Delta_{F_P} = \Delta_1(E_\nu) - \Delta_2(E_\nu). \tag{7.42}$$

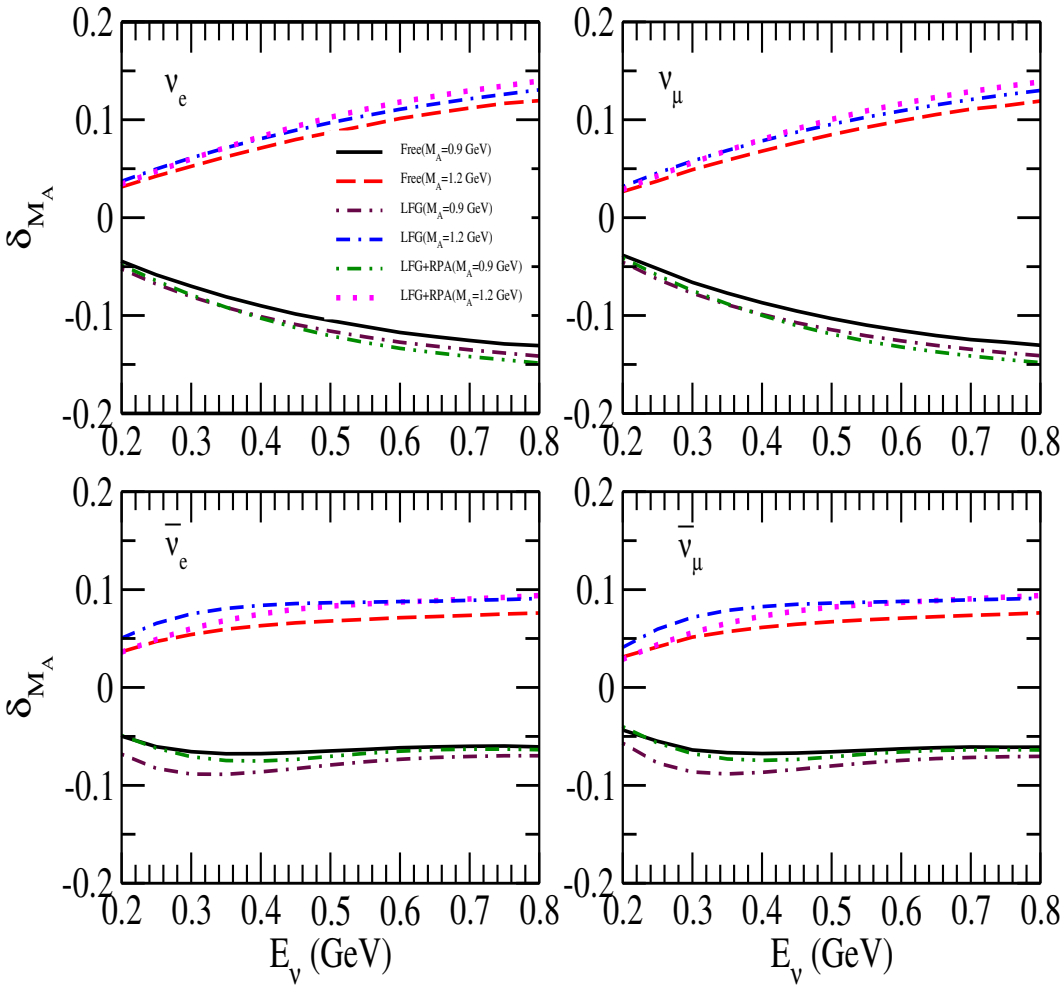

Figure 7.9: The dependence of cross section on M_A obtained using Eq. 7.37. The results are shown for $\nu_e(\bar{\nu}_e)$ and $\nu_\mu(\bar{\nu}_\mu)$ induced processes on free nucleon as well as on ^{40}Ar target using LFG with and without RPA effect. Solid(dashed) line denotes results for the free nucleon case with $M_A = 0.9\ GeV(1.2\ GeV)$, results obtained using LFG are shown by dashed dotted(double dashed dotted) with $M_A = 0.9\ GeV(1.2\ GeV)$ and results for LFG with RPA effect are shown by dashed double dotted(dotted) with $M_A = 0.9\ GeV(1.2\ GeV)$.

and the results for Δ_{F_P} are shown in Fig. 7.12. Similar expressions are also used for antineutrino induced processes.

We have calculated the fractional difference Δ_{F_P} as given in Eq. 7.42 for free nucleon case as well as for nucleons bound in ^{40}Ar nuclear target using the LFG with RPA effect. We observe that the inclusion of pseudoscalar form factor de-

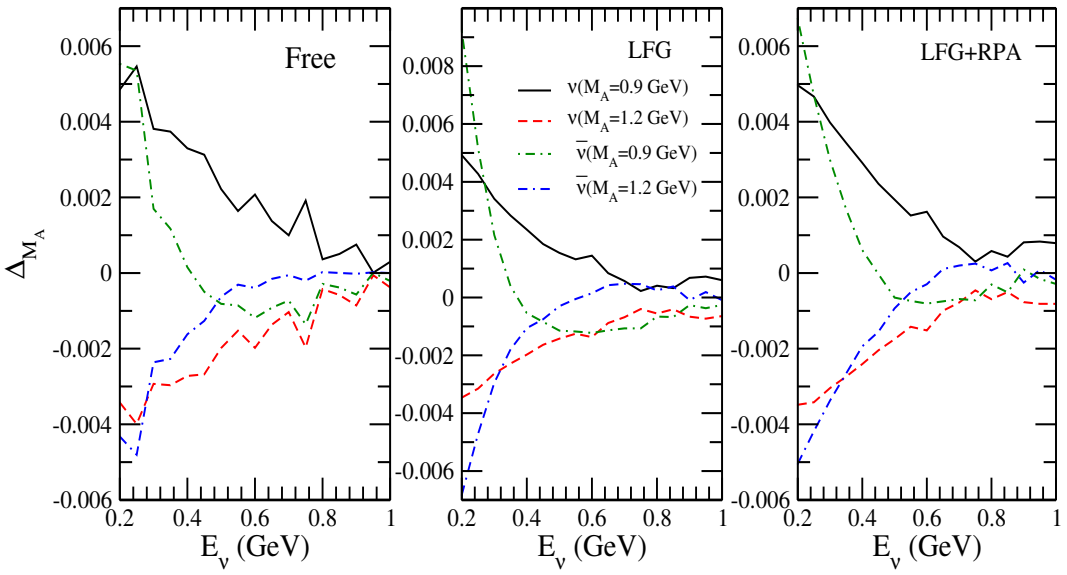

Figure 7.10: Effect of axial dipole mass on the cross section(from left to right): on free nucleon; LFG, with and without RPA effect on ^{40}Ar target. Here different values of M_A are taken such as 0.9 GeV and 1.2 GeV. The fractional difference(Eq. 7.38) has been obtained using the base value of M_A taken as the world average value. Solid(dashed) line denotes results for the neutrino induced processes while for antineutrino the results are shown by dashed dotted(double dashed dotted) with $M_A = 0.9\ GeV(1.2\ GeV)$.

creases the fractional change(Δ_{F_P}) by about 3(8)% at $E_{\nu(\bar{\nu})} \sim 0.2GeV$ and becomes smaller with the increase in energy. When the nuclear medium effects(LFG+RPA) are taken into account in the evaluation of cross sections in ^{40}Ar then this difference increases to 4(15)% at the same energy for neutrino(antineutrino) induced processes.

7.3.4 Second class currents

We have also studied the effect of second class current, due to which two additional form factors viz. $F_3^V(Q^2)$ and $F_3^A(Q^2)$ are introduced.

Second class vector current

The contribution of the second class vector form factor $F_3^V(Q^2)$ to the cross section

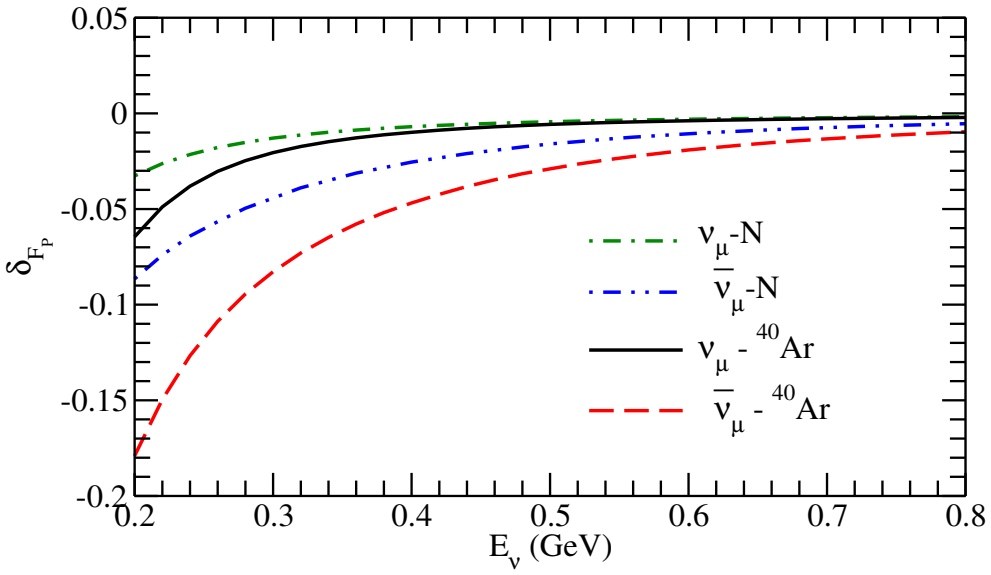

Figure 7.11: Results of the fractional change δ_{F_P} defined in Eq.7.39 as a function of (anti)neutrino energy. The results are shown for the ν_μ induced interaction cross section for the free nucleon case(dashed dotted line), as well as for the nucleons bound in ^{40}Ar(solid line) nuclear target obtained by using LFG with RPA effect. The results corresponding to $\bar{\nu}_\mu$ induced CCQE process are shown by dashed double dotted line(free nucleon case) and dashed line(^{40}Ar target).

is always proportional to the mass of the lepton so it is quite small in the case of $\nu_e(\bar{\nu}_e)$ as compared to $\nu_\mu(\bar{\nu}_\mu)$ reactions on free nucleons and nuclei. We first study the overall contribution made by the second class vector form factor $F_3^V(Q^2)$ to the cross section in the case of muon neutrinos and define

$$\delta_{F_3^V}(E_\nu) = \frac{\sigma_{\nu_\mu}(F_3^V \neq 0) - \sigma_{\nu_\mu}(F_3^V = 0)}{\sigma_{\nu_\mu}(F_3^V = 0)}. \tag{7.43}$$

Similar expression is used for antineutrino. For the numerical calculations we use Eq. 7.18 and the results are shown in Fig.7.13. We find that the contribution of $F_3^V(Q^2)$ to the cross section is very small for ν_μ scattering on free nucleons and nuclei. In the case of $\bar{\nu}_\mu$ scattering on nucleons at low energy, the contribution of $F_3^V(Q^2)$ at $E_{\nu/\bar{\nu}} = 0.2$ GeV is 5% which increases to 7% in ^{40}Ar when nuclear medium effects are taken into account.

We now study the sensitivity due to $F_3^V(Q^2)$ in the difference between the

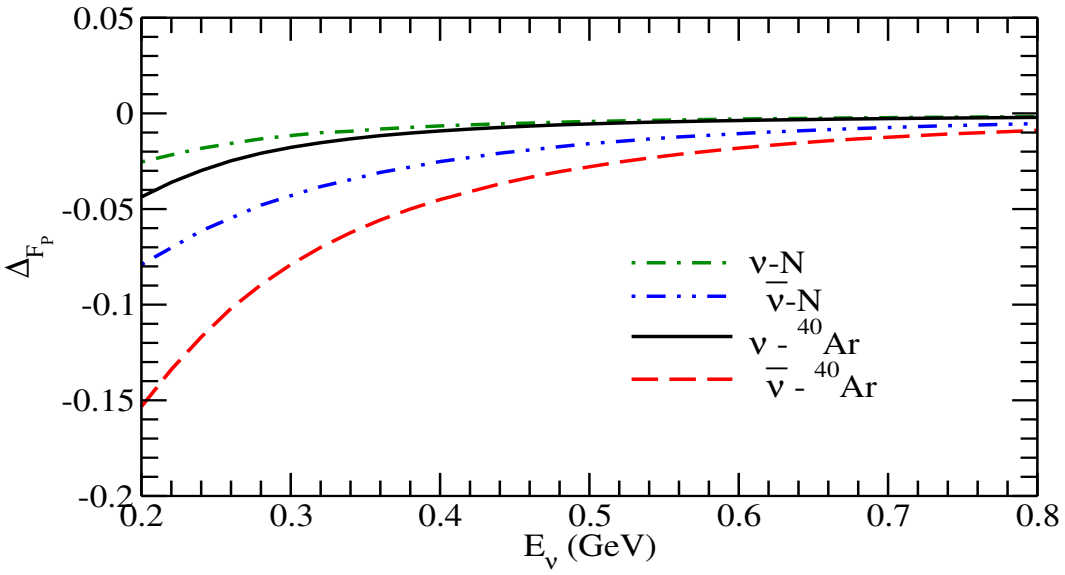

Figure 7.12: Results of the fractional change Δ_{F_P} defined in Eq.7.42 as a function of (anti)neutrino energy. The results are shown for the neutrino induced interaction cross section for the free nucleon case(dashed dotted line), as well as for the nucleons bound in ^{40}Ar(solid line) nuclear target obtained by using LFG with RPA effect. The results corresponding to antineutrino induced CCQE process are shown by dashed double dotted line(free nucleon case) and dashed line(^{40}Ar target).

electron and muon production cross sections for free nucleon and nuclei by defining

$$\Delta_1(E_\nu) = \frac{\sigma_{\nu_\mu}(F_3^V \neq 0) - \sigma_{\nu_e}(F_3^V \neq 0)}{\sigma_{\nu_e}(F_3^V \neq 0)} \tag{7.44}$$

$$\Delta_2(E_\nu) = \frac{\sigma_{\nu_\mu}(F_3^V = 0) - \sigma_{\nu_e}(F_3^V = 0)}{\sigma_{\nu_e}(F_3^V = 0)} \tag{7.45}$$

$$\Delta_{F_3^V} = \Delta_1(E_\nu) - \Delta_2(E_\nu). \tag{7.46}$$

First, we present the results for $\Delta_1(E_\nu)$ as a function of neutrino/antineutrino energies and the results are shown in Fig. 7.14. These results are presented for the free nucleon case as well as for the bound nucleons in ^{40}Ar and the cross sections are obtained using the expression of the hadronic current with second class vector current. We must point out that the contribution from the second class axial current is switched off. We find that $\Delta_1(E_\nu)$ is sensitive to the flavor of neutrinos especially at low energies ($E_{\nu/\bar{\nu}} < 0.3GeV$) which is mainly due to threshold effect. When we perform calculations on nuclear targets like ^{40}Ar using LFG, the

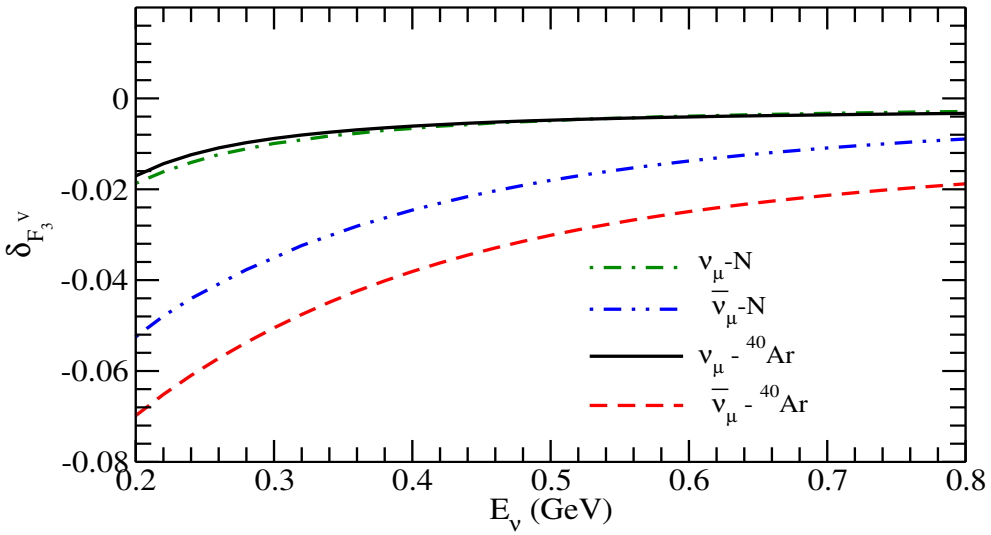

Figure 7.13: Results of the fractional change $\delta_{F_3^V}$ defined in Eq.7.43 as a function of (anti)neutrino energy. The results are shown for ν_μ induced interaction cross section for the free nucleon case(dashed dotted line), as well as for the nucleons bound in ^{40}Ar(solid line) nuclear target obtained by using LFG. The results corresponding to $\bar{\nu}_\mu$ induced CCQE process are shown by dashed double dotted line(free nucleon case) and dashed line(^{40}Ar target).

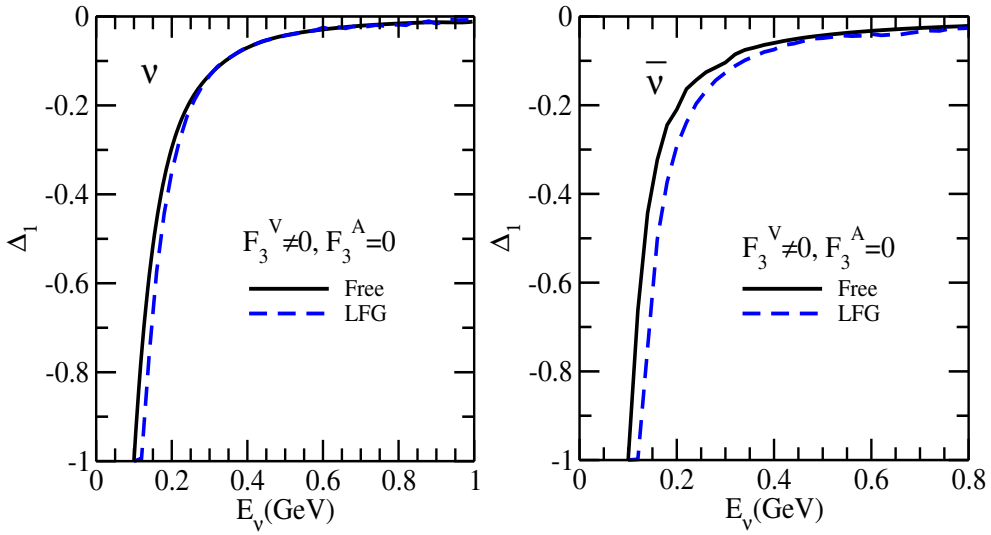

Figure 7.14: The difference of fractional changes Δ_1 defined in Eqs.7.44, for the free nucleon case(solid line), and in ^{40}Ar for neutrino(Left panel) and antineutrino(Right panel) induced processes using LFG(dashed line).

fractional difference $\Delta_1(E_\nu)$ changes from the free nucleon case. However, it is not sensitive to the choice of nuclear model.

In Fig. 7.15, we present the results for $\Delta_{F_3^V}$ using Eq. 7.46 and obtained it for the free nucleon case as well as for ^{12}C and ^{40}Ar nuclear targets. We find that the effects are energy dependent and more pronounced at low energies. From the figure it may be noticed that the fractional change is the same for both ^{12}C and ^{40}Ar nuclei. For example, for the case of neutrino, at $E_\nu = 0.2\ GeV$, $\Delta_{F_3^V}$ is $\sim 1\%$ for free nucleon as well as in ^{40}Ar evaluated using LFG and the difference becomes almost negligible beyond $E_\nu = 0.5\ GeV$. Similarly, for the case of antineutrino, at $E_\nu = 0.2\ GeV$, $\Delta_{F_3^V}$ is $\sim 4\%$ for the free nucleon case as well as in ^{40}Ar evaluated using LFG, which becomes $\sim 1\%$ at $E_\nu = 0.5\ GeV$.

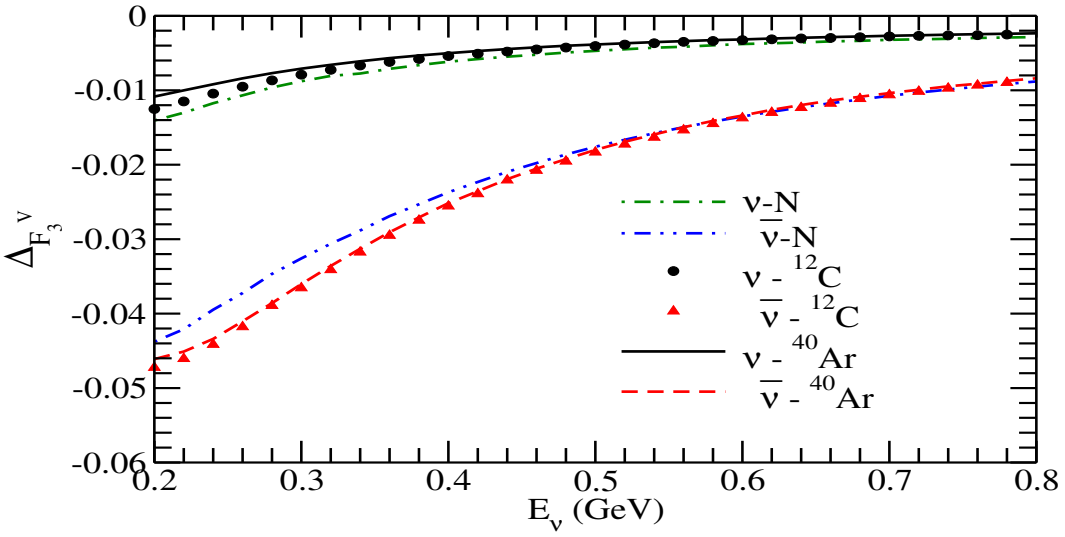

Figure 7.15: The difference of fractional changes $\Delta_{F_3^V}$ defined in Eq.7.46, for the free nucleon case(neutrino results shown by dashed-dotted line and antineutrino results by dashed-double dotted line) as well as for ^{12}C (circle for neutrino and triangle up for antineutrino) and ^{40}Ar (solid line for neutrino and dashed line for antineutrino) nuclear targets obtained by using LFG.

In general there is a large uncertainty associated with the determination of $F_3^V(Q^2)$ and $F_3^A(Q^2)$ form factors. We have also studied uncertainty due to various parameterizations of form factor $F_3^V(Q^2)$. Some of the alternative parameterizations of the form factor $F_3^V(Q^2)$ are given in Eqs.7.18, 7.19, which have been used

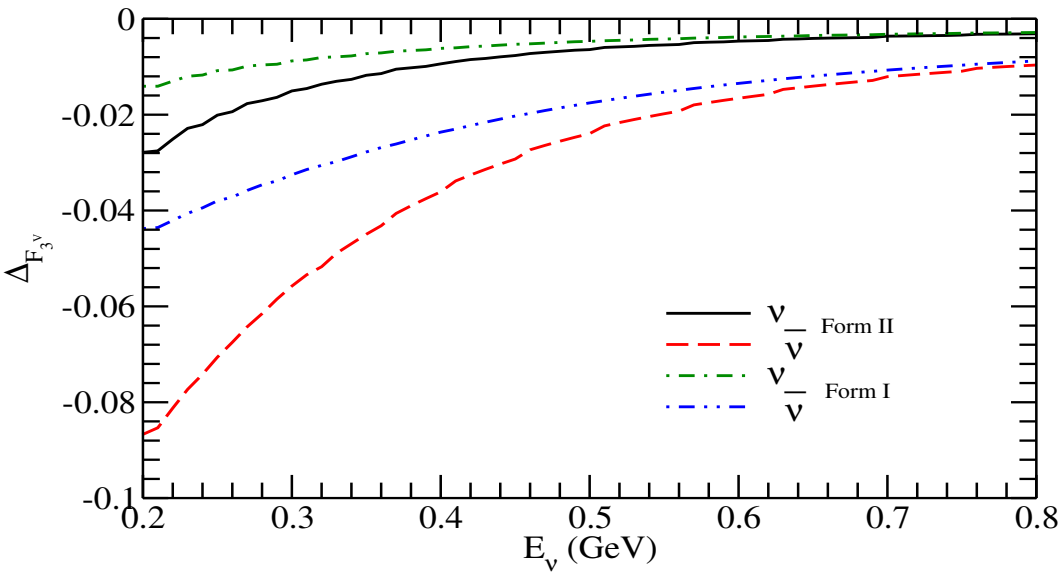

Figure 7.16: Variation of $\Delta_{F_3^V}$ as given in Eqs. 7.46 as a function of (anti)neutrino energies are shown for different forms of $F_3^V(Q^2)$ used in second class currents. We have performed the calculation for (anti)neutrino induced scattering processes on free nucleon target. The results are obtained for Form I and Form II using Eqs. 7.18 and 7.19, respectively for $M_A = 1.026\ GeV$. The results obtained by using Form I for neutrino(antineutrino) are shown by dashed-dotted(dashed-double dotted)line and with Form II are shown by solid(dashed)line, respectively.

for the numerical calculations. The results are shown in Fig.7.16. We find that for neutrino induced process on a free nucleon target, the difference in the results for ΔF_3^V obtained by using two different forms of $F_3^V(Q^2)$ (Form I using Eq. 7.18, Form II using Eq. 7.19) is very small. For example, this difference is $\sim 1\%$ at low energies($\sim 0.2\ GeV$) which almost vanishes with the increase in energy. In the case of antineutrino induced reaction on a free nucleon, this difference is around 3% at low energies which gradually vanishes with the increase in energy.

Second class axial current

The axial vector form factor associated with second class current($F_3^A(Q^2)$) also contributes to the cross section in addition to the second class vector form factor. To observe the effect of $F_3^A(Q^2)$ on $\nu_\mu(\bar{\nu}_\mu)$ induced cross section we define fractional

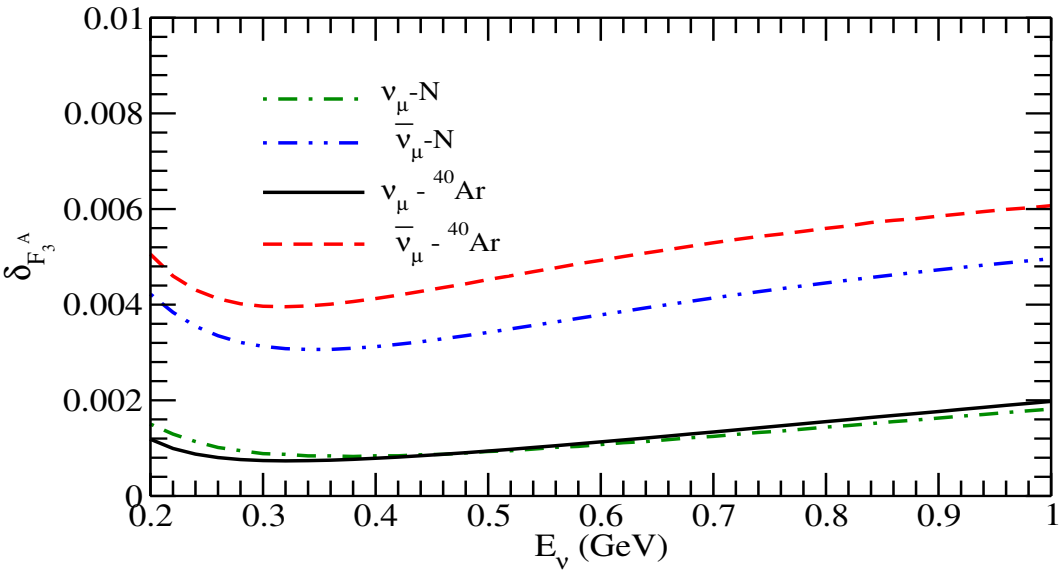

Figure 7.17: Results of the fractional change $\delta_{F_3^A}$ defined in Eq.7.47 as a function of (anti)neutrino energy. The results are shown for the ν_μ induced interaction cross section for the free nucleon case(dashed dotted line), as well as for the nucleons bound in ^{40}Ar(solid line) obtained by using LFG. The results corresponding to $\bar{\nu}_\mu$ induced CCQE process are shown by dashed double dotted line(free nucleon case) and dashed line(^{40}Ar target).

difference

$$\delta_{F_3^A}(E_\nu) = \frac{\sigma_{\nu_\mu}(F_3^A \neq 0) - \sigma_{\nu_\mu}(F_3^A = 0)}{\sigma_{\nu_\mu}(F_3^A = 0)}, \tag{7.47}$$

and similar expression for antineutrino is used. We show the numerical results in Fig.7.17. These results are presented for the free nucleon case as well as for the bound nucleons in ^{40}Ar and the cross sections are obtained using the expression of the hadronic current with second class axial vector current, keeping $F_3^V(Q^2) = 0$. We find that $\delta_{F_3^A}$ is hardly sensitive to the presence of $F_3^A(Q^2)$ in ν_μ and $\bar{\nu}_\mu$ scattering cross sections from the free nucleon and nuclear targets. We also study the sensitivity of the electron and muon production cross sections to $F_3^A(Q^2)$ for free nucleon and nuclei, by defining

$$\Delta_1(E_\nu) = \frac{\sigma_{\nu_\mu}(F_3^A \neq 0) - \sigma_{\nu_e}(F_3^A \neq 0)}{\sigma_{\nu_e}(F_3^A \neq 0)} \tag{7.48}$$

$$\Delta_2(E_\nu) = \frac{\sigma_{\nu_\mu}(F_3^A = 0) - \sigma_{\nu_e}(F_3^A = 0)}{\sigma_{\nu_e}(F_3^A = 0)} \tag{7.49}$$

$$\Delta_{F_3^A} = \Delta_1(E_\nu) - \Delta_2(E_\nu) \tag{7.50}$$

and the numerical results are shown in Fig.7.18, for $\Delta_1(E_\nu)$. We find the results to be similar in nature as found in the case of $F_3^V(Q^2)$. In Fig. 7.19, we present the results for $\Delta_{F_3^A}$. In this case also we find the sensitivity to be smaller than observed in the case of $\Delta_{F_3^V}$.

When we compare our present results for the difference in the electron and muon production cross sections on free nucleon target with the results of Day and McFarland [53], we find that our results for the contribution of the $F_3^V(Q^2)$ in the case of antineutrino reactions and the results for the contribution of $F_3^A(Q^2)$ for neutrino reactions agree qualitatively with their results. This is not so in the case of $F_3^V(Q^2)$ for neutrino reactions and $F_3^A(Q^2)$ for antineutrino reactions. This may be due the different expressions used for the contribution of the interference terms between first and second class currents. Our expressions agree with the general expressions given by Pais [85], Kuzmin et al. [183] but not with Eq.(3.18) of Llewellyn Smith [65] which has been used in Ref. [53].

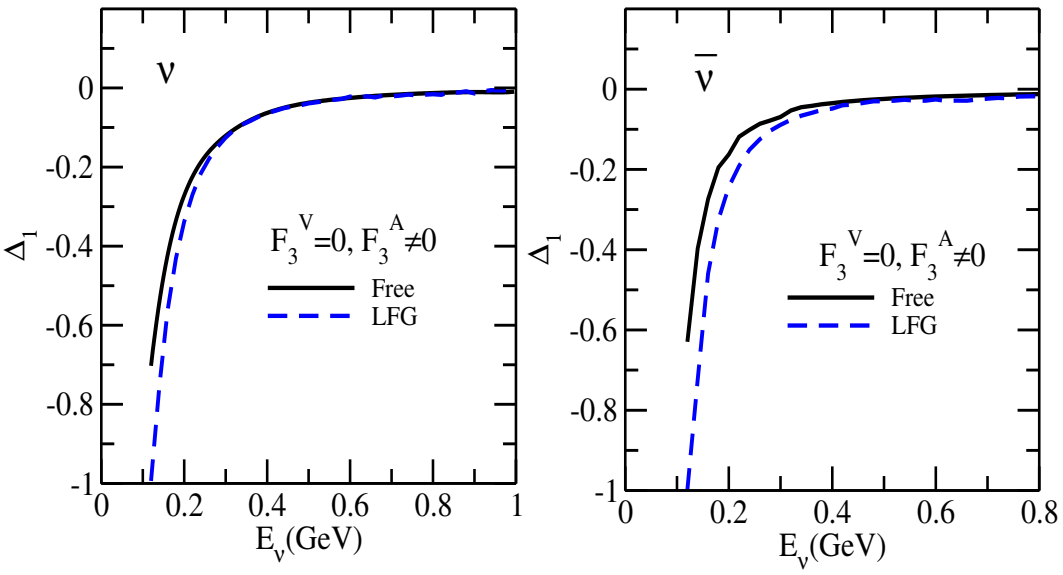

Figure 7.18: The difference of fractional changes Δ_1 defined in Eqs.7.48, for the free nucleon case(solid line), and in ^{40}Ar for neutrino(Left panel) and antineutrino(Right panel) induced processes using LFG(dashed line).

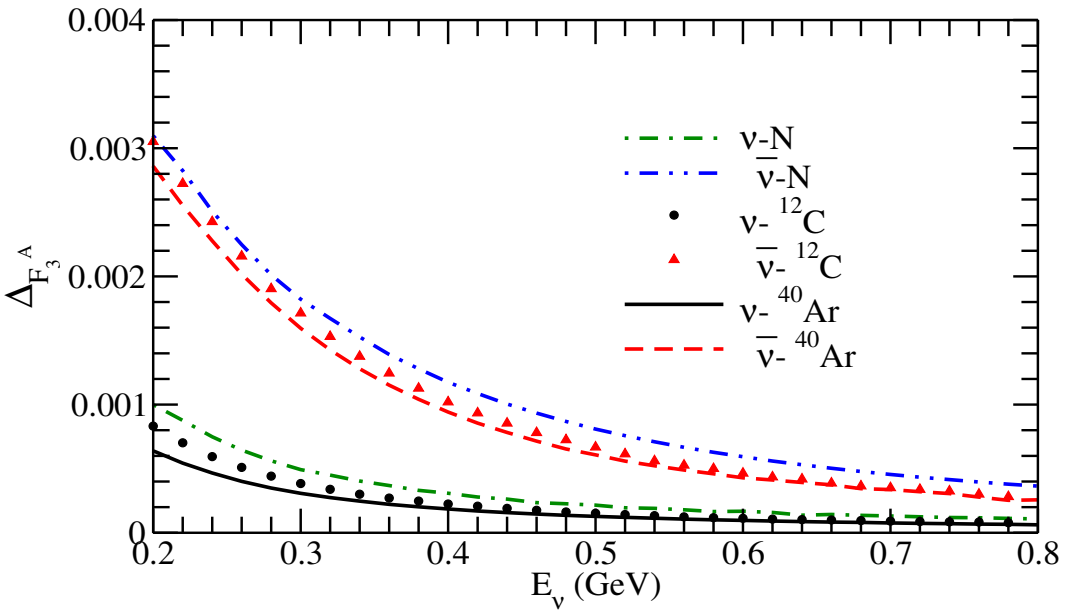

Figure 7.19: The difference of fractional changes $\Delta_{F_3^A}$ defined in Eq.7.50, for the free nucleon case(neutrino results shown by dashed-dotted line and antineutrino results by dashed-double dotted line) as well as for ^{12}C (circle for neutrino and triangle up for antineutrino) and ^{40}Ar (solid line for neutrino and dashed line for antineutrino) obtained by using LFG.

7.3.5 Radiative corrections

Radiative corrections are potential source of difference between electron and muon production cross sections in (anti)neutrino reactions due to their logarithmic dependence on the lepton mass through terms like $\log(\frac{E_l^*}{m_l})$, where E_l^* is some energy scale in the reaction. The radiative corrections in the charged current quasielastic neutrino-nucleon reactions relevant for the present oscillation experiments in the energy region of few GeV have been recently calculated by Bodek [184], Day and McFarland [53] and Graczyck [185]. Bodek [184] and Day and McFarland [53] make use of leading log approximation given by De Rujula et al. [186] to calculate the contribution of soft photon emission by the lepton leg bremsstrahlung diagram which gives major contribution to the radiative corrections depending on the lepton mass m_l. On the other hand, Graczyck [185] includes the contribution of other diagrams like two boson exchange involving W and γ, propagator correction

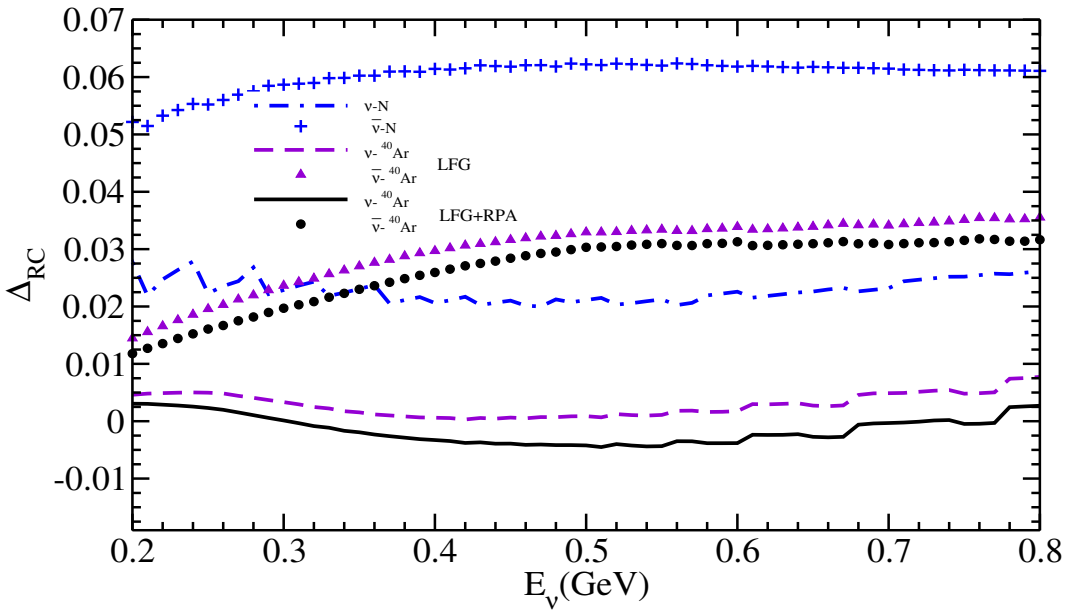

Figure 7.20: The effect of radiative corrections on fractional difference Δ_{RC} defined in Eq. 7.54 for (anti)neutrino induced processes on free nucleon as well as on ^{40}Ar target using LFG with and without RPA effect. For the neutrino(antineutrino) induced processes on free nucleon the results are shown by dashed dotted line(plus), results for calculations using LFG for neutrino(antineutrino) are shown by dashed line (triangle up) and results for calculations using LFG with RPA effect for neutrino(antineutrino) are shown by solid line(circle).

in addition to the soft photon bremsstrahlung. We have used the results of De Rujula et al. [186] for the radiative corrections in the neutrino nucleon scattering and study the effect of nuclear medium on these radiative corrections. In the work of De Rujula et al. [186], the modified cross section including radiative corrections is given by

$$\begin{aligned}\frac{d\sigma}{dE_l d\Omega_l} &\approx \frac{d\sigma_{free}}{dE_l d\Omega_l} + \frac{\alpha}{2\pi}\log\frac{4E_l^{*2}}{m_l^2}\int_0^1 dz \frac{1+z^2}{1-z} \\ &\times \left(\frac{1}{z}\frac{d\sigma_{free}}{d\hat{E}_l d\Omega_l}\bigg|_{\hat{E}_l=\frac{E_l}{z}}\theta(z-z_{min}) - \frac{d\sigma_{free}}{dE_l d\Omega_l}\right),\end{aligned} \tag{7.51}$$

where σ_{free} is the (anti)neutrino induced cross section obtained without radiative effects, E_l^* is the lepton energy in the center of mass of neutrino nucleon system and z_{min} is given by

$$z_{min} = \frac{4E_l^{*2}}{2ME_\nu} \tag{7.52}$$

with

$$E_l^* = \frac{s + m_l^2 - M^2}{2\sqrt{s}} \tag{7.53}$$

where $s = (k+p)^2$ is square of total energy in the center of mass system. k and p are the four momenta of incoming neutrino and target nucleon.

To show the effect of radiative corrections on the lepton event rates, we have obtained total scattering cross sections for ν_e and ν_μ induced reactions on free and bound nucleon, with and without radiative corrections and define

$$\begin{aligned} \Delta_1(E_\nu) &= \frac{\sigma_{\nu_\mu}(RC) - \sigma_{\nu_e}(RC)}{\sigma_{\nu_e}(RC)} \\ \Delta_2(E_\nu) &= \frac{\sigma_{\nu_\mu}(NR) - \sigma_{\nu_e}(NR)}{\sigma_{\nu_e}(NR)} \\ \Delta_{RC} &= \Delta_1(E_\nu) - \Delta_2(E_\nu) \end{aligned} \tag{7.54}$$

where $\sigma_{\nu_l}(RC),\ (l = e, \mu)$ represents the cross sections obtained by taking radiative corrections into account and $\sigma_{\nu_l}(NR),\ (l = e, \mu)$ represents the cross sections without radiative corrections. A similar definition has been used for antineutrino induced process. The results for Δ_{RC} are presented in Fig. 7.20. These results are shown for the free nucleon target as well as for per interacting nucleon in ^{40}Ar, for which the total cross sections are calculated in LFG with and without RPA effect. We find that the difference in electron and muon production cross section Δ_{RC} due to radiative corrections is quite small in case of neutrino induced reactions as compared to antineutrino reactions. Furthermore, the effect of nuclear medium is to further decrease Δ_{RC} and the reduction is larger in the case of antineutrino reactions as compared to neutrino reactions. For example, for the neutrino induced process on free nucleon the effect is around 2% at $E_\nu = 0.5\ GeV$ while for antineutrino the effect is around 5% at $E_\nu = 0.5\ GeV$. When we performed the calculations using LFG with and without RPA effect, the effect becomes less than 1% in the case of neutrinos. For antineutrino induced process, using LFG without RPA effect, it is around 3%, which becomes $\sim 2\%$ when RPA effect is included.

Chapter 8

Neutrino-nucleus cross sections in ^{12}C and ^{40}Ar with KDAR neutrinos

8.1 Introduction

The two body leptonic decay mode of the charged kaon decay-at-rest (KDAR) i.e. $K^+ \rightarrow \mu^+\nu_\mu$ with B.R. 63.55±1.1% [187] provides a unique and important source of monoenergetic muon neutrinos of energy 236 MeV. These neutrinos may be used to make high precision measurements of neutrino-nucleus cross sections for the charged current (CC) induced weak quasielastic (QE) production of muons from the various nuclear targets. The high precision neutrino-nucleus cross section measured with the well defined monoenergetic beam of muon neutrinos may serve as benchmark for validating many theoretical models currently being used to describe the nuclear medium effects in QE reactions [29, 188] relevant for the analysis of present day neutrino experiments in the low energy region of a few hundred MeVs [189, 190, 191, 192, 99, 193, 194, 195, 196, 197, 198, 199, 200, 201, 202, 203, 204, 205].

These KDAR neutrinos are proposed to be used as a probe to study the new neutrino oscillation modes to sterile neutrinos i.e. $\nu_\mu \rightarrow \nu_s$ by performing the

oscillation experiments in $\nu_\mu \rightarrow \nu_\mu$ disappearance mode and studying the CC interactions of ν_μ with nuclei and/or performing the oscillation experiments in $\nu_\mu \rightarrow \nu_e$ appearance mode and studying the CC interaction of ν_e with nuclei [199, 200, 201, 202, 203, 204, 205]. In the $\nu_\mu \rightarrow \nu_\mu$ disappearance mode, ν_μ from the three body $K\mu_3$ decays of charged kaons i.e. $K^+ \rightarrow \mu^+\pi^0\nu_\mu$ having continuous energy spectrum with the end point energy of 215 MeV constitute the major source of background while in the $\nu_\mu \rightarrow \nu_e$ appearance mode, ν_e from the Ke_3 decay mode of charged kaons i.e. $K^+ \rightarrow e^+\pi^0\nu_e$, having continuous energy spectrum with end point energy of 228 MeV constitute the major source of background. The background in both the channels from the decay in flight (DIF) neutrinos from pions, kaons and other mesons corresponds to higher energies. With sufficiently improved energy resolution for the detection of the final muon and the electron produced respectively in the CC weak interaction of ν_μ and ν_e with matter, the background events can be well separated in energy from the signal events for the oscillation experiments corresponding to $E_{\nu_\mu(\nu_e)} = 236$ MeV. Moreover, it has been recently suggested [206] that the observation of CC induced QE events with the monoenergetic neutrinos can also provide information about the dark matter which annihilates in its interaction with the solar matter in the center of the Sun into quark-antiquark pairs and produces the charged kaons through the hadronization process. The monoenergetic muon neutrinos produced by these charged kaons through the $K\mu_2$ decays can be identified by comparing the on-source and off-source event rates in the terrestrial detectors provided the background events for $E_\nu \sim 236$ MeV are well under control in the ν-oscillation experiments proposed with the KDAR neutrinos.

This type of experiments with high intensity KDAR neutrinos requires an accelerator facility capable of producing K^+ mesons with a very high yield. The 3 GeV proton accelerator facility at the J-PARC MLF facility in Tokai, Japan [199, 200, 201, 202, 203] and the 8 GeV proton accelerator facility at the BNB source facility at the Fermilab, USA [203, 204, 205] have the sufficient energy and power to produce high intensity charged kaons through the primary and/or secondary

interactions of protons with the nuclear targets which would be stopped in the surrounding material and their decay would give intense beam of ν_μ. At the J-PARC facility the neutrino oscillation experiments in the appearance mode i.e. $\nu_\mu \rightarrow \nu_e$ as well as in the disappearance mode i.e. $\nu_\mu \rightarrow \nu_\mu$ have been proposed respectively, through the JSNS experiment by the Japanese group [199, 200, 201], and the KPipe experiment by the MIT-Columbia group [202, 203, 204] using the liquid scintillator detector with active detector mass of 17 tons and 684 tons, respectively. At the Fermilab facility a neutrino oscillation experiment in the appearance mode i.e. $\nu_\mu \rightarrow \nu_e$ has been proposed with 2 kton LArTPC detector [204, 205]. Recently the MiniBooNE collaboration [68] has used the Booster Neutrino Beamline(BMB) and the Neutrinos at the Main Injector(NuMI) sources to do an experiment and the measurements of the total scattering cross section and shape only differential scattering cross section in ^{12}C.

One of the major sources of systematic errors in these experiments is due to the ν_μ flux arising from the uncertainty in the K^+ production yields in the proton-nucleus interaction predicted by the hadronic models for the kaon production and could be as large as 75% [202, 203, 207, 208]. The other source of systematic errors is due to the uncertainty in the $\nu_\mu(\nu_e)-$nucleus cross sections for $E_{\nu_\mu(\nu_e)} = 236$ MeV arising due to the nuclear medium effects [29, 188] and is the subject of the present work.

The present simulation studies [202, 203, 204], for estimating the neutrino oscillation parameters, use the neutrino nucleus cross sections for the KDAR neutrinos on ^{12}C and ^{40}Ar as predicted by the NuWro generator [209] which are reported to be about 25% smaller than the predictions by the GENIE Monte Carlo generator [59] and the results of Martini et al. [179, 210]. In the low energy region, the short range correlations and the meson exchange currents(MEC) are not expected to play an important role [211, 212, 180], but the effects of Pauli blocking, Fermi motion and the long range RPA correlations are found to be quite important. This has been shown by many theoretical attempts [213, 214, 215, 216, 217, 218, 219, 220, 148, 221, 222, 223, 224] made to explain the $\nu_\mu-^{12}$C cross section measured

in the LSND experiment [225, 226, 227] with the pion decay in flight (DIF) muon neutrinos in the energy region of $E_{\nu_\mu} < 320$ MeV with $< E_{\nu_\mu} >= 150$ MeV. These effects could therefore be very important in the energy region of KDAR neutrinos.

In view of the recent interest in the proposed neutrino oscillation experiments in $\nu_\mu \to \nu_\mu$ and $\nu_\mu \to \nu_e$ mode with liquid scintillator(LS) and LArTPC detectors and the search of sterile neutrinos through the $\nu_\mu \to \nu_s$ mode; it is topical to study the uncertainties in the $\nu_\mu(\nu_e)-$nucleus cross sections in the low energy region relevant for the monoenergetic KDAR neutrinos. In this chapter, we have studied the uncertainties in the neutrino-nucleus cross sections for the QE processes induced by the weak charged current interaction in $\nu_\mu(\nu_e)$ scattering from ^{12}C and ^{40}Ar nuclei relevant for the KDAR neutrinos with $E_{\nu_\mu} \leq 300$ MeV in a nuclear model using the local density approximation which takes into account the effects of nuclear medium arising due to the Pauli Blocking, Fermi motion and the long range RPA correlations. The model has been used by us earlier to calculate quite satisfactorily the low energy neutrino cross sections relevant for the supernova, Michel and pion decay in flight(DIF) neutrino spectra [228, 229, 230, 231]. We report the results on the energy dependence of the total cross section $\sigma(E_\nu)$ for E_ν <300MeV, and the angular distributions $(\frac{d\sigma}{dcos\theta_l})$ and the kinetic energy distributions $(\frac{d\sigma}{dT_l})$ for the electron and the muon produced in the CCQE reactions induced by ν_e and ν_μ at $E_\nu = 236$ MeV in ^{12}C and ^{40}Ar and compare these results with the other theoretical calculations available in the literature.

8.2 Formalism

The reaction for the CC neutrino interaction with a nucleus is given by

$$\nu_l + {}^{A}_{Z}X \to l^- + {}^{A}_{Z+1}Y \qquad (l = e, \mu) \tag{8.1}$$

for which the basic process is

$$\nu_l(k) + n(p) \to l^-(k') + p(p'). \tag{8.2}$$

${}^{A}_{Z}X({}^{A}_{Z+1}Y)$ is the initial(final) nucleus, and k, k' are the four momenta of the incoming and outgoing lepton and p, p' are the four momenta of the initial and final nucleon, respectively. The invariant matrix element given in Eq.8.2 is written as

$$\mathcal{M} = \frac{G_F}{\sqrt{2}} \cos\theta_c \; l_\mu \; J^\mu \tag{8.3}$$

where G_F is the Fermi coupling constant, θ_c is the Cabibbo angle. The leptonic current is given by

$$l_\mu \;\; = \;\; \bar{u}(k')\gamma_\mu(1-\gamma_5)u(k), \tag{8.4}$$

J^μ is the hadronic current given by

$$J^\mu \;\; = \;\; \bar{u}(p')\Gamma^\mu u(p), \tag{8.5}$$

with

$$\Gamma^\mu = F_1^V(Q^2)\gamma^\mu + F_2^V(Q^2)i\sigma^{\mu\nu}\frac{q_\nu}{2M} + F_A(Q^2)\gamma^\mu\gamma^5 + F_P(Q^2)\frac{q^\mu}{M}\gamma^5, \tag{8.6}$$

$Q^2(=-q^2) \geq 0$ is the four momentum transfer square and M is the nucleon mass. $F_{1,2}^V(Q^2)$ are the isovector vector form factors and $F_A(Q^2)$, $F_P(Q^2)$ are the axial and pseudoscalar form factors, respectively. We have not considered the contribution from the second class currents. The transition vector and axial vector form factors has already been discussed in detailed in Chapter-7 and in this chapter, we use the expressions for $F_{1,2}^V(Q^2)$, $F_A(Q^2)$ and $F_P(Q^2)$ as given in Eqs.7.10, 7.13 and 7.15.

The differential cross section corresponding to Eq. 8.2 is given by

$$\sigma_0(\mathbf{q^2}, \mathbf{k'}, \mathbf{p}) = \frac{1}{4\pi}\frac{k^2}{E_\nu E_l}\frac{M^2}{E_n E_p}\bar{\Sigma}\Sigma|\mathcal{M}^2|\delta(q_0 + E_n - E_p), \tag{8.7}$$

where $q_0 = E_{\nu_l} - E_l$, $E_n = \sqrt{|\mathbf{p}|^2 + M_n^2}$ and $E_p = \sqrt{|\mathbf{p}+\mathbf{q}|^2 + M_p^2}$. The matrix element square is obtained by using Eq.(8.3) and is given by

$$|\mathcal{M}|^2 = \frac{G_F^2}{2} \; L_{\mu\nu}J^{\mu\nu}. \tag{8.8}$$

In Eq.(8.8), $L_{\mu\nu}$ is the leptonic tensor calculated to be

$$L_{\mu\nu} = 8\left[k_\mu k'_\nu + k'_\mu k_\nu - g_{\mu\nu}\, k\cdot k' \pm \epsilon_{\mu\nu\alpha\beta}\, k'^{\alpha} k^{\beta}\right], \tag{8.9}$$

The hadronic tensor $J^{\mu\nu}$ given by:

$$J^{\mu\nu} = \bar{\Sigma}\Sigma J^{\mu\dagger} J^{\nu}, \tag{8.10}$$

where J^μ defined in Eq.8.5. The detailed expression for the hadronic tensor $J^{\mu\nu}$ is given in Appendix-A.

When the processes given by Eq.8.2 take place in a nucleus, various nuclear medium effects like Pauli blocking, Fermi motion, binding energy corrections and nucleon correlations, etc. come into play. Moreover, the charged lepton produced in the final state moves in the Coulomb field of the residual nucleus and which affects its energy and momenta. We have taken into account these effects which have been discussed in Chapter-7.

With the inclusion of these nuclear effects, the cross section $\sigma(E_\nu)$ is written as

$$\begin{aligned}\sigma(E_\nu) &= -2{G_F}^2\cos^2\theta_c \int_{r_{min}}^{r_{max}} r^2 dr \int_{{k'}_{min}}^{{k'}_{max}} k' dk' \int_{Q^2_{min}}^{Q^2_{max}} dQ^2 \frac{1}{E^2_{\nu_l} E_l} \\ &\times\ L_{\mu\nu} J^{\mu\nu}\, Im U_N(q_0^{eff}(r) - V_c(r), \mathbf{q}).\end{aligned} \tag{8.11}$$

We must point out that in the above expression the outgoing lepton momentum and energy are r-dependent i.e. $k' = k'(r)$ and $E_l = E_l(r)$, and only in the asymptotic limit ($r \to \infty$) they become independent of r. With the incorporation of the Coulomb effect, $E_l(r)$ is modified to $E_l(r) + V_c(r)$, and $|\mathbf{k'(r)}| = \sqrt{(\mathbf{E_l(r)} + \mathbf{V_c(r)})^2 - \mathbf{m_l^2}}$. Accordingly the energy transfer q_0 modifies to $q_0^{eff}(r) = q_0^{eff}(r) - V_c(r)$, and the three momentum transfer $\mathbf{q}$ modifies to $\mathbf{q(r)} = \mathbf{k} - \mathbf{k'(r)}$.

When the RPA correlation effects are also taken into account following the discussions given in Chapter-7 the expression for the total scattering cross section $\sigma(E_\nu)$ is given by Eq.8.11 with $J^{\mu\nu}$ replaced by $J^{\mu\nu}_{RPA}$ i.e.

$$\begin{aligned}\sigma(E_\nu) &= -2{G_F}^2 cos^2\theta_c \int_{r_{min}}^{r_{max}} r^2 dr \int_{{k'}_{min}}^{{k'}_{max}} k' dk' \int_{Q^2_{min}}^{Q^2_{max}} dQ^2 \frac{1}{E^2_{\nu_l} E_l} L_{\mu\nu} J^{\mu\nu}_{RPA} \\ &\times\ Im U_N(q_0^{eff}(r) - V_c(r)).\end{aligned} \tag{8.12}$$

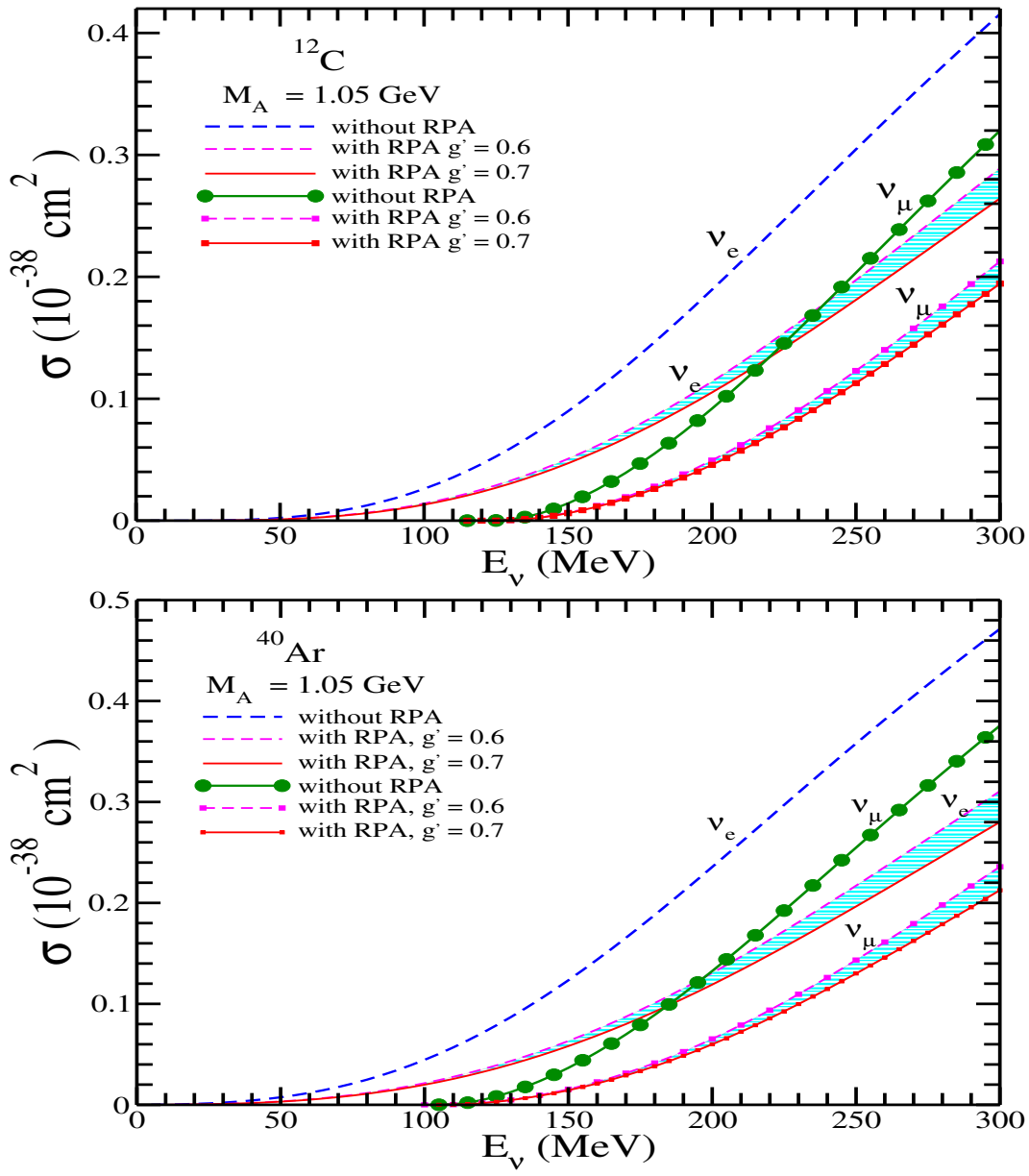

Figure 8.1: σ vs E_{ν_l}, for $\nu_l(l = e^-,\ \mu^-)$ induced scattering on ^{12}C(top panel) and ^{40}Ar(bottom panel) per nucleon target. The dashed line(line with circles) represents $\nu_e(\nu_\mu)$ cross section obtained in the LFG without RPA effects, while the bands upper(lower) represents $\nu_e(\nu_\mu)$ cross section with RPA. The bands correspond to the variation of g' in the range of 0.6-0.7.

8.3 Results and discussion

For the numerical calculations, we have used Eq. 8.11 to obtain the results for the charged current ν_e and ν_μ scattering cross sections on the nuclear targets in

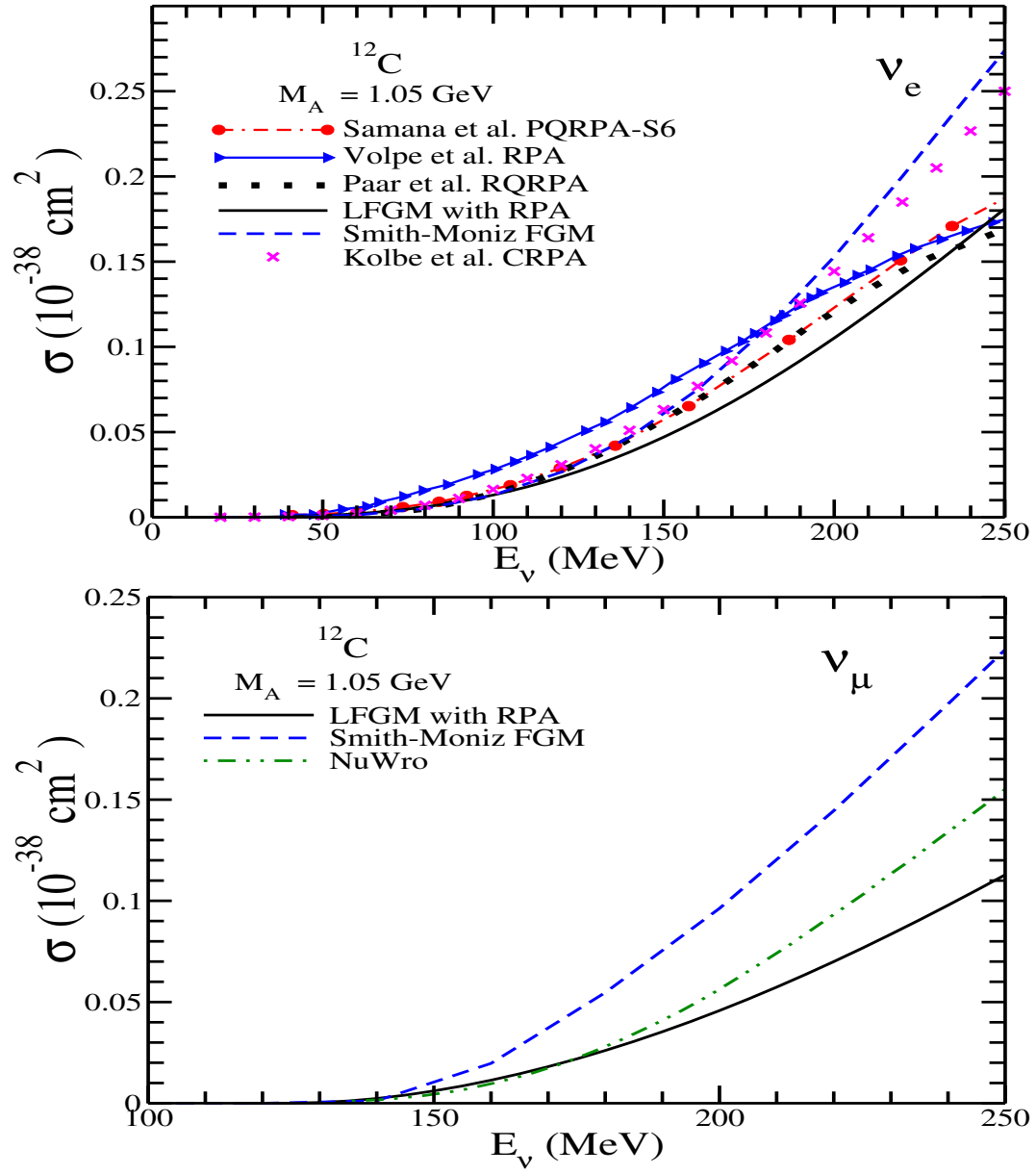

Figure 8.2: σ vs E_{ν_l}, for ν_e(top panel) and ν_μ(bottom panel) CCQE scattering cross sections on ^{12}C in the LFG model with RPA effect(solid line), the results of NuWro event generator taken from Ref. [204] (dashed double-dotted line), Volpe et al. [217] in RPA (triangle right), Kolbe et al. [219] in CRPA (cross), Paar et al. [221] in RQRPA (dotted line), Samana et al. [232] in PQRPA (circle), and Smith and Moniz [233] in RFGM (dashed line).

the local Fermi gas model(LFG) with the inclusion of Fermi momentum and Pauli blocking, and Eq. 8.12 when RPA effects are also included. Furthermore, we have taken Coulomb distortion effect on the outgoing charged lepton in both cases using

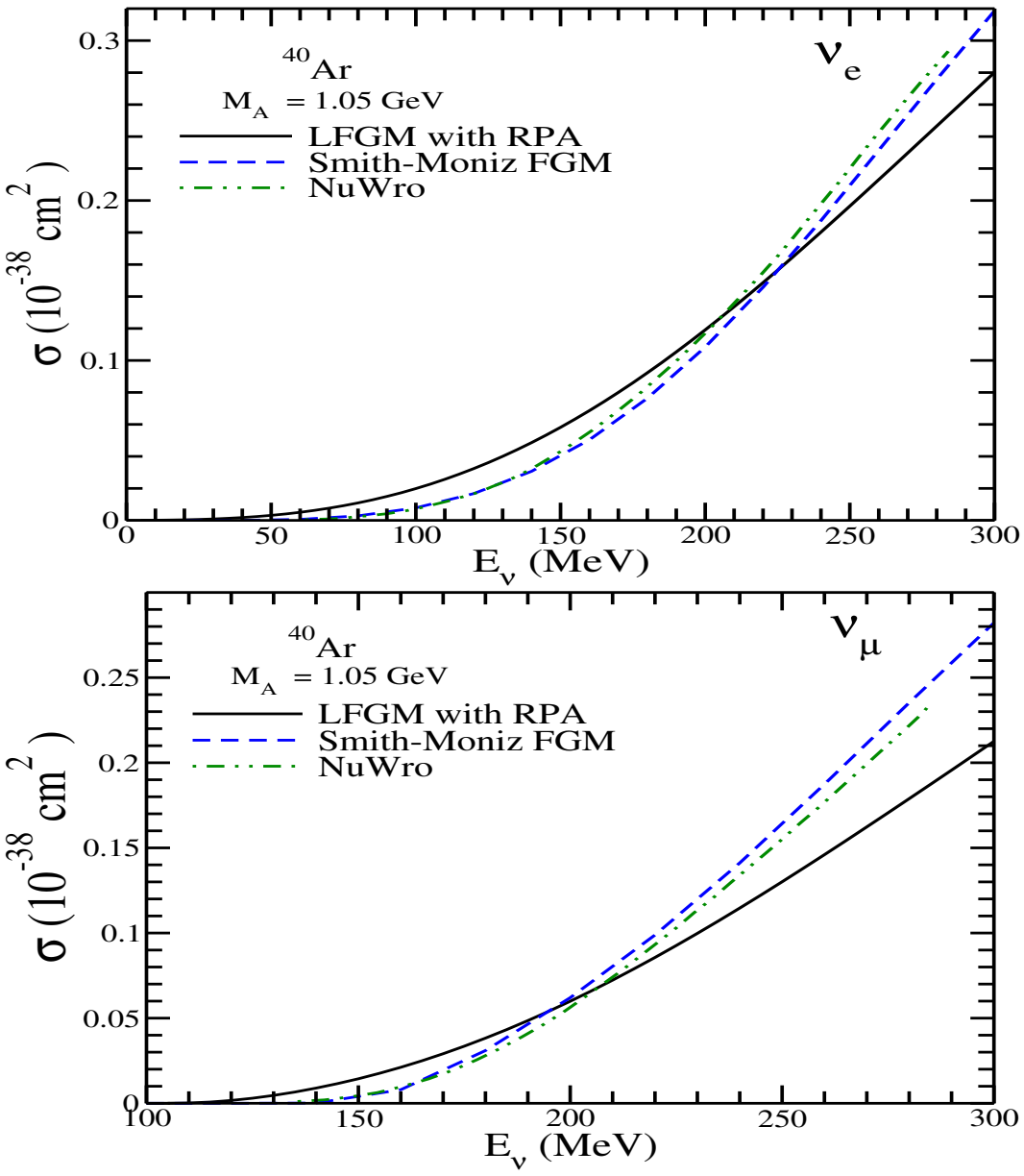

Figure 8.3: σ vs E_{ν_l}, for ν_e(top panel) and ν_μ(bottom panel) on ^{40}Ar in the LFG model with RPA effect(solid line), the results of NuWro generator taken from Ref. [204] (dashed - double dotted), and Smith and Moniz in RFGM [233, 59] (dashed line).

EMA with the Coulomb potential given in Eq. 7.30 of Chapter-7.

In Fig. 8.1, we present the results of ν_l(l=e, μ) induced charged lepton production cross sections σ vs E_{ν_l} in ^{12}C and ^{40}Ar. We find a large reduction in the cross section due to the nuclear medium effects. For example, in the case of ν_e

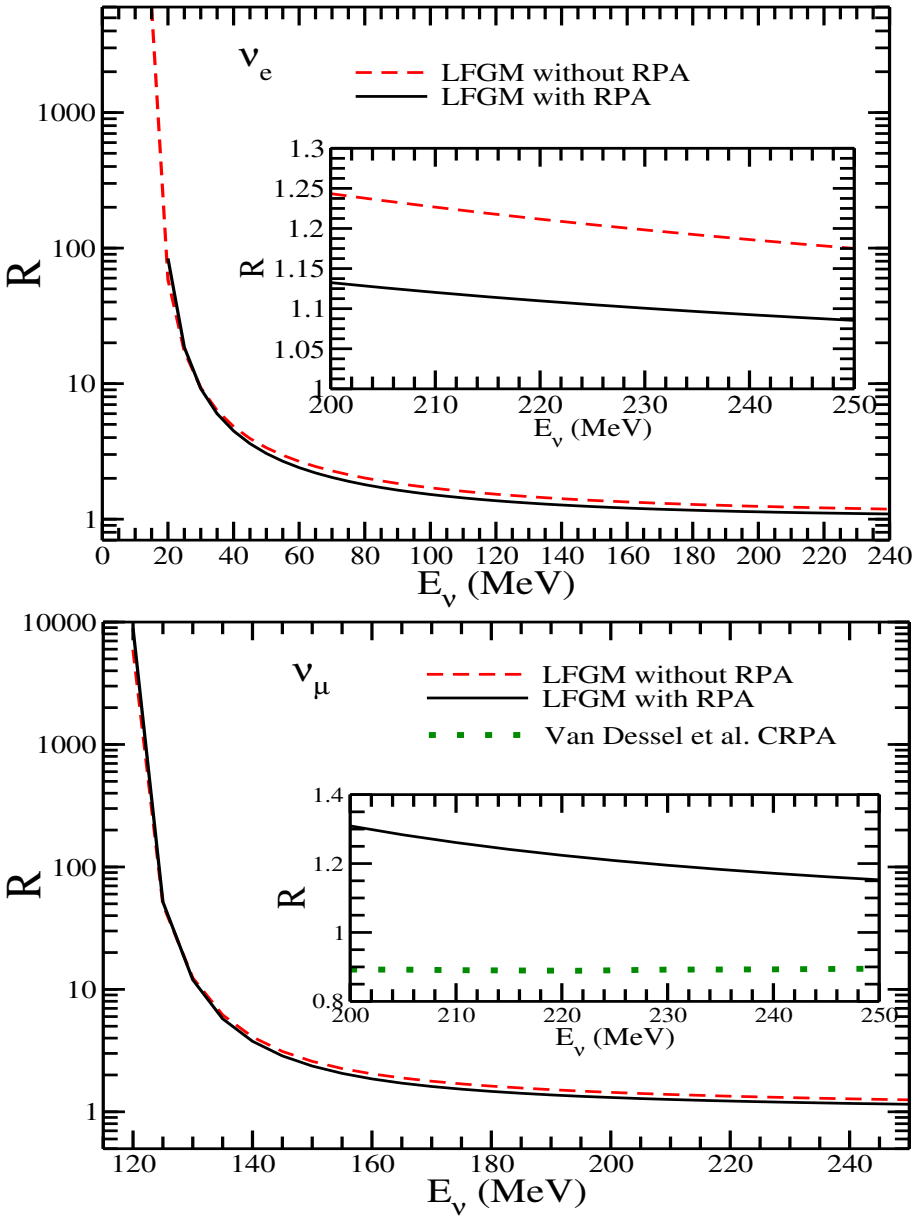

Figure 8.4: Ratio, $R = \frac{\sigma^{^{40}Ar}_{\nu_l}}{\sigma^{^{12}C}_{\nu_l}}$ vs E_ν for ν_e(top panel) and ν_μ(bottom panel). Solid(dashed) line represents the results obtained using LFG with(without) RPA. In the inset of ν_e case(top panel), the results of the ratio are obtained without(dashed line) and with(solid line) RPA. In the inset of ν_μ case(right panel), the results are compared with the results of Van Dessel et al. [234] in CRPA(dotted line).

scattering on $^{12}C(^{40}Ar)$ nuclear targets, when the cross section is obtained using the LFG without RPA effects, the reduction in the cross section from the free nucleon case(not shown here) is ∼50%(35%) at E_{ν_e} = 150 MeV, ∼38%(20%) at

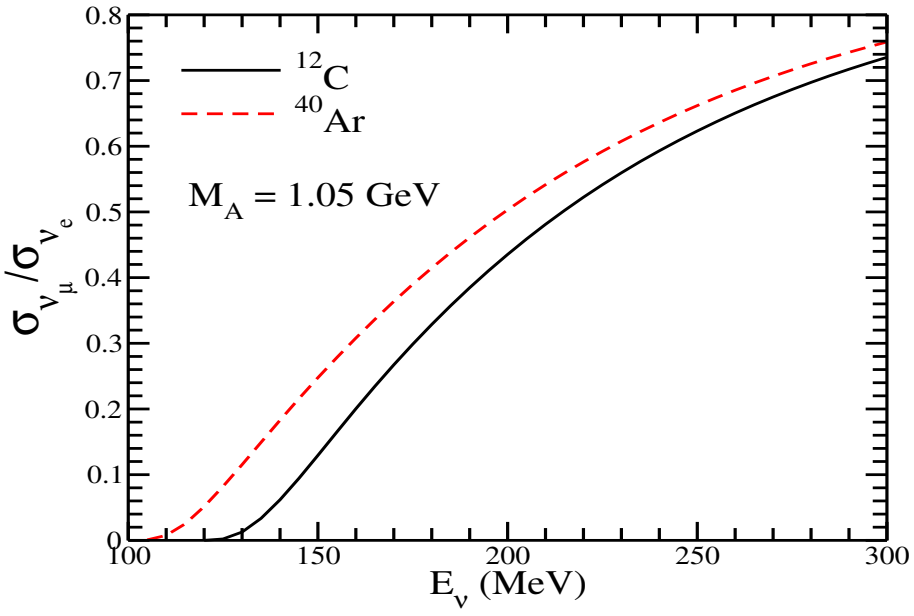

Figure 8.5: Ratio of ν_μ to ν_e scattering cross sections $\frac{\sigma_{\nu_\mu}}{\sigma_{\nu_e}}$ vs E_ν for ^{12}C(solid line) and ^{40}Ar(dashed line) in the LFG with RPA.

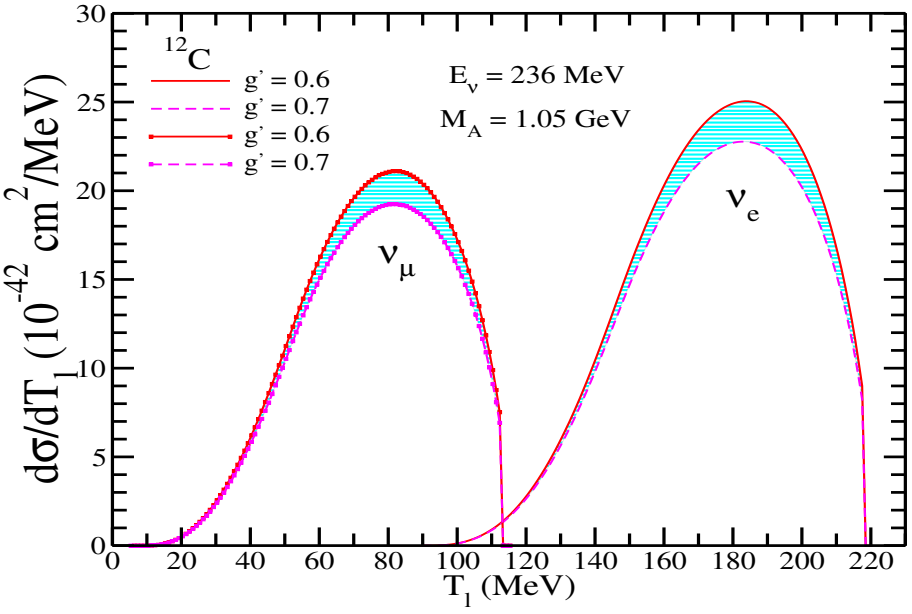

Figure 8.6: $\frac{d\sigma}{dT_l}$ vs T_l for ν_l induced processes on ^{12}C(top panel) and ^{40}Ar(bottom panel) per nucleon target at E_ν =236 MeV. The results are obtained using LFG with RPA. The variation of g' from 0.6 to 0.7 is represented by the band. The curves on the left(right) side of each panel represent the results for $\mu^-(e^-)$ kinetic energy distribution induced by $\nu_\mu(\nu_e)$ scattering.

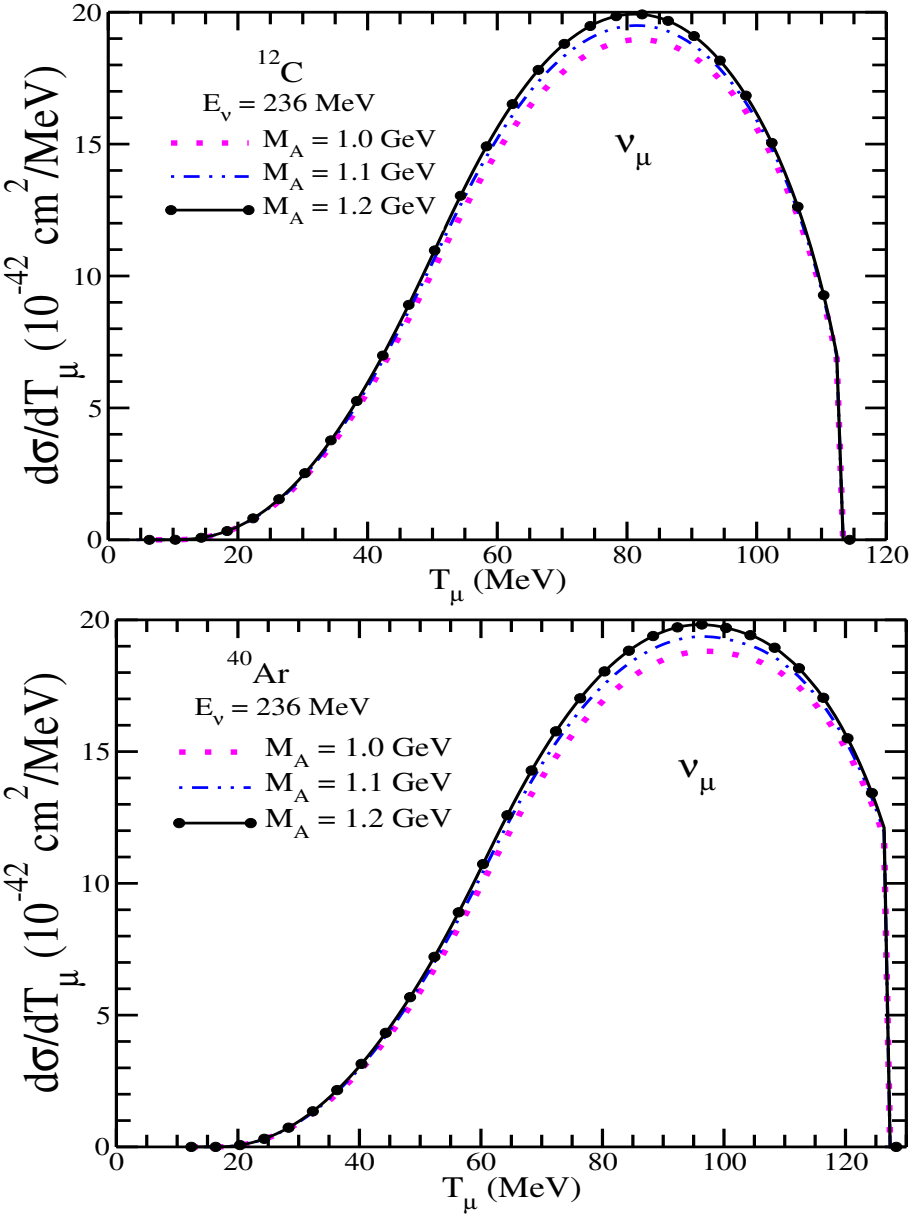

Figure 8.7: $\frac{d\sigma}{dT_\mu}$ vs T_μ for ν_μ induced processes on ^{12}C(top panel) and ^{40}Ar(bottom panel) per nucleon target at E_ν =236 MeV. The results are obtained using LFG with RPA for the different values of M_A viz. M_A = 1.0 GeV(dotted line), 1.1 GeV(dash double-dotted line) and 1.2 GeV(circle), respectively.

E_{ν_e} = 200 MeV and ∼30%(15%) at E_{ν_e} = 236 MeV. When the RPA effects are also taken into account there is a further reduction in the cross section which is about ∼48%(53%) at E_{ν_e} = 150 MeV, ∼45%(50%) at E_{ν_e} = 200 MeV and ∼42%(47%) at E_{ν_e} = 236 MeV. In the case of ν_μ scattering, this reduction is ∼85%(65%) at E_{ν_μ} = 150 MeV, ∼60%(43%) at E_{ν_μ} = 200 MeV and ∼47%(30%) at E_{ν_μ} =

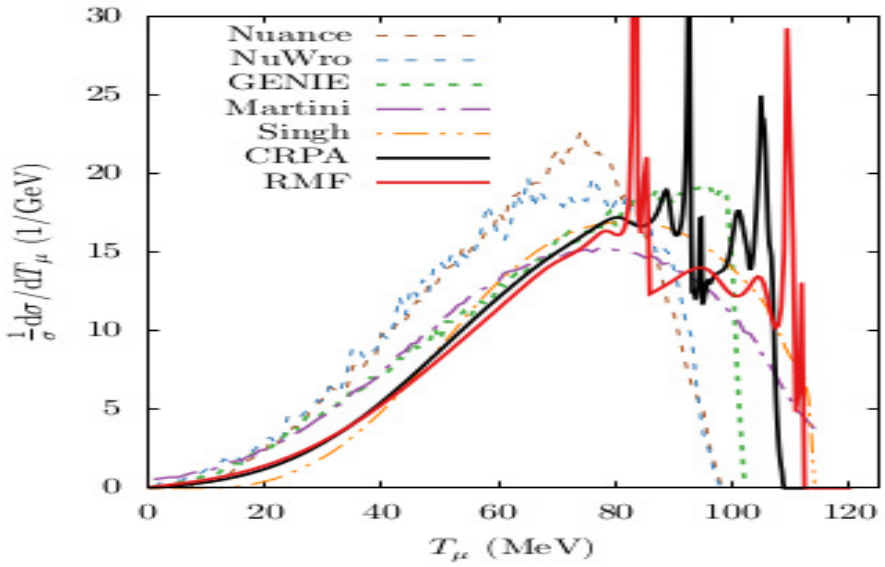

Figure 8.8: Kinetic energy distribution, $\frac{d\sigma}{dT_\mu}$ vs T_μ for ν_μ induced process on ^{12}C nuclear target at $E_\nu = 236$ MeV. Dashed-double-dotted line represents the results of the present model which are compared with the models of CRPA [235](black solid line), RMF [236](red solid line), Martini et al. [237](dashed-dotted line) as well as with MC generators like Nuance [238](red dashed line), NuWro [239](dashed line) and GENIE [240](short dashed line). The figure has been taken from Ref. [235].

236 MeV without the RPA correlation and a further reduction of ∼55%(60%) at $E_{\nu_\mu} = 150$ MeV, ∼50%(55%) at $E_{\nu_\mu} = 200$ MeV and ∼45%(50%) at $E_{\nu_\mu} = 236$ MeV, when RPA effects are included. We have also shown in these figures, the dependence of the cross section on g', the Landau-Migdal parameter (discussed in Appendix-A), by varying the value of g' in the range 0.6-0.7. The bands shown in the figures correspond to the change in the cross section due to the variation of g' in this range. We find that with $g' = 0.7$ the cross section in $^{12}C/^{40}Ar$ decreases by about 10% for $\nu_l(l = e, \mu)$ scattering at 236 MeV from the results obtained with $g' = 0.6$.

In Fig. 8.2, we have compared the present results in $\nu_e - ^{12}C$ with the results of NuWro generator [209], Volpe et al. [217] in RPA, Kolbe et al. [219] in Continuum Random Phase Approximation, Paar et al. [221] in Relativistic Quasiparticle

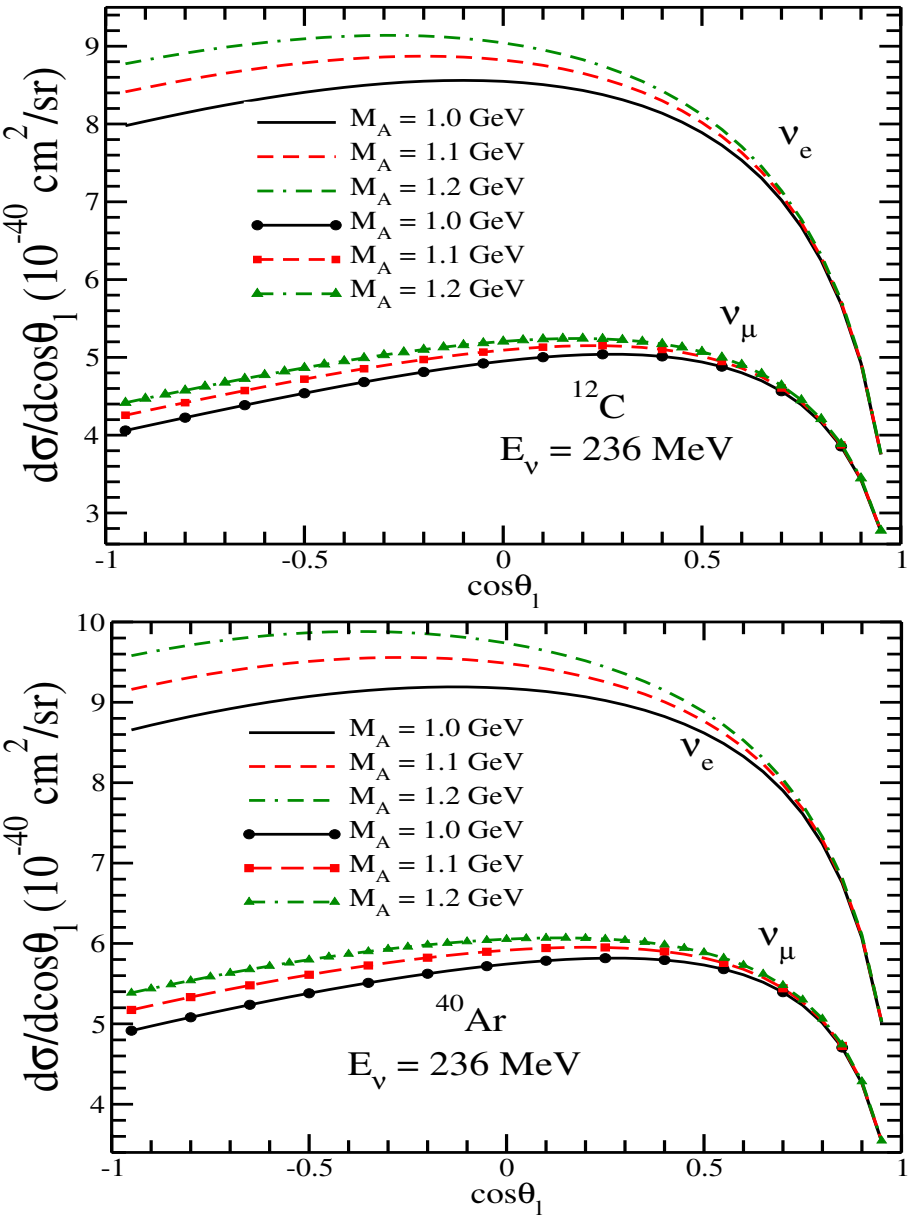

Figure 8.9: $\frac{d\sigma}{cos\theta_l}$ vs $cos\theta_l$ for ν_e(top curves) and ν_μ(bottom curves) induced processes on ^{12}C(left panel) and ^{40}Ar(right panel) per nucleon target at E_ν =236 MeV, obtained by using LFG with RPA for the different values of M_A viz. M_A = 1.0 GeV(circle), 1.1 GeV(dash double-dotted line) and 1.2 GeV(dotted line).

Random Phase Approximation, Samana et al. [232] in Projected Quasiparticle Random Phase Approximation-S6, and Smith and Moniz [233] in the relativistic Fermi gas model. We find that the results using Smith and Moniz [233] FGM are almost higher by 50% at E_{ν_e}=250MeV, while the results of Kolbe et al. [219] are higher by 38% at the same energy from the results obtained using LFG with RPA

effects. Furthermore, we find that in the energy region of $100 < E_{\nu_e} < 240$ MeV, the results of Volpe et al. [217] and Paar et al. [221] differ and these results are higher in the range $50 \leq E_{\nu} \leq 240$ MeV and $120 \leq E_{\nu} \leq 240$ MeV, respectively, with the present results. We have also compared the present theoretical results of the cross section in the case of $\nu_\mu - ^{12}C$ scattering with the results of Smith and Moniz [233] and NuWro generator [204, 209] in which the nucleon spectral function of Benhar et al. [212] has been used. We find that results of Smith and Moniz [233] are always higher than the results obtained by us using LFG with RPA effects. For example, at E_{ν_μ}=200MeV this enhancement is 100% which becomes 110% at E_{ν_μ}=250MeV. At lower ν_μ energies the results being used in the NuWro MC generator are close to our results but with the increase in energy they become larger, for example, at E_{ν_μ}=200MeV this enhancement is 40% which becomes 50% at E_{ν_μ}=250MeV.

In Fig. 8.3, we have compared the present results in $\nu_e - ^{40}Ar$ and $\nu_\mu - ^{40}Ar$ with the results of Smith and Moniz [233] and NuWro generator [204, 209] in which the nucleon spectral function of Benhar et al. [212] has been used. We find that at lower energies $E_{\nu_e} < 200$MeV, our results are slightly larger than the results of Smith and Moniz [233] and NuWro generator [204, 209], which themselves are in agreement throughout the energy spectrum. All the three results are well in agreement around $E_{\nu_e} \sim 220$MeV and then our results become slightly smaller than these two results. For example at $E_{\nu_e} \sim 300$MeV, our results are 12-14% smaller.

In the preliminary simulation studies for determining the neutrino oscillation parameters Spitz et al. [203, 204] have used NuWro [209] prediction of 1.3×10^{-38} cm^2 per neutron for the total cross section for $\nu_\mu - ^{12}C$ and $\nu_\mu - ^{40}Ar$ scattering at $E_\nu = 236$ MeV. and the same value has also been used by Axani et al. [202] for the $\nu_\mu - ^{12}C$ cross section.

In view of this we have studied the ratio R $= \frac{\sigma^{40}Ar}{\sigma^{12}C}$ as a function of E_ν. In Fig. 8.4, we have shown the results for R obtained using the present model with

and without RPA effects for the ν_e and ν_μ induced processes and also made a comparison with the recent results reported by Van Dessel et al. [234] in CRPA for the ν_μ induced process. It may be observed from the results shown for R in the case of ν_e induced scattering that the ratio obtained using (i) LFG only and (ii) LFG with RPA effect, are not the same (see the inset) in the energy region of present interest. The difference in the results for the ratio in the two models decreases with the increase in neutrino energy. A similar trend is observed in the case of ν_μ induced scattering. When the present results for the ratio in the case of ν_μ induced scattering are comapred with the results of Van Dessel et al. [234] who have used CRPA, we find a large difference at lower energies, and the difference reduces with the increase in energy, nevertheless it is quite significant event at E_{ν_μ}=250MeV.

The measurement of neutrino-nucleus cross section induced by ν_μ and ν_e and the ν_μ/ν_e cross section ratio is an important quantity in the analysis of $\nu_\mu \rightarrow \nu_e$ oscillations in the appearance channel. This ratio also provides an experimental validation of the theoretical calculations of the various effects arising due to the lepton mass dependent terms in the standard model specially the pseudoscalar form factors and the second class currents [67, 53] and could provide possible evidence of muon–electron non-universality. Moreover, this ratio is also a key parameter in improving the sensitivity of measuring the CP violation phase δ_{CP} in the future experiments on neutrino oscillations [241]. We have plotted in Fig. 8.5, the ratio of ν_μ/ν_e cross section as a function of energy in the low energy region relevant for the experiments with KDAR neutrinos. It may be observed from the figure that the ratio of the cross sections $\frac{\sigma_{\nu_\mu}}{\sigma_{\nu_e}}$ are not the same for ^{12}C and ^{40}Ar. This difference is due to the convolution of many effects like (i) Q-value of the reaction, (ii) different Fermi momentum, (iii) RPA effect, as well as (iv) Coulomb effect (different number of protons in Carbon and Argon). This difference is larger at lower energies and with the increase in energy it becomes smaller, for example, at ∼240MeV it is 10%.

In Fig.8.6, we have presented the results of $\frac{d\sigma}{dT_l}$ vs T_l $(l = e, \mu)$, for ν_e and ν_μ

induced processes in ^{12}C(top panel) and ^{40}Ar(bottom panel) per nucleon target at E_ν =236 MeV. The results are shown by varying g' in the range 0.6 to 0.7 using M_A=1.05GeV. It may be observed that in the peak region of kinetic energy spectrum, there is appreciable difference(lower in magnitude for higher value of g') in the results obtained with the two different values of g'. Moreover, this difference is not the same in ^{12}C and ^{40}Ar.

In Fig. 8.7, we have presented the results for $\frac{d\sigma}{dT_\mu}$ vs T_μ in ^{12}C and ^{40}Ar per nucleon target at E_ν = 236 MeV by varying M_A in the range of 1 - 1.2GeV. The differential cross section is obtained using local FGM with RPA effect. We observe that there is very little sensitivity on M_A in the case of kinetic energy distribution which is around 5% when we vary the value of M_A by 20%. This variation in M_A is almost the same in these two per nucleon target.

In Fig. 8.8 we show the T_μ distributions for several models recently compiled by Nikolakopoulos et al. [235]. These include models of Martini *et al.* [237], present model [69] using RPA, CRPA model[235] and Relativistic Mean Field model [236] results of as well as the results obtained using the Monte Carlo event generators NuWro [239], Nuance [238], and GENIE [240].

It may be observed that there is a large deviation in the peak region of the spectrum as well as in the tail region and no model explains the MiniBooNE data [68](not shown here).

In Fig. 8.9, we have presented the results for ν_e and ν_μ induced processes in ^{12}C and ^{40}Ar per nucleon target at E_ν = 236 MeV by varying M_A in the range of 1 - 1.2GeV. We observe that there is some sensitivity on M_A in the case of angular distribution specially at the backward angles corresponding to higher Q^2.

Chapter 9

Quasielastic production of polarized hyperons in antineutrino–nucleon reactions

9.1 Introduction

In this chapter, we have studied theoretically the production and polarization of hyperons produced in the following reactions:

$$\begin{aligned} \bar{\nu}_\mu + p &\longrightarrow \mu^+ + \Lambda \\ \bar{\nu}_\mu + p &\longrightarrow \mu^+ + \Sigma^0 \\ \bar{\nu}_\mu + n &\longrightarrow \mu^+ + \Sigma^-, \end{aligned} \tag{9.1}$$

on nucleons and nuclear targets using Cabibbo theory in the Standard Model with GIM mechanism for extension to strangeness sector. We also assume the T–invariance and the absence of second class currents which forbid the existence of hyperon polarization perpendicular to the reaction plane.

In section-9.2, we describe in brief the formalism for calculating the cross section and polarization of hyperons produced in the quasielastic antineutrino reac-

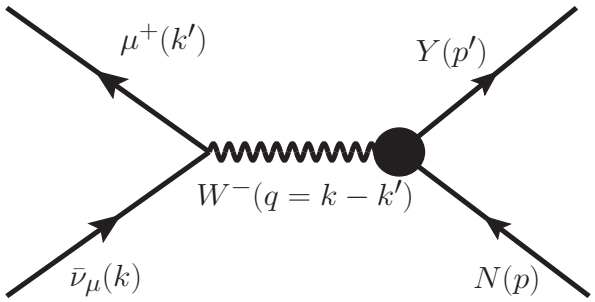

Figure 9.1: Feynman diagram for the process $\bar{\nu}_\mu(k) + N(p) \rightarrow \mu^+(k') + Y(p')$, where N and Y stand for initial nucleon and final hyperon, respectively. The quantities in the bracket represent four momentum of the corresponding particles.

tions on free and bound nucleons. The effect of nuclear medium arising due to Fermi motion and Pauli blocking of initial nucleon states are also considered. In section-9.3, we present the results and discussion.

9.2 Formalism

9.2.1 Matrix element and transition form factors

The transition matrix element for the process

$$\bar{\nu}_\mu(k) + N(p) \rightarrow \mu^+(k') + Y(p'), \quad (N = p,\ n;\ Y = \Lambda,\ \Sigma)$$

depicted in Fig. 9.1, is written as

$$\mathcal{M} = \frac{G_F}{\sqrt{2}} \sin\theta_c\, l^\mu \ [\bar{u}_Y(p') J_\mu u_N(p)]\,. \tag{9.2}$$

In the above expression G_F is the Fermi coupling constant and θ_c is the Cabibbo angle. l^μ is the leptonic current given by

$$l^\mu = \bar{u}(k')\gamma^\mu(1 + \gamma_5)u(k), \tag{9.3}$$

and J_μ is the hadronic current operator given by

$$J_\mu = V_\mu - A_\mu \tag{9.4}$$

where

$$V_\mu = \gamma_\mu f_1^{NY}(Q^2) + i\sigma_{\mu\nu}\frac{q^\nu}{M+M_Y}f_2^{NY}(Q^2) + \frac{q_\mu}{M+M_Y}f_3^{NY}(Q^2) \quad (9.5)$$

and

$$A_\mu = \gamma_\mu\gamma_5 g_1^{NY}(Q^2) + i\sigma_{\mu\nu}\gamma_5\frac{q^\nu}{M+M_Y}g_2^{NY}(Q^2) + \frac{q_\mu}{M+M_Y}g_3^{NY}(Q^2)\gamma_5. \quad (9.6)$$

M and M_Y are the masses of initial and final baryons, and $q_\mu(=p'_\mu - p_\mu)$ is the four momentum transfer. The six form factors $f_i^{NY}(Q^2)$ and $g_i^{NY}(Q^2)$ $(i = 1-3)$ are determined using following assumptions about the vector and axial vector currents in weak interactions:

(a) The assumptions of T–invariance, G–invariance and SU(3) symmetry have been used to determine all the form factors $f_i^{NY}(Q^2)$ and $g_i^{NY}(Q^2)$ defined in Eqs. 9.5 and 9.6 respectively.

(b) For the determination of vector form factors we have assumed CVC which leads to $f_3^{NY}(Q^2) = 0$. The remaining two vector form factors $f_1^{NY}(Q^2)$ and $f_2^{NY}(Q^2)$ are determined in terms of the electromagnetic form factors of nucleon i.e. $f_1^N(Q^2)$ and $f_2^N(Q^2)$ and are tabulated in Table-9.1 for different processes given in Eq. 9.1. The electromagnetic form factors of nucleon i.e. $f_1^N(Q^2)$ and $f_2^N(Q^2)$ are in turn written in terms of Sach's electric($G_E^{p,n}(Q^2)$) and magnetic($G_M^{p,n}(Q^2)$) form factors as already discussed in Chapter-7.

(c) In the axial vector sector, the form factor $g_2^{NY}(Q^2)$ vanishes due to G–invariance, T–invariance and SU(3) symmetry and the axial vector form factor $g_1^{NY}(Q^2)$ is given in terms of the axial form factor $g_A(Q^2)$ corresponding to n $\rightarrow$ p transitions. x is a parameter which describes the ratio of symmetric and antisymmetric coupling in the analysis of hyperon semileptonic decays(HSD) and is determined phenomenologically from the experimental data [70]. For each reaction considered in this work(Eq. 9.1), the form factor $g_1^{NY}(Q^2)$ is given in Table-9.1. A dipole parameterization for $g_A(Q^2)$ has been used with axial dipole mass M_A i.e.

$$g_A(Q^2) = g_A(0)\left(1 + \frac{Q^2}{M_A^2}\right)^{-2}, \quad (9.7)$$

with $g_A(0) = 1.2723$ determined from data on the β decay of neutron [242]. The numerical value of dipole mass M_A used in this work is discussed in section II(f) below.

(d) The pseudoscalar form factor $g_3^{NY}(Q^2)$ is obtained in terms of axial vector form factor $g_1^{NY}(Q^2)$ assuming PCAC and Goldberger–Treiman (GT) relation extended to strangeness sector. We use expressions given by Marshak et al. [86] and Nambu [243] where further details can be found. Explicitly, in our numerical calculations we use the following expressions for the pseudoscalar form factor $g_3^{NY}(Q^2)$,

(i) Marshak et al. [86]:

$$g_3^{NY}(Q^2) = \frac{(M+M_Y)^2}{Q^2}\left(\frac{g_1^{NY}(Q^2)(m_K^2+Q^2) - m_K^2 g_1^{NY}(0)}{m_K^2+Q^2}\right), \quad (9.8)$$

(ii) Nambu [243]:

$$g_3^{NY}(Q^2) = \frac{(M+M_Y)^2}{(m_K^2+Q^2)} g_1^{NY}(Q^2), \quad (9.9)$$

with m_K being mass of kaon and $g_1^{NY}(Q^2)$ for different NY transitions is given in terms of $g_A(Q^2)$ defined in Eq. 9.7.

(e) We see from Table-9.1 that SU(3) symmetry predicts a simple relation between the vector and axial vector form factors for reactions $\bar{\nu}_\mu p \to \mu^+\Sigma^0$ and $\bar{\nu}_\mu n \to \mu^+\Sigma^-$, which implies that

$$\left[\frac{d\sigma}{dQ^2}\right]_{\bar{\nu}_\mu p\to\mu^+\Sigma^0} = \frac{1}{2}\left[\frac{d\sigma}{dQ^2}\right]_{\bar{\nu}_\mu n\to\mu^+\Sigma^-} \quad (9.10)$$

and

$$[P_{L,P}]_{\bar{\nu}_\mu p\to\mu^+\Sigma^0} = [P_{L,P}]_{\bar{\nu}_\mu n\to\mu^+\Sigma^-}\,. \quad (9.11)$$

It should be emphasized that these relations and other implications of SU(3) symmetry and G–invariance can be tested in strangeness sector with the availability of precise data on weak hyperon production induced by antineutrinos.

(f) The numerical value of axial dipole mass(M_A) to be used in the calculations of neutrino–nucleus cross section is a subject of intense discussion in the

neutrino physics community and a wide range of M_A has been recently discussed in literature [188, 244, 245]. The old data available on (anti)neutrino scattering on hydrogen and deuterium targets [246, 247, 248] reanalyzed by Bodek et al. [249] gives a value of $M_A = 1.014 \pm 0.014$ GeV, while a recent analysis of the same data by Meyer et al. [250] gives a value in the range of 1.02–1.17 GeV depending upon which data of ANL [246], BNL [247] and FNAL [248] experiments are considered. Sometimes back, all the world data on quasielastic (anti)neutrino scattering from nuclear targets were analyzed by Bernard et al. [155] to yield $M_A = 1.026 \pm 0.021$ GeV.

Keeping in view this scenario regarding the numerical values of M_A to be needed to explain the quasielastic cross sections in $\Delta S = 0$ (anti)neutrino–nucleus scattering, we have varied the value of M_A between 1.026–1.2 GeV to study the $|\Delta S| = 1$ quasielastic antineutrino reactions on nuclear targets. A priori, there is no reason to assume the same value of M_A for antineutrino quasielastic reactions in $\Delta S = 0$ and $|\Delta S| = 1$ sectors as argued by Gaillard and Sauvage [71] and supported by Cabibbo et al. [70]. However, this range of M_A also accommodates the suggestion of Gaillard and Sauvage [71] that the value of M_A to be used in $|\Delta S| = 1$ quasielastic reactions should be rescaled upwards by a factor $\frac{m_K^*}{m_\rho}$(m_K^* and m_ρ be the masses of K^* and ρ mesons) over the M_A used in $\Delta S = 0$ reactions if effects of minimal SU(3) breaking are to be simulated by taking realistic hyperons and other masses in the theory of HSD.

9.2.2 Cross section

The differential cross section corresponding to the processes given in Eq. 9.1 may be written as

$$d\sigma = \frac{1}{(2\pi)^2}\frac{1}{4E_{\bar{\nu}_\mu}M}\delta^4(k + p - k' - p')\frac{d^3k'}{2E_{k'}}\frac{d^3p'}{2E_{p'}}\sum\overline{\sum}|\mathcal{M}|^2, \tag{9.12}$$

where $\mathcal{M}$ is the transition matrix element, square of which may be written in terms of hadronic and leptonic tensors as

$$|\mathcal{M}|^2 = \frac{G_F^2 \sin^2\theta_c}{2}\mathcal{J}^{\alpha\beta}\mathcal{L}_{\alpha\beta}. \tag{9.13}$$

	$f_1^{NY}(Q^2)$	$f_2^{NY}(Q^2)$	$g_1^{NY}(Q^2)$
$\bar{\nu}_\mu p \to \mu^+ \Lambda$	$-\sqrt{\frac{3}{2}}\ f_1^p(Q^2)$	$-\sqrt{\frac{3}{2}}\ f_2^p(Q^2)$	$-\frac{1}{\sqrt{6}}(1+2x)g_A(Q^2)$
$\bar{\nu}_\mu n \to \mu^+ \Sigma^-$	$-\left[f_1^p(Q^2)+2f_1^n(Q^2)\right]$	$-\left[f_2^p(Q^2)+2f_2^n(Q^2)\right]$	$(1-2x)g_A(Q^2)$
$\bar{\nu}_\mu p \to \mu^+ \Sigma^0$	$-\frac{1}{\sqrt{2}}\left[f_1^p(Q^2)+2f_1^n(Q^2)\right]$	$-\frac{1}{\sqrt{2}}\left[f_2^p(Q^2)+2f_2^n(Q^2)\right]$	$\frac{1}{\sqrt{2}}(1-2x)g_A(Q^2)$

Table 9.1: Vector and axial vector from factors for $\bar{\nu}_\mu(k) + N(p) \to \mu^+(k') + Y(p')$ processes.

The hadronic and leptonic tensors are given by

$$\begin{aligned} \mathcal{J}^{\alpha\beta} &= \mathrm{Tr}\left[\Lambda(p')J^\alpha \Lambda(p)\tilde{J}^\beta\right] \\ \mathcal{L}_{\alpha\beta} &= \mathrm{Tr}\left[\gamma_\alpha(1+\gamma_5)\not{k}\gamma_\beta(1+\gamma_5)(\not{k}'+m_\mu)\right], \end{aligned} \tag{9.14}$$

with $\tilde{J}_\beta = \gamma^0 J_\beta^\dagger \gamma^0$ and $\Lambda(p) = \not{p} + M$. Using the above definitions, the Q^2 distribution is written as

$$\frac{d\sigma}{dQ^2} = \frac{G_F^2 \sin^2\theta_c}{8\pi M E_{\bar{\nu}_\mu}^2}\mathcal{N}(Q^2, E_{\bar{\nu}_\mu}), \tag{9.15}$$

where the expression of $\mathcal{N}(Q^2, E_{\bar{\nu}_\mu})$ is given in the appendix.

When the reactions shown in Eq. 9.1 take place on nucleons which are bound in the nucleus, the neutrons and protons are not free and their momenta $p_{n,p}(r)$ at r are constrained to satisfy the Pauli principle, i.e., $p_{n,p}(r) < p_{F_{n,p}}(r)$, where $p_{F_n}(r)$ and $p_{F_p}(r)$ are the local Fermi momenta of neutrons and protons at the interaction point in the nucleus and are given by $p_{F_n}(r) = [3\pi^2\rho_n(r)]^{\frac{1}{3}}$ and $p_{F_p}(r) = [3\pi^2\rho_p(r)]^{\frac{1}{3}}$, $\rho_n(r)$ and $\rho_p(r)$ are the neutron and proton nuclear densities given by $\rho_n(r) = \frac{(A-Z)}{A}\rho(r)$ and $\rho_p(r) = \frac{Z}{A}\rho(r)$, $\rho(r)$ is the nuclear density which is determined from electron-nucleus scattering experiments.

The differential scattering cross section for the scattering of antineutrinos from nucleons in the nucleus is then given as

$$\left[\frac{d^2\sigma}{dE_l d\Omega_l}\right]_{\bar{\nu}_\mu A} = 2\int_{r_{min}}^{r_{max}} d^3r \int_0^{p_{F_N}(r)} \frac{d^3p}{(2\pi)^3} n_N(p,r)\left[\frac{d^2\sigma}{dE_l d\Omega_l}\right]_{\bar{\nu}_\mu N} \tag{9.16}$$

where $n_N(p,r)$ is local occupation number of the initial nucleon of momentum p at a radius r in the nucleus, which is 1 for $p < p_{F_N}(r)$ and 0 otherwise, and

$n_N(p,r)$ is related to the density as:

$$\rho = \frac{N}{V} = 2\int \frac{d^3p}{(2\pi)^3} n_N(p,r). \tag{9.17}$$

In the next section, we discuss briefly the construction of polarization vector for the final hyperon.

9.2.3 Polarization of hyperons

Using the covariant density matrix formalism, polarization 4-vector(ξ^τ) of the final hyperon produced in reaction (9.2) is written as [251]:

$$\xi^\tau = \frac{\mathrm{Tr}[\gamma^\tau\gamma_5\ \rho_f(p')]}{\mathrm{Tr}[\rho_f(p')]}, \tag{9.18}$$

where the final spin density matrix $\rho_f(p')$ is given by

$$\rho_f(p') = \mathcal{L}^{\alpha\beta}\Lambda(p')J_\alpha\Lambda(p)\tilde{J}_\beta\Lambda(p'). \tag{9.19}$$

Using the following relations [252, 253]

$$\Lambda(p')\gamma^\tau\gamma_5\Lambda(p') = 2M_Y\left(g^{\tau\sigma} - \frac{p'^\tau p'^\sigma}{M_Y^2}\right)\Lambda(p')\gamma_\sigma\gamma_5 \tag{9.20}$$

and

$$\Lambda(p')\Lambda(p') = 2M_Y\Lambda(p'), \tag{9.21}$$

ξ^τ defined in Eq. 9.18 may be rewritten as:

$$\xi^\tau = \left(g^{\tau\sigma} - \frac{p'^\tau p'^\sigma}{M_Y^2}\right)\frac{\mathcal{L}^{\alpha\beta}\mathrm{Tr}\left[\gamma_\sigma\gamma_5\Lambda(p')J_\alpha\Lambda(p)\tilde{J}_\beta\right]}{\mathcal{L}^{\alpha\beta}\mathrm{Tr}\left[\Lambda(p')J_\alpha\Lambda(p)\tilde{J}_\beta\right]}. \tag{9.22}$$

Note that in Eq. 9.22, ξ^τ is manifestly orthogonal to p'^τ i.e. $p'\cdot\xi = 0$. Moreover, the denominator is directly related to the differential cross section given in Eq. 9.15.

With $\mathcal{J}^{\alpha\beta}$ and $\mathcal{L}_{\alpha\beta}$ given in Eq. 9.14, an expression for ξ^τ is obtained. In the lab frame where the initial nucleon is at rest, the polarization vector ξ is calculated to be

$$\frac{d\sigma}{dQ^2}\xi = \frac{G_F^2\sin^2\theta_c}{8\pi\ MM_Y E_{\bar{\nu}_\mu}^2}\left[(\mathbf{k}+\mathbf{k}')M_Y\mathcal{A}(Q^2,E_{\bar{\nu}_\mu}) + (\mathbf{k}-\mathbf{k}')\mathcal{B}(Q^2,E_{\bar{\nu}_\mu})\right], \tag{9.23}$$

where the expressions of $\mathcal{A}(Q^2, E_{\bar{\nu}_\mu})$ and $\mathcal{B}(Q^2, E_{\bar{\nu}_\mu})$ are given in the appendix.

From Eq. 9.23, it follows that the polarization lies in scattering plane defined by $\mathbf{k}$ and $\mathbf{k}'$, and there is no component of polarization in a direction orthogonal to the scattering plane. This is a consequence of T–invariance which makes the transverse polarization in a direction perpendicular to the reaction plane to vanish [85, 87]. We now expand the polarization vector ξ along two orthogonal directions, $\mathbf{e_L}$ and $\mathbf{e_P}$ in the reaction plane corresponding to parallel and perpendicular directions to the momentum of hyperon[1] i.e.

$$\mathbf{e_L} = \frac{\mathbf{p}'}{|\mathbf{p}'|} = \frac{\mathbf{q}}{|\mathbf{q}|}, \qquad \mathbf{e_P} = \mathbf{e_L} \times \mathbf{e_T}, \qquad \mathbf{e_T} = \frac{\mathbf{k} \times \mathbf{k}'}{|\mathbf{k} \times \mathbf{k}'|}, \tag{9.24}$$

and write

$$\xi = \xi_\mathbf{P} \mathbf{e_P} + \xi_\mathbf{L} \mathbf{e_L}, \tag{9.25}$$

such that the longitudinal and perpendicular components of polarization vector(ξ) in the lab frame are given by

$$\xi_L(Q^2) = \xi \cdot \mathbf{e_L}, \qquad \xi_\mathbf{P}(\mathbf{Q^2}) = \xi \cdot \mathbf{e_P}. \tag{9.26}$$

From Eq. 9.26, the longitudinal and perpendicular components of polarization vector $P_L(Q^2)$ and $P_P(Q^2)$ defined in the rest frame of recoil nucleon are given by [252]:

$$P_L(Q^2) = \frac{M_Y}{E_{p'}} \xi_L(Q^2), \qquad P_P(Q^2) = \xi_P(Q^2), \tag{9.27}$$

where $\frac{M_Y}{E_{p'}}$ is the Lorentz boost factor along $\mathbf{p}'$. With the help of Eqs. 9.23, 9.24, 9.26 and 9.27, the longitudinal component $P_L(Q^2)$ is calculated to be

$$\frac{d\sigma}{dQ^2} P_L(Q^2) = \frac{G_F^2 \sin^2\theta_c}{8\pi |\mathbf{q}| E_{p'} M\, E_{\bar{\nu}_\mu}^2} \left[\left(E_{\bar{\nu}_\mu}^2 - E_\mu^2 + m_\mu^2 \right) M_Y \mathcal{A}(Q^2, E_{\bar{\nu}_\mu}) + |\mathbf{q}|^2 \mathcal{B}(Q^2, E_{\bar{\nu}_\mu}) \right], \tag{9.28}$$

where in the lab frame $E_{p'} = \sqrt{|\mathbf{q}^2| + M_Y^2}$. Similarly, the perpendicular component $P_P(Q^2)$ of the polarization 3-vector is given as

$$\frac{d\sigma}{dQ^2} P_P(Q^2) = -\frac{G_F^2 \sin^2\theta_c}{4\pi} \frac{|\mathbf{k}'|}{|\mathbf{q}|} \frac{\mathcal{A}(Q^2, E_{\bar{\nu}_\mu}) \sin\theta}{M E_{\bar{\nu}_\mu}}, \tag{9.29}$$

where θ is the scattering angle in the lab frame.

[1] It should be noted that our $\mathbf{e_P}$ is defined as in Bilenky and Christova [252] and is opposite to the sign used by Erriquez et al. [73].

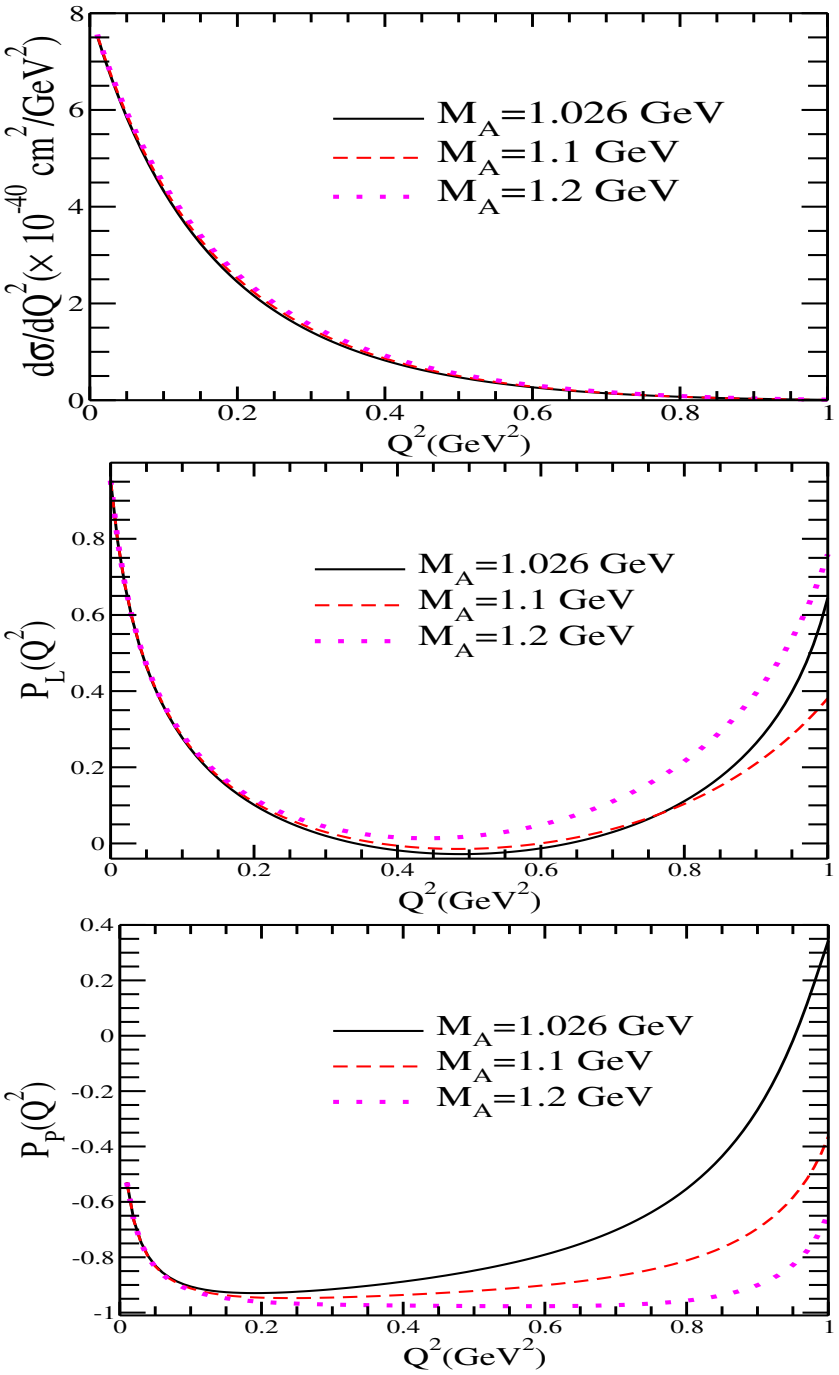

Figure 9.2: $\frac{d\sigma}{dQ^2}$, $P_L(Q^2)$ and $P_P(Q^2)$ vs Q^2 for the process $\bar{\nu}_\mu p \to \mu^+\Lambda$ at $E_{\bar{\nu}_\mu} = 1$ GeV for different values of M_A used in $g_1^{p\Lambda}(Q^2)$ viz. 1.026 GeV(solid line), 1.1 GeV(dashed) and 1.2 GeV(dotted line) with $m_\mu = 0$. $f_1^{p\Lambda}(Q^2)$, $f_2^{p\Lambda}(Q^2)$ and $g_1^{p\Lambda}(Q^2)$ from Table-9.1 and BBBA05 parameterization for nucleon form factor are used.

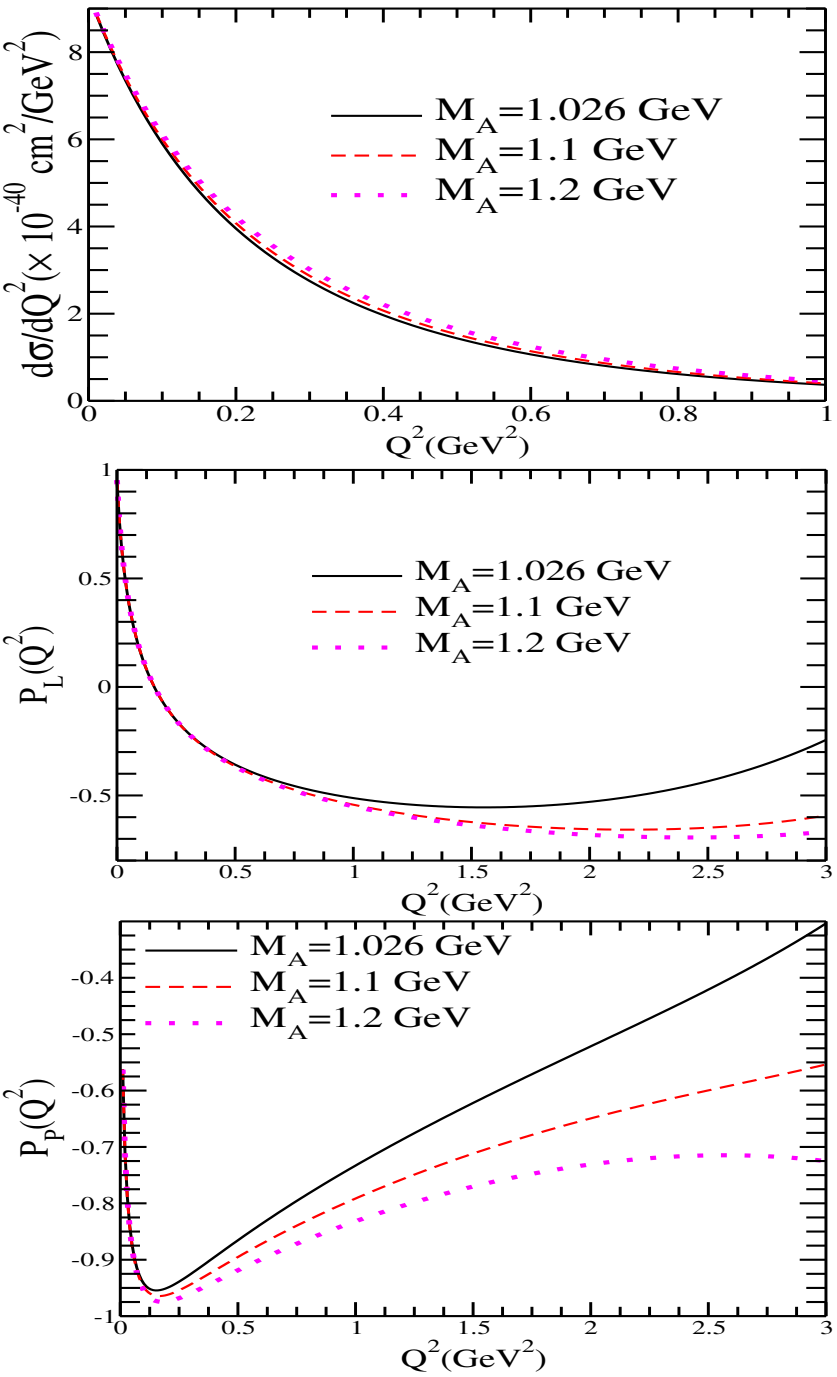

Figure 9.3: $\frac{d\sigma}{dQ^2}$, $P_L(Q^2)$ and $P_P(Q^2)$ vs Q^2 for the process $\bar{\nu}_\mu p \to \mu^+ \Lambda$ at $E_{\bar{\nu}_\mu}$ = 3 GeV for different values of M_A in $g_1^{p\Lambda}(Q^2)$. Lines and points have the same meaning as in Fig. 9.2.

Inside the nucleus, target nucleon is not at rest but moves with Fermi momentum, i.e. $\mathbf{p} \neq 0$. Because of this the polarization components of the final hyperon

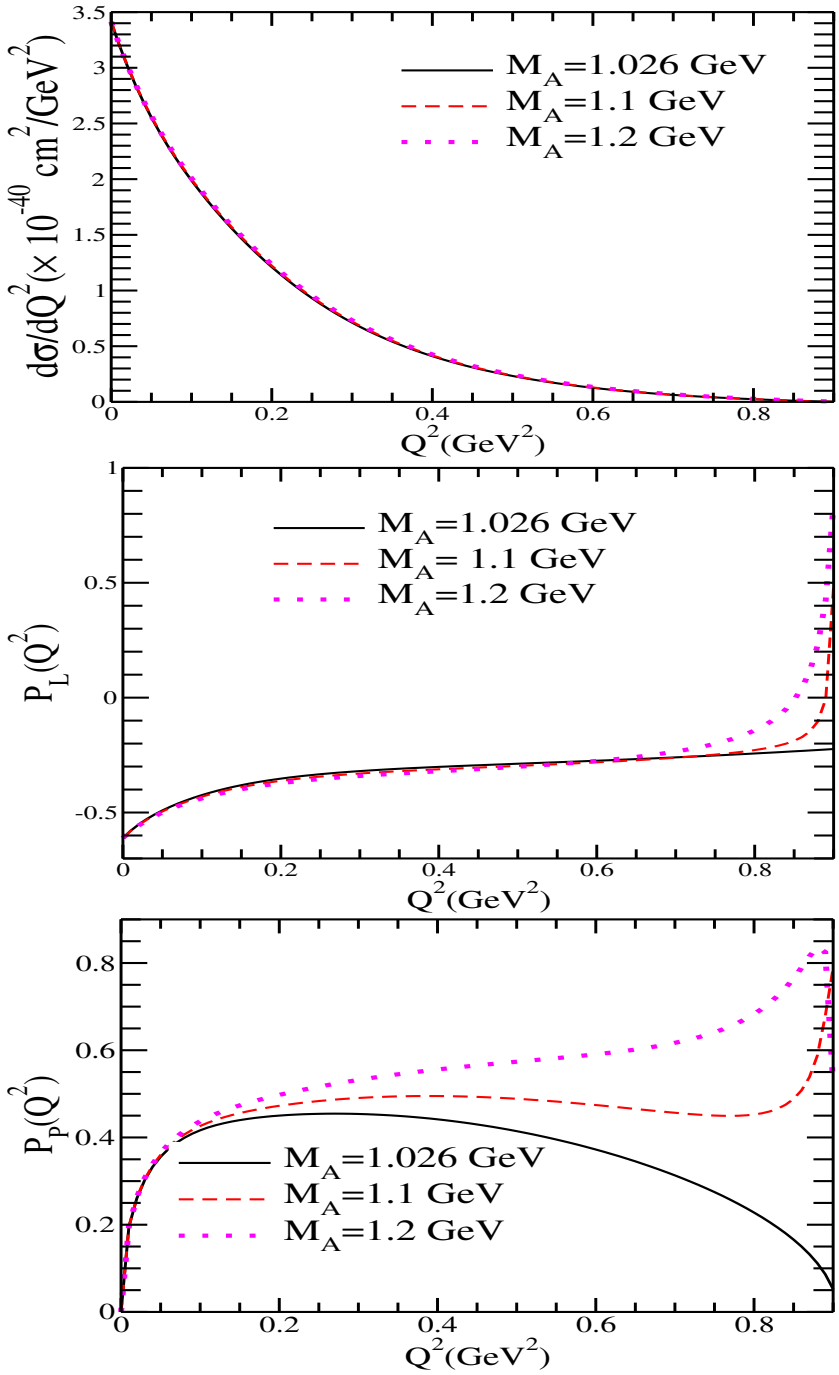

Figure 9.4: $\frac{d\sigma}{dQ^2}$, $P_L(Q^2)$ and $P_P(Q^2)$ vs Q^2 for the process $\bar{\nu}_\mu n \to \mu^+\Sigma^-$ at $E_{\bar{\nu}_\mu}$ = 1 GeV for different values of M_A in $g_1^{n\Sigma^-}(Q^2)$. Lines and points have the same meaning as in Fig. 9.2.

get modified to:

$$\left[P_{L,P}(Q^2)\right]_{\bar{\nu}_\mu A} = 2\int d^3r \int \frac{d^3p}{(2\pi)^3} n_N(p,r) \left[P_{L,P}(Q^2,\mathbf{p})\right]_{\bar{\nu}_\mu N}, \tag{9.30}$$

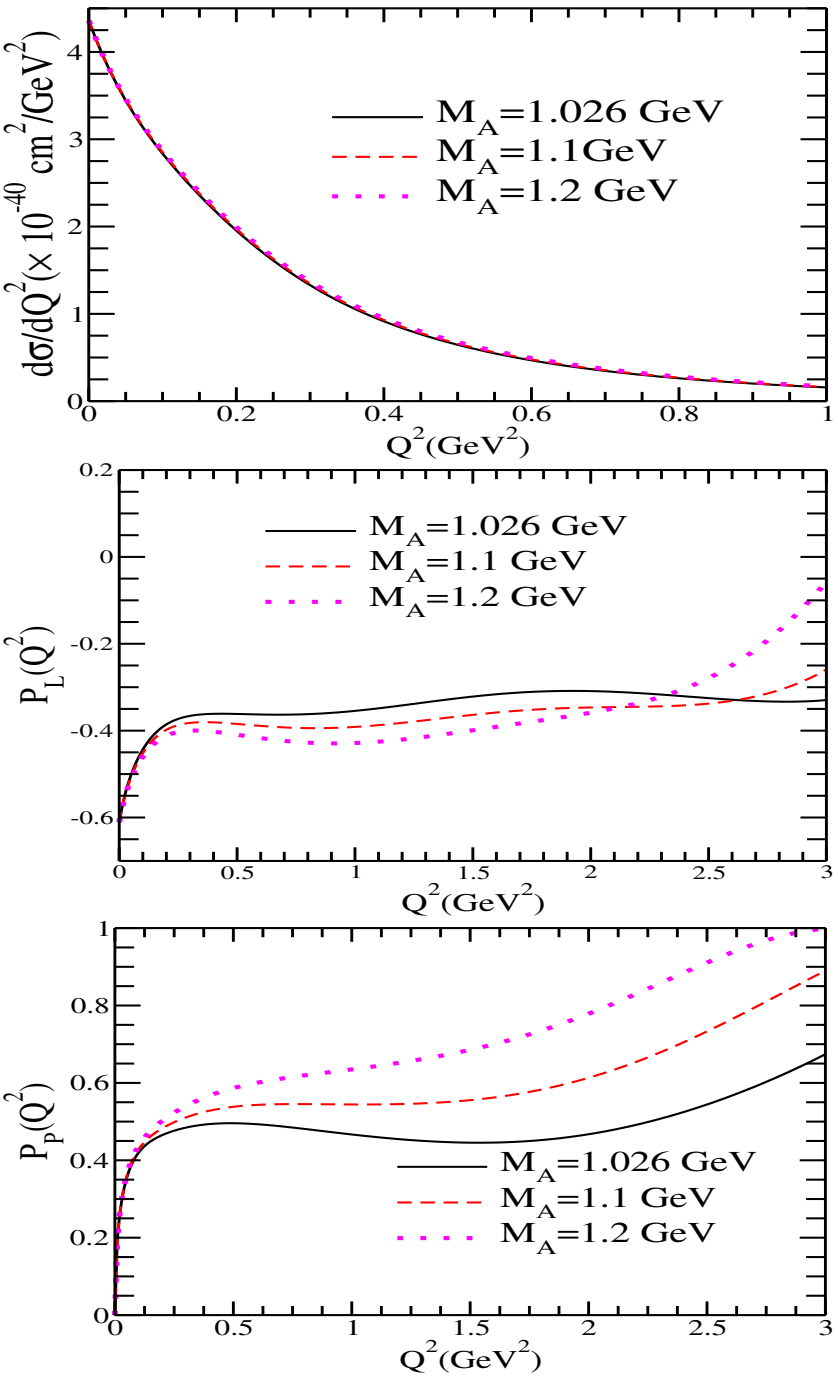

Figure 9.5: $\frac{d\sigma}{dQ^2}$, $P_L(Q^2)$ and $P_P(Q^2)$ vs Q^2 for the process $\bar{\nu}_\mu n \to \mu^+\Sigma^-$ at $E_{\bar{\nu}_\mu}=$ 3 GeV for different values of M_A in $g_1^{n\Sigma^-}(Q^2)$. Lines and points have the same meaning as in Fig. 9.2.

with longitudinal component:

$$P_L(Q^2,\mathbf{p}) = \frac{M_Y}{E_{p'}}\frac{G_F^2\sin^2\theta_c}{2}\frac{1}{|\mathcal{M}|^2}\frac{1}{|\mathbf{p}+\mathbf{q}|}\Big[\alpha(Q^2,\mathbf{p})\left(\mathbf{k}\cdot\mathbf{p}+E_{\bar{\nu}_\mu}^2-\mathbf{k}\cdot\mathbf{k}'\right) + \beta(Q^2,\mathbf{p})\left(\mathbf{k}'\cdot\mathbf{p}+\mathbf{k}\cdot\mathbf{k}'-|\mathbf{k}'|^2\right)+\eta(Q^2,\mathbf{p})\left(|\mathbf{p}|^2+\mathbf{p}\cdot\mathbf{q}\right)\Big], \quad (9.31)$$

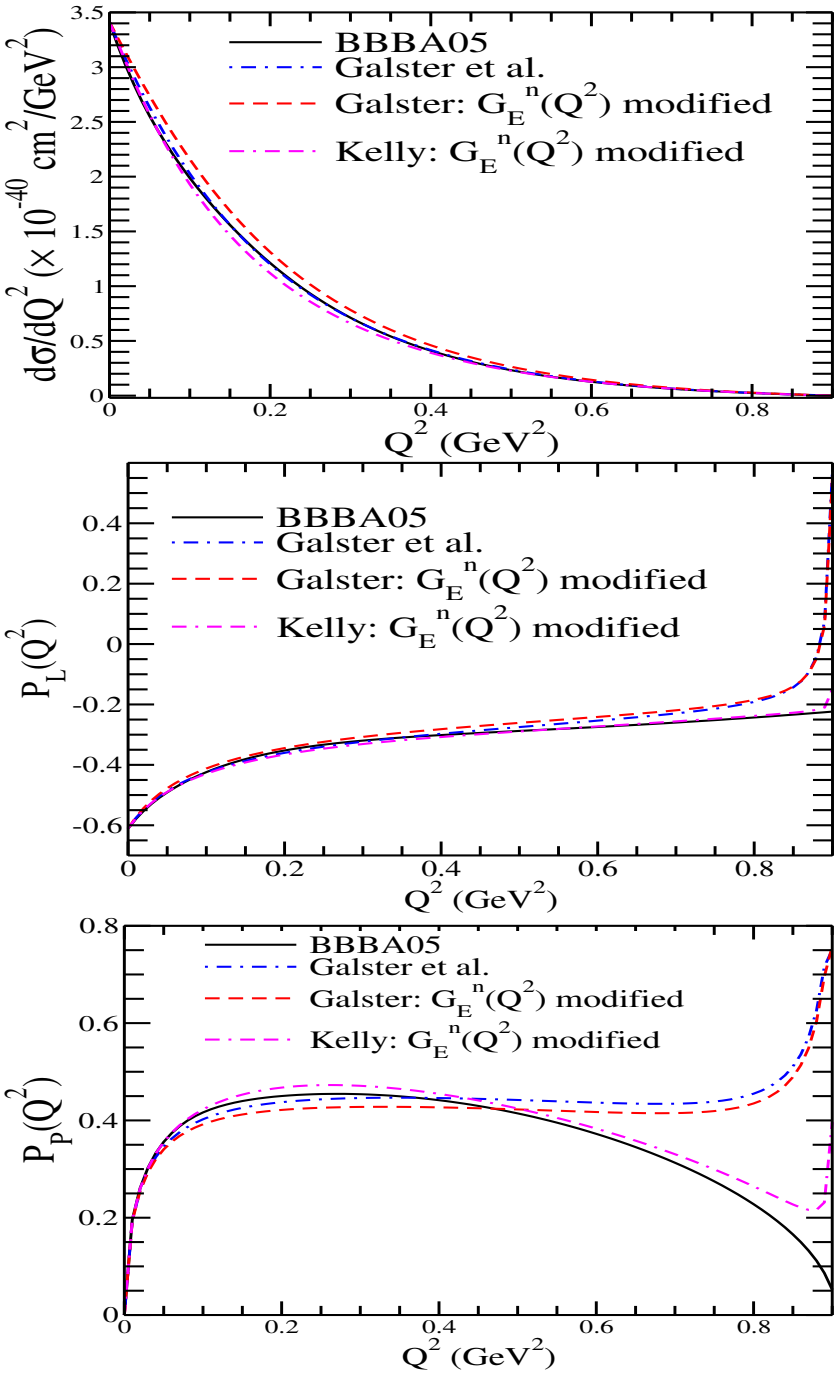

Figure 9.6: $\frac{d\sigma}{dQ^2}$, $P_L(Q^2)$ and $P_P(Q^2)$ vs Q^2 at $E_{\bar{\nu}_\mu}$= 1 GeV for $\bar{\nu}_\mu n \rightarrow \mu^+\Sigma^-$ process. The results are presented with the nucleon form factors using BBBA05 [151](solid line), Galster et al. [150](dashed-dotted line), modified form of $G_E^n(Q^2)$ in Galster parameterization [254](dashed line) and modified form of $G_E^n(Q^2)$ in Kelly parameterization [255](double dashed-dotted line).

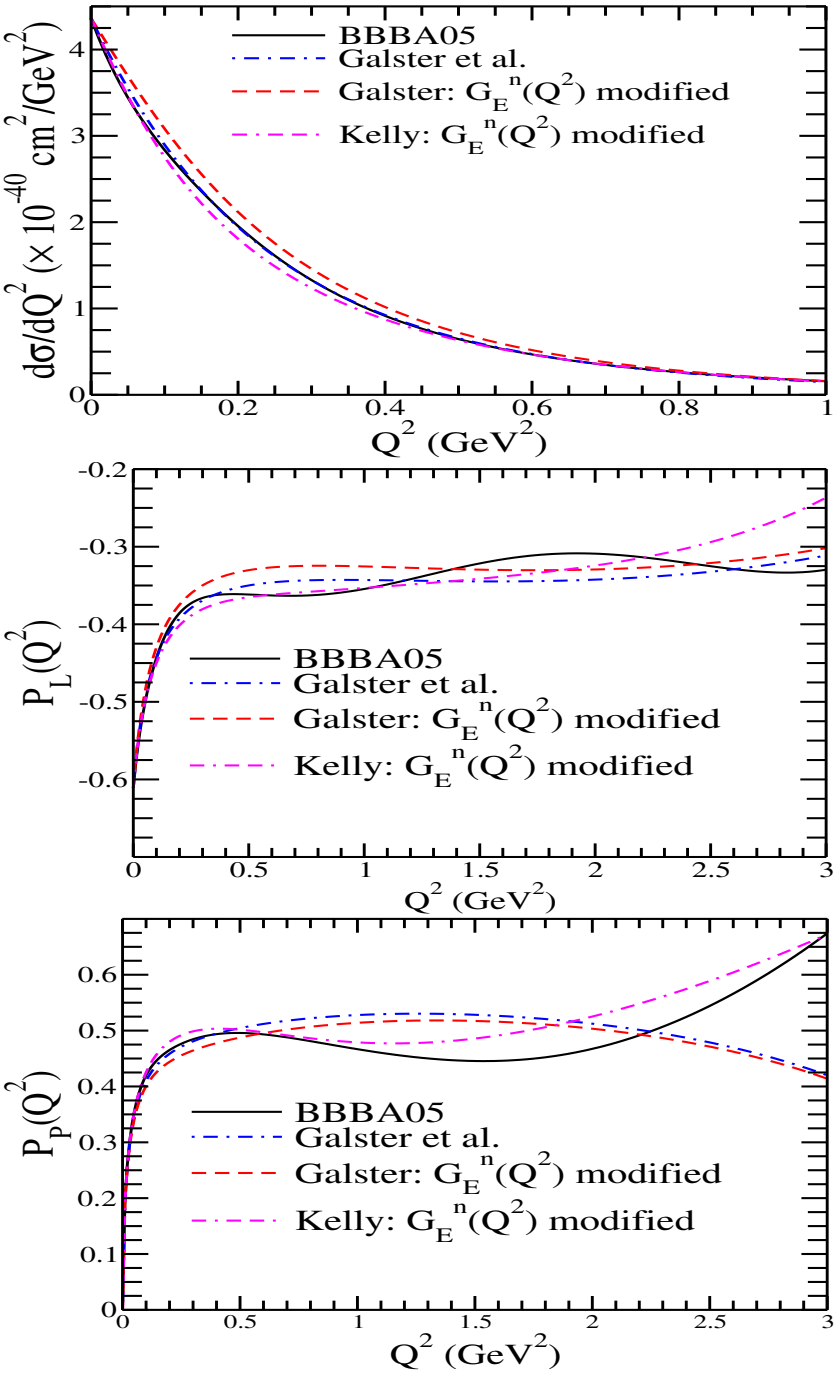

Figure 9.7: $\frac{d\sigma}{dQ^2}$, $P_L(Q^2)$ and $P_P(Q^2)$ vs Q^2 at $E_{\bar{\nu}_\mu} = 3$ GeV for $\bar{\nu}_\mu n \to \mu^+\Sigma^-$ process. Lines and points have the same meaning as Fig. 9.6.

and perpendicular component,

$$
\begin{aligned}
P_P(Q^2,\mathbf{p}) &= \frac{G_F^2\sin^2\theta_c}{2}\frac{1}{|\mathcal{M}|^2}\frac{1}{|\mathbf{p}+\mathbf{q}||\mathbf{k}||\mathbf{k}'|\sin\theta}\Big[\left(\mathbf{k}'\cdot\mathbf{p}+\mathbf{k}\cdot\mathbf{k}'-|\mathbf{k}'|^2\right)\{\alpha(Q^2,\mathbf{p})E_{\bar{\nu}_\mu}^2 \\
&+ \beta(Q^2,\mathbf{p})\mathbf{k}\cdot\mathbf{k}'+\eta(Q^2,\mathbf{p})\mathbf{k}\cdot\mathbf{p}\}-\left(\mathbf{k}\cdot\mathbf{p}+E_{\bar{\nu}_\mu}^2-\mathbf{k}\cdot\mathbf{k}'\right)\{\alpha(Q^2,\mathbf{p})\mathbf{k}\cdot\mathbf{k}' \\
&+ \beta(Q^2,\mathbf{p})|\mathbf{k}'|^2+\eta(Q^2,\mathbf{p})\mathbf{k}'\cdot\mathbf{p}\}\Big]\,. \qquad (9.32)
\end{aligned}
$$

The expressions of $\alpha(Q^2, \mathbf{p})$, $\beta(Q^2, \mathbf{p})$ and $\eta(Q^2, \mathbf{p})$ are given in the Appendix-B

9.3 Results and Discussion

9.3.1 Differential cross section $\frac{d\sigma}{dQ^2}$ and polarization components $P_L(Q^2)$ and $P_P(Q^2)$ for nucleon target

We have used Eqs. 9.15, 9.28 and 9.29 to numerically evaluate the differential cross section $\frac{d\sigma}{dQ^2}$, and longitudinal $P_L(Q^2)$ and perpendicular $P_P(Q^2)$ components of the polarization of hyperons in the quasielastic antineutrino reactions given in Eq. 9.1. For the vector and axial vector form factors we have used the expressions of $f_i^{NY}(Q^2)(i = 1, 2)$ and $g_1^{NY}(Q^2)$ given in Table-9.1 along with the pseudoscalar form factor $g_3^{NY}(Q^2)$ given in Eqs. 9.8 and 9.9. The Q^2 dependence of the nucleon form factors $f_{1,2}^{p,n}$ is taken from the parameterization of BBBA05 [151]. A dipole parameterization for the axial vector form factor $g_A(Q^2)$ given in Eq. 9.7 has been used for $g_{1,3}^{NY}(Q^2)$ with $g_A(0) = 1.2723$ [242], $x = 0.364$ [70] and axial dipole mass M_A = 1.026 GeV, 1.1 GeV and 1.2 GeV as mentioned in each figure.

In Fig. 9.2, we present the results of $\frac{d\sigma}{dQ^2}$, $P_L(Q^2)$ and $P_P(Q^2)$ for the reaction $\bar{\nu}_\mu p \to \mu^+ \Lambda$ at $E_{\bar{\nu}_\mu}$ = 1 GeV and in Fig. 9.3 at $E_{\bar{\nu}_\mu}$ = 3 GeV. We see that while there is very little sensitivity of $\frac{d\sigma}{dQ^2}$ to the variation of M_A, the components of polarization $P_L(Q^2)$ and $P_P(Q^2)$ are quite sensitive to the value of M_A specially in the region $Q^2 > 0.4$ GeV^2. It should, therefore, be possible to independently determine the value of M_A from the polarization measurements. However, the present available data on the total cross section for the single hyperon production are consistent with M_A = 1.026 GeV [96]. At higher values of Q^2, the sensitivity of $P_L(Q^2)$ and $P_P(Q^2)$ to M_A increases, but quantitatively, the cross section $\frac{d\sigma}{dQ^2}$ decreases, making the number of events quite small and the measurement of polarization observables becomes difficult. We have also studied the sensitivity of our results for $\frac{d\sigma}{dQ^2}$, $P_L(Q^2)$ and $P_P(Q^2)$ to various other param-

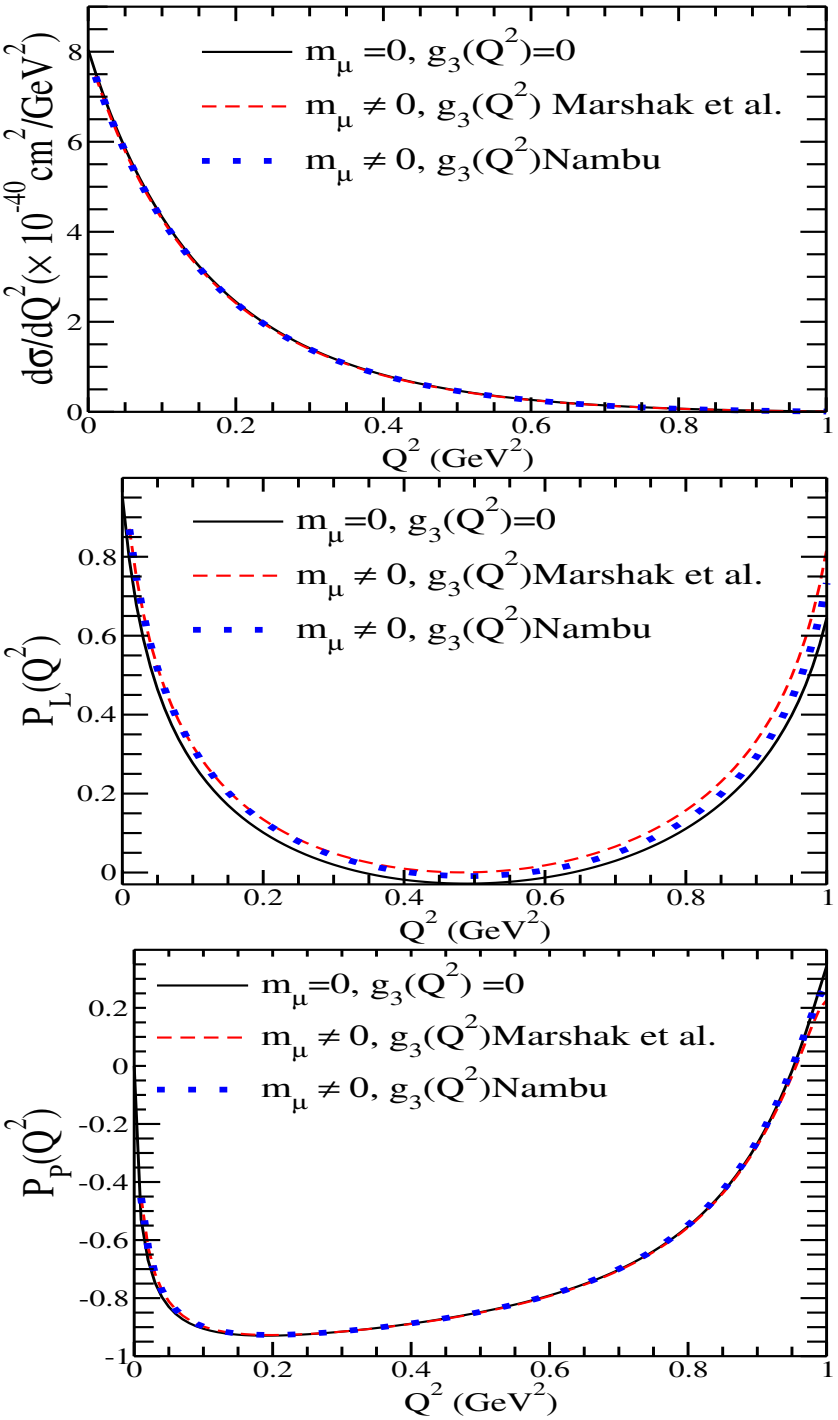

Figure 9.8: $\frac{d\sigma}{dQ^2}$, $P_L(Q^2)$ and $P_P(Q^2)$ vs Q^2 ($M_A = 1.026$ GeV) for the process $\bar{\nu}_\mu p \to \mu^+ \Lambda$ at $E_{\bar{\nu}_\mu} = 1$ GeV using $f_1^{p\Lambda}(Q^2)$, $f_2^{p\Lambda}(Q^2)$, $g_1^{p\Lambda}(Q^2)$ from Table-9.1 and BBBA05 [151] parameterization for the nucleon form factors, with $m_\mu = 0$ and $g_3^{p\Lambda} = 0$(solid line), $m_\mu \neq 0$ and $g_3^{p\Lambda} \neq 0$ from Marshak et al. [86] given in Eq. 9.8(dashed line) and $m_\mu \neq 0$ and $g_3^{p\Lambda} \neq 0$ from Nambu [243] given in Eq. 9.9(dotted line).

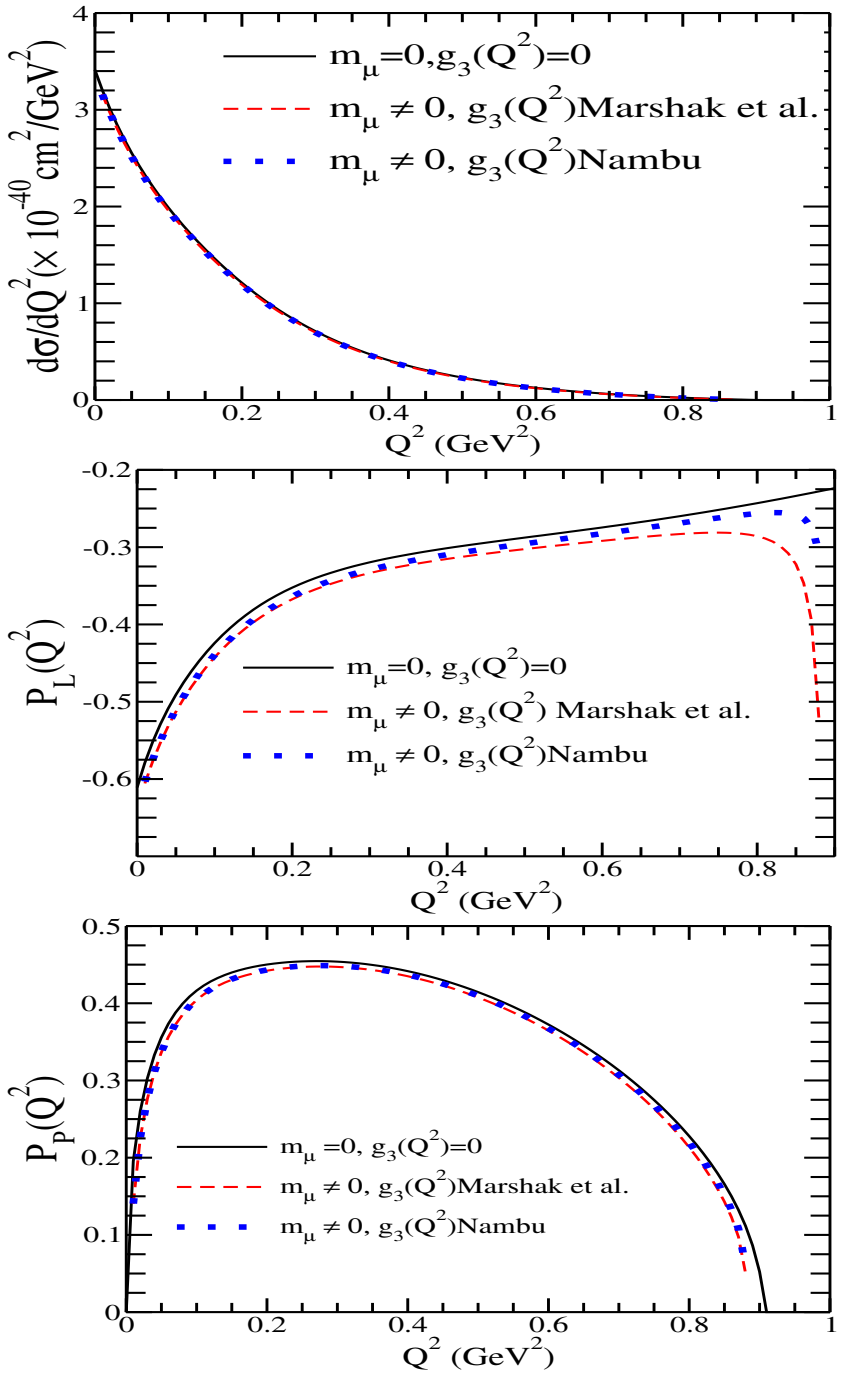

Figure 9.9: $\frac{d\sigma}{dQ^2}$, $P_L(Q^2)$ and $P_P(Q^2)$ vs Q^2 at $E_{\bar{\nu}_\mu}$ = 1 GeV for $\bar{\nu}_\mu n \to \mu^+\Sigma^-$ process. Lines and points have the same meaning as in Fig. 9.8.

eterizations of Q^2 dependence of the nucleon form factors $f_{1,2}^{p,n}(Q^2)$ available in literature [151, 150, 254, 255, 153, 152, 154, 257]. It is found that at $E_{\bar{\nu}_\mu}$ = 1 GeV, the results for $\frac{d\sigma}{dQ^2}$, $P_L(Q^2)$ and $P_P(Q^2)$ are not very sensitive to the choice of other parameterizations of vector form factors in the case of $\bar{\nu}_\mu p \to \mu^+\Lambda$ and

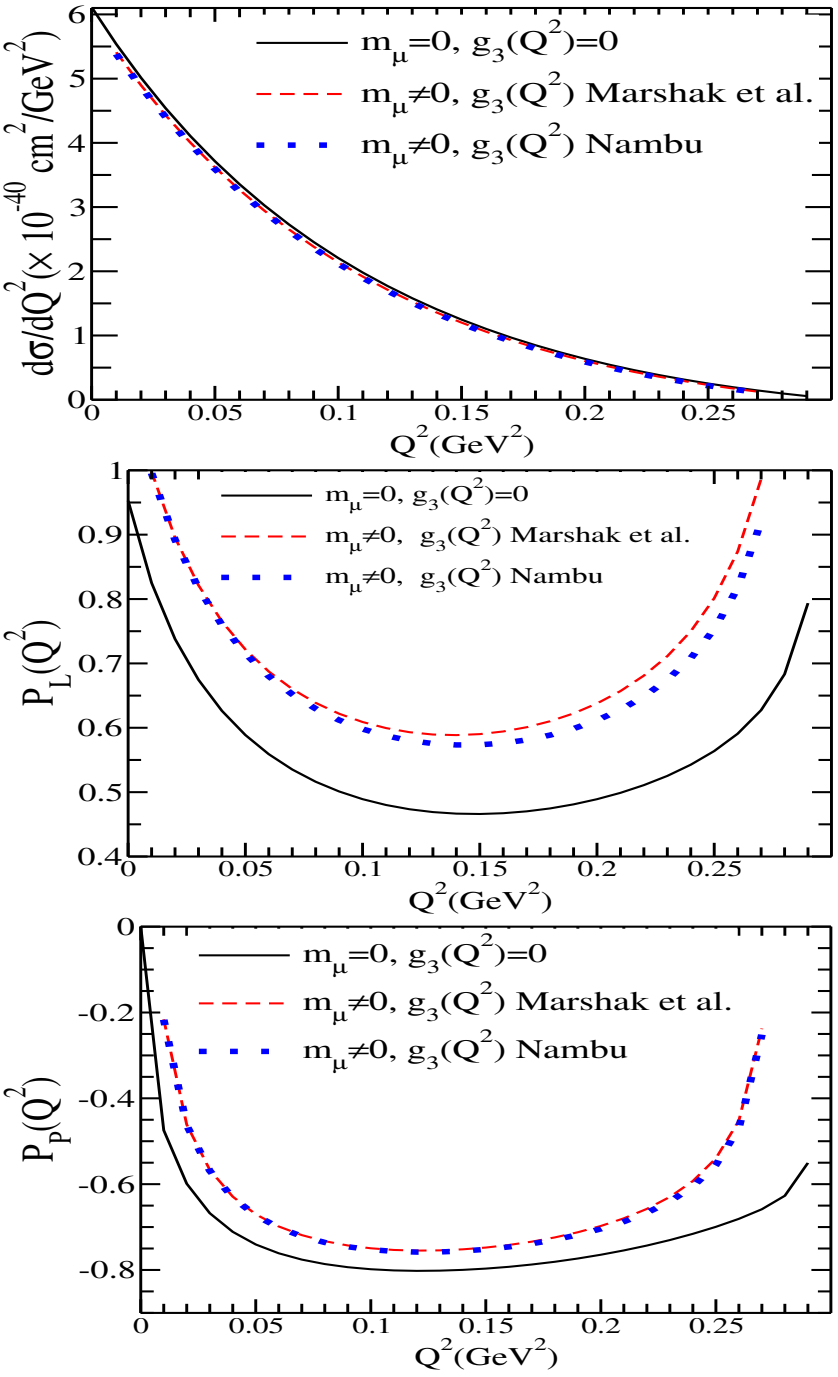

Figure 9.10: $\frac{d\sigma}{dQ^2}$, $P_L(Q^2)$ and $P_P(Q^2)$ vs Q^2 for the process $\bar{\nu}_\mu p \to \mu^+\Lambda$ at $E_{\bar{\nu}_\mu}$ = 0.5 GeV. Lines and points have the same meaning as in Fig. 9.8.

are not shown in these figures.

In Figs. 9.4 and 9.5, we present the results of $\frac{d\sigma}{dQ^2}$, $P_L(Q^2)$ and $P_P(Q^2)$ for the reaction $\bar{\nu}_\mu n \to \mu^+\Sigma^-$ at $E_{\bar{\nu}_\mu} = 1$ GeV and $E_{\bar{\nu}_\mu} = 3$ GeV, respectively. The results

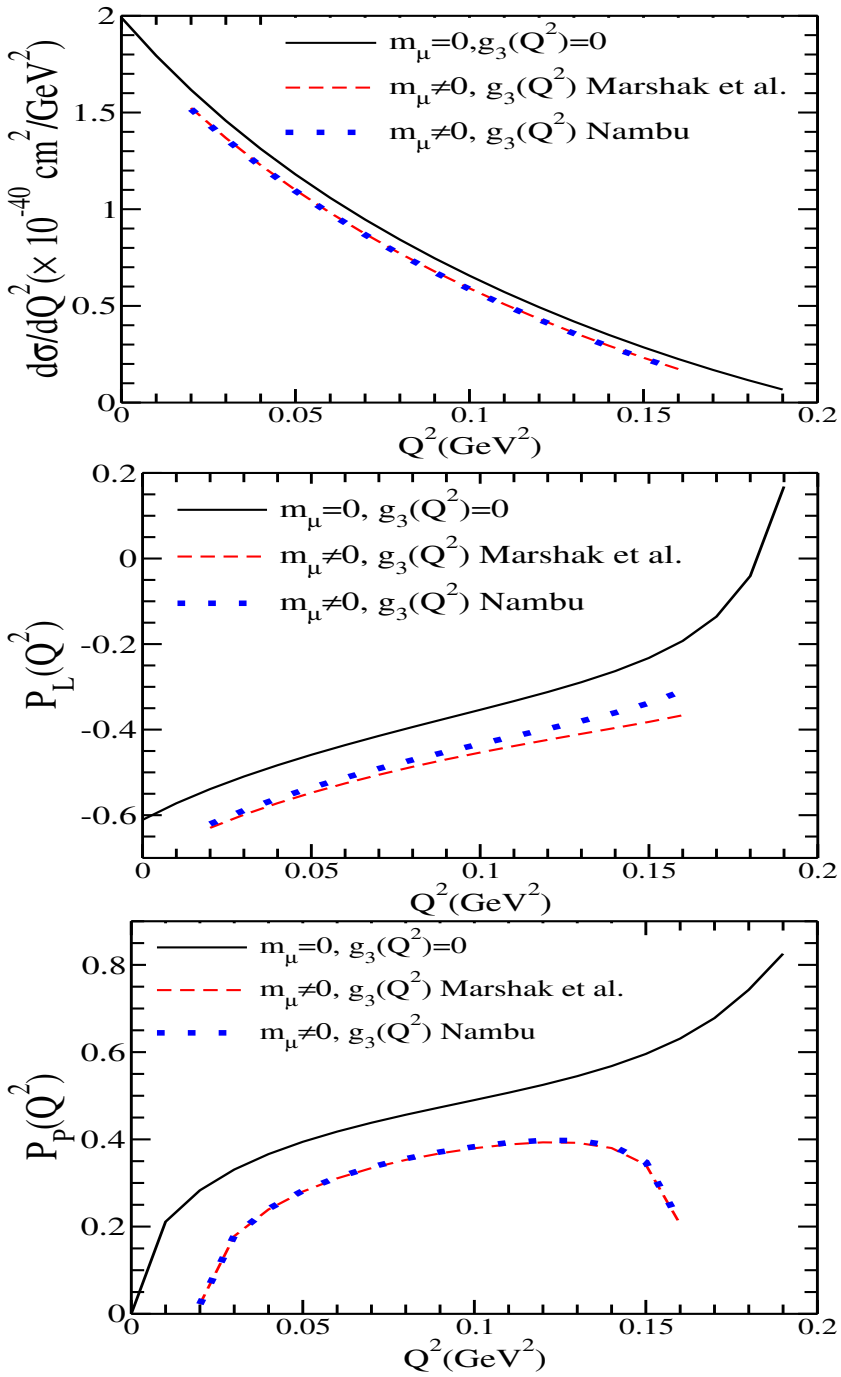

Figure 9.11: $\frac{d\sigma}{dQ^2}$, $P_L(Q^2)$ and $P_P(Q^2)$ vs Q^2 for the process $\bar{\nu}_\mu n \to \mu^+\Sigma^-$ at $E_{\bar{\nu}_\mu} = 0.5$ GeV. Lines and points have the same meaning as in Fig. 9.8.

for $\frac{d\sigma}{dQ^2}$, $P_L(Q^2)$ and $P_P(Q^2)$ are qualitatively similar to $\bar{\nu}_\mu p \to \mu^+\Lambda$ as far as the sensitivity to M_A is concerned. However, the differential cross sections are smaller and the components of the hyperon polarization are of the same order as in reaction $\bar{\nu}_\mu p \to \mu^+\Lambda$ but slightly higher in magnitude. We have chosen to show the results

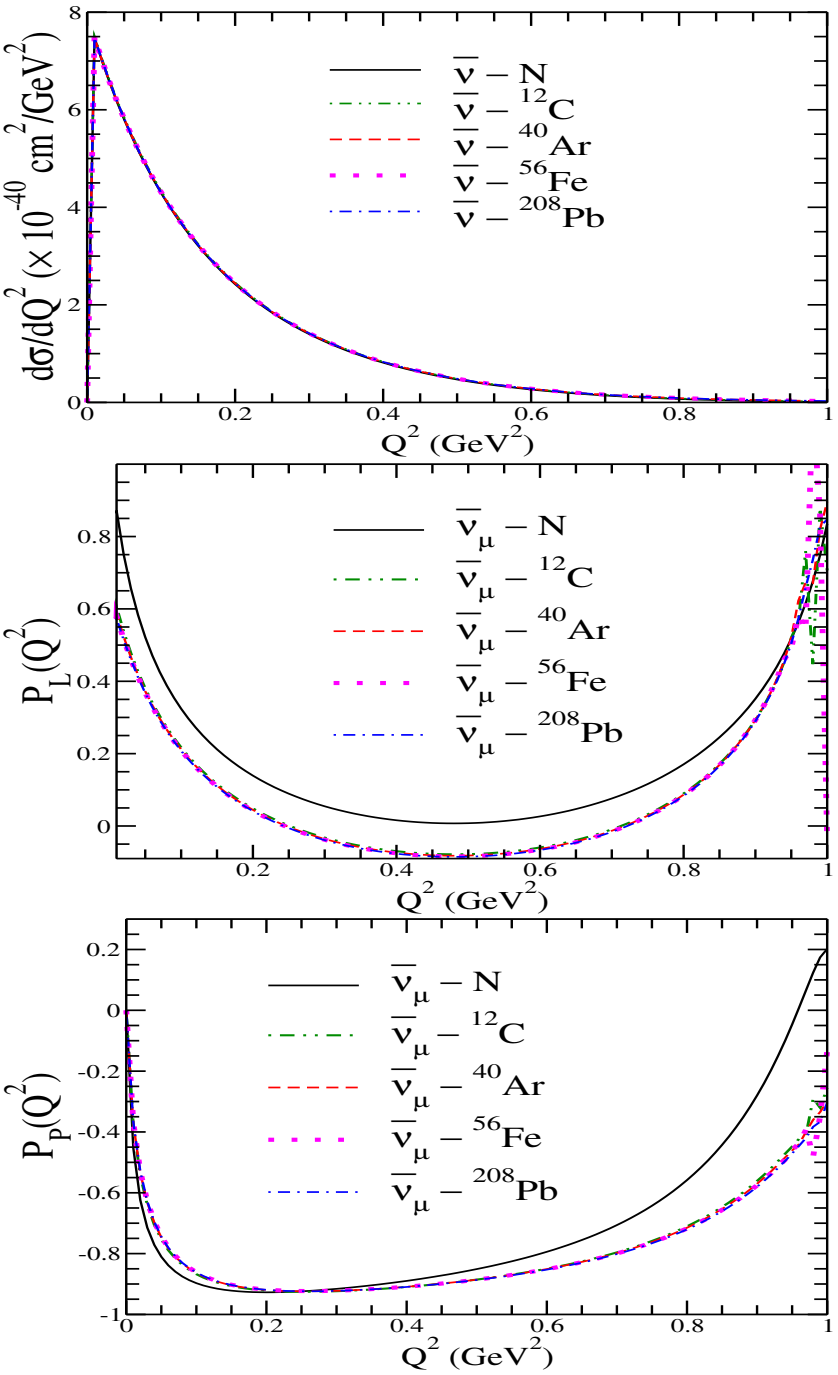

Figure 9.12: $\frac{d\sigma}{dQ^2}$, $P_L(Q^2)$ and $P_P(Q^2)$ vs Q^2 for the process $\bar{\nu}_\mu p \to \mu^+\Lambda$ at $E_{\bar{\nu}_\mu}$ = 1 GeV for free nucleon(solid line) and different nuclei per interacting particle viz. ^{12}C(dashed-double dotted), ^{40}Ar(dashed line), ^{56}Fe(dotted line) and ^{208}Pb(dashed-dotted line) with $m_\mu \neq 0$, M_A= 1.026 GeV. We have used $f_1^{p\Lambda}(Q^2)$, $f_2^{p\Lambda}(Q^2)$ and $g_1^{p\Lambda}(Q^2)$ from Table 9.1 and BBBA05 parameterization for nucleon form factors.

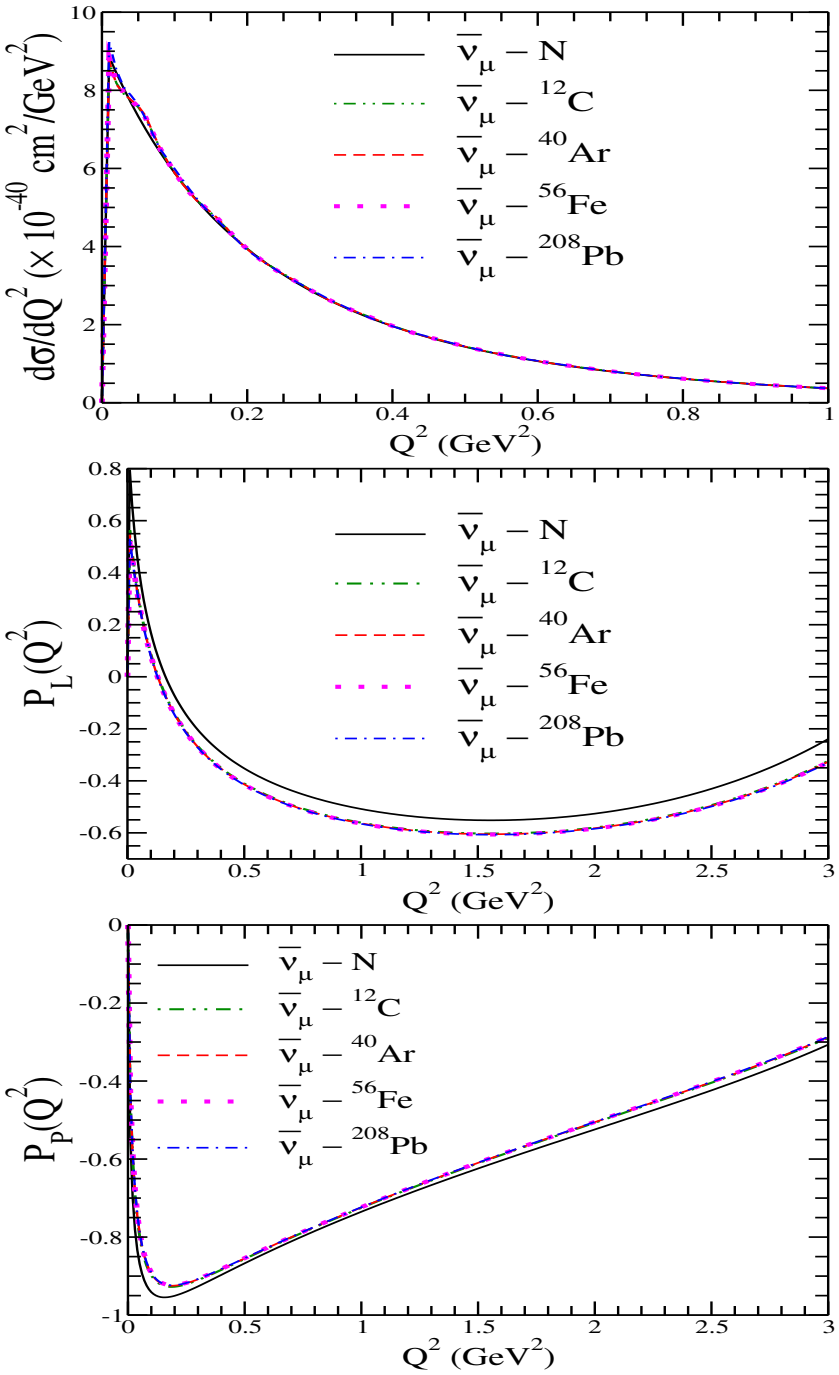

Figure 9.13: $\frac{d\sigma}{dQ^2}$, $P_L(Q^2)$ and $P_P(Q^2)$ vs Q^2 for the process $\bar{\nu}_\mu p \to \mu^+ \Lambda$ at $E_{\bar{\nu}_\mu}$ = 3 GeV. Lines and points have the same meaning as Fig. 9.12.

for $\bar{\nu}_\mu n \to \mu^+ \Sigma^-$ as the cross section for this process is larger by a factor of 2 as compared to $\bar{\nu}_\mu p \to \mu^+ \Sigma^0$. In the case of $\bar{\nu}_\mu n \to \mu^+ \Sigma^-$ process, the results for $\frac{d\sigma}{dQ^2}$, $P_L(Q^2)$ and $P_P(Q^2)$ are found to be sensitive to the vector form factors specially to the neutron form factors $f_{1,2}^n(Q^2)$ occurring in the expressions of $f_{1,2}^{n\Sigma^-}$(see Table-

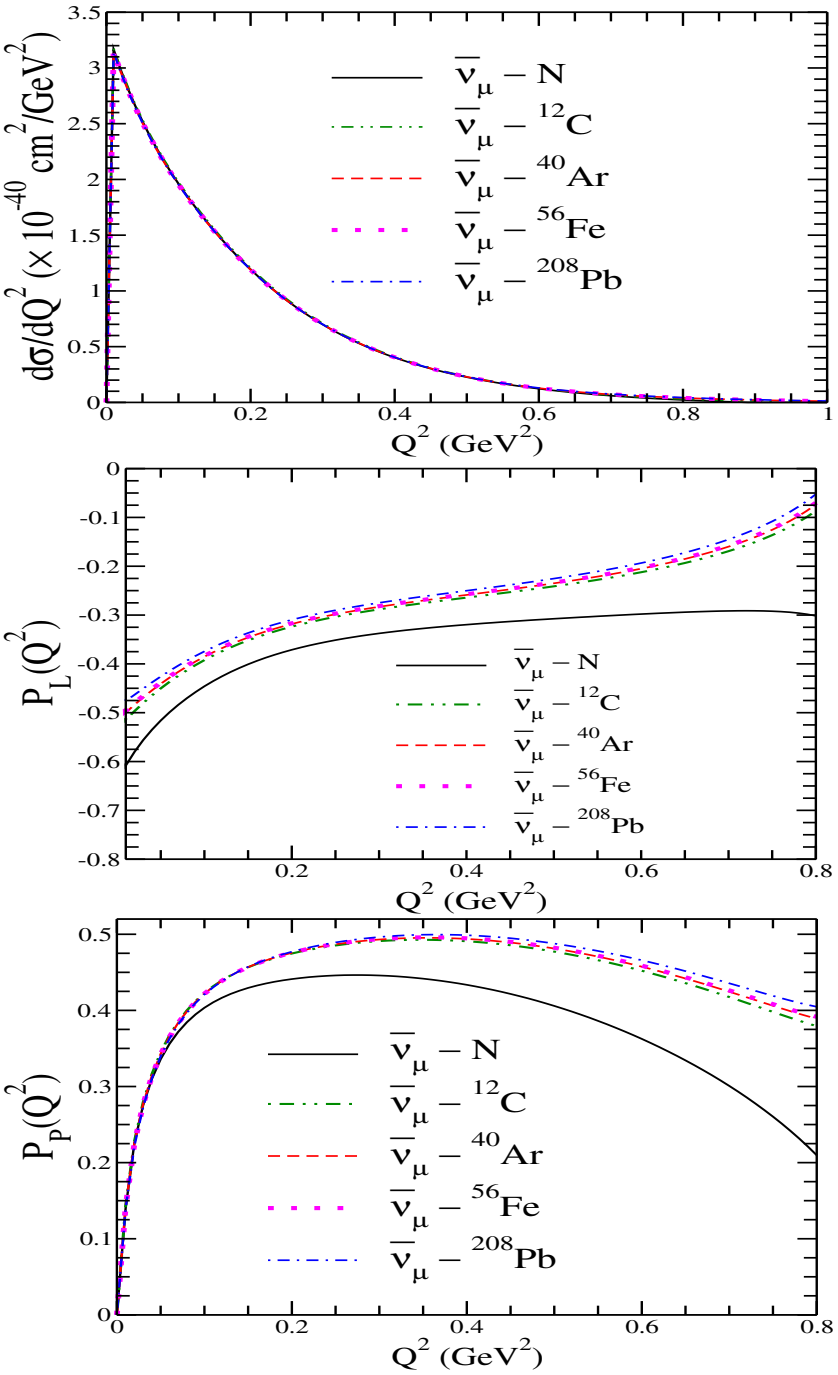

Figure 9.14: $\frac{d\sigma}{dQ^2}$, $P_L(Q^2)$ and $P_P(Q^2)$ vs Q^2 for the process $\bar{\nu}_\mu n \to \mu^+\Sigma^-$ at $E_{\bar{\nu}_\mu}$ = 1 GeV. Lines and points have the same meaning as Fig. 9.12.

9.1). This arises mainly due to the presence of charge form factor of neutron $G_E^n(Q^2)$ in the definition of $f_{1,2}^n(Q^2)$. We have, therefore, studied the sensitivity of our results to various parameterizations of charge form factor of neutron available in literature, and given in Appendix-A.1. We show in Figs. 9.6 ($E_{\bar{\nu}_\mu}$ = 1 GeV) and

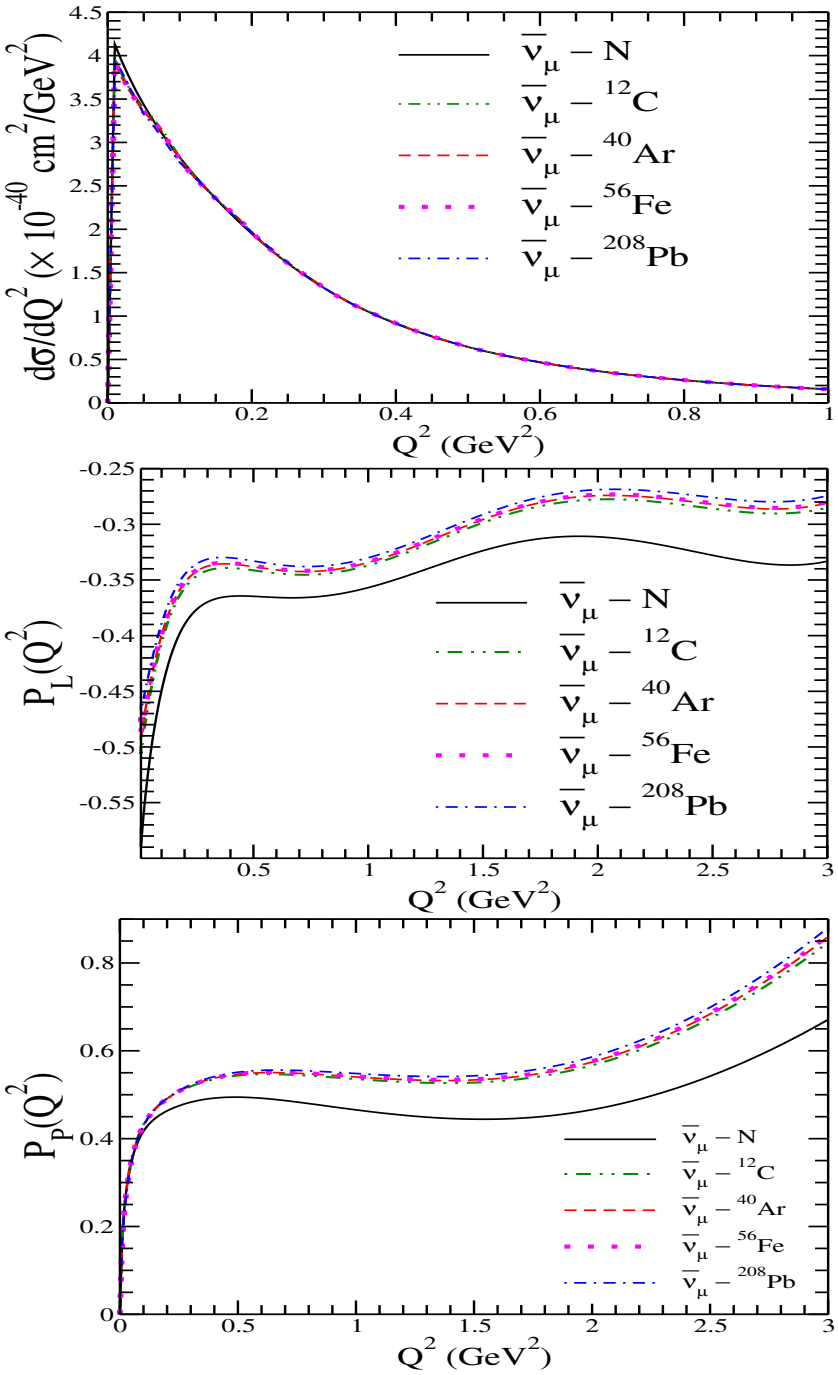

Figure 9.15: $\frac{d\sigma}{dQ^2}$, $P_L(Q^2)$ and $P_P(Q^2)$ vs Q^2 for the process $\bar{\nu}_\mu n \to \mu^+\Sigma^-$ at $E_{\bar{\nu}_\mu}$ = 3 GeV . Lines and points have the same meaning as Fig. 9.12.

9.7 ($E_{\bar{\nu}_\mu}$ = 3 GeV), the dependence of $\frac{d\sigma}{dQ^2}$, $P_L(Q^2)$ and $P_P(Q^2)$ on the different parameterization of $G_E^n(Q^2)$. It is seen that the polarization observables are quite sensitive to the neutron charge form factor in $\bar{\nu}_\mu n \to \mu^+\Sigma^-$ specially at $E_{\bar{\nu}_\mu} = 3$ GeV and it should be possible to determine, in principle, the charge form factor

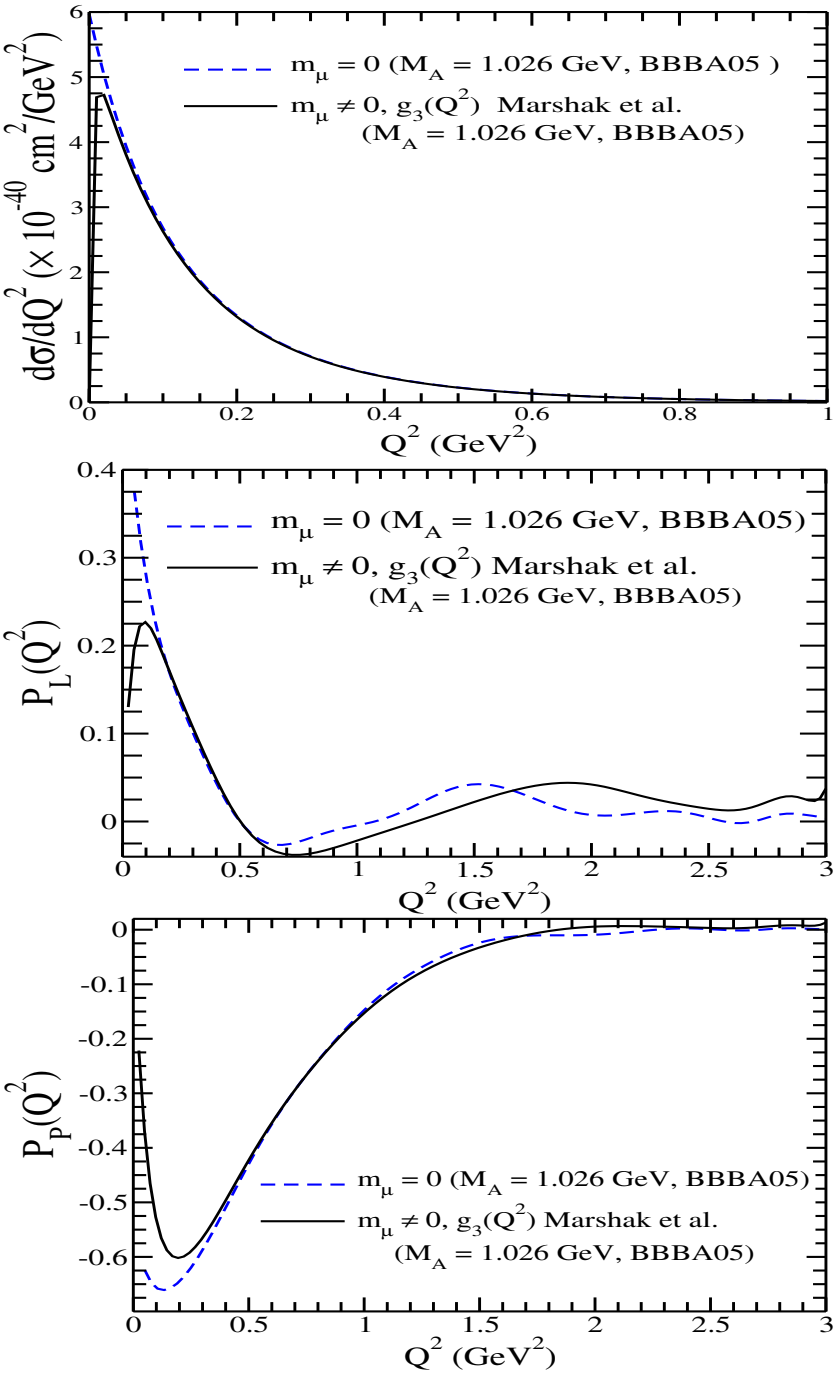

Figure 9.16: $\frac{d\sigma}{dQ^2}$, $P_L(Q^2)$ and $P_P(Q^2)$ vs Q^2 for the process $\bar{\nu}_\mu p \to \mu^+\Lambda(^{40}\text{Ar}$ target) averaged over the MicroBooNE [99] spectrum, using $f_1^{p\Lambda}(Q^2)$, $f_2^{p\Lambda}(Q^2)$, $g_1^{p\Lambda}(Q^2)$ from Table-9.1 and the BBBA05 parameterization [151] for the nucleon form factors with $m_\mu = 0$ and $M_A = 1.026$ GeV(dashed line), and $m_\mu \neq 0$, $M_A = 1.026$ GeV with $g_3^{p\Lambda}(Q^2)$ from Marshak et al. [86](solid line).

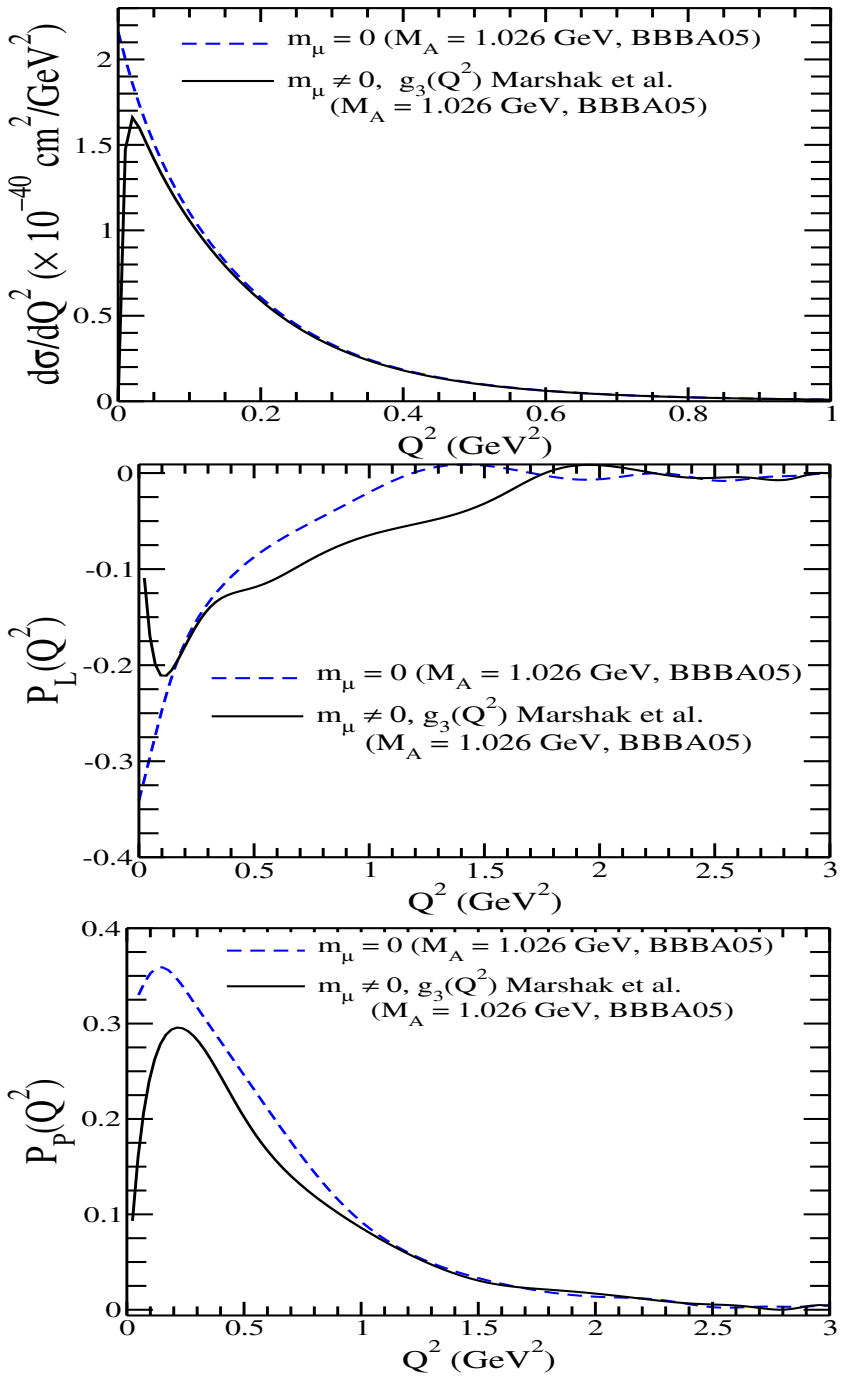

Figure 9.17: $\frac{d\sigma}{dQ^2}$, $P_L(Q^2)$ and $P_P(Q^2)$ vs Q^2 for the process $\bar{\nu}_\mu n \to \mu^+\Sigma^-$(^{40}Ar target) averaged over MicroBooNE [99] spectrum. Lines and points have the same meaning as in Fig. 9.16.

of neutron from the observation of $P_L(Q^2)$ and $P_P(Q^2)$ using this process.

We have explored the possibility of determining the pseudoscalar form factor

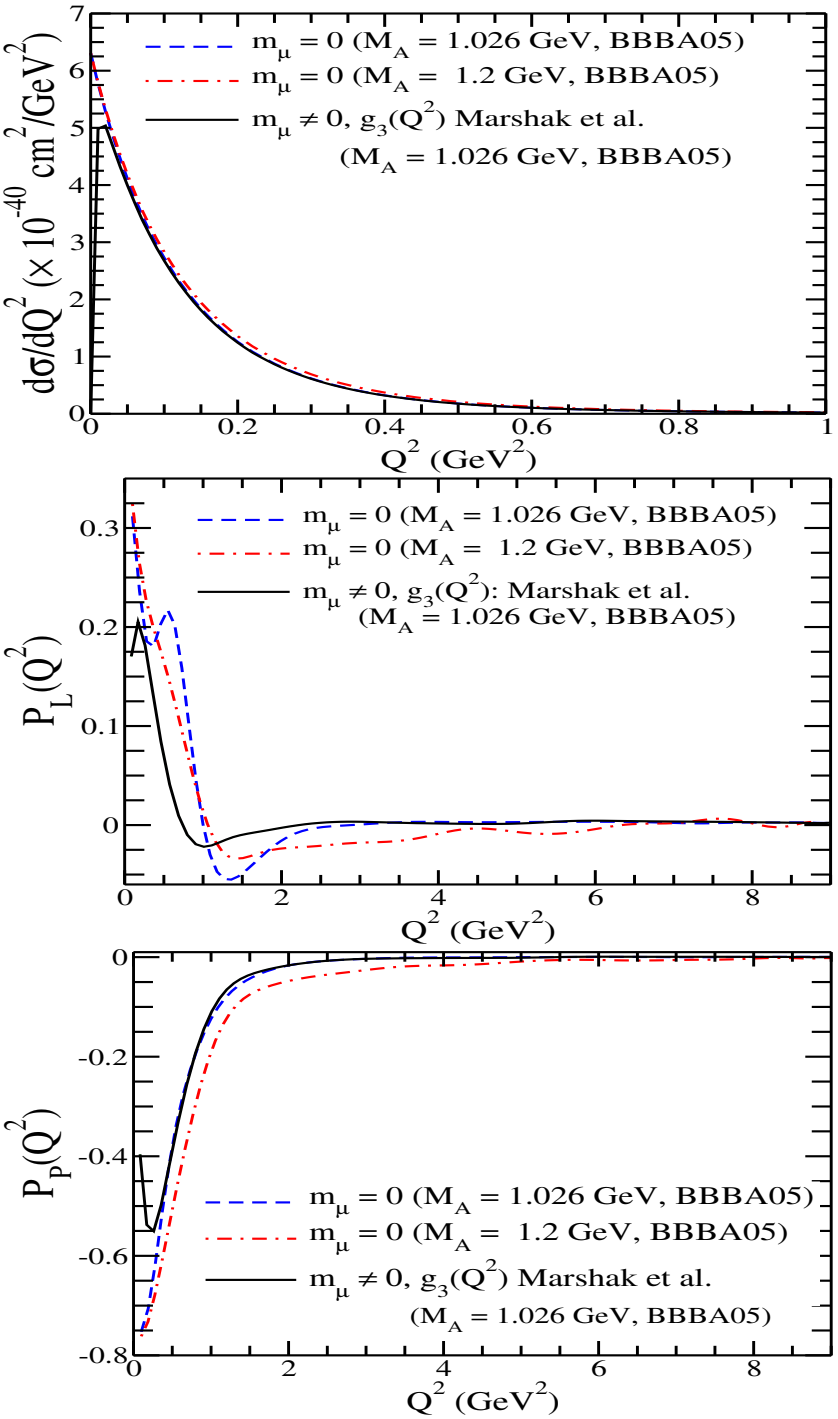

Figure 9.18: $\frac{d\sigma}{dQ^2}$, $P_L(Q^2)$ and $P_P(Q^2)$ vs Q^2 for the process $\bar{\nu}_\mu p \to \mu^+\Lambda(^{12}\text{C}$ target) averaged over T2K [256] spectrum, using $f_1^{p\Lambda}(Q^2)$, $f_2^{p\Lambda}(Q^2)$, $g_1^{p\Lambda}(Q^2)$ from Table-9.1 and the BBBA05 parameterization [151] for the nucleon form factors with $m_\mu = 0$ and $M_A = 1.026$ GeV(dashed line), $m_\mu = 0$ and $M_A = 1.2$ GeV(dashed–dotted line) and $m_\mu \neq 0$, $M_A = 1.026$ GeV with $g_3^{p\Lambda}(Q^2)$ from Marshak et al. [86](solid line).

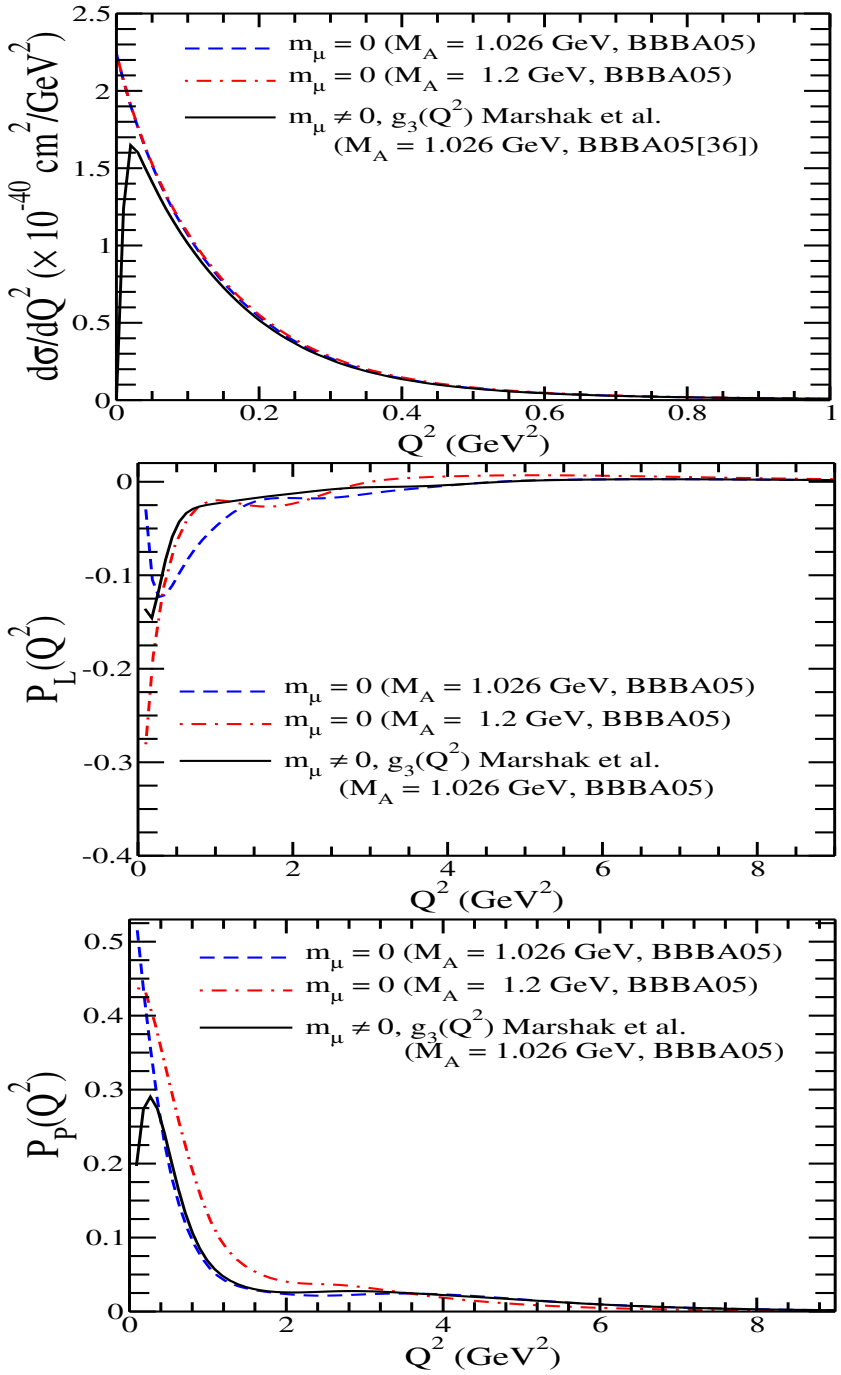

Figure 9.19: $\frac{d\sigma}{dQ^2}$, $P_L(Q^2)$ and $P_P(Q^2)$ vs Q^2 for the process $\bar{\nu}_\mu n \to \mu^+\Sigma^-$(^{12}C target) averaged over T2K [256] spectrum. Lines and points have the same meaning as in Fig. 9.18.

$g_3^{NY}(Q^2)$ in $|\Delta S| = 1$ sector by including two models for $g_3^{NY}(Q^2)$ based on PCAC and the corresponding Goldberger–Treiman relation in the strangeness sector using the parameterizations given in Eqs. 9.8(Marshak et al. [86]) and 9.9(Nambu [243]).

In Figs. 9.8 and 9.9, we show the effect of $g_3^{NY}(Q^2)$ on $\frac{d\sigma}{dQ^2}$, $P_L(Q^2)$ and $P_P(Q^2)$ calculated for the processes $\bar{\nu}_\mu p \to \mu^+\Lambda$ and $\bar{\nu}_\mu n \to \mu^+\Sigma^-$, respectively, at $E_{\bar{\nu}_\mu}$=1 GeV. We see from Figs. 9.8 and 9.9 that at $E_{\bar{\nu}_\mu} = 1$ GeV, sensitivity of the cross section or the polarization observables to the pseudoscalar form factor, $g_3^{NY}(Q^2)$ is quite small. However, at smaller antineutrino energies like $E_{\bar{\nu}_\mu}$=0.5 GeV, the polarization components $P_L(Q^2)$ and $P_P(Q^2)$ are quite sensitive to the value of the pseudoscalar form factor as shown in Figs. 9.10 and 9.11. It seems, therefore, possible in principle, to determine the pseudoscalar form factor in the hyperon polarization measurements at lower energies relevant for the MicroBooNE [99] and T2K [256] flux of antineutrinos.

9.3.2 Differential cross section and polarization components for nuclear target

In Figs. 9.12, 9.13, 9.14 and 9.15, we present the results for $\frac{d\sigma}{dQ^2}$, longitudinal ($P_L(Q^2)$) and perpendicular ($P_P(Q^2)$) components of Λ and Σ polarization at $E_{\bar{\nu}_\mu} = 1$ and 3 GeV for various nuclei like ^{12}C, ^{40}Ar, ^{56}Fe, and ^{208}Pb using Eqs. 9.16, 9.31 and 9.32. The results are compared with the results for the free nucleon case. We find that at $E_{\bar{\nu}_\mu} = 1$ GeV, $\frac{d\sigma}{dQ^2}$ hardly changes with the inclusion of nuclear medium effects. This is in contrast to the quasielastic reaction $\nu_l(\bar{\nu}_l) + n(p) \to l^-(l^+)+p(n)$. This is due to the lack of any Pauli blocking of the momentum of the final hyperon which has its own Fermi sea. The polarization observables $P_L(Q^2)$ and $P_P(Q^2)$ show some dependence on nuclear medium effects. The nature of this dependence is different for $P_L(Q^2)$ and $P_P(Q^2)$ as well as it is different for Λ and Σ hyperons. For example, in the case of $\bar{\nu}_\mu p \to \mu^+\Lambda$, the result for $P_L(Q^2)$ at low Q^2 is hardly affected by nuclear medium effects, however, with the increase in Q^2 the effect of nuclear medium increases. The effect becomes maximum for $Q^2 \sim 0.5$ GeV^2 and then decreases with further increase in Q^2. While in the case of $P_P(Q^2)$ the effect is smaller as compared to $P_L(Q^2)$ i.e. almost negligible for $Q^2 < 0.4$ GeV^2 and a slight increase for $Q^2 > 0.4$ GeV^2.

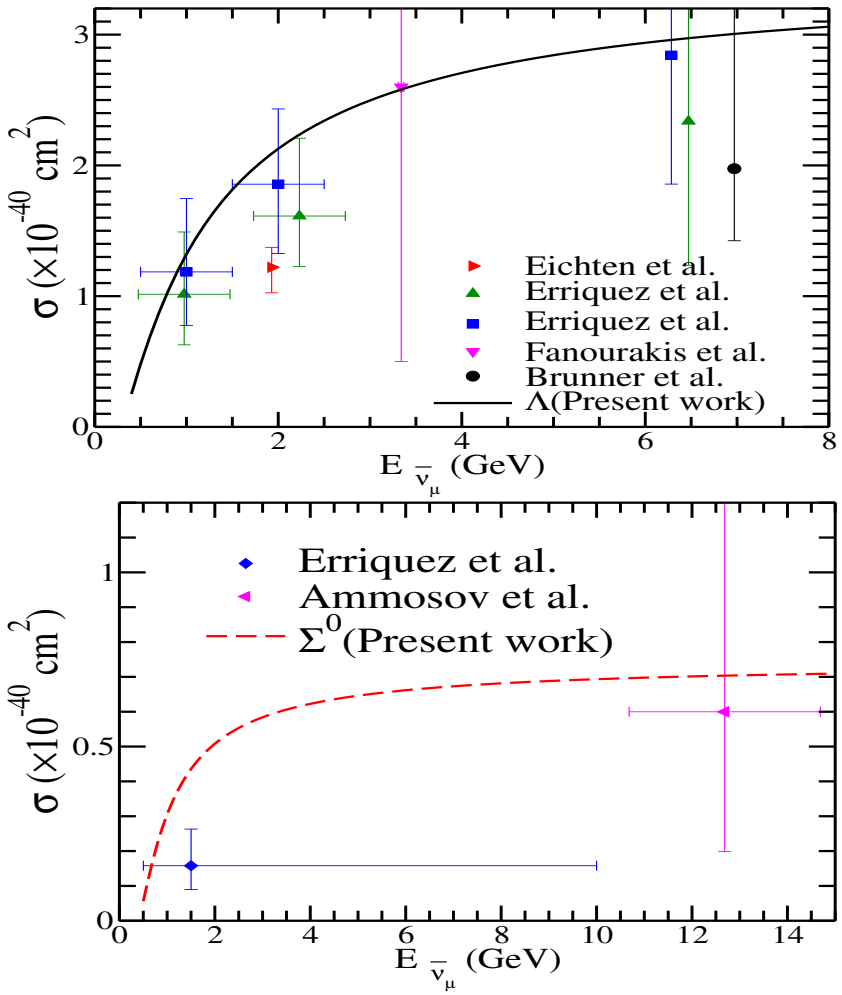

Figure 9.20: Theoretical curves for total cross section(σ) vs $E_{\bar{\nu}_\mu}$ corresponding to the processes $\bar{\nu}_\mu p \to \mu^+\Lambda$(solid line) in the left panel and $\bar{\nu}_\mu p \to \mu^+\Sigma^0$(dashed line) in the right panel using $f_1^{NY}(Q^2)$, $f_2^{NY}(Q^2)$, $g_1^{NY}(Q^2)$ from Table-9.1, $g_3^{NY}(Q^2)$ from Marshak et al. [86] given in Eq. 9.8 with $M_A = 1.026$ GeV. Experimental results for the process $\bar{\nu}_\mu p \to \mu^+\Lambda$ (triangle right [74], triangle up [73], square [75], triangle down($\sigma = 2.6^{+5.9}_{-2.1} \times 10^{-40} cm^2$) [76], circle [79]) and for the process $\bar{\nu}_\mu p \to \mu^+\Sigma^0$ (diamond [73]) are shown with error bars.

For $\bar{\nu}_\mu n \to \mu^+\Sigma^-$, the difference in the results obtained for nucleon and nuclear targets increases with the increase in Q^2, both for $P_L(Q^2)$ and $P_P(Q^2)$. Furthermore, we find that there is very little nuclear mass number(A) dependence of nuclear medium effects. Moreover, the nuclear effect becomes smaller with the increase in antineutrino energy.

9.3.3 Flux averaged differential cross section and polarization components

Currently, there are some neutrino experiments which are making measurements on neutrino–nucleus cross sections [102, 256, 100]. The LArTPC detector proposed for MicroBooNE [99], ArgoNeut [100], LAr1-ND, ICARUS-T600 [103] and DUNE [101] may be able to measure the tracks corresponding to nucleon and pion coming from Λ decay. A measurement of the asymmetry in the angular distribution of pions will give information about the hyperon (Λ, Σ^-) polarization. For the purpose of analyzing these experiments, we have convoluted $\frac{d\sigma}{dQ^2}$ and $P_{L,P}(Q^2)$ distributions over the flux $\Phi(E_{\bar{\nu}_\mu})$ available for different experiments using the expression given by,

$$\langle F(Q^2)\rangle = \frac{\int_{E_{th}}^{E_{max}} F(Q^2, E_{\bar{\nu}_\mu})\Phi(E_{\bar{\nu}_\mu})dE_{\bar{\nu}_\mu}}{\int_{E_{min}}^{E_{max}} \Phi(E_{\bar{\nu}_\mu})dE_{\bar{\nu}_\mu}}, \tag{9.33}$$

where the function $F(Q^2, E_{\bar{\nu}_\mu})$ represents $\frac{d\sigma}{dQ^2}(Q^2, E_{\bar{\nu}_\mu})$, $P_L(Q^2, E_{\bar{\nu}_\mu})$ and $P_P(Q^2, E_{\bar{\nu}_\mu})$ given in Eqs. 9.16, 9.31 and 9.32 respectively. E_{th}, E_{min}, E_{max} are the threshold energy and the minimum and maximum energies of the antineutrino fluxes corresponding to these experiments. In Figs. 9.16 and 9.17, we have shown the flux averaged $\langle\frac{d\sigma}{dQ^2}\rangle$, $\langle P_L(Q^2)\rangle$ and $\langle P_P(Q^2)\rangle$ for reactions $\bar{\nu}_\mu p \to \mu^+\Lambda$ and $\bar{\nu}_\mu n \to \mu^+\Sigma^-$, respectively, corresponding to the MicroBooNE [99] antineutrino experiment in ^{40}Ar using M_A=1.026 GeV and $g_3^{NY}(Q^2) \neq 0$.

We have also shown in Figs. 9.18 and 9.19, the flux averaged results of $\langle\frac{d\sigma}{dQ^2}\rangle$, $\langle P_L(Q^2)\rangle$ and $\langle P_P(Q^2)\rangle$ for reactions $\bar{\nu}_\mu p \to \mu^+\Lambda$ and $\bar{\nu}_\mu n \to \mu^+\Sigma^-$ respectively, for ^{12}C target corresponding to the T2K [256] antineutrino spectrum. It may be observed from these figures that polarization measurements on $\bar{\nu}_\mu p \to \mu^+\Lambda$ and $\bar{\nu}_\mu n \to \mu^+\Sigma^-$ in all these experiments will enable us to independently determine the value of axial vector form factor in the strangeness sector.

Moreover, at lower $\bar{\nu}_\mu$ energies relevant to MicroBooNE [99] and T2K [256] experiments, it is also possible to determine the pseudoscalar from factors and

test the hypothesis of PCAC in the strangeness sector.

	$\langle P_L \rangle$	$\langle P_P \rangle^2$	$\langle \sigma \rangle \times (10^{-40}$ cm$^2)$
Experiments			
Erriquez et al. [75]	-0.06± 0.44	1.05 ± 0.30	2.07 ± 0.75
Erriquez et al. [73]	–	–	1.40 ± 0.41(Propane)
Eichten et al. [74]	–	–	1.3 $\pm^{0.9}_{0.7}$(Freon)
Theory			
Present work($M_A = 0.84$ GeV)	0.10	–0.75	2.00
($M_A = 1.026$ GeV)	0.05	–0.85	2.15
($M_A = 1.2$ GeV)	0.03	–0.89	2.31
Erriquez et al. [75]($M_A = 0.84$ GeV)	0.14	0.73	2.07

Table 9.2: Flux averaged cross section $\langle \sigma \rangle$(using Eq. 9.35), longitudinal $\langle P_L \rangle$ and perpendicular $\langle P_P \rangle$ components of polarization(using Eq. 9.36) are given for the process $\bar{\nu}_\mu p \to \mu^+ \Lambda$.

Spectrum	$< \sigma > \times 10^{-40}$ cm^2		$< P_L >$		$< P_P >$	
	Σ^-	Λ	Σ^-	Λ	Σ^-	Λ
MicroBooNE [99]	0.31	0.76	–0.43	0.39	0.37	–0.78
MINERνA [102]	1.17	2.5	–0.42	–0.03	0.43	–0.85
T2K [256]	0.27	0.74	–0.44	0.43	0.37	–0.75

Table 9.3: Total cross section using Eq. 9.35, longitudinal and perpendicular components of polarization using Eq. 9.36 are integrated over various fluxes for $\bar{\nu}_\mu(k) + N(p) \to \mu^+(k') + Y(p')$ process using $f_1^{NY}(Q^2)$, $f_2^{NY}(Q^2)$, $g_1^{NY}(Q^2)$ from Table-9.1 and $g_3^{NY}(Q^2)$ from Eq. 9.8 with $m_\mu \neq 0$ and $M_A = 1.026$ GeV.

9.3.4 Energy dependence of total cross section

We have calculated the total cross section $\sigma(E_{\bar{\nu}_\mu})$ as a function of energy, given as:

$$\sigma(E_{\bar{\nu}_\mu}) = \int_{Q^2_{min}}^{Q^2_{max}} \frac{d\sigma}{dQ^2}(Q^2, E_{\bar{\nu}_\mu}) dQ^2 \tag{9.34}$$

for $\bar{\nu}_\mu p \to \mu^+ \Lambda$ and $\bar{\nu}_\mu p \to \mu^+ \Sigma^0$ reactions. We show the results for $\sigma(E_{\bar{\nu}_\mu})$ in Fig. 9.20, where a comparison is made with available experimental results from CERN [74, 73, 75], BNL [76], FNAL [77, 78] and Serpukhov [79] experiments. A reasonable agreement with the experimental results can be seen.

9.3.5 Total cross section and polarizations

We have integrated the differential cross section $\frac{d\sigma}{dQ^2}$ and polarization observables $P_L(Q^2)$ and $P_P(Q^2)$ over $E_{\bar{\nu}_\mu}$ and Q^2 distributions to obtain the total cross section $\langle\sigma\rangle$ defined as:

$$\langle\sigma\rangle = \frac{\int_{E_{th}}^{E_{max}} \int_{Q^2_{min}}^{Q^2_{max}} \frac{d\sigma}{dQ^2}\, dQ^2 \Phi(E_{\bar{\nu}_\mu}) dE_{\bar{\nu}_\mu}}{\int_{E_{min}}^{E_{max}} \Phi(E_{\bar{\nu}_\mu}) dE_{\bar{\nu}_\mu}} \tag{9.35}$$

and components of hyperon polarization $\langle P_{L,P}\rangle$ defined as:

$$\langle P_{L,P}\rangle = \frac{1}{\langle\sigma\rangle} \int_{E_{th}}^{E_{max}} \int_{Q^2_{min}}^{Q^2_{max}} P_{L,P}(Q^2, E_{\bar{\nu}_\mu})\, \frac{d\sigma}{dQ^2}\, dQ^2 \Phi(E_{\bar{\nu}_\mu}) dE_{\bar{\nu}_\mu}. \tag{9.36}$$

In order to compare with the experimental results of CERN [75], we have performed the numerical calculations for the flux averaged cross section $\langle\sigma\rangle$, longitudinal $\langle P_L\rangle$ and perpendicular $\langle P_P\rangle$ polarization components relevant for the antineutrino flux of SPS antineutrino beam of Gargamelle experiment at CERN [258] and present our results in Table-9.2. The results are compared with the available experimental results from CERN [73, 74, 75] and the theoretical results quoted by Erriquez et al. [75]. For reference we also show in Table-9.3, our results for $\langle\sigma\rangle$, $\langle P_L\rangle$ and $\langle P_P\rangle$ relevant for MicroBooNE [99], MINERνA [102] and T2K [256] experiments, which may be useful in the interpretation of the results from these experiments, whenever they become available.

Chapter 10

Weak quasielastic electroproduction of hyperons with polarization observables

10.1 Introduction

In the case of quasielastic reactions whenever the Λ and Σ^0 hyperons are produced by the charged current interaction, the observation of the differential cross section and the polarization of final hyperons can yield important information about the nucleon-hyperon transition form factors and enable the study of the applicability of Cabibbo model, G-invariance, T-invariance and SU(3) symmetry at high Q^2 in the strangeness sector. This would extend our understanding of the weak interaction phenomenology in the strangeness sector to high Q^2 which is presently available only at very low Q^2 from the study of semileptonic decays of hyperons [70, 71, 72]. The observation of hyperons in the final state through its decay products, *i.e.* $\Lambda/\Sigma \longrightarrow N\pi$, and the structure of the angular distribution of pions will give information about the polarization of hyperons. The polarization observables of the hyperons produced in the quasielastic reactions induced by $\bar{\nu}_\mu$ are shown to be more sensitive to the weak axial form factors [75, 96, 259, 85, 86, 87, 104].

In this chapter, we have studied the total cross section, differential cross section

and the polarization observables of the final hyperons produced in

$$e^- + p \longrightarrow \Lambda(\Sigma^0) + \nu_e \tag{10.1}$$

reactions and their sensitivity on the nucleon-hyperon transition form factors. In section-10.2.1, the formalism to calculate the quasielastic weak hyperon production cross section and the longitudinal ($P_L(Q^2)$) and perpendicular ($P_P(Q^2)$) components of the hyperon polarization are given. In section-10.2.3, we have given in brief the formalism to calculate the Δ^0 production cross section for the electron on the proton target. In section-10.3, we have presented the numerical results for the total cross section (σ), angular ($\frac{d\sigma}{d\Omega}$) and Q^2 ($\frac{d\sigma}{dQ^2}$) distributions and compared the results for the Q^2 distribution and σ for the $\Lambda(\Sigma^0)$ productions with the corresponding results for the Δ^0 production. We have presented the numerical results for $P_L(Q^2)$ and $P_P(Q^2)$ components of Λ/Σ^0 and discussed their sensitivity to the nucleon–hyperon transition from factors.

10.2 Formalism

10.2.1 $e^- + p \to \nu_e + Y$ process

The general expression of the differential cross section corresponding to the process presented in Fig. 10.1 may be written as

$$d\sigma = \frac{1}{(2\pi)^2}\frac{1}{4E_e^L M}\delta^4(k+p-k'-p')\frac{d^3k'}{2E_{k'}}\frac{d^3p'}{2E_{p'}}\overline{\sum}\sum|\mathcal{M}|^2, \tag{10.2}$$

where E_e^L is the electron energy in the lab frame and the square of the transition matrix element is defined in terms of the leptonic ($\mathcal{L}_{\alpha\beta}$) and hadronic ($\mathcal{J}^{\alpha\beta}$) tensors:

$$\overline{\sum}\sum|\mathcal{M}|^2 = \frac{G_F^2\sin^2\theta_c}{2}\mathcal{J}^{\alpha\beta}\mathcal{L}_{\alpha\beta}. \tag{10.3}$$

In the above expression, G_F is the Fermi coupling constant. The hadronic and leptonic tensors are given by

$$\mathcal{J}_{\alpha\beta} = \frac{1}{2}\mathrm{Tr}\left[\Lambda(p')J_\alpha\Lambda(p)\tilde{J}_\beta\right] \tag{10.4}$$

$$\mathcal{L}^{\alpha\beta} = \frac{1}{2}\mathrm{Tr}\left[\gamma^\alpha(1-\gamma_5)(\not{k}+m_e)\gamma^\beta(1-\gamma_5)\not{k}'\right], \tag{10.5}$$

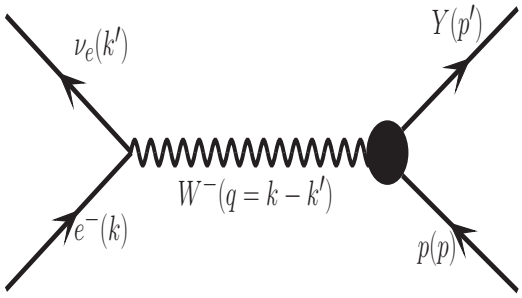

Figure 10.1: Feynman diagram for the process $e^-(k) + p(p) \rightarrow \nu_e(k') + Y(p')$, where Y stands for final hyperon. The quantities in the bracket represent four momentum of the corresponding particles.

with $\tilde{J}_\beta = \gamma^0 J_\beta^\dagger \gamma^0$ and $\Lambda(p) = \not{p} + m_p$.

J_α is the hadronic current operator given by

$$J_\alpha = V_\alpha - A_\alpha, \tag{10.6}$$

where

$$V_\alpha = \gamma_\alpha f_1^{NY}(Q^2) + i\sigma_{\alpha\beta}\frac{q^\beta}{M+M_Y} f_2^{NY}(Q^2) + \frac{q_\alpha}{M+M_Y} f_3^{NY}(Q^2), \tag{10.7}$$

and

$$A_\alpha = \gamma_\alpha\gamma_5 g_1^{NY}(Q^2) + i\sigma_{\alpha\beta}\gamma_5\frac{q^\beta}{M+M_Y} g_2^{NY}(Q^2) + \frac{q_\alpha}{M+M_Y} g_3^{NY}(Q^2)\gamma_5. \tag{10.8}$$

M and M_Y are the masses of the initial and final baryons.

Using the above definitions, the Q^2 distribution is written as

$$\frac{d\sigma}{dQ^2} = \frac{1}{64\pi M^2 E_e^{L2}} \overline{\sum}\sum |\mathcal{M}|^2. \tag{10.9}$$

In Eq. (10.9), $|\mathcal{M}|^2$ is calculated using Eq. (10.3) assuming the absence of the second class currents and neglecting the contribution from the pseudoscalar term due to the small mass of the electron. The transition form factors $f_i^{NY}(Q^2)$ and $g_i^{NY}(Q^2)$ $(i = 1-3)$, appearing in Eqs. (10.7) and (10.8), respectively, are determined using the conservation of vector current (CVC), the partial conservation of axial current (PCAC), the principles of T–invariance and G–invariance and the SU(3) symmetry as already discussed in the last chapter.

10.2.2 Polarization of hyperons

We have already discussed the polarization components of the final hyperon in the last chapter, however, in this section for completeness, we have only given the expressions for the longitudinal and perpendicular components of the final hyperon produced in the electron induced process as

$$P_L(Q^2) = \frac{M_Y}{E_{p'}}\left(\frac{\alpha(Q^2)\boldsymbol{k}\cdot\boldsymbol{p}' + \beta(Q^2)|\boldsymbol{p}'|^2}{|\boldsymbol{p}'|\ \mathcal{J}^{\alpha\beta}\mathcal{L}_{\alpha\beta}}\right), \tag{10.10}$$

$$P_P(Q^2) = \frac{(\boldsymbol{k}\cdot\boldsymbol{p}')^2 - |\boldsymbol{k}|^2|\boldsymbol{p}'|^2}{|\boldsymbol{p}'||\boldsymbol{p}'\times\boldsymbol{k}|\ \mathcal{J}^{\alpha\beta}\mathcal{L}_{\alpha\beta}}\alpha(Q^2), \tag{10.11}$$

where $E_{p'} = \sqrt{|\mathbf{p}'|^2 + M_Y^2}$ and the expressions for $\alpha(Q^2)$ and $\beta(Q^2)$ are given in Appendix-B.

10.2.3 $e^- + p \to \nu_e + \Delta^0$ process

In order to compare the cross section for the hyperon production with the cross section for the Δ^0 production, produced in the reaction

$$e^-(k) + p(p) \to \nu_e(k') + \Delta^0(p'), \tag{10.12}$$

we give the expression for the differential cross section for the Δ^0 production as [260]

$$\frac{d\sigma}{dQ^2} = \frac{1}{16\pi^2}\int d|\boldsymbol{p}'|\frac{|\boldsymbol{p}'|}{E_e^2 E_{\nu_e}}\frac{\frac{\Gamma_\Delta(W)}{2}}{(W-M_\Delta)^2 + \frac{\Gamma_\Delta^2(W)}{4}}\overline{\sum}\sum|\mathcal{M}|^2. \tag{10.13}$$

In the above expression $\overline{\sum}\sum|\mathcal{M}|^2 = \frac{G_F^2}{2}\cos^2\theta_c\,\mathcal{L}_{\mu\nu}\,J^{\mu\nu}$, where the leptonic tensor $\mathcal{L}_{\mu\nu}$ is given in Eq. (10.5) and the hadronic tensor $J^{\mu\nu} = \frac{1}{2}Tr\left[\frac{(\not{p}+M)}{2M}\tilde{\mathcal{O}}^{\alpha\mu}P_{\alpha\beta}\mathcal{O}^{\beta\nu}\right]$. The hadronic tensor is obtained by using the expression for the hadronic current j^μ as

$$< \Delta(p')|j^\mu|p(p) >= \bar{\Psi}_\beta(p')\mathcal{O}^{\beta\mu}u(p). \tag{10.14}$$

In the above expression $u(p)$ is the Dirac spinor for the proton and Ψ_β is a Rarita-Schwinger field for spin-$\frac{3}{2}$ particle. $\mathcal{O}^{\beta\alpha}$ is the $N-\Delta$ transition vertex, which is

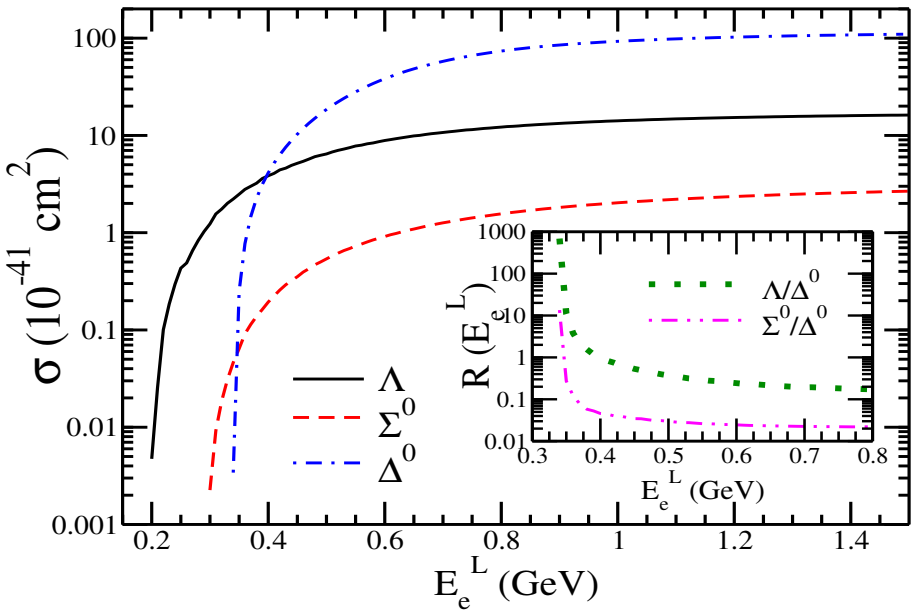

Figure 10.2: σ *vs.* E_e^L for Λ (solid line), Σ^0 (dashed line) and Δ^0 (dashed-dotted line) productions. In the inset the results are presented for the ratio $R(E_e^L) = \frac{\sigma_Y}{\sigma_{\Delta^0}}$ *vs.* E_e^L, for Y=Λ (dotted line), Σ^0 (dashed double-dotted line).

described in terms of the vector($C_i^V(q^2)$) and the axial vector($C_i^A(q^2)$) transition form factors with $\mathcal{O}^{\beta\alpha} = \mathcal{O}_V^{\beta\alpha} + \mathcal{O}_A^{\beta\alpha}$, which are given by

$$\begin{aligned}\mathcal{O}_V^{\beta\alpha} &= \left(\frac{C_3^V(q^2)}{M}(g^{\alpha\beta}\not{q} - q^\beta\gamma^\alpha) + \frac{C_4^V(q^2)}{M^2}(g^{\alpha\beta}q\cdot p' - q^\beta p'^\alpha)\right.\\ &+ \left.\frac{C_5^V(q^2)}{M^2}(g^{\alpha\beta}q\cdot p - q^\beta p^\alpha)\right)\gamma_5 \qquad (10.15)\end{aligned}$$

and

$$\mathcal{O}_A^{\beta\alpha} = \left(\frac{C_4^A(q^2)}{M}(g^{\alpha\beta}\not{q} - q^\beta\gamma^\alpha) + C_5^A(q^2)g^{\alpha\beta} + \frac{C_6^A(q^2)}{M^2}q^\beta q^\alpha\right). \qquad (10.16)$$

For the numerical calculations, we have taken the parameterization of Lalakulich *et al.* [261] for $C_i^V(Q^2)$ and $C_i^A(Q^2)$:

$$C_i^V(Q^2) = C_i^V(0)\left(1 + \frac{Q^2}{M_V^2}\right)^{-2}\mathcal{D}_i, \quad i = 3,4,5, \qquad (10.17)$$

with $C_3^V(0) = 2.13$, $C_4^V(0) = -1.51$ and $C_5^V(0) = 0.48$,

$$\begin{aligned}\mathcal{D}_{3,4} &= \left(1 + \frac{Q^2}{4M_V^2}\right)^{-1} \quad \text{and}\\ \mathcal{D}_5 &= \left(1 + \frac{Q^2}{0.776M_V^2}\right)^{-1}; \quad M_V = 0.84 \text{ GeV} \qquad (10.18)\end{aligned}$$

and

$$\begin{aligned} C_i^A(Q^2) &= C_i^A(0)\left(1+\frac{Q^2}{M_A^2}\right)^{-2}\left(1+\frac{Q^2}{3M_A^2}\right)^{-1}; \\ M_A &= 1.026 \text{ GeV} \end{aligned} \tag{10.19}$$

for $i = 3,4,5,6$ with $C_3^A(0) = 0$, $C_4^A(0) = -0.25\ C_5^A(0)$, $C_5^A(0) = -1.2$ and $C_6^A(0) = \frac{M^2}{(m_\pi^2+Q^2)}C_5^A(0)$.

$P_{\alpha\beta}$ is the spin-3/2 projection operator given by

$$P_{\alpha\beta} = -(\frac{\not{p}' + M_\Delta}{2M_\Delta})\left(g_{\alpha\beta} - \frac{2}{3}\frac{p'_\alpha p'_\beta}{M_\Delta^2} + \frac{1}{3}\frac{p'_\alpha\gamma_\beta - p'_\alpha\gamma_\beta}{M_\Delta} - \frac{1}{3}\gamma_\alpha\gamma_\beta\right), \tag{10.20}$$

and the delta decay width Γ is taken as the energy dependent P-wave decay width given by

$$\Gamma_\Delta(W) = \frac{1}{6\pi}\left(\frac{f_{\pi N\Delta}}{m_\pi}\right)^2\frac{M_\Delta}{W}|\boldsymbol{q}_{cm}|^3, \tag{10.21}$$

where the $N-\Delta$ coupling constant $f_{\pi N\Delta} = 2.127$, m_π is the pion mass, $|\boldsymbol{q}_{cm}|$ is the pion momentum in the rest frame of the resonance and is given by

$$|\boldsymbol{q}_{cm}| = \frac{\sqrt{(W^2 - m_\pi^2 - M_N^2)^2 - 4m_\pi^2 M_N^2}}{2W},$$

with W $[(M+m_\pi) \le W < 1.4$ GeV] as the center-of-mass energy.

10.3 Results and discussion

We have used Eq. (10.2) for the calculation of the total cross section $\sigma(E_e^L)$ and the differential cross sections ($\frac{d\sigma}{dQ^2}$ and $\frac{d\sigma}{d\Omega}$), and Eqs. (10.10) and (10.11) for the longitudinal $P_L(Q^2)$ and perpendicular $P_P(Q^2)$ components of polarization, respectively, for the processes $e^-p \to \nu_e\Lambda$ and $e^-p \to \nu_e\Sigma^0$. The form factors are given in Table-9.1. For the vector nucleon form factors, we have used the parameterization of Bradford *et al.* [151]. A dipole parameterization for the nucleon axial vector form factor with the dipole mass $M_A = 1.026$ GeV [155] has been used. For the Δ^0 production cross section, we have used Eq. (10.13) with the form factors

defined in Eqs. (10.17) –(10.19) and integrated over the angles to get the total cross section ($\sigma(\Delta)$).

In Fig. 10.2, we have presented the results of σ *vs.* E_e^L for Λ, Σ^0 and Δ^0 productions. In the inset of Fig. 10.2, we have also presented the results for the ratio $R(E_e^L) = \frac{\sigma_Y}{\sigma_{\Delta^0}}$, for Y = Λ and Σ^0 productions. We observe that for energies E_e^L < 0.4 GeV, the Λ production cross section is more than the Δ^0 production which reduces to $\sim 24\%$ of the Δ^0 production for E_e^L ~ 0.6 GeV and $\sim 16\%$ for $E_e^L = 1$ GeV. Thus, in the low electron energy range, the hyperons (Λ, Σ^0) give considerable contribution to the total cross section along with the Δ^0 production process. The hyperon and Δ^0 produced in these reactions decay to pion and nucleon. These particles may be observed in coincidence. With the availability of the high luminosity electron beam (say $10^{39}/\mathrm{cm}^2/\mathrm{s}$), we may be able to observe ~ 665 events for the Δ^0 production and ~ 248 and 20 events for Λ and Σ^0 productions in the duration of 1 hour for 0.5 GeV electron energy, while almost the same number of events ~ 150 for Λ and Δ^0 productions at E_e^L $= 0.4$ GeV.

In Fig. 10.3, we have presented the results for $\frac{d\sigma}{dQ^2}$ *vs.* Q^2 at different values of the electron energies *viz.* E_e^L=0.4, 0.8 and 1.2 GeV, for Λ, Σ^0 and Δ^0 productions. In the threshold region, at very low Q^2, there is almost equal contribution from the Λ and Δ^0 productions. For $Q^2 > 0.1$ GeV^2 there is a sharp fall in the Δ^0 production cross section, whereas the Λ production cross section decreases slowly, similar to $e^- p \to \nu_e n$ reaction. At $E_e^L = 0.8$ GeV, the Λ cross section is $\sim$ 10–30 % of the Δ^0 cross section in the low Q^2 region.

In Fig. 10.4, we have presented the results for the angular distribution $\frac{d\sigma}{d\Omega}$ for Λ and Σ^0 in $e^- p \to \nu_e \Lambda$ and $e^- p \to \nu_e \Sigma^0$ reactions at different electron energies E_e^L=0.5, 1, 2 and 5 GeV. In general, the nature of the angular distribution is qualitatively similar at these energies. However, the peak shifts towards the smaller angles at lower E_e^L. We find that (not shown here) for $e^- p \to \nu_e \Lambda$ process, the major contribution to the cross section comes from $g_1^2(Q^2)$ and $f_1^2(Q^2)$ terms. Quantitatively, the contribution of $g_1^2(Q^2)$ is larger at the smaller angles while

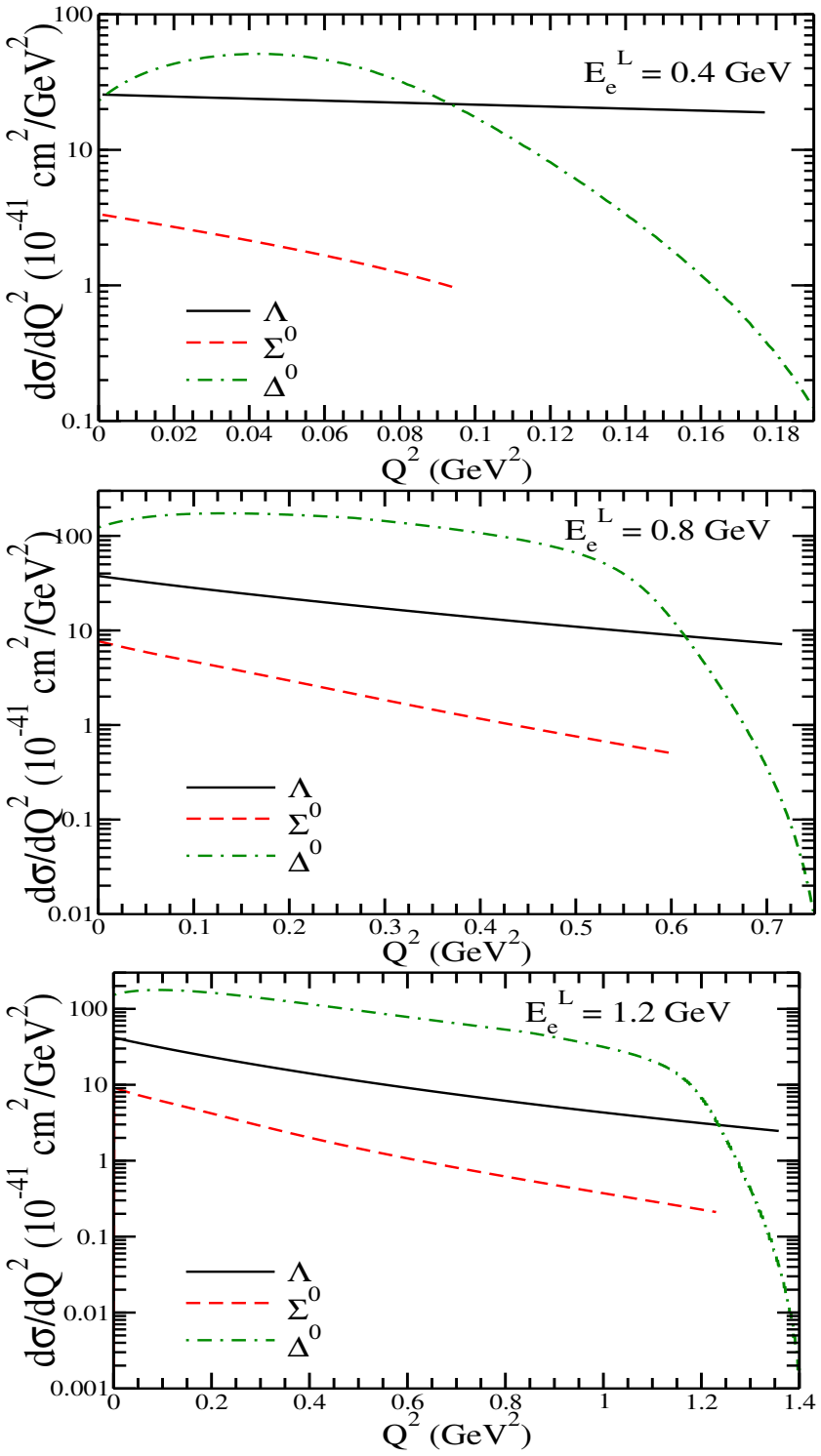

Figure 10.3: $\frac{d\sigma}{dQ^2}$ *vs.* Q^2 at $E_e^L = 0.4$ GeV (left panel), $E_e^L = 0.8$ GeV (central panel) and $E_e^L = 1.2$ GeV (right panel). The results are shown for Λ (solid line), Σ^0 (dashed line) and Δ^0 (dash-dotted line) productions.

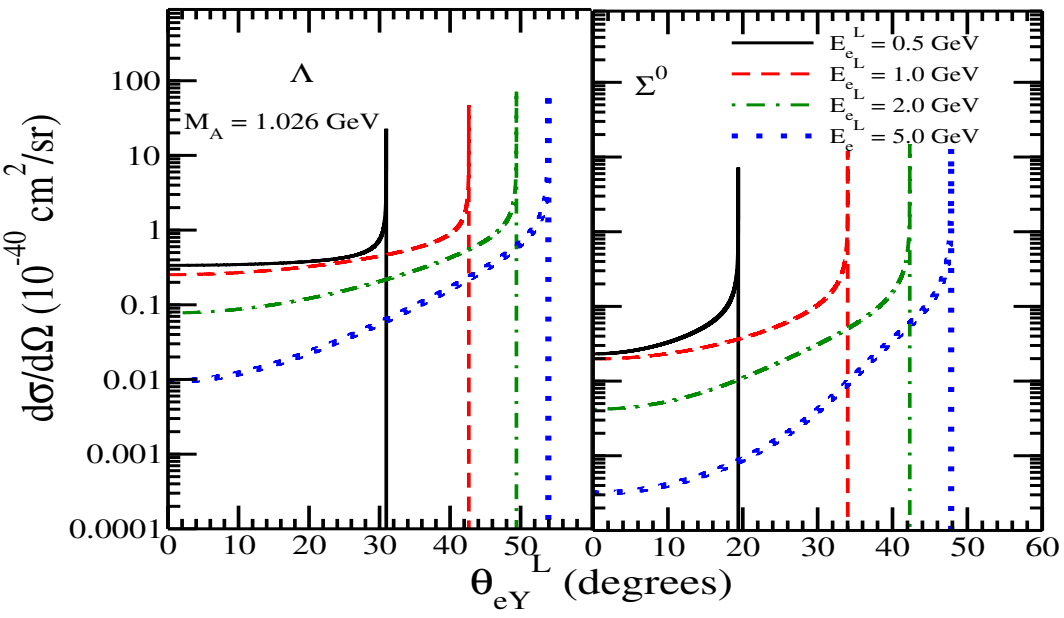

Figure 10.4: Hyperon angular distribution ($\frac{d\sigma}{d\Omega}$) *vs.* outgoing Y laboratory angle (θ^L_{eY}) for the processes $e^-p \to \nu_e\Lambda$ (left panel) and $e^-p \to \nu_e\Sigma^0$ (right panel) with M_A=1.026 GeV at different electron energies E^L_e= 0.5 GeV (solid line), 1 GeV (dashed line), 2 GeV (dash-dotted line) and 5 GeV (dotted line).

the contribution from $f_1^2(Q^2)$ is larger in the peak region. The contributions of the interference terms like $f_1(Q^2)g_1(Q^2)$ and $f_2(Q^2)g_1(Q^2)$ are almost of the same strength. The contribution from the $f_1(Q^2)f_2(Q^2)$ term is almost of equal strength at the smaller angles but becomes almost an order of magnitude smaller in the peak region as compared to the contribution of the vector-axial vector interference terms. For the process $e^-p \to \nu_e\Sigma^0$, it is the $f_2^2(Q^2)$ term which dominates at the smaller angles followed by the $g_1^2(Q^2)$ and $f_1^2(Q^2)$ terms. However, in the peak region, the $f_1^2(Q^2)$ term dominates followed by the $f_2^2(Q^2)$ and $g_1^2(Q^2)$ terms. The term $f_2(Q^2)g_1(Q^2)$ is the dominant interference term. We also find that there is not much effect of different parameterizations for the vector nucleon form factors $f_{1,2}^{p,n}$ available in the literature on the angular distribution for both Λ and Σ^0.

In Fig. 10.5, the results are presented for $\frac{d\sigma}{d\Omega}$ for the processes $e^-p \to \nu_e\Lambda$ and $e^-p \to \nu_e\Sigma^0$ by varying M_A from 0.9 GeV to 1.2 GeV at the two incident electron energies of $E^L_e = 0.5$ GeV and $E^L_e = 1$ GeV. We find that the sensitivity of $\frac{d\sigma}{d\Omega}$ to

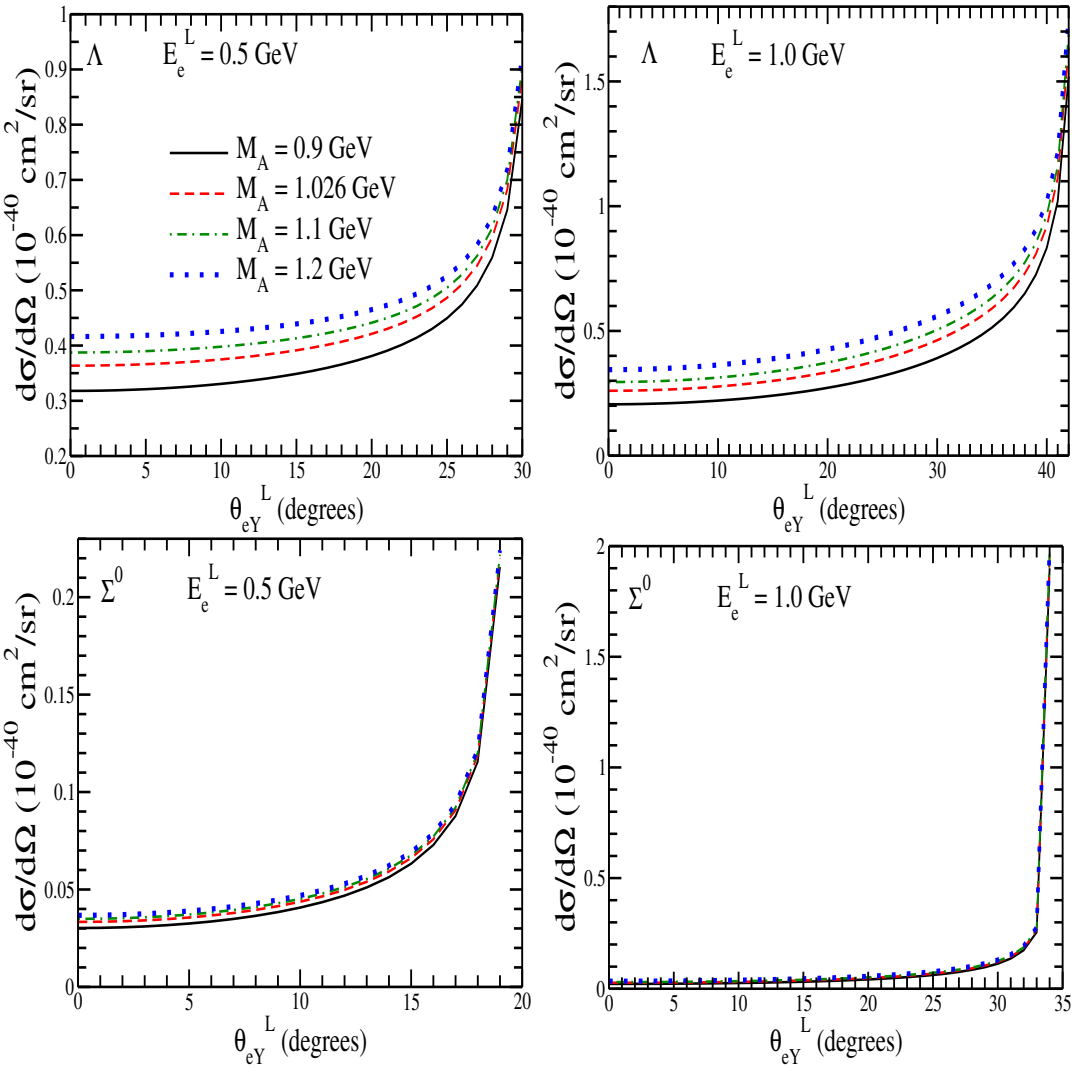

Figure 10.5: $\frac{d\sigma}{d\Omega}$ *vs.* outgoing θ_{eY}^{L} for the processes $e^- p \to \nu_e \Lambda$ (upper panel) and $e^- p \to \nu_e \Sigma^0$ (lower panel) at $E_e^L = 0.5$ GeV (left panel), $E_e^L = 1$ GeV (right panel). The results are presented for different values of M_A *viz.* 0.9 GeV (solid line), 1.026 GeV (dashed line), 1.1 GeV (dash-dotted line) and 1.2 GeV (dotted line).

the axial vector form factor is more for $e^- p \to \nu_e \Lambda$ than $e^- p \to \nu_e \Sigma^0$ process. It should be possible to determine the values of M_A from the observation of $\frac{d\sigma}{d\Omega}$ for $e^- p \to \nu_e \Lambda$.

To study the dependence of $P_L(Q^2)$ and $P_P(Q^2)$ on M_A, we have presented the results for $P_L(Q^2)$ and $P_P(Q^2)$ at the incident electron energies $E_e^L = 0.5$, 1 and 1.5 GeV for $e^- p \to \nu_e \Lambda$ process in Fig. 10.6 and $e^- p \to \nu_e \Sigma^0$ process in

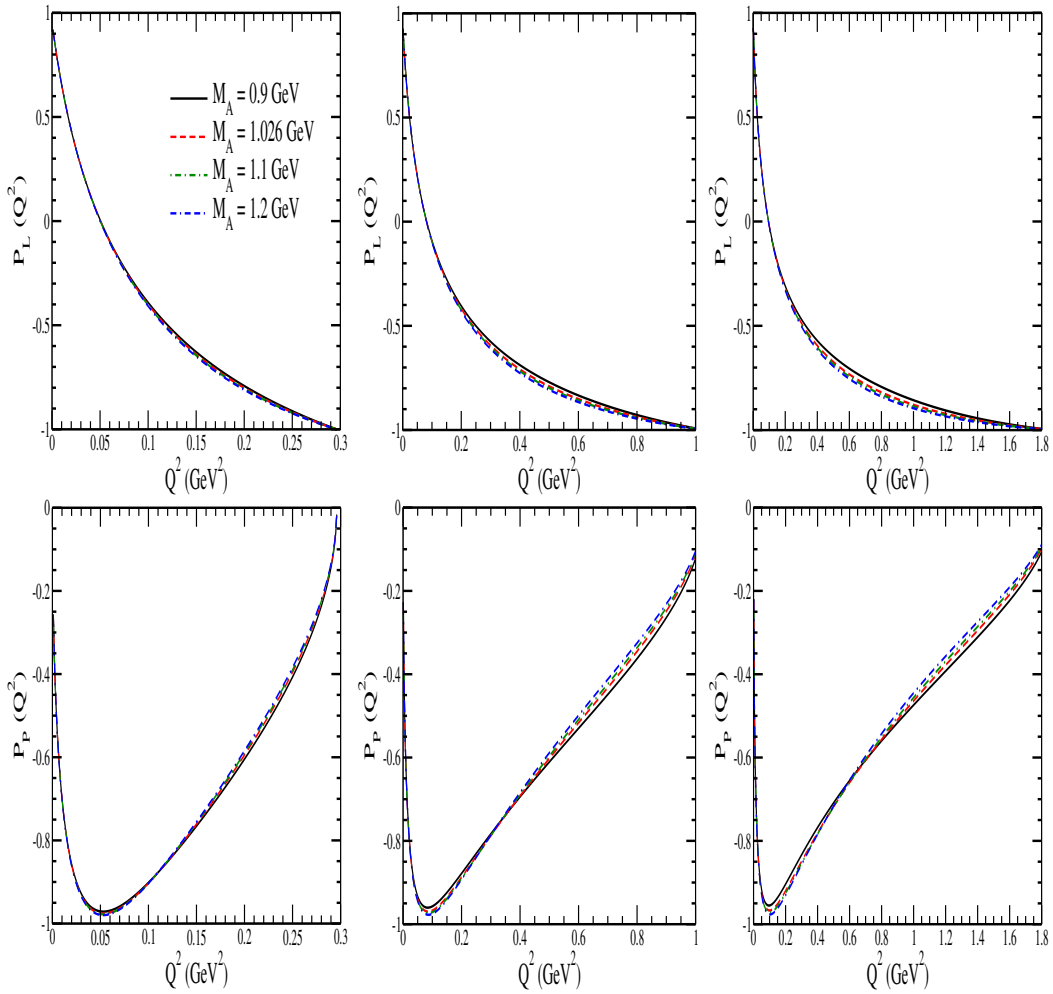

Figure 10.6: $P_L(Q^2)$ and $P_P(Q^2)$ *vs.* Q^2 for the process $e^- p \to \nu_e \Lambda$ at $E_e^L = 0.5$ GeV (left panel), $E_e^L = 1$ GeV (central panel) and $E_e^L = 1.5$ GeV (right panel). The results are presented for different values of M_A *viz.* 0.9 GeV (solid line), 1.026 GeV (dashed line), 1.1 GeV (dash-dotted line) and 1.2 GeV (dash–double-dotted line).

Fig. 10.7, respectively, by taking the different values of M_A, from 0.9 GeV to 1.2 GeV [262, 263, 264]. We observe that the polarization observables ($P_L(Q^2)$ and $P_P(Q^2)$) in case of the Σ^0 production are more sensitive to the variation in the value of M_A as compared to the Λ production. Also with the increase in energy, the sensitivity of the polarization observables especially $P_L(Q^2)$ increases for both Λ and Σ^0 which is clearly evident as the percentage difference in $P_L(Q^2)$ at $Q^2 = 0.15$ GeV^2 is $\sim 4\%(7\%)$ for $E_e^L = 0.5$ GeV for $\Lambda(\Sigma^0)$ and at $Q^2 = 0.8$ GeV^2 is $\sim$

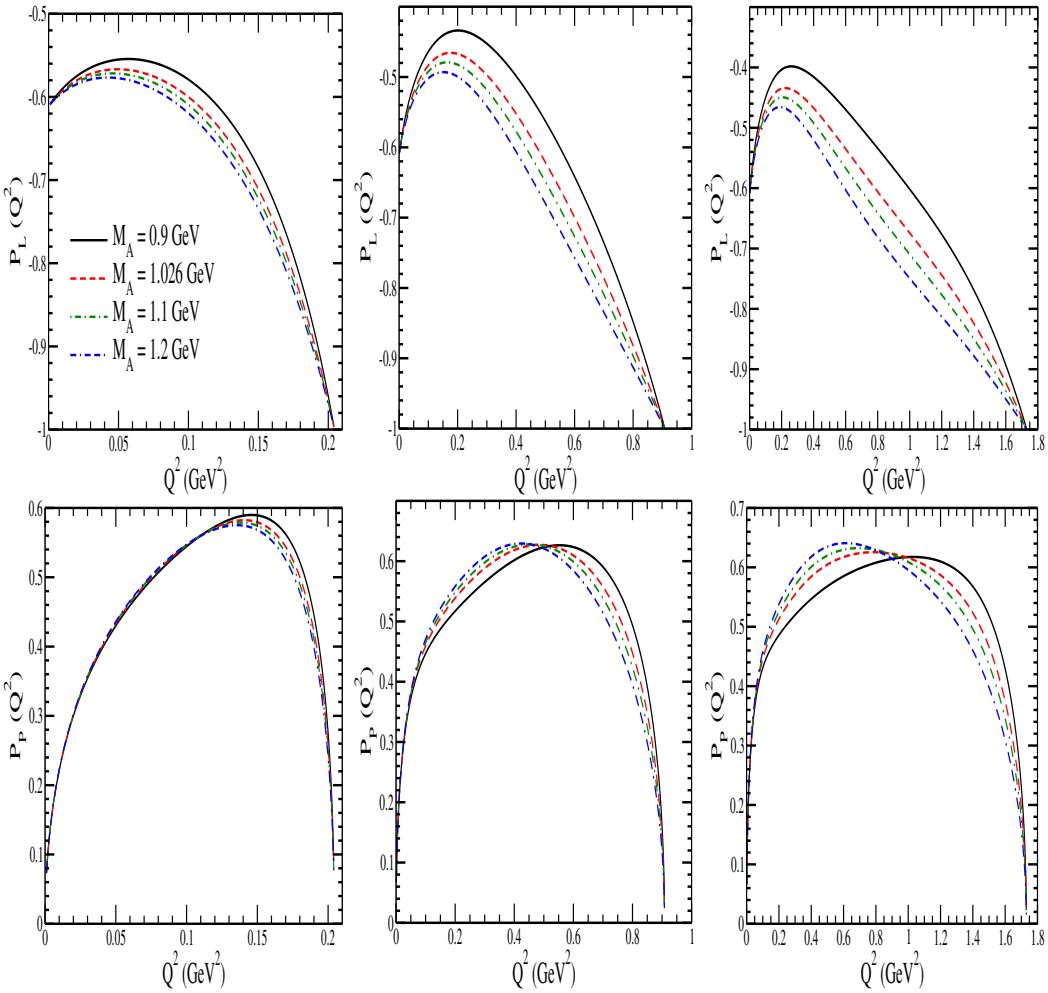

Figure 10.7: $P_L(Q^2)$ and $P_P(Q^2)$ *vs.* Q^2 for the process $e^- p \to \nu_e \Sigma^0$ at $E_e^L = 0.5$ GeV (left panel), $E_e^L = 1$ GeV (central panel) and $E_e^L = 1.5$ GeV (right panel). The results are presented for different values of M_A *viz.* 0.9 GeV (solid line), 1.026 GeV (dashed line), 1.1 GeV (dash-dotted line) and 1.2 GeV (dash–double-dotted line).

2%(7%) for $E_e^L = 1$ GeV and $\sim 6\%(28\%)$ for $E_e^L = 1.5$ GeV for $\Lambda(\Sigma^0)$.

Chapter 11

Summary and Conclusions

In this thesis, I have presented the work that I have performed during my four years stay at the Fermi National Accelerator Laboratory for the MINERvA experiment as well as the theoretical work of neutrino interactions with nucleons and nuclei during my earlier stay for the first three years at my home institution Aligarh Muslim University.

At MINERvA my analysis goal was to obtain the differential deep inelastic scattering cross section in the antineutrino mode, where the different nuclear targets are carbon, oxygen, iron and lead, and my analysis is still continuing. The idea is to perform EMC kind of measurements in near future which is only possible after the analysis of the differential and total scattering cross sections. With these data the other goal is to obtain the ratio of structure functions for the several nuclear targets. To obtain such results, we require to perform various steps like event selection, efficiency, background estimation and subtraction, etc., and most of these steps are already completed and we are ready for the final analysis as I have been also involved in preserving the MINERvA data which can be useful in the future analysis. This was a big milestone.

In Chapter-1, I introduced the topic, discussed about neutrino and its discovery, importance of weak interaction phenomenology and the target of intermediate

energy neutrino experiments.

In Chapter-2, I have explained briefly how the beam of neutrinos from the Fermilab accelerate complex is extracted using hydrogen atoms. 120 GeV protons are bombarded on a meter long graphite target. The collision of proton on carbon creates mesons, mainly pions (≥ 96 %) and kaons. A pair of pulsed magnetic horns is used to focus the charged mesons in a relatively narrow beam. These meson are allowed to pass through a decay volume held at a vacuum of ~ 1 atm where these mesons decay into charged muons and (anti)neutrinos. To achieve pure neutrino beam, secondary hadrons and the non-interacting protons are flushed out from the beam at the end of the decay pipe with the help of a hadron absorber consisting of aluminum, steel and concrete structure just downstream of the decay pipe. The beam passes through 240m of dolomite to filter out muons in the beam and reaches the MINERvA detector. Different components of the NuMI beamline are also briefly explained in the same chapter.

The goal of the analysis presented here, is to measure cross section for the DIS interaction of antineutrinos with different nuclear targets provided by the MINERvA detector and compare them with the cross section measured in plastic scintillator(tracker) part of the MINERvA detector. The detector is composed of many hexagonal plastic scintillator planes stacked together. For the nuclear target analysis, different nuclear materials(carbon, iron, lead and water) are interspersed between these plastic scintillator planes. The MINERvA detector is divided into two parts, viz. inner detector and outer detector. Further, the inner detector, consists of four sub-detectors arranged longitudinally. These four sub-detectors are (i) the nuclear target region, (ii) the fully active tracking region, (iii) downstream electromagnetic calorimeters, and (iv) downstream hadronic calorimeters. While the outer detector is a shell of hadronic calorimeters that surround the inner detector and also to physically support the inner detectors. The MINERvA collaboration also uses the MINOS-ND as a muon spectrometer for the determination of the charge and momentum of a muon. Each component of the MINERvA detector and it's working along with MINOS-ND as a muon spectrometer is briefly

explained in Chapter-3.

Data taken by the MINERvA detector needs to be converted in the analyzable form to extract physics information from the data. In Chapter-4, the steps for the reconstruction of the data are explained briefly. In the (anti)neutrino interaction, when a charged particle travels through the MINERvA detector it deposits energy. This energy and the time of energy deposition are read out from the detector electronics. This information is converted in the physics information which is used for the analysis. This is done by running reconstruction algorithms on the collected data. These algorithms separate individual event interactions from the larger readout window and groups them in time slices, identify energy formed into distinct clusters, muon tracks, matching these tracks in MINOS, and counting the dispersed energy in the detector. Different steps for track reconstruction in the MINERvA and MINOS-ND are briefly explained in this chapter.

For the nuclear target analysis, it is very important to locate the exact position of the interaction vertex. In the medium energy era, DIS antineutrino interactions deposit large amount of the hadronic energy near the interaction vertex which confuses the traditional vertex finding algorithms leading to the mis-identification of the vertex. In the tracker based analysis, misreconstruction of the interaction vertex by few centimeters does not affect the measurement of the cross section but this is not the case for nuclear target analysis. Misreconstruction of the interaction vertex may lead to the rejection of the events from the selection sample, resulting in lower efficiencies across all passive nuclear targets. It is not feasible to dismiss all of the events having vertex misreconstruction. To solve this problem, another approach for the track reconstruction is employed which is known as *Machine learning*. In Chapter-5, I have explained machine learning technique used for the reconstruction of the antineutrino interaction vertex in the DIS region. To implement this technique, the events from the MINERvA detector are taken as the images and the vertex finding problem is considered as image classification. The information of the hit energy and time of the hit are given as an input to a DCNN model for training. I have calculated loss and accuracy functions of the

DCNN model using a fraction of the MINERvA data set before making predictions for all of the simulated and reconstructed data. I have also compared the physics results using both traditional and machine learning vertex finding approaches and found that the machine learning approach improves the event selection in the nuclear targets considerably.

To measure the DIS cross section experimentally, we need to calculate different components. These components are explained briefly in Chapter-6. First step of measuring the cross section is to select a pure signal sample. This is done by passing the events from a set of selection cuts and then subtracting the background events accurately. In DIS analysis, we measure two different backgrounds, wrong target and non-DIS backgrounds. The machine learning approach reduces the wrong target background significantly. Background subtraction is performed after calculating the level of both backgrounds by using simulation data constrained to the real data. I have obtained a scale factor per nuclear target material separately for both backgrounds using χ^2 minimization. I have shown the plots for simulated and reconstructed data before and after apply the scale factor to the simulated data for ^{12}C, ^{56}Fe and ^{208}Pb nuclear targets. In this chapter, other components for the measurement of the cross section are also explained briefly.

In Chapter-7, we have studied the charged current induced quasielastic scattering of neutrinos and antineutrinos off the nuclear target like ^{12}C, ^{40}Ar, ^{56}Fe and ^{208}Pb in the energy range of $E_\nu \leq 1$ GeV. The numerical calculations have been performed using LFG model and the present results have been compared with different version of the Fermi gas model. We observe the following:

1. $\nu_\mu(\bar{\nu}_\mu)$ induced cross sections in free nucleon as well as nucleons bound in nuclear targets are more suppressed due to threshold effects at low energies than $\nu_e(\bar{\nu}_e)$ induced reaction cross sections. Moreover, when cross sections are evaluated in nuclear targets there is a further reduction in the cross sections due to nuclear medium effects. This reduction is energy dependent.

2. At low energies of $E_{\nu/\bar{\nu}} < 0.5\ GeV$ there is appreciable nuclear model de-

pendence on (anti)neutrino-nucleus cross sections for both flavors of neutrino(antineutrino). The suppression due to nuclear medium effects is larger in the LFG model as compared to the Fermi gas model of Llewellyn Smith [65]. The suppression in the Fermi gas models of Smith and Moniz [64] and Gaisser and O'Connell [66] are larger than LFG. When RPA effect is included in LFG, the suppression is largest.

3. The suppression due to nuclear medium effects is larger in the case of antineutrino as compared to the cross sections obtained for neutrino induced processes.

4. For a given set of parameters which determine the form factors and other coupling constants the percentage difference in electron and muon production cross sections is more for nuclear targets than for the free nucleon target. This difference decreases with neutrino/antineutrino energy. Also this difference increases with the increase in mass number.

5. The percentage difference in electron and muon production cross sections due to uncertainties in axial dipole mass is more in the case of nuclear targets as compared to free nucleon target. The difference increases with the increase in mass number.

6. The fractional difference in the cross sections due to the presence of pseudoscalar form factor is more in the case of $\bar{\nu}_\mu$ induced CCQE process than ν_μ induced process for the free nucleon case as well as in nuclear targets. The contribution of pseudoscalar form factor in $\nu_\mu(\bar{\nu}_\mu)$ nucleon scattering is about 3(9)% at low energies of $E_\nu = 0.2\ GeV$ and becomes $\sim 1(3)\%$ at $E_\nu = 0.4\ GeV$ in the case of free nucleon. When nuclear medium effects are taken into account this contribution increases.

7. The inclusion of second class vector current results in an increase in the total scattering cross section if present experimental limits of the second class form factor $F_3^V(Q^2)$ is used for $\nu_e(\bar{\nu}_e)$ as well as $\nu_\mu(\bar{\nu}_\mu)$ induced processes. With the inclusion of $F_3^V(Q^2)$, $\nu_\mu(\bar{\nu}_\mu)$ induced scattering cross section in-

creases about 1(4)% for free nucleon case and 1(8)% when we include RPA with LFG at $E_\nu = 0.4\ GeV$. For the $\nu_e(\bar{\nu}_e)$ induced processes this effect is smaller in comparison to the $\nu_\mu(\bar{\nu}_\mu)$ induced processes. The effect of including second class axial vector form factor $F_3^A(Q^2)$ (consistent with present experimental limits) is qualitatively similar to the effect of including second class vector form factor but quantitatively quite small as compared to the effect of $F_3^V(Q^2)$ summarized above.

8. The effect of radiative corrections being proportional to $log(\frac{E_l^*}{m_l})$ affects the $\nu_e(\bar{\nu}_e)$ scattering cross section more than $\nu_\mu(\bar{\nu}_\mu)$ scattering cross sections when a corresponding charged lepton is in the final state. This gives a difference in $\nu_e(\bar{\nu}_e)$ and $\nu_\mu(\bar{\nu}_\mu)$ scattering cross sections which is almost independent with energy in the case of neutrino induced process while it increases slightly with energy in the case of antineutrino induced process both for the free nucleon as well as the bound nucleons.

In Chapter-8, we have presented a theoretical description of the inclusive quasielastic scattering for ν_e and ν_μ induced by the weak charged current on ^{12}C and ^{40}Ar relevant for the future experiments planned to be done using KDAR neutrinos. These KDAR neutrinos are monoenergetic with $E_{\nu_\mu} = 236$ MeV. The calculations have been done in a microscopic model of nucleus which takes into account the effect of the Fermi motion, binding energy and long range nucleon-nucleon correlations through RPA. We observe the following

1. In the energy region of $E_\nu = 150 - 250$MeV , the overall reduction due to Pauli blocking and RPA correlations in ^{12}C(^{40}Ar) varies from the range of 70%(75%) to 55%(53%) in the case of ν_e-nucleus scattering and 95%(85%) to 68%(63%) in the case of $\nu_\mu-$nucleus scattering. There is an uncertainty of about 10% due to the Landau-Migdal parameter used in the treatment of RPA correlations.

2. The results have been compared with the results of the other calculations in the literature. The cross section obtained using the present model with

RPA effect is around 50% smaller than the results of the RFGM of Smith and Moniz [233]. The different treatment of nucleon-nucleon correlations in the various approaches results in an uncertainty of about 25% in the cross sections at $E_{\nu_\mu} = 236$MeV.

3. We have also presented the results for the energy and angular distributions for e^- and μ^- produced in these reactions for a fixed neutrino energy of E_ν =236MeV. A comparison has been made with the different theoretical predictions for the kinetic energy distribution for ν_μ induced interactions on ^{12}C target.

In Chapter-9, we have studied the differential cross section $\frac{d\sigma}{dQ^2}$ as well as longitudinal($P_L(Q^2)$) and perpendicular ($P_P(Q^2)$) components of polarization of Λ and Σ hyperons produced in the quasielastic reactions of antineutrinos on free and bound nucleons. The effect of nuclear medium arising due to Fermi motion and Pauli blocking for initial nucleon have been included. The form factors for the nucleon-hyperon transition have been obtained using Cabibbo theory assuming SU(3) invariance and the absence of second class currents. To summarize our results we find that:

1. The theoretical results for $\sigma(E_{\bar{\nu}_\mu})$ are found to be in satisfactory agreement with the earlier experimental results available from CERN, BNL and Serpukhov laboratories with $M_A = 1.026$ GeV, the world average value obtained from $\Delta S = 0$ experiments.

2. $P_L(Q^2)$ and $P_P(Q^2)$ are sensitive to the value of M_A. Therefore, it is possible to determine the value of M_A independent of the cross section measurements for the single hyperon production.

3. $\frac{d\sigma}{dQ^2}$ and $P_{L,P}(Q^2)$ are found to be sensitive to the neutron charge form factor in the case of $\bar{\nu}_\mu n \to \mu^+\Sigma^-$ process, specially for $Q^2 > 0.2$ GeV^2.

4. At lower antineutrino energies $E_{\bar{\nu}_\mu} \sim 0.5$ GeV, $\frac{d\sigma}{dQ^2}$ and $P_{L,P}(Q^2)$ are sensitive to the choice of the pseudoscalar form factor. It should be possible to

test PCAC and GT relation in the strangeness sector, from the quasielastic production of hyperons at lower energies relevant to MicroBooNE and T2K experiments.

5. The effect of nuclear medium on $\frac{d\sigma}{dQ^2}$, $P_L(Q^2)$ and $P_P(Q^2)$ arising due to Fermi motion and Pauli blocking of initial nucleon are studied quantitatively. They are found to be quite small and negligible for $\frac{d\sigma}{dQ^2}$. However, these effects are found to be non-negligible but small for $P_L(Q^2)$ and $P_P(Q^2)$ and show no appreciable dependence on the nucleon number A.

In Chapter-10, we have studied the differential and total scattering cross sections as well as the longitudinal and perpendicular components of the polarization for Λ and Σ^0 hyperons produced in the quasielastic reaction of the electron on free proton. The form factors for the nucleon-hyperon transition have been obtained using the Cabibbo theory assuming SU(3) invariance. The sensitivity of $\frac{d\sigma}{d\Omega}$, σ, $P_L(Q^2)$ and $P_P(Q^2)$ to the axial mass M_A has been studied. To summarize our results we find that:

1) Even though the production of the hyperons (Λ, Σ^0) is Cabibbo suppressed as compared to the Δ^0 production, it may be comparable to the Δ^0 production in the region of low electron energies due to the threshold effects. We find that in the energy region of 0.4 to 0.8 GeV, the Λ production could be $\sim$ 80%–17% of the Δ^0 production. The cross sections are of the order of 10^{-41} cm^2 which could be observed at the electron accelerators specifically at MAINZ and JLab with the low energy electron beams.

2) We observe that the differential as well as the total cross section for the Λ production is more sensitive to the variation in the value of M_A as compared to the Σ^0 case. This is because in the case of Λ production the dominant contribution to the cross section comes from the axial vector form factor $g_1(Q^2)$, whereas the vector form factor $f_2(Q^2)$ dominates in the case of Σ^0.

3) $P_L(Q^2)$ and $P_P(Q^2)$ are sensitive to the value of M_A, especially $P_L(Q^2)$ for

Λ as well as Σ^0 production. It will enable us to make the measurements for the axial vector form factor independent of the cross section measurements.

The analysis work presented in this thesis is still under progress. I will calculate absolute cross section for antineutrino DIS interaction in carbon, iron and lead nuclear targets and compare it with the cross section coming from the plastic scintillator part of the MINERvA detector. For the extraction of the structure functions we need to analyze simultaneously both neutrino as well as antineutrino differential scattering cross sections. The plan is to measure the differential scattering cross section for above mentioned nuclear targets as well.

Appendices

Appendix A

Hadronic tensor $J^{\mu\nu}$

A.1 Sachs' electric and magnetic form factors

In the following, we present the various parameterizations available in the literature for the nucleon Sachs' electric and magnetic form factors.

A. BBBA05:

The form of electric and magnetic Sachs form factor given by Bradford et al. [151] (BBBA-05) is

$$\begin{aligned} G_E^p(Q^2) &= \frac{1-0.0578\tau}{1+11.1\tau+13.6\tau^2+33.0\tau^3} \\ \frac{G_M^p(Q^2)}{\mu_p} &= \frac{1+0.15\tau}{1+11.1\tau+19.6\tau^2+7.54\tau^3} \\ G_E^n(Q^2) &= \frac{1.25\tau+1.30\tau^2}{1-9.86\tau+305\tau^2-758\tau^3+802\tau^4} \\ \frac{G_M^n(Q^2)}{\mu_n} &= \frac{1+1.81\tau}{1+14.1\tau+20.7\tau^2+68.7\tau^3}, \qquad \tau=\frac{Q^2}{4M^2}. \end{aligned} \tag{A.1}$$

B. BBA03:

Budd *et al.* [152] parameterized electric and magnetic Sachs form factors as

$$\begin{aligned} G_E^p(Q^2) &= \frac{1}{1+3.253Q^2+1.422Q^4+0.08582Q^6+0.3318Q^8-0.0937Q^{10}+0.01076Q^{12}} \\ \frac{G_M^p(Q^2)}{1+\mu_p} &= \frac{1}{1+3.104Q^2+1.428Q^4+0.1112Q^6-0.00698Q^8+0.00037Q^{10}} \end{aligned}$$

$$\begin{aligned}\frac{G_M^n(Q^2)}{\mu_n} &= \frac{1}{1+3.043Q^2+0.8548Q^4+0.6806Q^6-0.1287Q^8+0.0089Q^{12}} \\ G_E^n(Q^2) &= -\frac{0.942\tau}{1+4.61\tau}G_D(Q^2),\end{aligned} \tag{A.2}$$

with $\mu_p = 1.7927\mu_N$, $\mu_n = -1.913\mu_N$, $M_V = 0.84$ GeV and $\lambda_n = 5.6$ and $G_D(Q^2)$ is parameterized as

$$G_D(Q^2) = \frac{1}{\left(1+\frac{Q^2}{M_V^2}\right)^2}, \tag{A.3}$$

with $M_V = 0.84$ GeV and Q^2 is in units of GeV^2.

C. Galster *et al.*:

The parameterization of electric and magnetic form factors, as given by Galster *et al.* [150]:

$$\begin{aligned} G_E^p(Q^2) &= G_D(Q^2) & G_M^p(Q^2) &= (1+\mu_p)G_D(Q^2) \\ G_M^n(Q^2) &= \mu_n G_D(Q^2) & G_E^n(Q^2) &= (\frac{Q^2}{4M^2})\mu_n G_D(Q^2)\xi_n \\ \xi_n &= \frac{1}{\left(1-\lambda_n\frac{Q^2}{4M^2}\right)}. \end{aligned}$$

D. Platchkov *et al.* (modified Galster):

Platchkov *et al.* modified $G_E^n(Q^2)$ of Galster's parameterization as:

$$G_E^n(Q^2) = -\frac{a\mu_n\tau}{1+b\tau}G_D(Q^2), \tag{A.4}$$

with a=1.51 and b=8.4.

E. Kelly:

The parameterization for $G_E^{p,n}(Q^2)$ and $G_M^{p,n}(Q^2)$ given by Kelly [257] is

$$\begin{aligned} G_E^p(Q^2) &= \frac{1-0.24\tau}{1+10.98\tau+12.82\tau^2+21.97\tau^3} \\ \frac{G_M^p(Q^2)}{\mu_p} &= \frac{1+0.12\tau}{1+10.97\tau+18.86\tau^2+6.55\tau^3} \\ G_E^n(Q^2) &= \frac{1.7\tau}{1+3.3\tau}\frac{1}{(1-Q^2/(0.84)^2)^2} \\ \frac{G_M^n(Q^2)}{\mu_n} &= \frac{1+2.33\tau}{1+14.72\tau+24.20\tau^2+84.1\tau^3} \end{aligned} \tag{A.5}$$

F. Punjabi *et al.* (modified Kelly):

Punjabi *et al.* [255] have modified Kelly's fit [257] for G_E^n and G_E^p by including the new data since the Kelly fit was done. Their best fits for $\mu_n G_E^n/G_M^n$ and $\mu_p G_E^p/G_M^p$ are given as:

$$\begin{aligned} \frac{\mu_n G_E^n}{G_M^n} &= \frac{2.6316\tau}{1+4.118\sqrt{\tau}+0.29516\tau}, \\ \frac{\mu_p G_E^p}{G_M^p} &= \frac{1-5.7891\tau+14.493\tau^2-3.5032\tau^3}{1-5.5839\tau+12.909\tau^2+0.88996\tau^3+0.5420\tau^4}. \end{aligned}$$

G. Alberico *et al.*:

The parameterization for $G_E^{p,n}(Q^2)$ and $G_M^{p,n}(Q^2)$ given by Alberico *et al.* [154] is

$$\begin{aligned} G_E^p(Q^2) &= \frac{1-0.19\tau}{1+11.12\tau+15.16\tau^2+21.25\tau^3} \\ \frac{G_M^p(Q^2)}{\mu_p} &= \frac{1+1.09\tau}{1+12.31\tau+25.57\tau^2+30.61\tau^3} \\ G_E^n(Q^2) &= \frac{1.68\tau}{1+3.63\tau}G_D(Q^2) \\ \frac{G_M^n(Q^2)}{\mu_n} &= \frac{1+8.28\tau}{1+21.30\tau+77\tau^2+238\tau^3}. \end{aligned} \tag{A.6}$$

H. Bosted:

The parameterization for $G_E^{p,n}(Q^2)$ and $G_M^{p,n}(Q^2)$ given by Bosted [153] is

$$\begin{aligned} G_E^p(Q^2) &= \frac{1}{1+0.62Q+0.68Q^2+2.80Q^3+0.83Q^4} \\ \frac{G_M^p(Q^2)}{1+\mu_p} &= \frac{1}{1+0.35Q+2.44Q^2+0.5Q^3+1.04Q^4+0.34Q^5} \\ G_E^n(Q^2) &= -\mu_n\frac{1.25\tau}{1+18.3\tau}G_D(Q^2) \\ \frac{G_M^n(Q^2)}{\mu_n} &= \frac{1}{1-1.74Q+9.29Q^2-7.63Q^3+4.63Q^4}, \end{aligned} \tag{A.7}$$

where $Q=\sqrt{Q^2}$, is in units of GeV.

A.2 Relativistic expression for the hadronic tensor

The hadronic current J^μ is expressed as

$$\begin{aligned} J^\mu &= \bar{u}(p')\left(F_1^V(Q^2)\gamma^\mu + F_2^V(Q^2)i\sigma^{\mu\nu}\frac{q_\nu}{M_p+M_n} + F_3^V(Q^2)\frac{2q^\mu}{M_p+M_n}\right. \\ &+ \left. F_A(Q^2)\gamma^\mu\gamma^5 + F_P(Q^2)\frac{2q^\mu}{M_p+M_n}\gamma^5 + F_3^A(Q^2)\frac{2(p+p')^\mu}{M_p+M_n}\gamma^5\right)u(p). \end{aligned} \tag{A.8}$$

Using the above expression, the hadronic tensor $J^{\mu\nu}$ is obtained as

$$\begin{aligned} J^{\mu\nu} &= 4\left[(F_1^V)^2(p^\mu q^\nu + q^\mu p^\nu + 2p^\mu p^\nu + q^2 g^{\mu\nu}/2) - (F_2^V)^2\left\{\frac{-q^2g^{\mu\nu}}{2} + \left(1+\frac{q^2}{4M^2}\right)\frac{q^\mu q^\nu}{2}\right.\right. \\ &+ \left.\left.\frac{q^2}{4M^2}\left(p^\mu q^\nu + q^\mu p^\nu + 2p^\mu p^\nu\right)\right\} + (F_A)^2\left\{2M^2g^{\mu\nu}\left(\frac{q^2}{4M^2}-1\right) + q^\mu p^\nu + p^\mu q^\nu + 2p^\mu p^\nu\right\}\right. \\ &- (F_P)^2\frac{q^2q^\mu q^\nu}{2M^2} + 2(F_3^V)^2\left(1-\frac{q^2}{4M^2}\right)q^\mu q^\nu - (F_3^A)^2\frac{q^2}{2M^2}\left(2p^\mu+q^\mu\right)\left(2p^\nu+q^\nu\right) \\ &+ F_1^VF_2^V\left(q^2g^{\mu\nu}-q^\mu q^\nu\right) - 2i(F_1^VF_A+F_2^VF_A)\epsilon^{\mu\nu\alpha\beta}p_\alpha q_\beta - 2F_AF_Pq^\mu q^\nu \\ &- F_3^AF_P\frac{q^2}{M^2}(p^\mu q^\nu + q^\mu p^\nu + q^\mu q^\nu) - 2F_3^AF_A\left(p^\mu q^\nu + q^\mu p^\nu + q^\mu q^\nu\right) \\ &+ \left.2F_1^VF_3^V\left(p^\mu q^\nu + q^\mu p^\nu + q^\mu q^\nu\right) + F_2^VF_3^V\frac{q^2}{2M^2}(p^\mu q^\nu + q^\mu p^\nu + q^\mu q^\nu)\right] \end{aligned} \tag{A.9}$$

A.3 Lindhard function

The Lindhard function for the particle hole excitation given by (Fig. 7.1):

$$U_N(q_0,\mathbf{q}) = 2\int \frac{d^3p_n}{(2\pi)^3}\frac{M_nM_p}{E_nE_p}\frac{n_n(\mathbf{p})\left[1-n_p(\mathbf{p}+\mathbf{q})\right]}{q_0+E_n(\mathbf{p})-E_p(\mathbf{p}+\mathbf{q})+i\epsilon}, \tag{A.10}$$

where $q_0{=}E_\nu - E_l$, $n_n(\mathbf{p})$ and $n_p(\mathbf{p}+\mathbf{q})$ are occupation numbers for neutrons and protons, respectively. Taking the imaginary part of the Lindhard function in Eq. (A.10) corresponds to putting the intermediate particles in Fig. 7.1 on shell, thereby describing the process $\nu_l + n \to l^- + p$. In the static limit for the neutron ($E_n \to M_n$) and neglecting any Pauli blocking for the proton ($n_p \to 0$), one recovers the result for the free nucleons.

To evaluate the imaginary part of the Lindhard function(Eq. (A.10)), we use the following relation

$$\frac{1}{\omega \pm i\eta} = \mathcal{P}\frac{1}{\omega} \mp i\pi\delta(\omega). \tag{A.11}$$

which results

$$\mathrm{Im}(U_N(q_0,\mathbf{q})) = -2\pi\int \frac{d^3p_n}{(2\pi)^3}\, n_n(\mathbf{p})\,\left[1-n_p(\mathbf{p}+\mathbf{q})\right]\,\delta(q_0+E_n-E_p)\,\frac{M_pM_n}{E_pE_n}, \tag{A.12}$$

where $n_n(\mathbf{p})$ is the occupation number. Since $\mathbf{q} = \mathbf{p'} - \mathbf{p}$, we have

$$\begin{aligned} E_p &= \sqrt{(\mathbf{p}+\mathbf{q})^2+M^2} = \sqrt{|\mathbf{p}|^2+|\mathbf{q}|^2+2|\mathbf{p}||\mathbf{q}|cos\theta+M^2} \\ \text{and } E_n &= \sqrt{|\mathbf{p}|^2+\mathbf{M^2}}. \end{aligned} \tag{A.13}$$

Using $n_n(\mathbf{p}) = \mathbf{1}$ for $p \le p_{F_n}$, we evaluate Eq. (A.12) to obtain

$$\begin{aligned} \mathrm{Im}U_N(q_0,\mathbf{q}) &= -(2\pi)^2M_pM_n\int_0^{p_{F_n}}\frac{|\mathbf{p_n}|^2\mathbf{d}|\mathbf{p_n}|}{(2\pi)^3}\frac{\left[1-n_p(\mathbf{p}+\mathbf{q})\right]}{\sqrt{|\mathbf{p}|^2+\mathbf{M^2}}}\int_{-1}^{1}d(\cos\theta) \\ &\quad \Big(\frac{1}{\sqrt{|\mathbf{p}|^2+|\mathbf{q}|^2+\mathbf{2}|\mathbf{p}||\mathbf{q}|\cos\theta+\mathbf{M^2}}}\Big) \\ &\quad \delta\Big(q_0+\sqrt{|\mathbf{p}|^2+\mathbf{M^2}}-\sqrt{|\mathbf{p}|^2+|\mathbf{q}|^2+\mathbf{2}|\mathbf{p}||\mathbf{q}|\cos\theta+\mathbf{M^2}}\Big). \end{aligned} \tag{A.14}$$

Using the δ function property

$$\int f(x)\delta\left[g(x)\right]dx = \int f(x)\frac{\delta\left[g(x)\right]}{g'(x)}dg(x) = \sum_i \frac{f(x)}{|\partial g(x_i)/\partial x|}, \tag{A.15}$$

where

$$f(x) = \frac{1}{\sqrt{|\mathbf{p}|^2 + |\mathbf{q}|^2 + 2|\mathbf{p}||\mathbf{q}|cos\theta + M^2}}, \quad (A.16)$$

$$g(x) = q_0 + \sqrt{|\mathbf{p}|^2 + M^2} - \sqrt{|\mathbf{p}|^2 + |\mathbf{q}|^2 + 2|\mathbf{p}||\mathbf{q}|cos\theta + M^2}, \quad (A.17)$$

with $x = \cos\theta$. The points x_i are the real roots of $g(x)$=0 in the interval of integration, i.e.

$$q_0 + \sqrt{|\mathbf{p}|^2 + M^2} - \sqrt{|\mathbf{p}|^2 + |\mathbf{q}|^2 + 2|\mathbf{p}||\mathbf{q}|cos\theta + M^2} = 0$$
$$q_0 + \sqrt{|\mathbf{p}|^2 + M^2} = \sqrt{|\mathbf{p}|^2 + |\mathbf{q}|^2 + 2|\mathbf{p}||\mathbf{q}|cos\theta + M^2}$$

The $\cos\theta$ integral can be performed.

$$\cos\theta = \frac{q_0^2 - |\mathbf{q}|^2 + 2q_0\sqrt{|\mathbf{p}|^2 + M^2}}{2|\mathbf{p}||\mathbf{q}|} \leq 1. \quad (A.18)$$

Further,

$$[1 - n_p(\mathbf{p}+\mathbf{q})] = \Theta(|\mathbf{p}+\mathbf{q}| - p_{F_p}) \quad \Rightarrow \quad (\mathbf{p}+\mathbf{q})^2 > p_{F_p}^2.$$

Using expression for $\cos\theta$, the above expression becomes

$$\sqrt{q_0^2 - |\mathbf{p}|^2 + 2q_0\sqrt{|\mathbf{p}|^2 + M^2}} > p_{F_p}. \quad (A.19)$$

Thus, the expression for the Lindhard function(Eq. (A.14)) is obtained as:

$$\begin{aligned} \mathrm{Im}(U_N(q_0,\mathbf{q})) &= \frac{M_p M_n}{2\pi}\int_0^{p_{F_n}} \frac{d|\mathbf{p}|}{\sqrt{|\mathbf{p}|^2 + M^2}}\,\frac{|\mathbf{p}|}{|\mathbf{q}|}\,\Theta(1 - |\cos\theta|)\,\Theta(A_1 - p_{F_2}) \\ &= \frac{M_p M_n}{2\pi}\int_0^{p_{F_n}} \frac{dE}{|\mathbf{q}|}\,\Theta(1 - |\cos\theta|)\,\Theta(A_1 - p_{F_2}). \quad (A.20) \end{aligned}$$

Applying the kinematical constrain discussed above, we may re-write Eq. (A.20) as

$$\mathrm{Im}U_N(q_0,\mathbf{q}) = -\frac{1}{2\pi}\frac{M_p M_n}{|\mathbf{q}|}\,[E_{F_1} - A] \quad \text{with} \quad (A.21)$$

$$q^2 < 0, \quad E_{F_2} - q_0 < E_{F_1} \text{ and } \frac{-q_0 + |\mathbf{q}|\sqrt{1 - \frac{4M^2}{q^2}}}{2} < E_{F_1}, \quad (A.22)$$

where

$$\begin{aligned} E_{F_1} &= \sqrt{{p_{F_n}}^2 + {M_n}^2}, \quad E_{F_2} = \sqrt{{p_{F_p}}^2 + {M_p}^2} \quad \text{and} \\ A &= \text{Max}\left[M_n,\ E_{F_2} - q_0,\ \frac{-q_0 + |\mathbf{q}|\sqrt{\mathbf{1} - \frac{\mathbf{4M^2}}{\mathbf{q^2}}}}{2} \right]. \end{aligned} \tag{A.23}$$

Otherwise, $\text{Im}(U_N(q_0, \mathbf{q})) = 0$.

The energies E_n and E_p of the neutron and proton in the Lindhard function, refers to the local Fermi sea of the nucleons in the initial and final nucleus.

A.4 N-N correlation and RPA effect

In nuclei, the strength of the electroweak couplings may change from their free nucleon values due to the presence of strongly interacting nucleons. Though CVC forbids any change in the charge coupling, other couplings like magnetic, axial charge and pseudoscalar couplings are likely to change from their free nucleon values. Due to PCAC, the axial current is strongly coupled to the pion field in the nuclear medium and therefore axial couplings are more likely to change due to pionic effects modifying the nuclear response functions. To get an idea of these effects, we perform non-relativistic reduction of the hadronic current, we see the occurrence of $g_1\sigma\tau$, $f_2\sigma \times \mathbf{q}\tau$ and $g_3\sigma \cdot \mathbf{q}\tau$ terms in the weak current which are linked to spin-isospin excitation, while f_2 and g_3 are coupled to transverse and longitudinal channels, g_1 is coupled to both. There exists considerable work in understanding the quenching of magnetic moment and axial charge in nuclei due to the nucleon-nucleon correlations. In our approach, the nucleon-nucleon correlation effects are reflected in the modification of nuclear response in the longitudinal and transverse channels. We calculate this reduction in the vector-axial(VA) and axial-axial(AA) response functions due to the long range nucleon-nucleon correlations treated in the RPA, diagrammatically shown in Fig.(7.3).

The diagram shown in Fig. 7.3 simulates the effects of the strongly interacting

nuclear medium at the weak vertex. The $ph-ph$ interaction is shown by the dashed line in Fig. 7.3 and is described by the π and ρ exchanges modulated by the effect of short range correlations. For the $ph-ph$ potential, we use $V_N(q) = V_\pi(q)+V_\rho(q)$ in terms of the longitudinal and transverse components expressed as

$$V_N(q) = \frac{f^2}{m_\pi^2}\left[V_t(q)(\delta_{ij} - \hat{q}_i\hat{q}_j) + V_l(q)\hat{q}_i\hat{q}_j\right](\sigma_i\sigma_j)(\tau\cdot\tau) \tag{A.24}$$

for the ph case and a similar potential V_Δ in the case of $ph-\Delta$h interaction by substituting $\sigma \to \mathbf{S}$, $\tau \to \mathbf{T}$ and $f \to f^* = 2.15f$. V_l is the strength of the potential in the longitudinal channel and V_t is the strength of the potential in the transverse channel. The representation into longitudinal and transverse channels is useful when one tries to sum the geometric series in Fig.7.3 where the longitudinal and transverse channels decouple and can be summed independently.

Using the matrix elements at the weak WNN vertex and the $ph-ph$ potential, the contribution of Fig.7.3 is written as

$$U(q) = U(q) + U(q)V_N(q)U(q) + U(q)V_N(q)U(q)V_N(q)U(q) + ... \tag{A.25}$$

Writing the potential $V_N(q)$ in terms of V_l and V_t, the series in Eq. (A.25) can be separated in the longitudinal and transverse components using the following relationship

$$\left.\begin{aligned}(\delta_{ij} - \hat{q}_i\hat{q}_j)(\delta_{jl} - \hat{q}_j\hat{q}_l) &= \delta_{il} - \hat{q}_i\hat{q}_l \\ \hat{q}_i\hat{q}_j\hat{q}_j\hat{q}_l &= \hat{q}_i\hat{q}_l \\ (\delta_{ij} - \hat{q}_i\hat{q}_j)\hat{q}_j\hat{q}_l &= 0\end{aligned}\right\}. \tag{A.26}$$

The longitudinal part is then written as

$$\begin{aligned}U_L(q) &= [U(q) + U(q)V_l\hat{q}_i\hat{q}_j\sigma_i\sigma_jU(q) + U(q)V_l\hat{q}_i\hat{q}_k\sigma_i\sigma_kU(q)V_l\hat{q}_k\hat{q}_j\sigma_k\sigma_jU(q) + ...]\ \tau_\mathbf{1}\cdot\tau_\mathbf{2} \\ &= [U(q) + U(q)V_lU(q) + U(q)V_lU(q)V_lU(q) + ...]\ \hat{q}_i\hat{q}_j\ \sigma_i\sigma_j\ \tau_\mathbf{1}\cdot\tau_\mathbf{2} \\ &= U(q)[1 + V_lU(q) + (V_lU(q))^2 + ...]\ \hat{q}_i\hat{q}_j\ \sigma_i\sigma_j\ \tau_\mathbf{1}\cdot\tau_\mathbf{2} \\ &= \left[\frac{U(q)}{1-U(q)V_l}\right]\ \hat{q}_i\hat{q}_j\ \sigma_i\sigma_j\ \tau_\mathbf{1}\cdot\tau_\mathbf{2}.\end{aligned} \tag{A.27}$$

Similarly, the transverse part is given by

$$U_T(q) = \left[\frac{U(q)}{1-U(q)V_t}\right]\ (\delta_{ij} - \hat{q}_i\hat{q}_j)\ \sigma_i\sigma_j\ \tau_\mathbf{1}\cdot\tau_\mathbf{2}. \tag{A.28}$$

Therefore, we can write Eq. (A.27) as:

$$\bar{U}(q) = \left[\left(\frac{U(q)}{1-U(q)V_t}\right)\ (\delta_{ij} - \hat{q}_i\hat{q}_j) + \left(\frac{U(q)}{1-U(q)V_l}\right)\ \hat{q}_i\hat{q}_j\right]\ \sigma_\mathbf{i}\ \sigma_\mathbf{j}\tau_\mathbf{1}\cdot\tau_\mathbf{2}, \tag{A.29}$$

where $U_N \to U = U_N + U_\Delta$, with U_N and U_Δ as the Lindhard function for particle-hole(ph) and Δh excitations, respectively, in the medium and the expressions for U_N and U_Δ are taken from [168]. The different couplings of N and Δ are incorporated in U_N and U_Δ and then the same interaction strengths $V_l(q)$ and $V_t(q)$ are used to calculate the RPA response.

We have followed the prescription of Nieves et al. [148] while taking RPA correlations into account. The difference is that we have also included the contribution coming due to the second class currents.

A.5 Component form of $J^{\mu\nu}$ incorporating RPA in the lowest order

Here the three momentum transfer $\mathbf{q}$ is taken along z-axis and RPA is applied in the leading terms. The different components of the hadronic tensors $J^{\mu\nu}$ with RPA effect are

$$
\begin{aligned}
J^{00}_{\rm RPA} &= 4\Big[2(F_1^V)^2\left(\underline{\mathbf{C_N}}\,E^2(\mathbf{p}) + \frac{\mathbf{q^2}}{\mathbf{4}} + \mathbf{q^0}\mathbf{E}(\mathbf{p})\right) - \frac{q^2}{2}(F_2^V)^2\left(\frac{(q^0)^2}{q^2} + \frac{\mathbf{p^2} + \mathbf{q^0}\mathbf{E}(\mathbf{p}) + \mathbf{(q^0)^2/4}}{M^2}\right)\\
&+ 2(F_A)^2\left(q^0E(\mathbf{p}) + \frac{\mathbf{q^2}}{\mathbf{4}} + \mathbf{p^2}\right) - \underline{\mathbf{C_L}}\,(F_P)^2\frac{q^2q_0^2}{2M^2} + 2(F_3^V)^2(q^0)^2\left(1 - \frac{q^2}{4M^2}\right)\\
&- (F_3^A)^2\frac{q^2}{2}\left(\frac{q^0 + 2E(\mathbf{p})}{M}\right)^2 - \underline{\mathbf{C_N}}F_1^VF_2^V\mathbf{q^2} + \mathbf{2F_1^VF_3^V}(\mathbf{(q^0)^2} + \mathbf{2E(p)q^0})\\
&+ F_2^VF_3^V\frac{q^2}{M^2}\left(E(\mathbf{p})\mathbf{q^0} + \frac{\mathbf{(q^0)^2}}{\mathbf{2}}\right) - 2F_PF_A(q^0)^2 - 4F_AF_3^A\left(E(\mathbf{p})\mathbf{q^0} + \mathbf{(q^0)^2}\right)\\
&- 2F_PF_3^A\frac{q^2}{M^2}\left(E(\mathbf{p})\mathbf{q^0} + \mathbf{(q^0)^2}\right)\Big] \qquad \text{(A.30)}\\
J^{0\tilde{z}}_{\rm RPA} &= 4\Big[(F_1^V)^2\left(\underline{\mathbf{C_N}}E(\mathbf{p})(\mathbf{2p_z} + \mathbf{|q|}) + \mathbf{q^0p_z}\right) - \frac{q^2}{4}(F_2^V)^2\left(\frac{E(\mathbf{p})}{M}\frac{2p_z + |\mathbf{q}|}{M} + 2\frac{q^0|\mathbf{q}|}{q^2} + \frac{q^0(2p_z + |\mathbf{q}|)}{2M^2}\right)\\
&+ (F_A)^2\left(\underline{\mathbf{C_L}}E(\mathbf{p})(\mathbf{2p_z} + \mathbf{|q|}) + \mathbf{q^0p_z}\right) - \underline{\mathbf{C_L}}\,(F_P)^2q^0|\mathbf{q}|\frac{\mathbf{q^2}}{\mathbf{2M^2}} + \mathbf{2(F_3^V)^2q^0|q|}\left(\mathbf{1} - \frac{\mathbf{q^2}}{\mathbf{4M^2}}\right)\\
&- (F_3^A)^2\frac{q^2}{2M^2}(|\mathbf{q}| + \mathbf{2p_z})(\mathbf{q^0} + \mathbf{2E(p)}) - \mathbf{F_1^VF_2^Vq^0|q|} + \mathbf{2F_1^VF_3^V}(\mathbf{E(p)|q|} + \mathbf{q^0p_z} + \mathbf{q^0|q|})\\
&+ F_2^VF_3^V\frac{q^2}{2M^2}(E(\mathbf{p})|\mathbf{q}| + \mathbf{q^0p_z} + \mathbf{q^0}|\mathbf{q}|) - \mathbf{2F_PF_Aq^0|q|} - \mathbf{2F_AF_3^A}(\mathbf{E(p)|q|} + \mathbf{q^0p_z} + \mathbf{q^0|q|})\\
&- F_PF_3^A\frac{q^2}{M^2}(E(\mathbf{p})|\mathbf{q}| + \mathbf{q^0p_z} + \mathbf{q^0}|\mathbf{q}|)\Big] \qquad \text{(A.31)}\\
J^{zz}_{\rm RPA} &= 4\Big[2(F_1^V)^2\left(p_z^2 + |\mathbf{q}|\,\mathbf{p_z} - \frac{\mathbf{q^2}}{\mathbf{4}}\right) - \frac{q^2}{2}(F_2^V)^2\left(\left(\frac{2p_z + |\mathbf{q}|}{2M}\right)^2 + \frac{(q^0)^2}{q^2}\right)\\
&+ 2(F_A)^2M^2\left(\underline{\mathbf{C_L}} + \frac{p_z^2 + |\mathbf{q}|\,\mathbf{p_z} - \mathbf{q^2/4}}{M^2}\right) - \underline{\mathbf{C_L}}\,(F_P)^2\frac{q^2\mathbf{q^2}}{2M^2} + 2(F_3^V)^2\mathbf{q^2}\left(\mathbf{1} - \frac{\mathbf{q^2}}{\mathbf{4M^2}}\right)\\
&- (F_3^A)^2\frac{q^2}{2M^2}(2p_z + |\mathbf{q}|)^2 - (q^0)^2F_1^VF_2^V + 2F_1^VF_3^V(2p_z|\mathbf{q}| + \mathbf{q^2}) + \mathbf{F_2^VF_3^V}\frac{\mathbf{q^2}}{\mathbf{2M^2}}(\mathbf{2p_z|q|} + \mathbf{q^2})
\end{aligned}
$$

$$- \quad F_P F_3^A \frac{q^2}{M^2}(2p_z|\mathbf{q}| + \mathbf{q^2}) - \mathbf{2F_A F_P q^2} - \mathbf{2F_A F_3^A}(\mathbf{2p_z}|\mathbf{q}| + \mathbf{q^2})\Big] \tag{A.32}$$

$$J^{xx}_{\rm RPA} = 4\left[2(F_1^V)^2\left(p_x^2 - \frac{q^2}{4}\right) - \frac{q^2}{2}(F_2^V)^2\left(\underline{\mathbf{C_T}} + \frac{p_x^2}{M^2}\right) + 2F_A^2M^2\left(\underline{\mathbf{C_T}} + \frac{p_x^2 - q^2/4}{M^2}\right)\right.$$

$$\left. - \quad 2(F_3^A)^2\frac{q^2p_x^2}{M^2} - \underline{\mathbf{C_T}}q^2F_1^VF_2^V\right] \tag{A.33}$$

$$J^{xy}_{\rm RPA} = -8\mathrm{i}F_AM^2(F_1^V + F_2^V)\,(\underline{\mathbf{C_T}}|\mathbf{q}|\mathbf{E(p)} - \mathbf{q^0p_z}) \tag{A.34}$$

$$\mathbf{C_N} = \frac{1}{|1 - c_0f'(\rho)U_N(q,k_F)|^2}, \quad \mathbf{C_T} = \frac{1}{|1 - U(q,k_F)V_t(q)|^2}, \quad \mathbf{C_L} = \frac{1}{|1 - U(q,k_F)V_l(q)|^2}$$

where V_l and V_t are the longitudinal and transverse part of the nucleon-nucleon potential calculated with π and ρ exchanges and are given by

$$V_l(q) = \frac{f^2}{m_\pi^2}\left\{\left(\frac{\Lambda_\pi^2 - m_\pi^2}{\Lambda_\pi^2 - q^2}\right)^2\frac{\mathbf{q}^2}{q^2 - m_\pi^2} + g'\right\},$$

$$V_t(q) = \frac{f^2}{m_\pi^2}\left\{C_\rho\left(\frac{\Lambda_\rho^2 - m_\rho^2}{\Lambda_\rho^2 - q^2}\right)^2\frac{\mathbf{q}^2}{q^2 - m_\rho^2} + g'\right\}, \tag{A.35}$$

where $\frac{f^2}{4\pi} = 0.08$, $\Lambda_\pi = 1.2\ GeV$, $m_\pi = 0.14\ GeV$, $C_\rho = 2, \Lambda_\rho = 2.5\ GeV, m_\rho = 0.77\ GeV$ g' is the Landau-Migdal parameter taken to be 0.7 which has been used quite successfully to explain many electromagnetic and weak processes in nuclei. $U(q,k_F) = U_N(q,k_F) + U_\Delta(q,k_F)$ is the Lindhard function for the particle-hole excitation and $U_\Delta(q,k_F)$ is the Lindhard function for the delta-hole excitation. The details are given in Ref.[148, 168].

Appendix B

Expressions for $\mathcal{N}$, $\mathcal{A}$ and $\mathcal{B}$

The expressions for $\mathcal{N}(Q^2, E_{\bar{\nu}_\mu})$ (used in Eq. 9.15), $\mathcal{A}(Q^2, E_{\bar{\nu}_\mu})$ and $\mathcal{B}(Q^2, E_{\bar{\nu}_\mu})$ used in Eq. 9.23 of different polarization components, are given as:

$$
\begin{aligned}
\mathcal{N}(Q^2, E_{\bar{\nu}_\mu}) &= f_1^2(2E_{\bar{\nu}_\mu}(\mathbf{k}\cdot\mathbf{k}' + \mathbf{2ME}_\mu - \mathbf{m}_\mu^2) - \mathbf{2k}\cdot\mathbf{k}'(\mathbf{M_Y} + \mathbf{E}_\mu)) + \\
&\quad \frac{f_2^2}{(M+M_Y)^2}(4(\mathbf{k}\cdot\mathbf{k}')^2(\mathbf{M_Y} + \mathbf{E}_\mu - \mathbf{E}_{\bar{\nu}_\mu}) + \mathbf{k}\cdot\mathbf{k}'(\mathbf{M}(4(\mathbf{E}_\mu^2 + \mathbf{E}_{\bar{\nu}_\mu}^2) - \mathbf{m}_\mu^2) - \\
&\qquad 3m_\mu^2(M_Y + E_\mu - E_{\bar{\nu}_\mu})) - 4Mm_\mu^2 E_{\bar{\nu}_\mu}^2) + \\
&\quad g_1^2(2(\mathbf{k}\cdot\mathbf{k}'(\mathbf{M_Y} - \mathbf{E}_\mu + \mathbf{E}_{\bar{\nu}_\mu}) - \mathbf{E}_{\bar{\nu}_\mu}(\mathbf{m}_\mu^2 - \mathbf{2ME}_\mu))) + \\
&\quad g_3^2((\mathbf{k}\cdot\mathbf{k}')^2\mathbf{m}_\mu^2(\mathbf{M} - \mathbf{M_Y} - \mathbf{E}_\mu + \mathbf{E}_{\bar{\nu}_\mu})) + \\
&\quad \frac{f_1 f_2}{M+M_Y}(8(\mathbf{k}\cdot\mathbf{k}')^2 + \mathbf{k}\cdot\mathbf{k}'(\mathbf{4(M - M_Y)}(\mathbf{E}_\mu - \mathbf{E}_{\bar{\nu}_\mu}) - \mathbf{6m}_\mu^2) + \\
&\qquad 2m_\mu^2 E_{\bar{\nu}_\mu}(M - M_Y)) + \\
&\quad f_1 g_1(-4(\mathbf{k}\cdot\mathbf{k}'(\mathbf{E}_\mu + \mathbf{E}_{\bar{\nu}_\mu}) - \mathbf{m}_\mu^2\mathbf{E}_{\bar{\nu}_\mu})) + \\
&\quad \frac{f_2 g_1}{M+M_Y}(-4(M+M_Y)(\mathbf{k}\cdot\mathbf{k}'(\mathbf{E}_\mu + \mathbf{E}_{\bar{\nu}_\mu}) - \mathbf{m}_\mu^2\mathbf{E}_{\bar{\nu}_\mu})) + \\
&\quad g_1 g_3(-2m_\mu^2(\mathbf{k}\cdot\mathbf{k}' + \mathbf{E}_{\bar{\nu}_\mu}(\mathbf{M_Y} - \mathbf{M}))) \qquad \text{(B.1)} \\
\mathcal{A}(Q^2, E_{\bar{\nu}_\mu}) &= f_1^2(-\mathbf{2k}\cdot\mathbf{k}' - (\mathbf{M} - \mathbf{M_Y})(\mathbf{E}_\mu - \mathbf{E}_{\bar{\nu}_\mu}) + \mathbf{m}_\mu^2) + \\
&\quad \frac{f_2^2}{(M+M_Y)^2}((2\mathbf{k}\cdot\mathbf{k}' - \mathbf{m}_\mu^2)(\mathbf{2k}\cdot\mathbf{k}' + (\mathbf{M} - \mathbf{M_Y})(\mathbf{E}_\mu - \mathbf{E}_{\bar{\nu}_\mu}) - \mathbf{m}_\mu^2)) + \\
&\quad g_1^2(2\mathbf{k}\cdot\mathbf{k}' + (\mathbf{M} + \mathbf{M_Y})(\mathbf{E}_\mu - \mathbf{E}_{\bar{\nu}_\mu}) - \mathbf{m}_\mu^2) + \\
&\quad \frac{f_1 f_2}{M+M_Y}(-2(2\mathbf{k}\cdot\mathbf{k}'(\mathbf{M_Y} + \mathbf{E}_\mu - \mathbf{E}_{\bar{\nu}_\mu}) + \mathbf{M}(\mathbf{E}_\mu - \mathbf{E}_{\bar{\nu}_\mu})^2 + \\
&\qquad m_\mu^2(-(M_Y + E_\mu - E_{\bar{\nu}_\mu})))) + \\
&\quad f_1 g_1(2M_Y(E_\mu + E_{\bar{\nu}_\mu})) + f_1 g_3(m_\mu^2(-M + M_Y + E_\mu - E_{\bar{\nu}_\mu})) + \\
&\quad \frac{f_2 g_1}{M+M_Y}(-4\mathbf{k}\cdot\mathbf{k}'(\mathbf{E}_\mu + \mathbf{E}_{\bar{\nu}_\mu}) + \mathbf{M}(\mathbf{m}_\mu^2 - \mathbf{2E}_\mu^2 + \mathbf{2E}_{\bar{\nu}_\mu}^2) + \mathbf{m}_\mu^2(\mathbf{M_Y} + \mathbf{E}_\mu + \mathbf{3E}_{\bar{\nu}_\mu})) + \\
&\quad \frac{f_2 g_3}{M+M_Y}(m_\mu^2(-\mathbf{2k}\cdot\mathbf{k}' - (\mathbf{M} - \mathbf{M_Y})(\mathbf{E}_\mu - \mathbf{E}_{\bar{\nu}_\mu}) + \mathbf{m}_\mu^2)), \qquad \text{(B.2)} \\
\mathcal{B}(Q^2, E_{\bar{\nu}_\mu}) &= f_1^2((E_\mu + E_{\bar{\nu}_\mu})(\mathbf{2k}\cdot\mathbf{k}' + \mathbf{M_Y}(\mathbf{M_Y} - \mathbf{M})) + \mathbf{m}_\mu^2(\mathbf{M_Y} - \mathbf{2E}_{\bar{\nu}_\mu})) + \\
&\quad \frac{f_2^2}{(M+M_Y)^2}(4(\mathbf{k}\cdot\mathbf{k}')^2(\mathbf{E}_\mu + \mathbf{E}_{\bar{\nu}_\mu}) + \mathbf{2k}\cdot\mathbf{k}'((\mathbf{E}_\mu + \mathbf{E}_{\bar{\nu}_\mu})(\mathbf{M}(\mathbf{M_Y} + \mathbf{2E}_\mu - \mathbf{2E}_{\bar{\nu}_\mu}) + \\
&\qquad M_Y^2) - m_\mu^2(M_Y + E_\mu + 3E_{\bar{\nu}_\mu})) + m_\mu^2(-M(M_Y(E_\mu + E_{\bar{\nu}_\mu}) + 4E_{\bar{\nu}_\mu}(E_\mu - E_{\bar{\nu}_\mu})) + \\
&\qquad m_\mu^2(M_Y + 2E_{\bar{\nu}_\mu}) + M_Y^2(E_\mu - 3E_{\bar{\nu}_\mu}))) + \\
&\quad g_1^2((E_\mu + E_{\bar{\nu}_\mu})(2\mathbf{k}\cdot\mathbf{k}' + \mathbf{M_Y}(\mathbf{M} + \mathbf{M_Y})) - \mathbf{m}_\mu^2(\mathbf{M_Y} + \mathbf{2E}_{\bar{\nu}_\mu})) + \\
&\quad \frac{f_1 f_2}{M+M_Y}(2(M(E_\mu + E_{\bar{\nu}_\mu})(2\mathbf{k}\cdot\mathbf{k}' + \mathbf{M_Y}(\mathbf{E}_{\bar{\nu}_\mu} - \mathbf{E}_\mu)) + \mathbf{m}_\mu^2(\mathbf{M_Y}(\mathbf{M_Y} + \mathbf{E}_\mu) - \\
&\qquad E_{\bar{\nu}_\mu}(2M + M_Y)))) +
\end{aligned}
$$

$$
\begin{aligned}
& f_1 g_1 (2E_\mu (2\mathbf{k}\cdot\mathbf{k}' + \mathbf{M_Y^2}) - \mathbf{2E}_{\bar{\nu}_\mu}(\mathbf{2k}\cdot\mathbf{k}' + \mathbf{4ME}_\mu - \mathbf{2m_\mu^2} + \mathbf{M_Y^2})) + \\
& f_1 g_3 (m_\mu^2 (2\mathbf{k}\cdot\mathbf{k}' - \mathbf{M}(\mathbf{M_Y} + \mathbf{2E}_{\bar{\nu}_\mu}) + \mathbf{M_Y}(\mathbf{M_Y} + \mathbf{E}_\mu - \mathbf{E}_{\bar{\nu}_\mu}))) + \\
& \frac{f_2 g_1}{M + M_Y}(-8(\mathbf{k}\cdot\mathbf{k}')^\mathbf{2} + \mathbf{k}\cdot\mathbf{k}'(\mathbf{6m_\mu^2} - \mathbf{4(ME}_\mu - \mathbf{ME}_{\bar{\nu}_\mu} + \mathbf{M_Y^2})) \\
& \quad + M(m_\mu^2 (M_Y - 2E_{\bar{\nu}_\mu}) - 2M_Y (E_\mu + E_{\bar{\nu}_\mu})^2) + m_\mu^2 M_Y (M_Y + E_\mu + 3E_{\bar{\nu}_\mu})) + \\
& \frac{f_2 g_3}{M + M_Y}(m_\mu^2 ((E_\mu + E_{\bar{\nu}_\mu})(2\mathbf{k}\cdot\mathbf{k}' + \mathbf{M_Y}(\mathbf{M_Y} - \mathbf{M})) + \mathbf{m_\mu^2}(\mathbf{M_Y} - \mathbf{2E}_{\bar{\nu}_\mu}))). \qquad \text{(B.3)}
\end{aligned}
$$

$$
\begin{aligned}
\alpha(Q^2, \mathbf{p}) \;=\; & \frac{64}{M_Y}\Big[f_1^2\left(k\cdot k' k\cdot p - MM_Y\left(k\cdot k' + k'\cdot p - m_\mu^2\right) + k\cdot k' k'\cdot p - k\cdot p m_\mu^2 + k'\cdot p M_Y^2\right) \\
& + \frac{f_2^2}{(M+M_Y)^2}\Big(2k\cdot k'^2(k\cdot p + k'\cdot p + MM_Y) - k\cdot k'\Big(2k\cdot p^2 + 3k\cdot p m_\mu^2 - 2k\cdot p M_Y^2 - 2k'\cdot p^2 \\
& -2k'\cdot p MM_Y + k'\cdot p m_\mu^2 + 3M m_\mu^2 M_Y\Big) + m_\mu^2\Big(2k\cdot p^2 + k\cdot p\left(-2k'\cdot p + m_\mu^2 - 2M_Y^2\right) \\
& + M_Y\left(-k'\cdot pM + k'\cdot pM_Y + M m_\mu^2\right)\Big)\Big) \\
& g_1^2\left(k\cdot k'(k\cdot p + k'\cdot p + MM_Y) - k\cdot p m_\mu^2 + M_Y\left(k'\cdot p(M + M_Y) - M m_\mu^2\right)\right) \\
& \frac{f_1 f_2}{M + M_Y}\Big(2\left(k\cdot k' M(k\cdot p + k'\cdot p) + M_Y(k\cdot p - k'\cdot p)\left(k\cdot k' + k'\cdot p - m_\mu^2\right)\right. \\
& \left. + MM_Y^2\left(m_\mu^2 - k\cdot k'\right) - k\cdot pM m_\mu^2\right)\Big) \\
& + f_1 g_1\left(2\left(k\cdot k'(k'\cdot p - k\cdot p) + k\cdot p\left(m_\mu^2 - 2k'\cdot p\right) + k'\cdot p M_Y^2\right)\right) \\
& + f_1 g_3\left(m_\mu^2(k\cdot k' M - k\cdot p(M + M_Y) + M_Y(k'\cdot p + MM_Y - M))\right) \\
& \frac{f_2 g_1}{M + M_Y}\Big(-4k\cdot k'^2 M + k\cdot k'\left(M\left(2k\cdot p - 2k'\cdot p + 3m_\mu^2\right) - 2M_Y(k\cdot p + k'\cdot p) - 2MM_Y^2\right) \\
& -m_\mu^2(k\cdot p(M - 3M_Y) - M_Y(k'\cdot p + MM_Y + M)) - 2k'\cdot p M_Y(k\cdot p + k'\cdot p)\Big) \\
& + \frac{f_2 g_3}{M + M_Y}\left(m_\mu^2\left(k\cdot k' k\cdot p - MM_Y\left(k\cdot k' + k'\cdot p - m_\mu^2\right) + k\cdot k' k'\cdot p - k\cdot p m_\mu^2 + k'\cdot p M_Y^2\right)\right)\Big] \\
\beta(Q^2, \mathbf{p}) \;=\; & \frac{64}{M_Y}\Big[f_1^2\left(k\cdot p\left(M_Y(M - M_Y) + m_\mu^2\right) - k\cdot k'(k\cdot p + k'\cdot p + MM_Y)\right) \\
& \frac{f_2^2}{(M+M_Y)^2}\Big(-2k\cdot k'^2(k\cdot p + k'\cdot p - MM_Y) + k\cdot k'\left(2k\cdot p^2 - MM_Y\left(2k\cdot p + m_\mu^2\right)\right. \\
& \left. +3k\cdot p m_\mu^2 - 2k'\cdot p^2 + k'\cdot p m_\mu^2 - 2k'\cdot p M_Y^2\right) + k\cdot p m_\mu^2\left(-2k\cdot p + 2k'\cdot p + M_Y(M + M_Y) - m_\mu^2\right)\Big) \\
& g_1^2\left(k\cdot p\left(m_\mu^2 - M_Y(M + M_Y)\right) - k\cdot k'(k\cdot p + k'\cdot p - MM_Y)\right) \\
& \frac{f_1 f_2}{M + M_Y}\left(-2\left(k\cdot k' M(k\cdot p + k'\cdot p) - M_Y(k\cdot k' - k\cdot p)(k\cdot p - k'\cdot p) + k\cdot k' MM_Y^2 - k\cdot pM m_\mu^2\right)\right) \\
& f_1 g_1\left(2\left(k\cdot k'(k\cdot p - k'\cdot p) + k\cdot p\left(2k'\cdot p - m_\mu^2 + M_Y^2\right)\right)\right) \\
& f_1 g_3\left(M m_\mu^2(k\cdot p - k\cdot k')\right) \\
& \frac{f_2 g_1}{M + M_Y}\Big(M\left(4k\cdot k'^2 + k\cdot k'\left(-2k\cdot p + 2k'\cdot p - 3m_\mu^2\right) + k\cdot p m_\mu^2\right) \\
& -2\ M_Y(k\cdot k' - k\cdot p)(k\cdot p + k'\cdot p) + 2k\cdot k' MM_Y^2\Big) \\
& \frac{f_2 g_3}{M + M_Y}\left(m_\mu^2\left(k\cdot p\left(M_Y(M - M_Y) + m_\mu^2\right) - k\cdot k'(k\cdot p + k'\cdot p + MM_Y)\right)\right)\Big] \qquad \text{(B.4)} \\
\eta(Q^2, \mathbf{p}) \;=\; & \frac{64}{M_Y}\Big[f_1^2\left(k\cdot k'(k\cdot p + k'\cdot p) - k\cdot p m_\mu^2\right) \\
& \frac{f_2^2}{(M+M_Y)^2}\left(\left(2(k\cdot k' - k\cdot p + k'\cdot p) - m_\mu^2\right)\left(k\cdot k'(k\cdot p + k'\cdot p) - k\cdot p m_\mu^2\right)\right) \\
& g_1^2\left(k\cdot k'(k\cdot p + k'\cdot p) - k\cdot p m_\mu^2\right) \\
& \frac{f_1 f_2}{M + M_Y}\left(2M\left(k\cdot k'(k\cdot p + k'\cdot p) - k\cdot p m_\mu^2\right)\right) \\
& f_1 g_1\left(2k\cdot k'(k'\cdot p - k\cdot p) + 2k\cdot p\left(m_\mu^2 - 2k'\cdot p\right)\right) \\
& f_1 g_3\left(m_\mu^2(k\cdot k' - k\cdot p)(M - M_Y)\right) \\
& \frac{f_2 g_1}{M + M_Y}\Big(-4k\cdot k'^2 M + k\cdot k'\left(2k\cdot pM - 2k'\cdot pM\right. \\
& \left. +\ m_\mu^2(3M + M_Y)\right) - k\cdot p m_\mu^2(M + M_Y)\Big) \\
& \frac{f_2 g_3}{M + M_Y}\left(k\cdot k' m_\mu^2(k\cdot p + k'\cdot p) - k\cdot p m_\mu^4\right)\Big] \qquad \text{(B.5)}
\end{aligned}
$$

Bibliography

Bibliography

[1] M. Gell-Mann, Phys. Lett. **8**, 214 (1964).

[2] G. Zweig, CERN-TH-401.

[3] W. Pauli, Letter to L. Meitner and her colleagues dated 4 December 1930 (letter open to the participants of the conference in Tübingen) (1930), recorded in W. Pauli, Wissenschaftlicher Briefwechsel mit Bohr, Einstein, Heisenberg u.a ., Band 11(Springer, Berlin, 1985) p. 39. A reference to 'neutrino' is seen in a letter from Heisenberg to Pauli on 1 December 1930: "Zu Deinen Neutronen möchte ich noch bemerken: ..." .

[4] M. Sajjad Athar and S. K. Singh,

Cambridge University Press, Cambridge 2020 doi:10.1017/9781108489065

[5] E. C. G. Sudarshan and R. E. Marshak, *Phys. Rev.* **109**, 1860 (1958).

[6] R. P. Feynman and M. Gell-Mann, *Phys. Rev.* **109**, 193 (1958).

[7] J. J. Sakurai, Nuovo Cim. **7**, 649 (1958).

[8] C. S. Wu, E. Ambler, R. W. Hayward, D. D. Hoppes and R. P. Hudson, *Phys. Rev.* **105**, 1413 (1957).

[9] A. Salam, *Nuovo Cim.* **5**, 299 (1957).

[10] L. D. Landau, *Nucl. Phys.* **3**, 127 (1957).

[11] T. D. Lee, C. N. Yang, *Phys. Rev.* **105**, 1671 (1957).

[12] M. Goldhaber, L. Grodzins and A. W. Sunyar, Phys. Rev. **109** (1958) 1015.

[13] B. Pontecorvo, Sov. Phys. JETP **6** (1957) 429 [Zh. Eksp. Teor. Fiz. **33** (1957) 549].

[14] M. Gell-Mann and A. Pais, Phys. Rev. **97**, 1387 (1955).

[15] Z. Maki, M. Nakagawa and S. Sakata, Prog. Theor. Phys. **28** (1962) 870.

[16] V. N. Gribov and B. Pontecorvo, Phys. Lett. B **28** (1969) 493.

[17] J. N. Bahcall and H. Primakoff, Phys. Rev. D **18**, 3463 (1978); J N Bahcall, Neutrino Astrophysics, Cambridge University Press, Cambridge 1989.

[18] R. Davis, Bull. Am. Phys. Soc., Washington meeting, 1959.

[19] R. Davis, Jr., D. S. Harmer and K. C. Hoffman,

Phys. Rev. Lett. **20**, 1205 (1968).

[20] R. Davis, Prog. Part. Nucl. Phys. **32**, 13 (1994); R. Davis, A. K. Mann and L. Wolfenstein, Ann. Rev. Nucl. Part. Sci. **39**, 467 (1989); R. Davis, Int. J. Mod. Phys. A **18**, 3089 (2003).

[21] J N Bahcall Neutrino Astrophysics, Cambridge University Press, Cambridge 1989.

[22] K. S. Hirata *et al.* [Kamiokande-II Collaboration], Phys. Lett. B **205**, 416 (1988).

[23] K. S. Hirata *et al.* [Kamiokande-II Collaboration], Phys. Rev. Lett. **65**, 1297 (1990).

[24] J. M. LoSecco *et al.*, Phys. Rev. Lett. **54**, 2299 (1985).

[25] Q. R. Ahmad *et al.* [SNO Collaboration], Phys. Rev. Lett. **89**, 011301 (2002).

[26] B. Aharmim *et al.* [SNO Collaboration], Phys. Rev. C **88**, 025501 (2013).

[27] Y. Fukuda *et al.* [Super-Kamiokande Collaboration], Phys. Rev. Lett. **81**, 1562 (1998).

[28] R. Wendell *et al.* [Super-Kamiokande Collaboration], Phys. Rev. D **81**, 092004 (2010)

[29] T. Katori and M. Martini, arXiv:1611.07770 [hep-ph].

[30] J. A. Formaggio and G. P. Zeller, Rev. Mod. Phys. **84**, 1307 (2012).

[31] L. Alvarez-Ruso *et al.* [NuSTEC Collaboration], Prog. Part. Nucl. Phys. **100**, 1 (2018).

[32] R. Acciarri *et al.* [ArgoNeuT Collaboration], Phys. Rev. D **98**, 052002 (2018)

[33] R. Acciarri *et al.* [ArgoNeuT Collaboration], Phys. Rev. D **89**, 112003 (2014).

[34] P. Abratenko *et al.* [MicroBooNE Collaboration], arXiv:2006.00108 [hep-ex].

[35] K. Abe *et al.* [T2K Collaboration], Phys. Rev. D **100**, no. 11, 112009 (2019).

[36] B. Behera [NOvA Collaboration], Springer Proc. Phys. **234**, 329 (2019).

[37] L. Ren *et al.* [MINERvA Collaboration], Phys. Rev. D **95**, no. 7, 072009 (2017) Addendum: [Phys. Rev. D **97**, no. 1, 019902 (2018)].

[38] J. Devan *et al.* [MINERvA Collaboration], Phys. Rev. D **94**, no. 11, 112007 (2016).

[39] C. L. McGivern *et al.* [MINERvA Collaboration], Phys. Rev. D **94**, no. 5, 052005 (2016).

[40] P. Adamson *et al.*, Nucl. Instrum. Meth. A **806**, 279 (2016)

[41] C. G. Callan, Jr. and D. J. Gross, Phys. Rev. Lett. **22**, 156 (1969).

[42] A. D. Martin *et al.*, Eur. Phys. J. C **4**, 463 (1998).

[43] M. Gluck *et al.*, Eur. Phys. J. C **5**, 461 (1998).

[44] M. Gluck *et al.*, Eur. Phys. J. C **53**, 355 (2008).

[45] A. D. Martin *et al.*, Eur. Phys. J. C **63**, 189 (2009).

[46] S. Alekhin *et al.*, arXiv:1609.03327 [hep-ph].

[47] S. Chekanov *et al.* [ZEUS Collaboration], Phys. Rev. D **67**, 012007 (2003).

[48] Z. Zhang [H1 and ZEUS Collaborations], Acta Phys. Polon. Supp. **8**, 957 (2015).

[49] L. Del Debbio *et al.* [NNPDF], JHEP **03**, 039 (2007).

[50] P. M. Nadolsky *et al.*, Phys. Rev. D **78**, 013004 (2008).

[51] A. Accardi, M. E. Christy, C. E. Keppel, W. Melnitchouk, P. Monaghan, J. G. Morfín and J. F. Owens, Phys. Rev. D **81**, 034016 (2010).

[52] L. A. Harland-Lang, A. D. Martin, P. Motylinski and R. S. Thorne, Eur. Phys. J. C **75**, no. 5, 204 (2015).

[53] M. Day and K. S. McFarland, Phys. Rev. D **86**, 053003 (2012).

[54] V. Bernard, N. Kaiser and U. G. Meissner, Phys. Rev. D **50**, 6899 (1994).

[55] V. Bernard, H. W. Fearing, T. R. Hemmert and U. G. Meissner, Nucl. Phys. A **635**, 121 (1998) [Nucl. Phys. A **642**, 563 (1998)].

[56] V. Bernard, T. R. Hemmert and U. G. Meissner, Nucl. Phys. A **686**, 290 (2001).

[57] M. R. Schindler, T. Fuchs, J. Gegelia and S. Scherer, Phys. Rev. C **75**, 025202 (2007).

[58] A. Tsapalis, eConf C **070910**, 168 (2007).

[59] C. Andreopoulos *et al.*,

Nucl. Instrum. Meth. A **614**, 87 (2010).

[60] Y. Hayato, Acta Phys. Polon. B **40**, 2477 (2009).

[61] D. Casper, Nucl. Phys. Proc. Suppl. **112**, 161 (2002).

[62] T. Golan, J. T. Sobczyk and J. Zmuda, Nucl. Phys. Proc. Suppl. **229-232**, 499 (2012).

[63] O. Lalakulich, K. Gallmeister and U. Mosel, J. Phys. Conf. Ser. **408**, 012053 (2013).

[64] R. A. Smith and E. J. Moniz, Nucl. Phys. B **43**, 605 (1972) [Erratum-ibid. B **101**, 547 (1975)].

[65] C. H. Llewellyn Smith, Phys. Rept. **3**, 261 (1972).

[66] T. K. Gaisser and J. S. O'Connell, Phys. Rev. D **34**, 822 (1986).

[67] F. Akbar *et al.*, Int. J. Mod. Phys. E **24**, 1550079 (2015).

[68] A. A. Aguilar-Arevalo *et al.* [MiniBooNE Collaboration], Phys. Rev. Lett. **120**, no. 14, 141802 (2018)

[69] F. Akbar, M. Sajjad Athar and S. K. Singh, J. Phys. G **44**, no. 12, 125108 (2017).

[70] N. Cabibbo, E. C. Swallow, R. Winston, Annu. Rev. Nucl. Part. Sci. **53**, 39 (2003).

[71] J. M. Gaillard, G. Sauvage, Annu. Rev. Nucl. Part. Sci. **34**, 351 (1984).

[72] A. Garcia, P. Kielanowski, in Lect. Notes Phys., edited by A. Bohm, Vol. **222** (Springer,1985).

[73] O. Erriquez et al., Phys. Lett. B **70**, 383 (1977).

[74] T. Eichten et al., Phys. Lett. B **40**, 593 (1972).

[75] O. Erriquez *et al.*, Nucl. Phys. B **140**, 123 (1978).

[76] G. Fanourakis et al., Phys. Rev. D **21**, 562 (1980).

[77] V. V. Ammosov et al., Z Phys. C **36**, 377 (1987).

[78] V. V. Ammosov et al., JETP Lett. **43**, 716 (1986) [Pisma Zh. Eksp. Teor. Fiz. **43**, 554 (1986)].

[79] J. Brunner et al. [SKAT Collaboration], Z. Phys. C **45**, 551 (1990).

[80] J. S. Bell and S. M. Berman, Nuovo Cim., **25**, 404, (1962).

[81] F. Chilton, Nuovo Cim. **31**, 447 (1964).

[82] S. L. Adler, Nuovo Cim. **30**, 1020 (1965).

[83] L. Egardt, Nuovo Cim. **29**, 954 (1963).

[84] N. Cabibbo and F. Chilton, Phys. Rev. **137**, B1628 (1965).

[85] A. Pais, Annals Phys. **63**, 361 (1971).

[86] R. E. Marshak, Riazuddin, C. P. Ryan, *Theory of Weak Interactions in Particle Physics* (Wiley-Interscience, 1969).

[87] C. H. Llewellyn Smith, Phys. Rep. **3**, 261 (1972).

[88] J. Finjord and F. Ravndal, Nucl. Phys. B **106**, 228 (1976).

[89] M. M. Block et al., Phys. Rev. Letts. **12**, 262 (1964).

[90] A. Sirlin, Nuovo Cim. **37**, 137 (1965).

[91] S. K. Singh and M. J. Vicente Vacas, Phys. Rev. D **74**, 053009 (2006).

[92] S. L. Mintz and L. Wen, Eur. Phys. J. A **33**, 299 (2007).

[93] S. L. Mintz and L. L. Wen, Nucl. Phys. A **766**, 219 (2006).

[94] K. S. Kuzmin and V. A. Naumov, Phys. Atom. Nucl. **72**, 1501 (2009)

[95] J. J. Wu and B. S. Zou, Few Body Syst. **56**, 165 (2015).

[96] M. Rafi Alam, M. Sajjad Athar, S. Chauhan, S. K. Singh, J. Phys. G **42**, 055107 (2015).

[97] http://www.fnal.gov/

[98] http://j-parc.jp/index-e.html

[99] R. Acciarri *et al.* [MicroBooNE Collaboration], JINST **12**, no. 02, P02017 (2017).

[100] O. Palamara [ArgoNeuT Collaboration], Nucl. Phys. Proc. Suppl. **217**, 189 (2011).

[101] R. Acciarri et al. [DUNE Collaboration], for DUNE at LBNF," arXiv:1512.06148 [physics.ins-det].

[102] L. Fields *et al.* [MINERνA Collaboration], Phys. Rev. Lett. **111**, 022501 (2013).

[103] A Proposal for a Three Detector Short-Baseline Neutrino Oscillation Program in the Fermilab Booster Neutrino Beam arXiv:1503.01520v1.

[104] F. Akbar, M. Rafi Alam, M. Sajjad Athar, S. K. Singh, Phys. Rev. D **94**, 114031 (2016).

[105] F. Akbar, M. Sajjad Athar, A. Fatima and S. K. Singh, Eur. Phys. J. A **53**, 154 (2017).

[106] Nuruzzaman, POT for the Medium Energy Run, internal Document (2017).

[107] P. Adamson, *et al.*, The NuMI Neutrino Beam, Nucl. Instrum. Meth. A **806** 279–306 (2016). arXiv:1507.06690, doi:10.1016/j.nima.2015.08.063.

[108] https://targets.fnal.gov/NuMI_neutrino_beam.html

[109] https://lss.fnal.gov/archive/thesis/2000/fermilab-thesis-2005-73.pdf

[110] https://arxiv.org/pdf/1705.03075.pdf

[111] MINERvA DocDB 12235

[112] https://lss.fnal.gov/archive/thesis/2000/fermilab-thesis-2016-03.pdf

[113] pdf copy of Cheryl's Thesis

[114] https://www.fnal.gov/pub/science/particle-accelerators/accelerator-complex.html

[115] Fermilab target systems. https://targets.fnal.gov/NuMI_target.html

[116] https://targets.fnal.gov/NuMI_horns.html

[117] Internal document, DocDB 27462, https://minerva-docdb.fnal.gov/cgi-bin/private/ShowDocument?docid=27462

[118] Nuclear Instruments and Methods in Physics Research A 806 (2016) 279–306.

[119] arXiv:1507.06690 [physics.acc-ph]

[120] L. Aliaga et al., Design, calibration, and performance of the MINERvA detector. Nucl. Instrum. Methods A743, 130–159 (2014).

[121] http://tomaszgolan.github.io/reveal_talks/html/ml_ift_seminar.html?print-pdf

[122] http://tomaszgolan.github.io/reveal_talks/html/minerva_review.html?print-pdf

[123] Minos Collaboration, D. G. Michael, P. Adamson, T. Alexopoulos, W. W. M. Allison, G. J. Alner, K. Anderson, C. Andreopoulos, M. Andrews, R. Andrews, , et al., The magnetized steel and scintillator calorimeters of the MINOS experiment, Nuclear Instruments and Methods in Physics Research A 596 (2008) 190–228. arXiv:0805.3170, doi:10.1016/j.nima.2008.08.003.

[124] https://journals.aps.org/prd/pdf/10.1103/PhysRevD.81.072002

[125] G. N. Perdue, Event Reconstruction in MINERvA (slide 15) , internal Document (2015). URL https://minerva-docdb.fnal.gov/cgi-bin/private/RetrieveFile?docid=10017

[126] R. Fruhwirth, Application of Kalman filtering to track and vertex fitting, Nucl. Instrum. Meth. A262 (1987) 444–450.

[127] W. D. Hulsbergen, Decay chain fitting with a Kalman filter, Nuclear Instruments and Methods in Physics Research A 552 (2005) 566–575.

[128] T HE MINOS COLLABORATION , P-875: A Long-baseline Neutrino Oscillation Experiment at the Fermilab, Technical report (1996) 105.

[129] P. Adamson et al. [MINOS Collaboration], Phys. Rev. D 81 (2010) 072002.

[130] Anne Norrick, DocDB ID 12851 Updated Calorimetry Tech Note, internal Document (2017). https://minerva-docdb.fnal.gov/cgi-bin/private/ShowDocument?docid=12851

[131] Oscar Moreno, DocDB ID 27737 Using the MINERvA Downstream Calorimeters, internal Document (2020). https://minerva-docdb.fnal.gov/cgi-bin/private/RetrieveFile?docid=27737&filename=TechnicalNotes.pdf&version=1

[132] Internal document, DocDB 16995. https://minerva-docdb.fnal.gov/cgi-bin/private/RetrieveFile?docid=16995&filename=MachineLearningVertexing.pdf&version=

[133] I. Goodfellow, Y. Bengio, A. Courville, Deep Learning, MIT Press, 2016, http://www.deeplearningbook.org.

[134] C. M. Bishop, Pattern Recognition and Machine Learning (Information Science and Statistics), 1st Edition, Springer, 2007.

[135] M. A. Nielsen, Neural Networks and Deep Learning, Determination Press, 2015.

[136] G. N. Perdue, et al., MINERvA collaboration *Reducing model bias in a deep learning classifier using domain adversarial neural networks in the MINERvA experiment*, JINST 13 11 P11020, 2018.

[137] C. M. Bishop, Pattern recognition and machine learning, 5th Edition, Information science and statistics, Springer, 2007.

[138] G. Perdue el at., Journal of Instrumentation, Volume 13, Number 11, 2018

[139] I. Goodfellow, Y. Bengio, A. Courville, Deep Learning, MIT Press, 2016, http://www.deeplearningbook.org.

[140] https://alphabold.com/neural-networks-and-deep-learning-an-overview/

[141] M. Abadi, et al., TensorFlow: Large-scale machine learning on heterogeneous systems, software available from tensorflow.org (2015). URL https://www.tensorflow.org/

[142] G. D'Agostini, A multidimensional unfolding method based on Bayes' theorem, Nuclear Instruments and Methods in Physics Research A 362 (1995) 487–498.

[143] M. Sajjad Athar, S. Chauhan and S. K. Singh, Eur. Phys. J. A **43**, 209 (2010).

[144] M. Sajjad Athar, S. Chauhan and S. K. Singh, J. Phys. G **37**, 015005 (2010).

[145] M. Sajjad Athar, S. Ahmad and S. K. Singh, Eur. Phys. J. A **24**, 459 (2005).

[146] M. Sajjad Athar and S. K. Singh, Phys. Rev. C **61**, 028501 (2000).

[147] S. K. Singh and E. Oset, Nucl. Phys. A **542**, 587 (1992).

[148] J. Nieves, J. E. Amaro and M. Valverde, Phys. Rev. C **70**, 055503 (2004) [Phys. Rev. C **72**, 019902 (2005)].

[149] S. Weinberg, Phys. Rev. **112**, 1375 (1958).

[150] S. Galster, H. Klein, J. Moritz, K. H. Schmidt, D. Wegener and J. Bleckwenn, Nucl. Phys. B **32**, 221 (1971).

[151] R. Bradford, A. Bodek, H. S. Budd and J. Arrington, Nucl. Phys. Proc. Suppl. **159**, 127 (2006).

[152] H. Budd, A. Bodek and J. Arrington, Nucl. Phys. (Proc. Suppl.) **139**, 90 (2005).

[153] P. E. Bosted, Phys. Rev. C **51**, 409 (1995).

[154] W. M. Alberico, S. M. Bilenky, C. Giunti and K. M. Graczyk, Phys. Rev. C **79**, 065204 (2009).

[155] V. Bernard, L. Elouadrhiri and U. G. Meissner, J. Phys. G **28**, R1 (2002).

[156] L. A. Ahrens *et al.*, Phys. Lett. B **202**, 284 (1988).

[157] T. Bhattacharya, V. Cirigliano, S. D. Cohen, A. Filipuzzi, M. Gonzalez-Alonso, M. L. Graesser, R. Gupta and H. W. Lin, Phys. Rev. D **85**, 054512 (2012).

[158] V. Cirigliano, S. Gardner and B. Holstein, Prog. Part. Nucl. Phys. **71**, 93 (2013).

[159] C. W. de Jager *et al.*, Atomic data and Nuclear data tables, **14**, 479 (1974); H. de Vries *et al.*, Atomic data and Nuclear data tables, **36**, 495 (1987).

[160] C. Garcia-Recio, J. Nieves and E. Oset, Nucl. Phys. A **547**, 473-487 (1992).

[161] S. K. Singh and E. Oset, Phys. Rev. C **48**, 1246 (1993).

[162] Quantum Theory of Many-Particle Systems by Alexander L. Fetter and John Dirk Walecka, McGraw-Hill, New York, 1971

[163] C. Itzykson and J.-B. Zuber, Quantum Field Theory, McGraw-Hill, 1980.

[164] J. Engel, Phys. Rev. C **57**, 2004 (1998).

[165] K. S. Kim, L. E. Wright, Y. Jin and D. W. Kosik, Phys. Rev. C **54**, 2515 (1996).

[166] M. Traini, Nucl. Phys. A **694**, 325 (2001).

[167] A. Aste, C. von Arx, and D. Trautmann, Eur. Phys. J. A **26** 167 (2005).

[168] E. Oset, D. Strottman, H. Toki and J. Navarro, Phys. Rev. C **48**, 2395 (1993); E. Oset, P. Fernandez de Cordoba, L. L. Salcedo and R. Brockmann, Phys. Rept. **188**, 79 (1990).

[169] G. A. Fiorentini *et al.* [MINERνA Collaboration], Phys. Rev. Lett. **111**, 022502 (2013).

[170] Y. Nakajima *et al.* [SciBooNE Collaboration], Phys. Rev. D **83**, 012005 (2011).

[171] V. Lyubushkin *et al.* [NOMAD Collaboration], Eur. Phys. J. C **63**, 355 (2009).

[172] R. Gran *et al.* [K2K Collaboration], Phys. Rev. D **74**, 052002 (2006).

[173] A. A. Aguilar-Arevalo *et al.* [MiniBooNE Collaboration], Phys. Rev. D **82**, 092005 (2010).

[174] A. A. Aguilar-Arevalo *et al.* [MiniBooNE Collaboration], Phys. Rev. D **81**, 092005 (2010).

[175] A. A. Aguilar-Arevalo *et al.* [MiniBooNE Collaboration], Phys. Rev. D **88**, 032001 (2013).

[176] M. Dorman [MINOS Collaboration], AIP Conf. Proc. **1189**, 133 (2009).

[177] A. Bodek, S. Avvakumov, R. Bradford and H. S. Budd, Eur. Phys. J. C **53**, 349 (2008).

[178] J. Nieves, I. Ruiz Simo and M. J. Vicente Vacas, Phys. Lett. B **707**, 72 (2012).

[179] M. Martini, M. Ericson and G. Chanfray, Phys. Rev. C **84**, 055502 (2011).

[180] M. Martini, M. Ericson and G. Chanfray, Phys. Rev. D **87**, 013009 (2013).

[181] A. M. Ankowski, O. Benhar and M. Sakuda, Phys. Rev. D **91**, 033005 (2015).

[182] O. Lalakulich, U. Mosel and K. Gallmeister, Phys. Rev. C **86**, 054606 (2012).

[183] K. S. Kuzmin, V. V. Lyubushkin and V. A. Naumov, Eur. Phys. J. C **54**, 517 (2008).

[184] A. Bodek, arXiv:0709.4004 [hep-ex].

[185] K. M. Graczyk, Phys. Lett. B **732**, 315 (2014).

[186] A. De Rujula, R. Petronzio and A. Savoy-Navarro, Nucl. Phys. B **154**, 394 (1979).

[187] C. Patrignani *et al.* [Particle Data Group], Chin. Phys. C **40**, 100001 (2016).

[188] L. Alvarez-Ruso, Y. Hayato and J. Nieves, New J. Phys. **16**, 075015 (2014).

[189] K. N. Abazajian *et al.*, arXiv:1204.5379 [hep-ph].

[190] K. Abe *et al.* [T2K Collaboration], K. Abe *et al.* [T2K Collaboration], arXiv:1706.04257 [hep-ex]. Phys. Rev. Lett. **112**, 061802 (2014).

[191] M. Antonello *et al.* [MicroBooNE and LAr1-ND and ICARUS-WA104 Collaborations], arXiv:1503.01520 [physics.ins-det].

[192] Y. T. Tsai [MicroBooNE Collaboration], arXiv:1705.07800 [hep-ex].

[193] Marcos Dracos, Physics Procedia 61, 459 (2015).

[194] E. Baussan *et al.* [ESSnuSB Collaboration], Nucl. Phys. B **885**, 127 (2014)

[195] W. G. S. Vinning and A. Blake, arXiv:1705.06561 [hep-ph].

[196] J. Cao *et al.*, Phys. Rev. ST Accel. Beams **17**, 090101 (2014)

[197] D. Adey, R. Bayes, A. Bross and P. Snopok, Ann. Rev. Nucl. Part. Sci. **65**, 145 (2015).

[198] A. Liu, A. Bross, D. Neuffer and S. Y. Lee, PAC-2013-TUPBA18, FERMILAB-CONF-13-451-APC.

[199] S. Ajimura *et al.*, arXiv:1705.08629 [physics.ins-det].

[200] M. Harada *et al.*, arXiv:1601.01046 [physics.ins-det].

[201] M. Harada *et al.*, arXiv:1502.02255 [physics.ins-det].

[202] S. Axani, G. Collin, J. Conrad, M. Shaevitz, J. Spitz and T. Wongjirad, Phys. Rev. D **92**, 092010 (2015).

[203] J. Spitz, Phys. Rev. D **89**, 073007 (2014).

[204] J. Spitz, Phys. Rev. D **85**, 093020 (2012).

[205] J. Grange Private communication.

[206] C. Rott, S. In, J. Kumar and D. Yaylali, JCAP **1701**, 016 (2017).

[207] S. Agostinelli *et al.* [GEANT4 Collaboration], Nucl. Instrum. Meth. A **506**, 250 (2003).

[208] N. V. Mokhov *et al.*, Radiat. Prot. Dosim. **116**, 99 (2005)

[209] C. Juszczak, "Running NuWro," Acta Phys. Polon. B **40**, 2507 (2009); http://borg.ift.uni.wroc.pl/nuwro/

[210] M. Martini, M. Ericson, G. Chanfray and J. Marteau, Phys. Rev. C **80**, 065501 (2009).

[211] J. Nieves, F. Sanchez, I. Ruiz Simo and M. J. Vicente Vacas, Phys. Rev. D **85**, 113008 (2012).

[212] O. Benhar, N. Farina, H. Nakamura, M. Sakuda and R. Seki, Phys. Rev. D **72**, 053005 (2005).

[213] T. S. Kosmas and E. Oset, Phys. Rev. C **53**, 1409 (1996).

[214] J. Engel, E. Kolbe, K. Langanke and P. Vogel, Phys. Rev. C **54**, 2740 (1996).

[215] N. Auerbach, N. Van Giai and O. K. Vorov, Phys. Rev. C **56**, R2368 (1997).

[216] S. K. Singh, N. C. Mukhopadhyay and E. Oset, Phys. Rev. C **57**, 2687 (1998).

[217] C. Volpe, N. Auerbach, G. Colo, T. Suzuki and N. Van Giai, Phys. Rev. C **62**, 015501 (2000).

[218] A. C. Hayes and I. S. Towner, Phys. Rev. C **61**, 044603 (2000).

[219] E. Kolbe, K. Langanke and P. Vogel, Nucl. Phys. A **652**, 91 (1999).

[220] E. Kolbe, K. Langanke, G. Martinez-Pinedo and P. Vogel, J. Phys. G **29**, 2569 (2003).

[221] N. Paar, D. Vretenar, T. Marketin and P. Ring, Phys. Rev. C **77**, 024608 (2008).

[222] N. Auerbach and B. A. Brown, Phys. Rev. C **65**, 024322 (2002).

[223] N. Paar, D. Vretenar and P. Ring, J. Phys. G **35**, 014058 (2008).

[224] J. Nieves and J. E. Sobczyk, Annals Phys. **383**, 455 (2017).

[225] M. Albert *et al.* [LSND Collaboration], Phys. Rev. C **51**, 1065 (1995).

[226] C. Athanassopoulos *et al.* [LSND Collaboration], Phys. Rev. C **56**, 2806 (1997).

[227] L. B. Auerbach *et al.* [LSND Collaboration], Phys. Rev. C **66**, 015501 (2002).

[228] M. Sajjad Athar and S. K. Singh, Phys. Lett. B **591**, 69 (2004).

[229] M. Sajjad Athar, S. Ahmad and S. K. Singh, Phys. Rev. C **71**, 045501 (2005).

[230] M. Sajjad Athar, S. Ahmad and S. K. Singh, Nucl. Phys. A **764**, 551 (2006).

[231] S. Chauhan, M. Sajjad Athar and S. K. Singh, Int. J. Mod. Phys. E **26**, 1750047 (2017).

[232] A. R. Samana, F. Krmpotic, N. Paar and C. A. Bertulani, J. Phys. Conf. Ser. **312**, 072009 (2011).

[233] R. A. Smith and E. J. Moniz, Nucl. Phys. B **43**, 605 (1972).

[234] N. Van Dessel, N. Jachowicz, R. González-Jiménez, V. Pandey and T. Van Cuyck, arXiv:1704.07817 [nucl-th].

[235] A. Nikolakopoulos, V. Pandey, J. Spitz and N. Jachowicz, arXiv:2010.05794 [nucl-th].

[236] R. Gonzalez-Jimenez, A. Nikolakopoulos, N. Jachowicz, and J.M. Udias, Phys. Rev. C **100**, 045501 (2019).

[237] M. Martini, M. Ericson, G. Chanfray, and J. Marteau, Phys. Rev. C **80**, 065501 (2009); M. Martini, M. Ericson, and G. Chanfray, Phys. Rev. C **84**, 055502 (2011).

[238] D. Casper, Nucl. Phys. Proc. Suppl. **112**, 161 (2002).

[239] C. Juszczak, Acta Phys. Pol. B **40**, 2507 (2009); T. Golan, C. Juszczak, and J. Sobczyk, Phys. Rev. C **86**, 015505 (2012).

[240] C. Andreopoulos *et al.*, Nucl. Instr. Meth. A **614**, 87 (2010).

[241] P. Huber, M. Mezzetto and T. Schwetz, JHEP **0803**, 021 (2008).

[242] K. A. Olive et al. (Particle Data Group), Chin. Phys. C, **38**, 090001 (2014).

[243] Y. Nambu, Phys. Rev. Lett. **4**, 380 (1960).

[244] J. G. Morfin, J. Nieves and J. T. Sobczyk, Adv. High Energy Phys. **2012**, 934597 (2012).

[245] H. Gallagher, G. Garvey and G. P. Zeller, Ann. Rev. Nucl. Part. Sci. **61**, 355 (2011).

[246] K. L. Miller et al., Phys. Rev. D **26**, 537 (1982).

[247] N. J. Baker et al., Phys. Rev. D **23**, 2499 (1981).

[248] T. Kitagaki et al., Phys. Rev. D **28**, 436 (1983).

[249] A. Bodek, M. E. Christy and B. Coopersmith, Eur. Phys. J. C **74**, 3091 (2014).

[250] A. S. Meyer, M. Betancourt, R. Gran and R. J. Hill, arXiv:1603.03048 [hep-ph].

[251] S. M. Bilenky, *Basics of Introduction to Feynman Diagrams and Electroweak Interactions Physics* (Editions Frontières, 1994).

[252] S. M. Bilenky, E. Christova, J. Phys. G **40**, 075004 (2013).

[253] S. M. Bilenky, E. Christova, Phys. Part. Nucl. Lett. **10**, 651 (2013).

[254] S. Platchkov et al., Nucl. Phys. A **510**, 740 (1990).

[255] V. Punjabi, C. F. Perdrisat, M. K. Jones, E. J. Brash and C. E. Carlson, Eur. Phys. J. A **51**, 79 (2015).

[256] K. Abe et al. [T2K Collaboration], Phys. Rev. Lett. **116**, 181801 (2016); Phys. Rev. D **91**, 072010 (2015); Phys. Rev. D **92**, 112003 (2015).

[257] J. J. Kelly, Phys. Rev. C **70**, 068202 (2004).

[258] N. Armenise et al., Nucl. Phys. B **152**, 365 (1979).

[259] M. Rafi Alam, M. Sajjad Athar, S. Chauhan, S. K. Singh, Phys. Rev. D **88**, 077301 (2013).

[260] L. Alvarez-Ruso, S. K. Singh, M. J. Vicente Vacas, Phys. Rev. C **57**, 2693 (1998).

[261] O. Lalakulich, E. A. Paschos, G. Piranishvili, Phys. Rev. D **74**, 014009 (2006).

[262] C. Wilkinson *et al.*, Phys. Rev. D **93**, 072010 (2016).

[263] A. M. Ankowski, O. Benhar, C. Mariani, E. Vagnoni, Phys. Rev. D **93**, 113004 (2016).

[264] P. Stowell, S. Cartwright, L. Pickering, C. Wret, C. Wilkinson, arXiv:1611.03275 [hep-ex].